

LEVEL

AGARD-AG-264

AGARD-AG-264

AGARD

ADVISORY GROUP FOR AEROSPACE RESEARCH & DEVELOPMENT

7 RUE ANCELLE 92200 NEUILLY SUR SEINE FRANCE

AD A 1 0 6 0 3 0

AGARDograph No. 264

Aircraft Excrescence Drag

This document has been approved for public release and sale; its distribution is unlimited.

DTIC
ELECTIC
S OCT 22 1981 D

A

DTIC FILE COPY

NORTH ATLANTIC TREATY ORGANIZATION



DISTRIBUTION AND AVAILABILITY
ON BACK COVER

81 10 21

14

NORTH ATLANTIC TREATY ORGANIZATION
ADVISORY GROUP FOR AEROSPACE RESEARCH AND DEVELOPMENT
(ORGANISATION DU TRAITE DE L'ATLANTIQUE NORD)

11 J 1 8 1

AGARDograph No. 264

1

AIRCRAFT EXCRESCENCE DRAG

by

10

A.D. Young
Queen Mary College (University of London)

and

J.H. Paterson
Lockheed-Georgia Company

Edited by

J. Lloyd Jones
Past Chairman, Fluid Dynamics Panel

12

J 1 1 2

This AGARDograph was prepared at the request of the Fluid Dynamics Panel of AGARD.

400043

THE MISSION OF AGARD

The mission of AGARD is to bring together the leading personalities of the NATO nations in the fields of science and technology relating to aerospace for the following purposes:

- Exchanging of scientific and technical information;
- Continuously stimulating advances in the aerospace sciences relevant to strengthening the common defence posture;
- Improving the co-operation among member nations in aerospace research and development;
- Providing scientific and technical advice and assistance to the North Atlantic Military Committee in the field of aerospace research and development;
- Rendering scientific and technical assistance, as requested, to other NATO bodies and to member nations in connection with research and development problems in the aerospace field;
- Providing assistance to member nations for the purpose of increasing their scientific and technical potential;
- Recommending effective ways for the member nations to use their research and development capabilities for the common benefit of the NATO community.

The highest authority within AGARD is the National Delegates Board consisting of officially appointed senior representatives from each member nation. The mission of AGARD is carried out through the Panels which are composed of experts appointed by the National Delegates, the Consultant and Exchange Programme and the Aerospace Applications Studies Programme. The results of AGARD work are reported to the member nations and the NATO Authorities through the AGARD series of publications of which this is one.

Participation in AGARD activities is by invitation only and is normally limited to citizens of the NATO nations.

The content of this publication has been reproduced directly from material supplied by AGARD or the authors.

Published July 1981

Copyright © AGARD 1981
All Rights Reserved

ISBN 92-835-1392-4



*Printed by Technical Editing and Reproduction Ltd
Harford House, 7-9 Charlotte St, London, W1P 1HD*

SUMMARY

A review has been undertaken of the available data on the subject of the drag of excrescences on aircraft surfaces. Information from this review has been summarized and resented in a way that is readily usable for prediction and design purposes. The basic characteristics of boundary layers are discussed and, where possible, the drag of excrescences is related to those characteristics.

In particular, because the size of many types of surface imperfection is small in comparison with boundary layer thicknesses, the drag of such imperfections can be correlated in terms of the properties of inner regions of the boundary layer. Several previously published analyses of this type are highlighted and, where possible, extensions to other data sources or other types of excrescence are presented. The practical problems of applying these data in the varying velocity gradients existing on aircraft surfaces are treated and one section is devoted to the drag of auxiliary air inlet and exit openings. Gaps in existing data which offer opportunities for research effort are pointed out.

Accession For	
ADP	<input checked="" type="checkbox"/>
ADP	<input type="checkbox"/>
ADP	<input type="checkbox"/>
Classification	
No.	
Distribution	
Availability Codes	
Dist	Special
A	

CONTENTS

<u>Section</u>	<u>Title</u>	<u>Page</u>
	SUMMARY	iii
	NOMENCLATURE	ix
1.	INTRODUCTION	1
2.	BASIC CHARACTERISTICS OF BOUNDARY LAYERS	3
2.1	Laminar and Turbulent Boundary Layers on Smooth Surfaces	3
2.1.1	Introductory Remarks	3
2.1.2	Boundary Layer Velocity Profiles and Basic Skin Friction Laws	5
2.1.3	The Boundary Layer Equations	14
2.1.4	Prediction Methods (Two-Dimensional Incompressible Flow)	16
2.1.5	Extension to Compressible Flow and Three Dimensions	18
2.2	Roughness Effects on Transition	21
2.2.1	Introduction	21
2.2.2	The First Critical Roughness Height $k_{crit.1}$	22
2.2.3	The Second Critical Roughness Height $k_{crit.2}$	26
2.2.4	The Effects of Sweep	27
3.	DISTRIBUTED ROUGHNESS IN TURBULENT BOUNDARY LAYERS (ZERO OR SMALL PRESSURE GRADIENTS)	34
3.1	Basic Effects - Sand Roughness and Critical Roughness Heights	34
3.2	Velocity Distributions in the Boundary Layer	39
3.3	Equivalent Sand Roughness Concept	45
3.4	Discontinuous Changes of Roughness	47
4.	DISCRETE ROUGHNESS	
4.1	General Considerations	50
4.2	Individual Excrescences or Protuberances	51
4.2.1	Fastener Drag	51
4.2.1.1	Method A: Young (1939), Reference 4.8	54
4.2.1.2	Method B: Schlichting (1936), Reference 4.13	55
4.2.1.3	Method C: Wieghardt (1942), Later Hoerner	58
4.2.1.4	Method D: Modified Wieghardt Correlation	60
4.2.2	Two-Dimensional Cylinders	61
4.2.2.1	Circular Cylinder Drag	61
4.2.2.2	Roughness Effects	62
4.2.2.3	Cross-Sectional Shape Variations	62
4.2.2.4	Cylinder Inclined to Flow (Wires)	64
4.2.3	Finite Length Cylinders	65
4.2.3.1	Cylinders Deeply Submerged in the Boundary Layer	65
4.2.3.2	General Method for Cylinders in a Turbulent Boundary Layer	66
4.2.3.3	Cylinders Completely Submerged in Boundary Layer	70
4.2.3.4	Cylinders Extending Outside the Boundary Layer	70

CONTENTS (Cont'd)

<u>Section</u>	<u>Title</u>	<u>Page</u>
4.2.4	Stub Wings/Antennae	70
4.2.5	Drag of Holes and Surface Cut-Outs	71
	4.2.5.1 Circular Holes	72
	4.2.5.2 Holes with Elliptical Planform	74
	4.2.5.3 Holes with Rectangular Planform	76
4.3	Spanwise/Longitudinal Discontinuities	76
4.3.1	Spanwise Steps and Ridges	77
	4.3.1.1 Forward - Facing Step	77
	4.3.1.1.1 Two-Dimensional Step Normal to the Flow	77
	4.3.1.1.2 Effect of Chamfering or Rounding	80
	4.3.1.1.3 Effect of Flow Angle	82
	4.3.1.2 Rearward - Facing Step	82
	4.3.1.2.1 Two-Dimensional Step Normal to the Flow	82
	4.3.1.2.2 Effects of Chamfering or Rounding	85
	4.3.1.2.3 Effect of Flow Angle	87
4.3.2	Combined Forward and Aft Facing Steps - Ridges and Plates	87
	4.3.2.1 Two-Dimensional Ridge Normal to the Flow with Vertical Faces	88
	4.3.2.2 Ridges with Different Cross-Section	93
	(a) Rounded Edges	93
	(b) Other Profile Shapes	95
	4.3.2.3 Effect of Flow Angle	96
	4.3.2.4 Multiple Ridges in Series	97
4.3.3	Gaps and Grooves	98
	4.3.3.1 Gaps Normal or Parallel to the Flow	99
	4.3.3.2 Gaps Inclined to the Flow	100
4.3.4	Surface Waviness	101
5.	FLOW OVER ROUGH SURFACES WITH NON-UNIFORM PRESSURE DISTRIBUTION	106
5.1	Drag and Momentum Loss Magnification Factors of Isolated Excrescences	106
5.2	Modification Factors for Multiple Excrescences and Distributed Roughnesses	111
5.3	Effect of Excrescences on C_{LMAX} of Airfoils	116
5.4	The Effect of Control Gaps	118
5.5	Prediction Methods for Distributed Roughness	121
6.	DRAG OF AUXILIARY INLETS AND OUTLETS	136
6.1	Introduction	136
6.2	Auxiliary Inlets	138
	6.2.1 Protruding Inlets	139
	6.2.2 Submerged Inlets	141
	6.2.3 Flush Inlets	145

CONTENTS (Cont'd)

<u>Section</u>	<u>Title</u>	<u>Page</u>
6.3	Auxiliary Outlets	146
6.3.1	Protruding Outlets	146
6.3.2	Flush Outlets	148
6.3.3	Recessed Outlets	152
6.3.4	Drains	152
6.4	Leakage Drag	153
6.4.1	Non Pressurized Aircraft	154
6.4.2	Pressurized Aircraft	155
6.5	Supplementary Information	156
7.	CONCLUDING REMARKS AND SUGGESTIONS FOR FUTURE RESEARCH	158
	ACKNOWLEDGEMENTS	159

NOMENCLATURE

a	pipe radius
A,B,C,D	Constants in "law of the wall" velocity distribution equation
A	cross section area of air inlet or exit
A_F	aspect ratio of air inlet or exit
c	chord
C_D	wing drag coefficient, $D/q_o S_w$
C_{De}	excrecence drag coefficient, $D/q_e f_e$
C_{Dm}	excrecence drag coefficient, $D/\bar{q} f_e$
C_{DP}	excrecence drag coefficient, $D/q_e S_p$
$C_{D\delta}$	drag coefficient of excrecence having height equal to boundary layer thickness, $D/q_o f_e$
$C_{D\infty}$	drag coefficient of cylinder of infinite length
C_{D_w}	component drag coefficient, $D/q_o f_e$
C_f	local skin friction coefficient, $2\tau_w / \rho_w V_o^2$
C_{fe}	local skin friction coefficient, $2\tau_w / \rho_w u_e^2$
C_F	skin friction coefficient of complete body
C_T	thrust coefficient, thrust/ $q_o A$
D	drag
ΔD	drag increase due to excrecence
d	diameter of excrecence
f_e	projected frontal area of excrecence
h^+	roughness Reynolds number, $u_\tau h/\nu$
H	boundary layer shape factor, δ^*/θ
H_1	boundary layer shape factor, $(\delta - \delta^*)/\theta$
ΔH	loss of total pressure
h	height of discrete roughness; mean enthalpy per unit mass
k	height of distributed roughness

k_s	equivalent sand grain roughness
$k_{crit.1}$	maximum roughness height which will not cause transition
$k_{crit.2}$	minimum roughness height which will result in transition immediately behind roughness
K	von Karman constant, 0.4-0.41
l	length proportional to mixing length
M	Mach number
m_d	drag magnification factor
m_m	momentum magnification factor
m_i	inlet mass flow per unit area, $\rho_i V_i$
m_o	free stream mass flow per unit area, $\rho_o V_o$
q	dynamic pressure
q_o	free stream dynamic pressure
q_e	local dynamic pressure at edge of boundary layer
\bar{q}	mean dynamic pressure from surface to height of excrescence
r	radius of curvature, or recovery factor
R	Reynolds number (subscript indicates characteristic length) C-chord, θ -momentum thickness, x-length from stagnation point
T	temperature (with following subscripts) W-wall e-edge of boundary layer
S_p	planform area of excrescence
S_w	wing planform area
u	velocity component in streamwise direction
u_e	local velocity at edge of boundary layer
u_h	local velocity at height of roughness element
u_τ	friction velocity, $(\tau_w / \rho_w)^{1/2}$
u^+	u/u_τ
u'	fluctuating component of longitudinal velocity
\bar{U}	mean longitudinal velocity

V_0	undisturbed freestream velocity
V_i	inlet velocity
V_e	outlet velocity
W_e	weight flow from exit
x	surface length from stagnation point
y	height above surface
y^+	$y u_\tau / \nu$
δ_i	thickness of viscous sublayer
α	inclination of cylinder from flow direction
γ	intermittency factor or ratio of specific heats
δ	boundary layer thickness, also ramp angle, flap angle
δ^*	displacement thickness = $\int_0^\delta (1-U/U_e) dy$
θ	momentum thickness, also submerged inlet inclination angle, exhaust flow angle relative to free stream
μ	viscosity
ν	kinematic viscosity, μ/ρ
ρ	mass density
τ_i	laminar shear stress, $\mu du/dy$
τ_t	turbulent eddy shear stress, $-\overline{\rho u'v'}$
τ_w	wall shear stress

1. INTRODUCTION

In the highly competitive field of aircraft development and procurement, aerodynamic performance is frequently the outstanding factor in final decisions. It is very important therefore for aerodynamic designers, and for technical evaluators, to be able to predict aircraft drag with the best possible precision. Relatively small advantages in speed or in fuel consumption can contribute significantly to operational efficiency of transport aircraft, and for combat aircraft, small margins in performance may be ultimately decisive. In addition to these basic considerations, conservation of fuel is becoming a more and more important independent criterion in the design of all types of aircraft.

Surface imperfections have long been recognized as a drag source and numerous studies have been devoted to quantifying this drag problem. These studies have been approached in various ways in the course of aerodynamic development with the result that information on this subject exists in many widely diverse forms. Reference 1.1, first published in 1951, contains a chapter on drag due to surface irregularities which is an excellent collection of data available (in later editions) up to about 1955. Since that time, a greater understanding of boundary layer phenomena and of roughness drag mechanisms has been developed, and through that understanding substantive generalizations have been made possible in a number of cases. Later experimental work has also been dedicated to Mach number and Reynolds number regimes which are pertinent to modern aircraft. Recent useful, if brief, reviews are provided in References 1.5 and 1.6.

When proper attention is paid to design and manufacturing tolerances, the roughness drag of transport aircraft can be reduced to rather small (but still significant) values. Drag attributable to this source on the Lockheed C-5 airplane is estimated to be approximately 3-1/2% of cruise drag (Reference 1.2). At the time the C-5 was designed, it was felt that the smoothness standards accepted represented a rational compromise of fabrication costs versus performance benefits. As fuel costs continue to rise, a reassessment of this question might justify more stringent specifications. On smaller aircraft the same machining and assembly tolerances of course result in greater relative roughness, and for fighter aircraft, larger ratios of wetted area to wing area cause a further escalation.

Reference 1.3 presents a detailed review of three fighter aircraft showing that roughness drag varied from about 10% to 20% of total drag at subsonic speeds. When considered in comparison with other configuration changes which could cause the same drag increment, this roughness drag assumes rather large significance. It is also apparent that, if all other factors were constant, a fighter aircraft with roughness at the low end of this range would enjoy a substantial advantage over an adversary at the high end.

In a paper presented in 1967 (Reference 1.4), Haines reviewed the drag of a number of transport aircraft. A breakdown of drag sources on those aircraft indicates contributions from surface imperfections and excrescences varying from 15% to 24-1/2% of profile drag which probably represents 8% to 12% of cruise drag. A detailed analysis of the drag effects of excrescences on the VFW 614 aircraft (a small short range aircraft) in Reference 1.7 leads to a similar penalty of 22% of the profile drag. References 1.2, 1.3, and 1.4 each present details on the specific roughness items which contribute to this extraneous drag. The outstanding indication from these details, however, is the fact that the problem is all-pervasive. Roughness drag can be minimized only by aggressive attention to details of the surface condition of all parts of the aircraft.

The objective of this work is, therefore, to provide up to date information on the drag of surface imperfections. Modern boundary layer theory is reviewed to highlight the phenomena underlying drag due to surface roughnesses to provide an understanding of the mechanisms of such drag increases. The authors have attempted to collect the best available methods for prediction of roughness drag increments in the light of that basic understanding.

It is expected that this collection of information will be of assistance to aircraft designers who must assess the drag resulting from surface imperfections and make decisions on cost effective design and manufacturing standards. Finally, it is hoped that the review presented here will highlight those areas where data are meager or lacking and will therefore provide the incentive for further research and development.

REFERENCES

- | | | | |
|-----|---|------|--|
| 1.1 | Hoerner, S. F. | 1958 | Fluid Dynamic Drag (2nd Edition), published by the author. |
| 1.2 | Paterson, J. H.
Mac Wilkenson, D. G.
& Blackerby, W. T. | 1973 | A Survey of Drag Prediction Techniques Applicable to Subsonic and Transonic Aircraft Design. AGARD CP No. 124 Aerodynamic Drag, Paper 1. |
| 1.3 | Horton, E. A. &
Tetervin, N. | 1962 | Measured Surface Defects on Typical Transonic Airplanes and Analysis of their Drag Contribution. NASA TND-1024. |
| 1.4 | Haines, A. B. | 1967 | Subsonic Aircraft Drag: An Appreciation of Present Standards. ARA Wind Tunnel Note No. 66. |
| 1.5 | Bertelrud, A. | 1978 | A Literature Survey of Surface Roughness on the Drag of Subsonic Aircraft. FFA Tech. Note AU-1224. |
| 1.6 | Bertelrud, A. | 1978 | A Practical Method for Predicting Roughness Effects on Aircraft. FFA Tech. Note AU-1413. |
| 1.7 | Kranczoch, M. | 1978 | Widerstandsverbesserungsprogramm VFW 614 - Teil. Schädlicher Oberflächenwiderstand. Vereinigte Flugtechnische Werke - Fokker. |

2. BASIC CHARACTERISTICS OF BOUNDARY LAYERS

2.1 Laminar & Turbulent Boundary Layers on Smooth Surfaces

2.1.1 Introductory Remarks

In this section we shall briefly review the main features of boundary layers on smooth surfaces and the associated theories since they are an essential preliminary to the consideration of the effects of roughness. We shall only present the subject in summary form since it is a vast one and is well covered in existing text books (see for example References 2.1, 2.2, 2.3, 2.4). We shall largely confine the discussion to two-dimensional incompressible flow but shall briefly indicate the extension of the topics discussed to three-dimensional and compressible flow where convenient.

In most engineering situations involving a body immersed in a fluid moving relative to it the Reynolds number based on the relative velocity and a typical body length is very large compared with unity. In such cases we can identify a thin layer of fluid adjacent to the body surface in which the velocity relative to the body changes rapidly with distance normal to the surface from zero at the surface (the "no-slip condition") to the local freestream velocity at the outer edge of the layer. The layer is therefore a region of large rate of shear and in consequence viscous stresses can be important within it, but outside the layer these stresses are generally negligible and the flow behaves as if it were inviscid. This layer is known as the boundary layer.

Over some forward part of the body we find that the flow in the boundary layer is laminar, i.e. the fluid particles follow smooth paths. Then at some stage, depending on the pressure distribution, the level of free stream disturbances and the surface condition, the flow in the boundary layer more or less rapidly changes to turbulent and the process of this change is called transition. In turbulent flow the fluid particles experience random variations in velocity magnitude and direction additional to their mean motion and typically the fluctuations in velocity magnitude can be of the order of 10% of the mean velocity. These fluctuations introduce momentum transport terms in the equations of motion additional to and generally much larger than those associated directly with viscosity and these transport terms can be regarded as equivalent to additional stresses usually referred to as Reynolds stresses or eddy stresses. Similar eddy transport terms arise in the energy equation.

If x denotes the distance from the forward stagnation point along a body surface in the streamwise direction and δ denotes the boundary layer thickness then for a laminar boundary layer $\delta/x \propto R_x^{-1/2}$, where $R_x = V_0 x/\nu$, V_0 being the undisturbed main stream velocity and ν the kinematic viscosity. If τ_w denotes the shear stress at the surface (or skin friction) then we define the skin friction coefficient as $c_f = 2\tau_w/\rho V_0^2$, where ρ is the fluid density, and we find that likewise $c_f \propto R_x^{-1/2}$ for a laminar boundary layer. With the boundary layer turbulent we find that to a good approximation $\delta/x \propto R_x^{-n}$ and $c_f \propto R_x^{-n}$, where n is about $1/5$. Thus, for a flat plate at zero incidence in a uniform stream and hence with zero pressure gradient:-

$\delta/x \approx 5R_x^{-1/2}$ and $c_f = 0.664 R_x^{-1/2}$, with the boundary layer laminar, and $\delta/x \approx 0.37 R_x^{-1/5}$ and $c_f \approx 0.06 R_x^{-1/5}$, with the boundary layer turbulent. These figures illustrate how thin the boundary layer is in most practical applications where the characteristic Reynolds number is rarely less than 10^4 and can reach values of the order of 10^9 .

The thinness of the boundary layer and the associated high rate of shear are used to justify approximations to the equations of motion of a viscous fluid (the Navier-Stokes equations) as well as the equation of energy which lead to the so-called boundary layer equations. In particular velocity and temperature gradients with respect to x are treated as small compared with the gradients with respect to y , the distance normal to the surface, and this is reflected in the relative magnitudes of the corresponding stresses and heat conduction terms. A consequence is that the pressure change across the boundary layer can generally be neglected. It is also inferred that the thin boundary layer displaces the external "inviscid" flow outwards by a small amount (the so-called "displacement thickness") and hence slightly displaces the effective boundary of the external flow from the body surface. However, for many purposes this weak interaction between boundary layer flow and external flow can be ignored.

The above discussion relates strictly to unseparated boundary layers. But in the presence of a strong enough streamwise rise in pressure the innermost regions of the boundary layer can be so retarded as to reverse in flow direction beyond some point and then the boundary layer develops into a separated shear layer moving away from the surface over an inner region of upstream moving flow. The boundary layer is then said to be separated, and if the external flow is not time-dependent the point at the surface where the gradient of the streamwise velocity component (u) with respect to y is zero is referred to as the separation point. With a separating boundary layer the interaction between it and the external flow can be strong, since the separated boundary layer can move a considerable distance from the body and so profoundly modify the effective shape of the boundary which determines the external flow. Thus, flow separation from a wing at high enough incidence is the cause of the stall and is associated with a marked reduction of lift, an increase of drag and development of pressure fluctuations and buffeting. The reversed flow plus the inner region of the separated shear layer comprise a relatively large scale eddy which tends to be unstable and is convected downstream whilst it breaks up into smaller eddies, meanwhile a new eddy forms from the wing surface to take its place and so on. Hence the associated pressure fluctuations and buffeting.

The streamwise extent of the region over which the transition from laminar to turbulent flow takes place depends strongly on the Reynolds number. At Reynolds numbers less than about 10^6 in terms of body length the transition region can be of significant extent, but for Reynolds numbers greater than about 2×10^6 it is sufficiently small to be regarded as a point (or line in three dimensions) referred to as the transition point (or line). Laminar and turbulent boundary layers have very different characteristics. The turbulent boundary layer is fuller in velocity profile, grows at a faster rate, has a greater frictional stress at the surface and is much less easily caused to separate than the laminar boundary layer. The transition process is a manifestation of the tendency to instability of the laminar boundary layer and this tendency is enhanced not only by increase of Reynolds number but by positive (adverse) pressure gradients and surface imperfections.

The main effects of such imperfections and excrescences in general on drag are threefold. Firstly, they can cause transition to occur upstream of its position on a smooth surface, and to that extent they increase the drag because of the greater streamwise extent of turbulent boundary layer flow. Secondly, local flow separations may occur from the excrescences which involve increased momentum losses and therefore increased drag. If the excrescences are well immersed in the boundary layers the eddies associated with these separations are small, being of scale comparable to the excrescence size and they are then readily absorbed into the general structure of the boundary layer turbulence. If the excrescences are large in relation to the boundary

layer then they will result in correspondingly large eddying wakes which can strongly interact with the external flow. Thirdly, under conditions of strong, positive pressure gradients surface imperfections and excrescences even when well immersed in the boundary layer, may by virtue of their effect on the boundary layer trigger an earlier flow separation from the surface than would occur if the surface were smooth.

2.1.2 Boundary Layer Velocity Profiles and Basic Skin Friction Laws

For the attached laminar boundary layer on a surface with prescribed pressure distribution the velocity distribution at any streamwise station can be determined as accurately as one wishes from the boundary layer equations and prescribed boundary conditions (see Section 2.1.3) since they require no further assumptions for their solution. The velocity profile on a flat plate in a uniform pressure distribution in incompressible flow is illustrated in Figure 2.1 where u/u_e is plotted as a function of $\zeta = y/2 \sqrt{u_e/\nu x}$, u_e is the free stream velocity at the outer edge of the boundary layer. It can be approximately fitted by various formulae of which the simplest offering a tolerably good fit in terms of y/δ is

$$\frac{u}{u_e} = \sin\left(\frac{\pi}{2} \frac{y}{\delta}\right), \quad (1)$$

where δ is the boundary layer thickness. The thickness δ cannot be defined exactly since strictly the boundary layer extends to infinity in the y direction, but in practice at all but small distances depending on the Reynolds number the difference in velocity ($u_e - u$) is small enough to be neglected. Thus we may choose to define δ as the value of y for which $u = 0.995 u_e$, say; this provides a unique definition and δ is then small enough in relation to x for the boundary layer assumptions to be seen to be valid for Reynolds numbers of normal engineering interest.

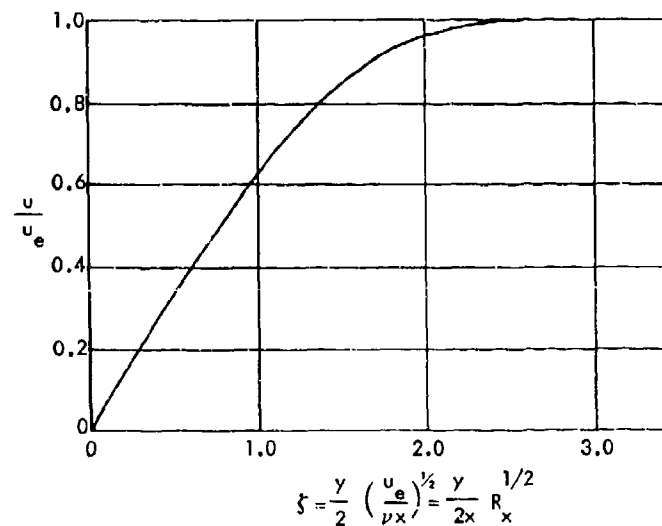


Figure 2.1. Velocity Distribution in Laminar Boundary Layer on Flat Plate at Zero Incidence (Blasius Profile)

In the presence of a negative (favourable) pressure gradient the velocity profile is fuller than that for zero pressure gradient, whilst with a positive (adverse) pressure gradient the profile is less full and develops a point of inflection. We have already noted that in a sufficiently strong adverse pressure gradient, there can develop a reversal with separation of the boundary layer (see Figure 2.2).

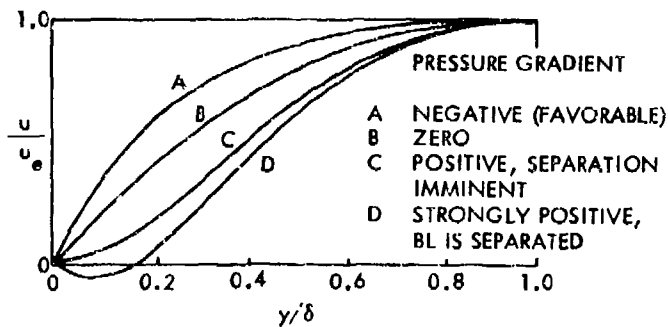


Figure 2.2. Typical Velocity Distributions for Laminar Boundary Layer in Negative Zero and Positive Pressure Gradients

A typical turbulent boundary layer profile is much fuller than a laminar boundary layer profile and consequently has a higher shear stress at the surface. This is because the vigorous mixing associated with the turbulence helps to even out the velocity distribution across the boundary layer. Figure 2.3 shows a typical profile for a turbulent boundary layer on a flat plate in zero pressure gradient in incompressible flow compared with that for a laminar boundary layer. Adverse and favourable pressure gradients change the profile in the same sense as for a laminar boundary layer but to a much smaller degree, and it generally requires a much greater pressure rise to cause a turbulent boundary layer to separate.

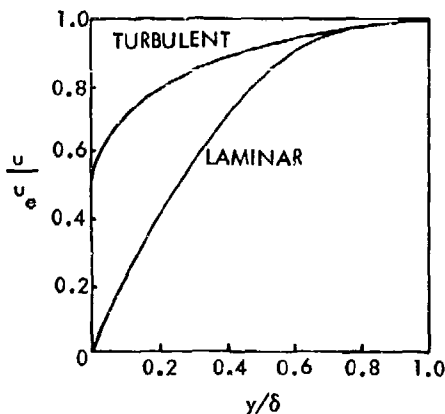


Figure 2.3. Typical Velocity Distributions for Laminar and Turbulent Boundary Layers on a Flat Plate at Zero Incidence

An empirically determined overall approximation to a turbulent boundary layer velocity profile in incompressible flow in zero or small pressure gradients is the so-called power law:-

$$\frac{u}{u_\tau} = C_1 \left(\frac{y u_e}{\nu} \right)^{1/n} \quad 2(2)$$

where $u_\tau = \sqrt{\tau_w/\rho}$ (the friction velocity) and C_1 is a constant. The number n is usually taken as 7 for a range of Reynolds numbers in terms of x from about 5×10^5 to 10^7 , with $C_1 = 8.74$. For higher Reynolds numbers in the range 10^6 to 10^8 a closer fit to experimental data is given by $n = 9$ with $C_1 = 10.6$. From 2(2) it follows that

$$\frac{u}{u_\tau} = \left(\frac{y}{\delta} \right)^{1/n} \quad 2(3)$$

From equation 2(2) and the use of the momentum integral equation (see Section 2.1.3) one can readily deduce a number of useful empirical relations between δ , c_f , C_F , R_x , R_c and R_θ for the basic case of a flat plate at zero incidence in incompressible flow. Here C_F is the overall skin friction coefficient for one face of a plate of chord c (i.e. $C_F = 1/c \int_0^\delta c_f \cdot dx$),

$R_c = u_e c / \nu$, $R_\theta = u_e \theta / \nu$, and θ is the momentum thickness:-

$$\theta = \int_0^\delta \frac{u}{u_e} \left(1 - \frac{u}{u_e}\right) dy$$

These relations are

$$\left. \begin{aligned} \delta/x &= 0.37 R_x^{-1/5}, & c_f &= 0.0592 R_x^{-1/5}, & C_F &= 0.074 R_c^{-1/5} \\ & & c_f &= 0.026 R_\theta^{-1/4}, & & \end{aligned} \right\} \text{for } n=7$$

and

$$\left. \begin{aligned} \delta/x &= 0.27 R_x^{-1/6}, & c_f &= 0.0375 R_x^{-1/6}, & C_F &= 0.0450 R_c^{-1/6} \\ & & c_f &= 0.0176 R_\theta^{-1/5}, & & \end{aligned} \right\} \text{for } n=9$$
2 (4)

Somewhat closer and more general approximations to experimental data for the skin friction coefficients are provided by the Prandtl-Schlichting semi-empirical relations:-

$$\left. \begin{aligned} c_f &= (2 \log_{10} R_x - 0.65)^{-2.3} \\ C_F &= 0.455 (\log_{10} R_c)^{-2.58} \end{aligned} \right\}$$
2 (5)

These relations are compared with the corresponding ones for a laminar boundary layer in Figure 2.4 & 2.5.

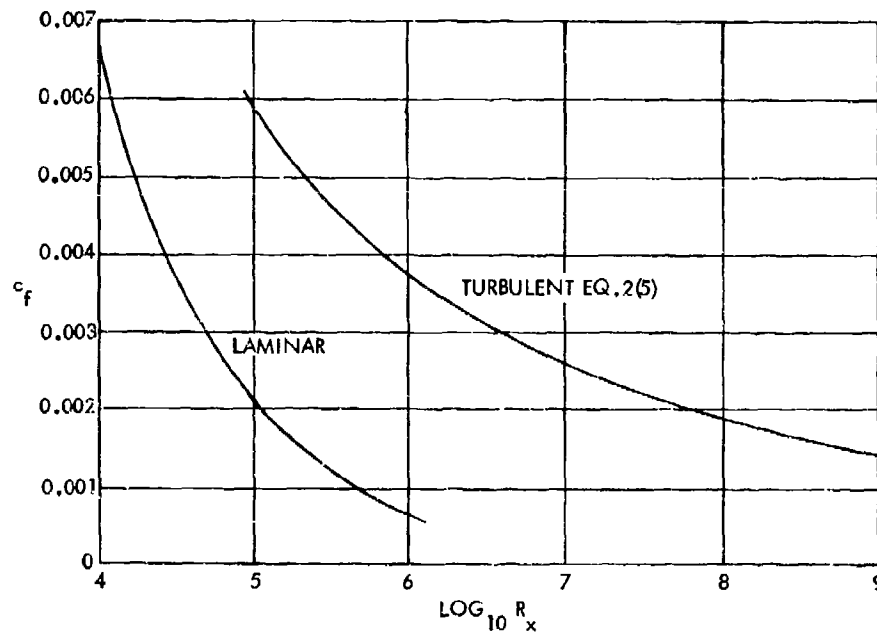


Figure 2.4. $c_f - R_x$ Relations for Laminar and Turbulent Boundary Layers on a Smooth Flat Plate at Zero Incidence

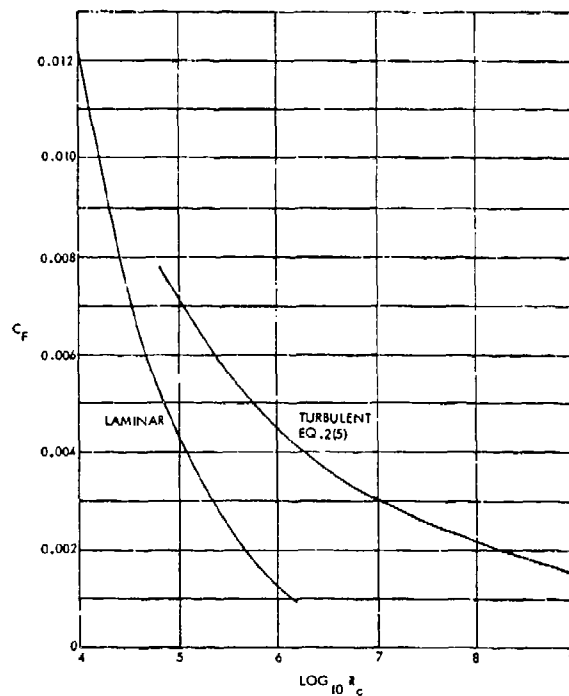


Figure 2.5. $C_F - R_c$ Relations for Laminar and Turbulent Boundary Layers on a Smooth Flat Plate at Zero Incidence

A detailed examination of the structure of the turbulent boundary layer on a smooth surface reveals that it can be conveniently regarded as made up of three regions. Adjacent the surface there is the viscous sub-layer in which the turbulent fluctuations are relatively small and the dominant shear stress is the purely viscous one, $\tau_t = \mu \partial u / \partial y$, which is generally regarded as constant across the sub-layer. This layer is very thin, its thickness y_t is given by $y_t u_t / \nu = O(10)$ and is of the order of one hundredth of the boundary layer thickness. Above the sub-layer there is an inner region of the boundary layer about 0.4δ in thickness in which the turbulence intensity is large, the flow is continuously turbulent and the dominant shear stress is the Reynolds stress, $\tau_t = -\rho \overline{u'v'}$. Here, dashes denote the turbulence velocity components, and a bar denotes a time mean. A wide spectrum of eddy sizes and frequencies are present in this region. From about 0.4δ upwards there is an outer region characterised by large low frequency eddies. The outer edge of the boundary layer therefore presents a convoluted appearance at any instant and the smooth curve with which it is normally represented is really a time mean. The turbulence at any point in this outer region is not continuous but intermittent reflecting the passage of large eddies with intervals of laminar flow between them. We speak of an intermittency factor γ , which is the fraction of time that hot wire measurements at a point show the flow there to be turbulent, and decreases from 1.0 at about $y = 0.4 \delta$ to zero at about $y = 1.2 \delta$ (see Figure 2.6 from Reference 2.5). The Reynolds stress continues to be far greater than the viscous stress in the outer region just as it is in the inner region. It should be emphasised that the three regions merge into each other, the boundaries between them cannot be identified with any precision and can change with changes in external pressure distribution or surface condition.

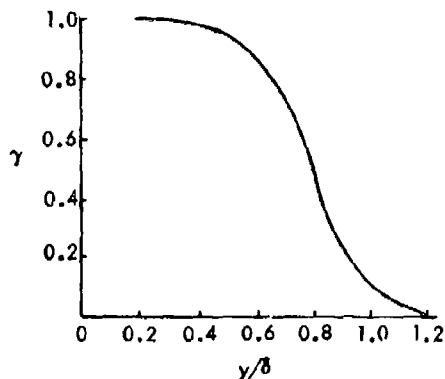


Figure 2.6. Intermittency Factor Distribution in Turbulent Boundary Layer on Smooth Flat Plate at Zero Incidence (Krebanoff)

There is an alternative if complementary way of looking at the structure of the turbulent boundary layer. Within the lowest one-tenth or so of the boundary layer the so-called law of the wall holds. There it is argued that the velocity distribution is determined solely by the distance y from the wall, the velocity u_τ (since the shear stress is practically constant over this region) and the kinematic viscosity ν . The presence of the wall therefore dominates the flow in this region. Dimensional reasoning then leads to the relation

$$\frac{u}{u_\tau} = f\left(\frac{yu_\tau}{\nu}\right)$$

or $u^+ = f(y^+)$, where $u^+ = \frac{u}{u_\tau}$, $y^+ = \frac{yu_\tau}{\nu}$ 2 (6)

and f denotes some function to be determined. This is the law of the wall in its most general form. In the viscous sub-layer where $\tau = \mu \partial u / \partial y = \tau_w$, the law of the wall takes the particular simple form

$$u^+ = y^+ \quad 2 (7)$$

To determine the form of the function f in the rest of the law of the wall region we can appeal to a number of different turbulence models and associated processes of reasoning of which the simplest if crudest is based on the concept of the turbulence mixing length, analogous to the mean free path of molecular motion. Thus, it is postulated that there is an average length normal to the wall over which a fluid particle moves retaining its initial mean momentum and then it mixes with its surrounding flow. The mixing length is assumed small compared with the boundary layer thickness. This simple picture does not reflect in any realistic sense the complexities of turbulent shear flow but it yields semi-empirical relations of proven practical value. It readily leads to the result

$$\tau_t = -\overline{\rho u'v'} = \rho l^2 \left| \frac{\partial u}{\partial y} \right| \frac{\partial u}{\partial y} \quad 2 (8)$$

where l is a length proportional to the mixing length. This can be written

$$\tau_t = \mu_t \left(\frac{\partial u}{\partial y} \right) \quad 2 (9)$$

where $\mu_t = \rho l^2 |\partial u / \partial y|$ can be regarded as an effective eddy viscosity coefficient. It is however a variable of the mean flow unlike the ordinary viscosity coefficient μ .

Two further assumptions are made. Firstly, that in the region of the law of the wall (other than in the viscous sub-layer)

$$l = Ky \tag{2 (10)}$$

where K is a constant, the Von Karman constant, found experimentally to be 0.4 - 0.41; secondly that in this region $\tau_t = \tau_w$. It can then be readily deduced that

$$u = \frac{u_\tau}{K} \ln y + \text{const}$$

If, proceeding further, we take account of the presence of the viscous sub-layer, we arrive at

$$u^+ = \frac{u}{u_\tau} = \frac{1}{K} \ln y^+ + B \tag{2 (11)}$$

where B is a constant. This is the so-called logarithmic form of the law of the wall.

A different approach due to Squire (Reference 2.6) provides a realistic merging with the viscous sub-layer. He started with the eddy viscosity assumption of equation 2(9) and on dimensional grounds inferred that

$$\mu_t = \text{const } \rho u_\tau (y - y_0),$$

where y_0 is related to the viscous sub-layer thickness, since it defines the lower boundary of the law of the wall region in which the eddy stress is dominant. Further, on dimensional grounds it is argued that

$$y_0 = \text{const } \nu / u_\tau$$

The total shear stress

$$\tau = \tau_t + \tau_i = (\mu_t + \mu) \partial u / \partial y = \tau_w$$

from which the law of the wall follows in the form

$$u^+ = \frac{u}{u_\tau} = \frac{1}{K} \ln \left[\frac{u_\tau (y - y_0)}{\nu} + \frac{1}{K} \right] + B, \text{ for } y \geq y_0 \tag{2 (12)}$$

Values of K and B are variously quoted in the experimental literature, favoured values of K are 0.4 and 0.41 whilst corresponding values of B of 5.5 and 5 are often quoted. These differing values in part reflect experimental errors but there may be some small dependence of K and B on Reynolds number. With $K = 0.4$ and $B = 5.5$, equation 2(12) gives continuity for u^+ at y_0 with the viscous sub-layer (equation 2(7)) if $u_\tau y_0/\nu = 7.8$, whilst with $K = 0.41$ and $B = 5.0$, continuity follows if $u_\tau y_0/\nu = 7.17$. Equation 2(12) and equation 2(11) are in good agreement for y^+ greater than about 30, whilst for values of y^+ between about 7 and 30 equation 2(12) is in good agreement with measurements of Reichardt in the buffer region between the viscous sub-layer where τ_i is the dominant part of τ and the fully turbulent part of the law of the wall region where τ_t is dominant.

An alternative approach to encompass the viscous sub-layer is that adopted by Van Driest (Reference 2.7) who suggested that the relation $l = Ky$ should be changed to

$$l = Ky \left[1 - \exp. (-y^+/A_0) \right], \quad 2 (13)$$

the additional factor $F = [1 - \exp. (-y^+/A_0)]$, is presumed to account for the damping effect on the turbulence as the wall is approached. Van Driest found the constant A_0 empirically to be 26, although the value 25 is sometimes quoted. The resulting expression for u^+ is somewhat more complex than 2(11) but tends to it for y^+ greater than about 100 and to the viscous sub-layer relation (equation 2(7)) for small y^+ .

It will be clear from 2(11) that a plot of u^+ against $\ln y^+$ (or $\log_{10} y^+$) will take the form of a straight line with slope $1/K$ (or $1/K \ln 10$) for the law of the wall region. With a uniform external flow (zero pressure gradient) this straight line extends for values of y^+ from about 30 to about 500 depending on the Reynolds number (see Figure 2.7).

Consistent with the argument that the law of the wall region is independent of the external flow conditions it is found that for an attached turbulent boundary layer there is always a region in which the law of the wall holds whatever the external pressure distribution. However, the relative extent of that region diminishes as the external pressure distribution becomes increasingly adverse and for a boundary layer approaching separation it becomes difficult to identify a law of the wall region with any confidence (see Figure 2.7).

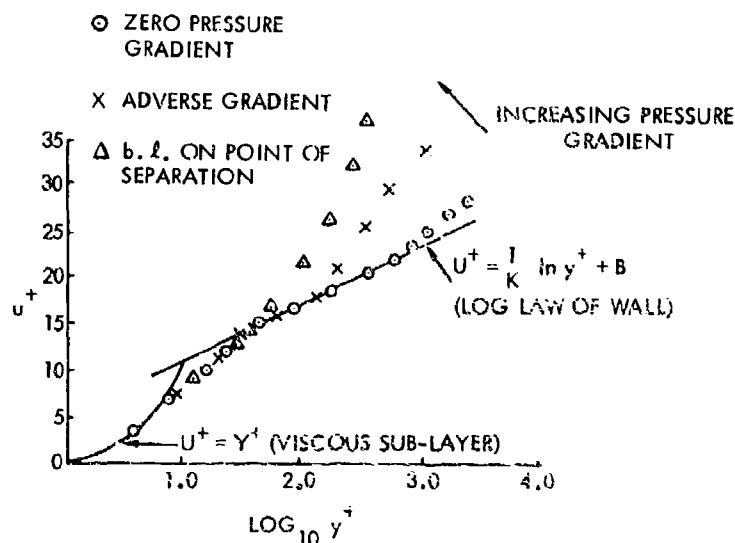


Figure 2.7. Typical Plots of $u^+ - \log_{10} y^+$ for Different Pressure Gradients on a Smooth Surface

12

Outside the law of the wall region we have the remainder of the boundary layer (some 90% of it in thickness). It is argued that in this region viscosity plays no direct part and that the velocity defect relative to the external velocity, $u_e - u$, is solely a function of u_τ , y , δ and some parameter characterising the streamwise pressure distribution. With a uniform external flow it is therefore inferred that

$$\frac{u_e - u}{u_\tau} = f(y/\delta) \quad 2(14)$$

where f is a function to be determined experimentally. Equation 2(14) is well supported by experimental data and the function f deduced by Coles (Reference 2.8) is illustrated in Figure 2.8. Equation 2(14) is referred to as the velocity defect relation.

A self-preserving, or equilibrium, turbulent boundary layer is defined as one where the velocity defect ratio, $(u_e - u)/u_\tau$, is the same function of y/δ for all x . From 2(14) it follows that the case of uniform external flow offers one example of such a boundary layer. Clauser (Reference 2.9) introduced the parameter

$$G = \int_0^\infty \left(\frac{u_e - u}{u_\tau} \right)^2 dy / \int_0^\infty \left(\frac{u_e - u}{u_\tau} \right) dy \quad 2(15)$$

which is a constant for self-preserving boundary layers and is related to $H = \delta^*/\theta$, where δ^* is the displacement thickness $= \int_0^\delta (1 - \frac{u}{u_e}) dy$, by the relation

$$G = \frac{(H-1)}{H} \frac{u_e}{u_\tau} \quad 2(16)$$

Clauser (Reference 2.10) also demonstrated that boundary layers which were very close to self-preserving resulted when the pressure gradient parameter

$$\beta_p = \frac{v^*}{\tau_w} \frac{dp}{dx} \quad 2(17)$$

is constant.

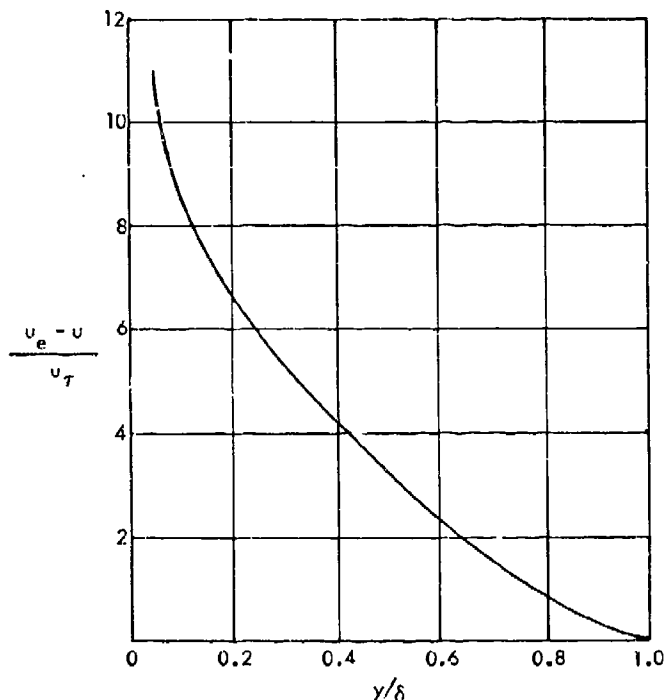


Figure 2.8. Velocity Defect Relation for Smooth Flat Plate at Zero Incidence as Derived by Coles

Coles (Reference 2.11) proposed on the basis of his analysis of a considerable body of data for turbulent boundary layers in non-uniform external pressure distributions that

$$u^+ = \frac{1}{K} \ln y^+ + B + \frac{\Pi(x)}{K} w(y/\delta) \quad 2 (18)$$

We see that the third term on the right describes the deviation with y of the velocity profile from the law of the wall. The function $w(y/\delta)$ is such that $w(0) = 0$ and $w(1) = 2$ and it is very similar to the normalised velocity distribution typical of a half wake. Equation 2(18) is therefore generally referred to as the law of the wake. The basic concept is that away from the wall the boundary layer tends to develop as if it were part of a wake but it is modified by the presence of the wall. The function $w(y/\delta)$ was determined empirically by Coles but a close fit is

$$w(y/\delta) = 2 \sin^2 \left(\frac{\pi}{2} \frac{y}{\delta} \right) = 1 - \cos \left(\frac{\pi y}{\delta} \right) \quad 2 (19)$$

Putting $y = \delta$ in 2(18) it follows that

$$\Pi(x) = \frac{K}{2} \left[\frac{u_e}{u_\tau} - \frac{\ln \delta^+}{K} - B \right] \quad 2 (20)$$

where $\delta^+ = \delta u_\tau / \nu$, so that $\Pi(x)$ can be determined at any station x given u_τ and δ . We can regard $\Pi(x)$ as a scaling factor determined by the external pressure distribution.

It can be shown that $\Pi(x)$ is a function of the Clauser parameter G so that it is constant for self-preserving boundary layers. With zero pressure gradient $\Pi \approx 0.55$ for values of R_θ greater than about 5000.

Reverting to the law of the wall region we note that if we multiply both sides of 2(11) by u_τ / u_e we get

$$\frac{u}{u_e} = \frac{u_\tau}{u_e} \ln \left(\frac{u_e y}{\nu} \right) + B \frac{u_\tau}{u_e} - \frac{u_\tau}{u_e} \ln \frac{u_e}{u_\tau}$$

If we now write the local skin friction coefficient as

$$c_{fe} = 2 \tau_w / \rho u_e^2 = 2 (u_\tau / u_e)^2$$

or
$$u_\tau / u_e = (c_{fe} / 2)^{1/2}$$

then it follows that

$$\frac{u}{u_e} = \sqrt{\frac{c_{fe}}{2}} \ln \left(\frac{u_e y}{\nu} \right) + \sqrt{\frac{c_{fe}}{2}} \left[B + \ln \sqrt{\frac{c_{fe}}{2}} \right] \quad 2 (21)$$

Hence, a family of curves can be plotted of u/u_e against $\ln(u_e y/\nu)$ each corresponding to a specified value of c_{fe} . Once plotted, such a chart can be compared with measurements made in the law of the wall region of u/u_e as a function of $u_e y/\nu$ and the corresponding value of the skin friction coefficient c_{fe} can be deduced. This method of determining c_{fe} is referred to as the Clauser plot method since Clauser first suggested it (Reference 2.9).

We can use equation 2(9) to determine, from measurements for which τ_t is known, the distribution of the eddy viscosity μ_t across the boundary layer. It is found to rise to a maximum with y/δ up to $y/\delta \approx 0.3$ and then it falls slowly. Further

$$\mu_t/u_e \delta^{*0} = f(y/\delta) \quad 2 (22)$$

where the function f is found to be practically the same for all self-preserving flows. Indeed outside the law of the wall region the function f is approximately proportional to γ , the intermittency function, so that

$$\nu_t = \mu_t/\rho = 0.0168 u_e \delta^{*0} \gamma \quad 2 (23)$$

Likewise, equation 2(8) can be used to determine experimentally the distribution of the length l across a boundary layer. Within the logarithmic law of the wall region we find as expected $l/\delta = K(y/\delta)$, but outside that region l/δ tends to a constant value of about 0.08 to 0.09 for self-preserving boundary layers. A commonly used formula is

$$l/\delta = 0.085 \tanh\left(\frac{K}{0.085} \frac{y}{\delta}\right) \quad 2 (24)$$

2.1.3 The Boundary Layer Equations

In this section, it is convenient to include the terms arising from compressibility, so that ρ and μ are variables.

With the boundary layer approximations referred to in Section 2.1.1 the mean equations of continuity, motion and energy for a viscous fluid in two dimensions, with the flow at infinity steady, become

$$\frac{\partial}{\partial x}(\rho u) + \frac{\partial}{\partial y}(\rho v) = 0 \quad 2 (25)$$

$$\rho \frac{Du}{Dt} = \rho \left(u \frac{du}{dx} + v \frac{du}{dy} \right) = - \frac{dp}{dx} + \frac{\partial \tau}{\partial y}, \quad 2 (26)$$

where

$$\begin{aligned} \tau &= \mu \frac{\partial u}{\partial y}, \text{ for laminar flow,} \\ &= \mu \frac{\partial u}{\partial y} - \overline{\rho u'v'}, \text{ for turbulent flow.} \end{aligned}$$

$$\rho \frac{Dh}{Dt} = \rho \left(u \frac{\partial h}{\partial x} + v \frac{\partial h}{\partial y} \right) = \frac{\partial q}{\partial y} + u \frac{dp}{dx} + \tau \frac{\partial u}{\partial y} \quad 2 (27)$$

where $q = k \frac{\partial T}{\partial y}$, for laminar flow,
 $= k \frac{\partial T}{\partial y} - \rho v \overline{h'}$, for turbulent flow.

Here, u, v are the mean velocity components in the streamwise direction parallel to the surface (x) and normal to the surface (y), respectively, T is the mean temperature, h is the mean enthalpy per unit mass ($\cong \int C_p dT$), k is the coefficient of conductivity and like μ is a variable in compressible flow, dashes denote turbulence fluctuations and a bar denotes a mean value i.e. an average taken over a period that is long compared with that typical of the turbulence fluctuations.

An alternative to 2(27) can be obtained by adding it to $u \times$ equation 2(26) whence we get

$$\rho \frac{Dh_T}{Dt} = \rho \left(u \frac{\partial h_T}{\partial x} + v \frac{\partial h_T}{\partial y} \right) = \frac{\partial}{\partial y} (q + u\tau), \quad 2(28)$$

where $h_T = h + (u^2/2)$ and is sometimes called the total enthalpy per unit mass.

The boundary conditions are:-

$$y=0, \quad u=v=0, \quad T \text{ or } \partial T/\partial y \text{ are specified,}$$

$$y=\infty \text{ (or } \delta), \quad u = u_e(x), \quad T = T_e(x).$$

The momentum integral equation can be obtained by integrating equation 2(26) with respect to y from the surface to beyond the edge of the boundary layer. It can be expressed for a perfect gas in the form (see Reference 2.1):-

$$\frac{d\theta}{dx} + \frac{\theta}{u_e} \frac{du_e}{dx} \left[H + 2 - M_e^2 \right] = \frac{\tau_w}{\rho_e u_e^2}, \quad 2(29)$$

where now $\theta = \int_0^\delta \frac{\rho u}{\rho_e u_e} \left(1 - \frac{u}{u_e} \right) dy$, $\delta^* = \int_0^\delta \left(1 - \frac{\rho u}{\rho_e u_e} \right) dy$, $H = \delta^*/\theta$

and M_e is the local free stream Mach number. Equation 2(29) is applicable to both laminar and turbulent boundary layers.

A kinetic energy integral equation can be obtained by multiplying equation 2(26) by u and then integrating with respect to y across the boundary layer. This takes the form for a perfect gas:-

$$\frac{d\delta_E}{dx} + \frac{\delta_E}{u_e} \frac{du_e}{dx} \left[3 + 2 \frac{\delta_H}{\delta_E} - M_e^2 \right] = \frac{2}{\rho_e u_e^2} \int_0^\delta \tau \frac{\partial u}{\partial y} dy \quad 2(30)$$

Here $\delta_E = \int_0^\delta \frac{\rho u}{\rho_e u_e} \left(1 - \frac{u^2}{u_e^2} \right) dy$, (the kinetic energy thickness)

and $\delta_H = \int_0^\delta \frac{\rho u}{\rho_e u_e} \left(\frac{h}{h_e} - 1 \right) dy$, (the enthalpy thickness).

In incompressible flow $\delta_H = 0$.

2.1.4 Prediction Methods (Two-Dimensional Incompressible Flow)

The laminar boundary layer equations are complete in themselves and require no additional relations for their solution, and they can be solved to any required accuracy given adequate computer capacity. However approximate methods have been developed that are quick and simple to use and these are essentially based on the solution of the momentum integral equation (equation 2(29)). They are well covered in many existing text books (see, for example, References 2.1 and 2.2) and need not be considered further here. At transition the momentum thickness θ is assumed continuous.

In contrast the turbulent boundary layer equations are not complete in themselves since the turbulence quantities are unknown and additional relations (so called closure relations) are required linking these quantities with the mean flow to solve the boundary layer equations. In the absence of a thorough understanding of the physics of turbulence these closure relations must be empirically based and as such their validity range cannot be confidently assessed.

We can classify the existing methods for providing the development of turbulent boundary layers with specified external velocity distributions as either integral or differential.

Integral methods have been developed since the earliest days of boundary layer theory. They generally involve the solution of equation 2(29) coupled with two additional and empirically based relations between θ , H , and τ_w . Such a solution leads to overall quantities such as θ , δ^* and c_f , which for many engineering requirements are all that is needed, but such methods do not provide details of the flow e.g. velocity and shear stress distributions. The auxiliary relations used have ranged from the simple assumptions of $H = \text{constant}$ plus the local use of zero pressure gradient power law relations (e.g. equations 2(4)) to empirically determined equations for dH/dx plus the Ludwig-Tillmann relation (Reference 2.12)

$$C_{f_e} = \frac{2 \tau_w}{\rho U_e^2} = 0.246 R_\theta^{-0.268} 10^{-0.678H} \quad 2(31)$$

The resulting integration of the momentum integral equation yields the momentum thickness θ in the form of a simple quadrature with good accuracy irrespective of the particular auxiliary relations used. However, the determination of δ^* (or H) and c_f depends more sensitively on these relations and can justify the use of the more complex ones. Amongst the most effective of such relations is the entrainment equation of Head (Reference 2.13). This is based on the argument that the rate of entrainment of fluid into the boundary layer is a function of the velocity profile in the outer part of the boundary layer. This leads to a relation of the form

$$\frac{d}{dx} (U_e \theta H_1) = U_e F(H_1) \quad 2(32)$$

where $H_1 = (\delta - \delta^*)/\theta$, and $F(H_1)$ is an empirically determined function. Further, by making the assumption common to almost all integral methods that the velocity profiles in a turbulent boundary layer can be regarded as uni-parametric, and if we take the parameter as H , then

$$H_1 = G(H), \text{ say,}$$

where $G(H)$ can also be determined empirically (approximately $G(H) = 2H/(H-1)$). The required auxiliary relation then follows. The assumption that the boundary layer is uni-parametric is equivalent to assuming near-equilibrium and Head & Patel subsequently modified the method to include the effects of non-equilibrium (Reference 2.14).

The kinetic energy integral equation (equation 2(30)) can also be used to provide an auxiliary relation and reference should be made to the method of Truckenbrodt in which this equation plays a central part. (See References 2.1, 2.15 and 2.16).

The successful development of differential methods has taken place within the last decade and a half and started with a now classical paper by Bradshaw et al (Reference 2.17). They involve the direct numerical solution of the equations of motion (and of energy for compressible flow). To solve the equation of motion we must relate in some way the unknown Reynolds stress $\tau = -\overline{\rho u'v'}$ to the mean motion. This can be done by making use of the eddy viscosity concept coupled with a relation such as equation 2(23), or the mixing length concept coupled with a relation such as equation 2(24), (see for example References 2.18 and 2.19). Alternatively, or additionally, use can be made of one or more transport equations for turbulence quantities, e.g. Reynolds stress, turbulence kinetic energy or turbulence dissipation rate (see for example, References 2.20 and 2.21). With such relations the closure cannot be completed without additional assumptions based on the available experimental data. The complexity of the calculations rapidly increases with the number of equations involved and the required input of initial conditions correspondingly increases.

This complexity must be weighed against the considerable amount of detailed information, e.g. mean velocity profiles, shear stress profiles, turbulence intensities that can be predicted by such methods. To illustrate the complexity the following is the transport equation for the Reynolds stress $-\overline{u'v'}$ in two dimensional incompressible flow, as derived from the Navier-Stokes equations and then simplified by the usual boundary layer approximations.

$$\begin{aligned} \frac{D}{Dt} (-\overline{u'v'}) &= \left(\frac{\partial}{\partial t} + u \frac{\partial}{\partial x} + v \frac{\partial}{\partial y} \right) (-\overline{u'v'}) \\ &= v'^2 \frac{\partial u}{\partial y} - \frac{p'}{\rho} \left(\frac{\partial u'}{\partial y} + \frac{\partial v'}{\partial x} \right) + \frac{\partial}{\partial y} \left(\frac{p'u'}{\rho} + \overline{u'v'^2} \right) \\ &\quad - \nu (\overline{u'^2 v'^2} + \overline{v'^2 u'^2}) \end{aligned} \quad 2(33)$$

The left hand side is the rate of change of $-\overline{u'v'}$ for a fluid particle, the first term on the right hand side is the rate of generation by mean shear, the second is the pressure-strain term and represents the tendency of pressure fluctuations to make the turbulence more isotropic, the third term arises from diffusion normal to the wall, and the fourth term represents viscous dissipation effects which are due to viscous action on the smaller eddies. The terms involving the pressure fluctuations present great difficulty in approximating to them by suitable empirical approximations since they are not directly measurable. Likewise, the corresponding transport equation for the turbulence kinetic energy per unit mass $k_t = \frac{1}{2} (\overline{u'^2} + \overline{v'^2} + \overline{w'^2})$ is

$$\frac{D}{Dt} k_t = -\overline{u'v'} \frac{\partial u}{\partial y} - \frac{\partial}{\partial y} \left[\overline{v'(k_t + \frac{p'})}{\rho} \right] + \nu \frac{\partial^2 k_t}{\partial y^2} - \epsilon, \quad 2(34)$$

where ϵ is the dissipation rate term = $1/2 \nu \left(\frac{\partial u'_i}{\partial x_j} + \frac{\partial u'_j}{\partial x_i} \right)^2$, in tensor notation. Again the pressure fluctuation term presents the greatest problem for acceptable modeling.

A third transport equation that is also sometimes invoked is that for ϵ . This need not be reproduced here but it likewise includes terms involving p' as well as gradients of the turbulence components which call for a delicate combination of skill and faith to model them by empirical relations of acceptable simplicity and reliability.

Bradshaw's method (Reference 2.17) still remains one of the most successful. He converted the equation for k_t (equation 2(34)) into one for $\overline{-u'v'}$ by making use of the experimental observation that their ratio is nearly constant i.e.

$$\frac{\overline{-u'v'}}{k_t} = 2\alpha_1, \text{ where } \alpha_1 = 0.15. \quad 2 (35)$$

Further, he introduced a length $L = (\overline{-u'v'})^{3/2} / \epsilon$ and a quantity

$$G_B = \frac{v' (k_t + p'/\rho)}{(\overline{-u'v'}) (\overline{-u'v'})_{\max}^{1/2}} \quad 2 (36)$$

and he argued that L and G_B could be regarded as functions of y/δ only, which he determined from experimental data. He then solved numerically the combination of the equations of continuity, momentum and the modified turbulence energy equation with boundary conditions determined close to the wall by assuming that the law of the wall holds there.

Later workers such as Launder and his colleagues (References 2.20 and 2.21) have simplified the transport equations for k_t and ϵ by making use of similar empiricisms to those of Bradshaw and solved them in combination with the mean flow equations with the use of some empirically determined constants.

No one method has established itself as clearly superior to the others. Accuracy does not necessarily increase with complexity and for many engineering purposes the simpler methods (whether integral or differential) are quite adequate as well as relatively economic in computing time. Interesting survey papers are to be found in Reference 2.22.

2.1.5 Extension to Compressible Flow and Three Dimensions

The extension to compressible flow of prediction methods developed for incompressible flow is frequently achieved by suitable transformation of the main equations (which must now include the energy equation) so that they become similar in form to the corresponding equations in incompressible flow. The methods of solution already developed for the latter can then be adapted to the former. A complicating factor is the important part played by the thermal boundary conditions at the surface. Such processes are, however, not without simplifying assumptions whose validity can only be tested by comparison with experiment. Reference 2.23 is a classic of this approach.

Another approach of appealing simplicity is the use of the so-called mean temperature (or enthalpy) method. This is based on the hypothesis that the results of incompressible flow apply if the values of density and viscosity are taken at a

reference temperature, T_m , which is some mean temperature in the boundary layer, the formula for which is determined empirically. Sommer and Short (Reference 2.24), for example derived for a turbulent boundary layer the relation,

$$T_m = 0.55 T_e + 0.45 T_w + 0.2 (T_r - T_e) \quad 2 (37)$$

where T_e is the free stream temperature, T_w is the wall temperature, and T_r is the recovery temperature (i.e. the wall temperature for zero heat transfer) given by $T_r = T_e (1 + 0.2 M_e^2 \sigma^{1/3})$. Here σ is the Prandtl number = $\mu_e c_p / k_e$, k_e being the thermal conductivity of the free stream fluid and c_p is the specific heat at constant pressure.⁺

As examples of the use of this concept we note that the power law relations between c_f and R_x and between C_F and R_c on a flat plate at zero incidence (equation 2(4)) become

$$c_f = 0.0592 R_x^{-1/5} (T_e/T_m)^{0.62}, \quad C_F = 0.074 R_c^{-1/5} (T_e/T_m)^{0.62} \quad \text{for } n = 7, \quad 2 (38)$$

$$\text{and } c_f = 0.0375 R_x^{-1/6} (T_e/T_m)^{0.685}, \quad C_F = 0.045 R_c^{-1/6} (T_e/T_m)^{0.685} \quad \text{for } n = 9.$$

Here it is assumed that the ambient temperature T_e is that appropriate to normal aircraft flight.

The corresponding heat transfer rates are given approximately by

$$S_t = 0.6 c_f,$$

$$\text{where } S_t \text{ (the Stanton number)} = -q_w / [\rho_e u_e C_p (T_w - T_r)] \quad 2 (39)$$

The mean temperature concept has been shown to give reasonably accurate results up to moderate supersonic Mach number with zero or small pressure gradients. It can more generally be adapted in the simpler integral methods for non-uniform pressure distributions by providing local relations of adequate accuracy (see, for example, Reference 2.26). There are still relatively few experimental data for checking prediction methods, but provided the flow is not close to separation and the Mach number M_e is not greater than about 2.0 it seems that for many engineering needs methods using mean temperature approximations are fairly reliable.

Head's entrainment method has been extended to compressible flow by Green (Reference 2.27). Green's method is generally accepted as one of the more reliable integral methods for cases involving large pressure gradients whilst still remaining relatively simple and economic in computing time.

Spalding and Chi (Reference 2.53) have established a relation between skin friction and Reynolds number for a smooth flat plate in zero pressure gradient for a wide range

⁺ The corresponding mean temperature for a laminar boundary layer is (Reference 2.25)

$$T_m = 0.45 T_e + 0.55 T_w + 0.18 (T_r - T_e) \\ \text{with } T_r = T_e [1 + 0.2 M_e^2 \sigma^{1/2}]$$

of Mach number with heat transfer by taking a mean of the results predicted by a number of existing methods. Their relation is convenient to use and has been made the basis of a comprehensive ESDU Data Sheet (Reference 2.54).

Differential methods have also been extended to compressible flow usually by the use of suitable transformations to preserve the equations in forms for which the computing programs already developed can be readily adapted. They cannot be easily summarised here and the reader is referred to the extension by Bradshaw (Reference 2.28) of his method, to a method based on the mixing length hypothesis developed by Michel et al (Reference 2.18) and further developed by Quemard and Archibaud (Reference 2.29) and an extension of the Jones-Launder method utilising the k_t and ϵ transport equations by Prieur (Reference 2.30). Reference must also be made to methods directed at solving the Navier-Stokes equations in which modeling is confined to small scale turbulence whilst large scale eddies are calculated. Such methods developed for compressible flow are discussed by Rubesin (Reference 2.22, Paper 11). A valuable review is provided by Fernholz and Finlay (Reference 2.31).

For the development of prediction methods to three dimensional flows a basic difficulty arises in so far as the shear stress direction as well as magnitude are not simply related to the direction and magnitude of the velocity gradient. This casts further doubt on the validity of simple mixing length or eddy viscosity methods.

As long as the cross flow velocity component (i.e. the component normal to the local free stream direction) is small it is possible to treat the velocity components in the streamwise direction as independent of the cross flow. Two dimensional methods can then be applied to the streamwise flow and the momentum equation for the cross flow can subsequently be solved without difficulty (References 2.32 and 2.33). For more general cases a number of workers have used the mixing length or eddy viscosity concept. Some have treated the eddy viscosity as a scalar quantity, so assuming coincidence in direction of the resultant shear stress and velocity gradient (References 2.34 and 2.35). Such methods are relatively simple and it is fair to note that in the viscous sub-layer as well as towards the outer edge of the boundary layer the directions of the shear stress and velocity gradient do coincide so that in many cases the difference between the two directions may be small enough for the assumptions made not to lead to serious error. Other workers have attempted to distinguish between the eddy viscosity in different directions and a seminal piece of analysis for such work was provided by Rotta (Reference 2.36).

A widely used integral method with assumed forms for the cross flow velocity profiles is that of P. D. Smith (Reference 2.37) who has developed an extension of Green's method in generalised curvilinear coordinates to three dimensional flows. Bradshaw (Reference 2.39) has extended his two dimensional flow method to three dimensions in which he used simplified forms of the shear stress transport equations in two suitable orthogonal directions parallel to the surface. The method therefore does not involve any identification of the resultant shear stress direction and the velocity gradient direction. As for prediction methods in two dimensional flow no method has yet established itself as the best, and for most engineering needs simplicity and economy in computing costs must rightly play a major part in the decision as to which to use. A valuable comparison with experimental data of the predictions of a wide range of methods will be found in Reference 2.39.

2.2 Roughness Effects on Transition

2.2.1 Introduction

The complexity of the process of transition in a boundary layer from the laminar to the turbulent condition is only partially understood and no general theory is as yet available to provide a comprehensive predictive method. This was clear from the AGARD Symposium on Laminar - Turbulent Transition held in Lyngby, Denmark, in 1977, (Reference 2.40). For the needs of the engineer and designer we must have recourse to predictions based on empirical formulae that are inevitably of limited validity.

These comments apply particularly to the effects of roughness on transition. We know that surface imperfections can induce an earlier transition than on a smooth surface because they generate disturbances in the boundary layer in the form of eddies and vortices which modify the shape of the boundary layer velocity profile in their neighborhood and wake so that the boundary layer is rendered more unstable. In addition the drag of the roughness is manifest in an increase of the boundary layer momentum thickness and the associated boundary layer Reynolds number and this will also tend to enhance the instability of the boundary layer and hasten the transition process.

If we consider an isolated excrescence located in the laminar boundary layer on a particular body in motion we find that there is a critical roughness height below which no significant effect on transition is apparent. This height depends primarily on the roughness shape, location, the pressure distribution over the body, the body Reynolds number, the external turbulence and on the transition position on the smooth surface. As the height is increased, the transition moves upstream until a second critical height is reached at which transition occurs just downstream of the roughness and no further transition movement occurs with further increase of roughness height. At that stage, if the spanwise extent of the excrescence is of the same order as its height then the turbulent region downstream takes the form of a wedge in plan of angle about 11° and apex very close to the excrescence. On the other hand, if the spanwise extent of the excrescence is large compared with its height then transition is induced over its entire span.

These two critical roughness heights are of particular practical interest. An early transition caused by surface roughness or imperfections can result in a significant increase in drag and hence in fuel consumption, as explained in Section 2.1.1. It may also result in changes, usually deleterious, in any downstream interaction of a shock wave and the boundary layer. It is therefore important to know the maximum height of roughness which can be accepted as having no effect on the transition position. We will call this critical height $k_{crit.1}$. On the other hand, on wind tunnel models it is often desirable to use a transition trip in the form of roughness band fixed on the surface to induce transition immediately downstream of it. The object is to fix the location of transition on the model so that (1) the drag measurements will not be subject to variations in transition location and (2) the measured drag values can be corrected to the full scale transition location. For this purpose we need to estimate with some confidence the minimum size of trip required to result in the desired transition position without incurring undue extra drag due to it. The second critical roughness height, which we will denote as $k_{crit.2}$, is clearly useful in this context. In any case we need to take note of likely differences between the effects of isolated excrescences such as rivet heads, distributed roughness such as paint and of excrescences of considerable spanwise extent (e.g. gaps between wing planks, lap joints) which are sometimes described as two dimensional.

2.2.2 The First Critical Roughness Height $k_{crit.1}$

An early approach to predicting this critical roughness height was that of Schiller (Reference 2.41), who noted that for a given bluff body in steady motion at low Reynolds number there is a critical value of the Reynolds number above which the laminar wake behind the body becomes unsteady and vortices generated at the body move downstream in the form of a vortex street. For a circular cylinder, for example, $R_{crit} = V_0 d/\nu \approx 150$. Schiller argued that for a roughness immersed in a laminar boundary layer there should similarly be a critical Reynolds number, R_k , based on the roughness height k and the velocity u_k in the undisturbed boundary layer at the height k , above which we can expect the roughness to shed eddies into the boundary layer which would help to destabilise it and so cause transition to move upstream. We can then identify the roughness height k with $k_{crit.1}$. This suggests that

$$R_{k\text{ crit.1}} = (u_k k/\nu)_{\text{crit.1}} = \text{const.} = C, \text{ say.} \quad 2(40)$$

If $k/\delta \ll 1$, where δ is the boundary layer thickness, then for the basic case of an excrescence on a flat plate with zero pressure gradient in incompressible flow, we can write

$$\begin{aligned} u_k &= k \left(\frac{\partial u}{\partial y} \right)_w = \frac{k \tau_w}{\mu} = \frac{k u_\tau^2}{\nu} \\ &= \frac{k}{2\nu} c_f u_e^2 = \frac{0.664 k}{2\nu \sqrt{R_{xk}}} u_e^2, \end{aligned} \quad 2(41)$$

where τ_w = shear stress at the plate surface, $u_\tau = \sqrt{\tau_w/\rho}$ (friction velocity), $R_{xk} = u_e x_k/\nu$, x_k = distance of excrescences from the plate leading edge.

$$\text{Hence } R_k = \left(\frac{k u_\tau}{\nu} \right)^2 = 0.332 \left(\frac{k}{x_k} \right)^2 R_{xk}^{3/2} \quad 2(42)$$

$$\text{Also } u_e k/\nu = \left(\frac{R_k}{0.332} \right)^{1/2} R_{xk}^{1/4} \quad 2(43)$$

Thus, given the values of $R_{k\text{ crit.1}}$ and x_k we can determine the corresponding value of $k_{crit.1}$.

If k/δ is not small compared with unity then the above estimate for u_k cannot be applied. However, any standard mode of solution of the laminar boundary layer equations can be used to yield u_k , and for the basic case considered of a flat plate with zero pressure gradient in incompressible flow, we can use either the approximate Pohlhausen quartic form,

$$\frac{u}{u_e} = 2 \left(\frac{y}{\delta} \right) - 2 \left(\frac{y}{\delta} \right)^3 + \left(\frac{y}{\delta} \right)^4$$

or the approximate trigonometric form

$$\frac{u}{u_e} = \sin\left(\frac{\pi}{2} \frac{y}{\delta}\right)$$

together with the relation $\delta/x \approx 5/\sqrt{R_x}$, where $R_x = u_e x/\nu$. With the trigonometric form we obtain instead of 2(43)

$$R_k = \frac{u_e k}{\nu} \sin\left[\frac{\pi}{10} \frac{u_e k}{\nu} R_{xk}^{-1/2}\right] \quad 2(44)$$

Again, given the values of $R_k \text{ crit.1}$ and x_k this relation can be used to determine the corresponding value of $k_{\text{crit.1}}$. However, as this is a more complicated relation than 2(43) it is convenient to present it graphically in the form of $\log_{10}(u_e k/\nu)$ as a function of $(R_k)^{1/2}$ for various values of R_{xk} as in Figure 2.9.

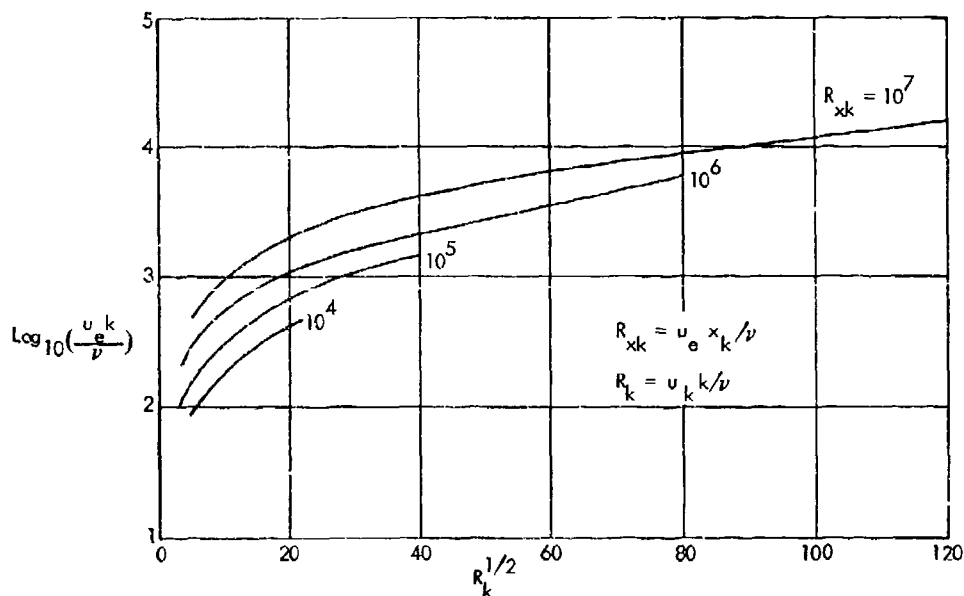


Figure 2.9. Chart for Determining $k_{\text{crit.1}}$. Given $R_k \text{ crit.1}$ and R_{xk} for Basic Case of Zero Pressure Gradient, Incompressible Flow (Equation 2(44))

Experiments by Smith & Clutter (Reference 2.42) on a variety of excrescence shapes in both zero and non-zero pressure gradients (mostly favourable) and a range of intensities of tunnel turbulence yielded the following values of $R_k \text{ crit.1}$.

<u>Roughness</u>	<u>Range of $R_k \text{ crit.1}$</u>
Spanwise wires	40 - 260
Protruding discs of circular section (dia. = 1.6 mm)	100 - 550
Spanwise strips of sandpaper (width = 6.4 mm)	180 - 330

They found the effects of pressure gradient and of tunnel turbulence on $R_{k \text{ crit.1}}$ to be small. At first sight this is surprising but one notes that whilst a favourable pressure gradient would tend to reduce the boundary layer thickness and make its velocity profile fuller, and to that extent would enhance the disturbances produced by a given roughness, it also tends to increase the stability of the boundary layer. Similar balancing factors apply to the effects of free stream turbulence.

Braslow (Reference 2.43) has analysed a wide range of data to present $(R_{k \text{ crit.1}})^{1/2}$ as a function of d/k , where d is the spanwise dimension of a typical roughness, on the argument that this is a parameter of the roughness shape which must play an important part in determining $R_{k \text{ crit.1}}$. His results are represented in Figure 2.10 not in detail but as a band showing the variation about the mean curve. It will be seen that for $d/k = 2.0$ (hemi-spherical roughness) the value of $(R_{k \text{ crit.1}})^{1/2} \approx 23 \pm 6$, but for $d/k = 30$ the value of $(R_{k \text{ crit.1}})^{1/2} \approx 12 \pm 4$. Judging by Smith & Clutter's results the value for two dimensional excrescences ($d/k \approx \infty$) would be about 11 ± 4 .

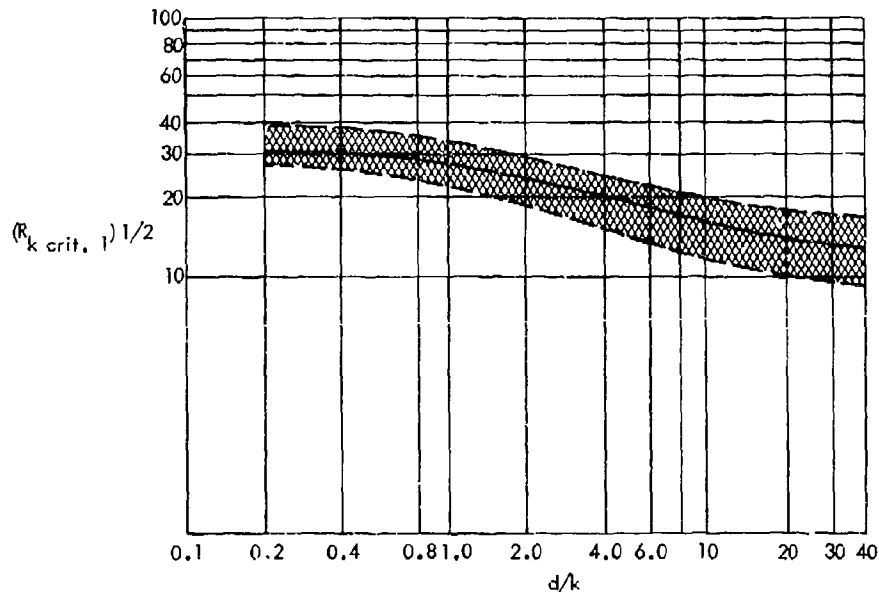


Figure 2.10. $(R_{k \text{ crit.1}})^{1/2}$ as Function of Roughness Shape Parameter d/k (Braslow)

Braslow also demonstrated that there is a significant interference effect with a pair of cylindrical excrescence elements if their spanwise spacing is less than about $3d$ apart (see Figure 2.11). Their disturbing effects then evidently augment each other and $R_{k \text{ crit.1}}$ is reduced by the interference. On the other hand, if they are spaced streamwise then the interference effect is such as to increase $R_{k \text{ crit.1}}$ if the spacing is less than about $4d$ but for higher spacings up to $20d$ the effect is to reduce $R_{k \text{ crit.1}}$ (see Figure 2.12). It seems that at a close enough spacing a steady vortex system forms between the excrescences and the disturbances shed by the rear excrescence are somewhat less intense than from an isolated excrescence. At higher spacings the excrescence experiences the unsteady wake from the front one and the final downstream disturbance level is somewhat enhanced as a result.

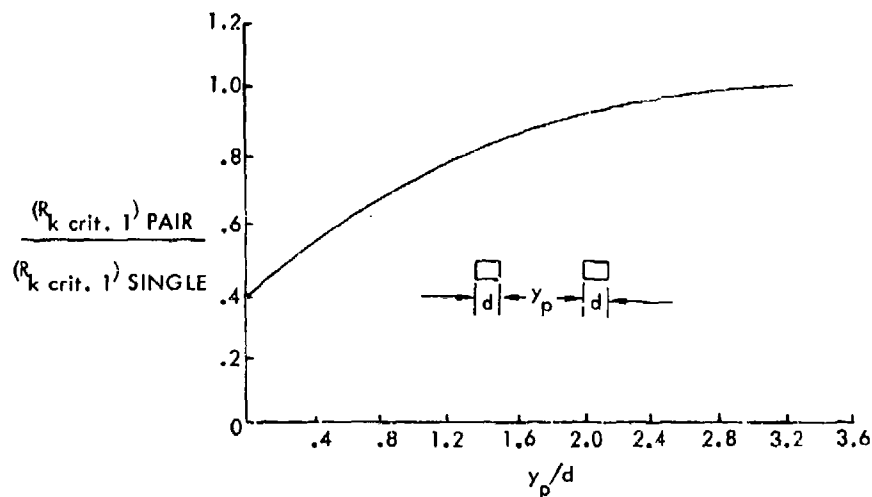


Figure 2.11. Effect of Spanwise Spacing of Pair of Cylindrical Elements on $R_{k \text{ crit. } 1}$ (Braslow)

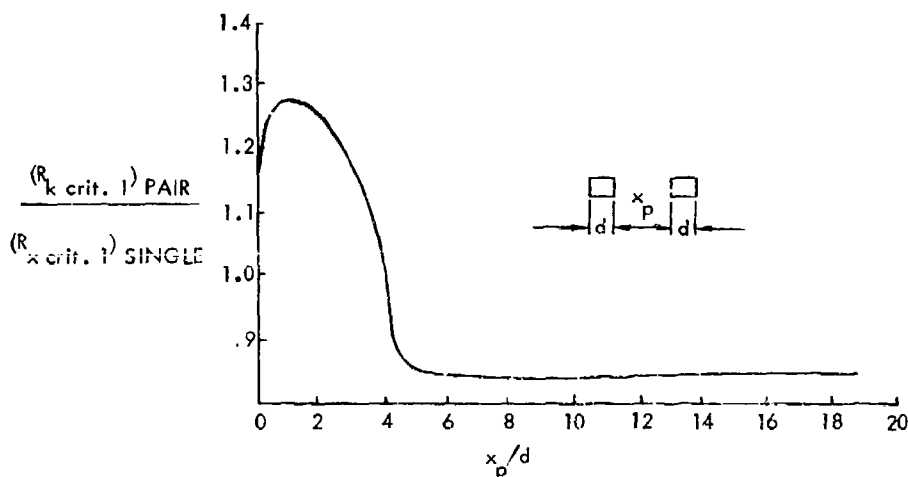


Figure 2.12. Effect of Streamwise Spacing of Pair of Cylindrical Elements on $R_{k \text{ crit. } 1}$ (Braslow)

Braslow's analysis showed little effect of Mach number on $R_{k \text{ crit. } 1}$ up to a main stream Mach number of 3.0 but with some indication of a reduction for higher Mach numbers ($\sqrt{R_{k \text{ crit. } 1}} \approx 15$ for $M_e = 3.7$ and $d/k = 1.0$). It should be noted that if $R_{k \text{ crit. } 1}$ is independent of Mach number then $k_{\text{crit. } 1}$ must increase with Mach number since the velocity at a given height in the boundary layer decreases with increase of Mach number.

To sum up, for general predictive purposes the available data are such that one is not likely to be able to do better than to make use of Figure 2.10 for determining the value of $R_{k \text{ crit. } 1}$. Where it is important to avoid early transition it is best to choose a value near the lower limit of the band. From the value of $R_{k \text{ crit. } 1}$ and the given value of x_k the corresponding value of $k_{\text{crit. } 1}$ can be determined from a solution of the laminar boundary layer equations or more approximately from equation 2(43) or 2(44) (or from Figure 2.9) depending on the magnitude of $k_{\text{crit. } 1}/\delta$.

2.2.3 The Second Critical Roughness Height $k_{crit.2}$

The available data show that $k_{crit.2}$ is of the order of twice $k_{crit.1}$. Early work of Fage & Preston (Reference 2.44) indicated that $R_{k_{crit.2}} \approx 400$ for a wire trip, but Klebanoff et al (Reference 2.45) obtained values ranging from 140 to 1000 depending on the local pressure gradient and the level of tunnel turbulence. Gibbings & Hall (Reference 2.46) inferred the following relation mainly from the data of Tani (Reference 2.47).

$$\frac{u_e k_{crit.2}}{\nu} = 163.7 R_{xk}^{0.15} \quad 2(45)$$

Smith & Clutter (Reference 2.42) found the value of $R_{k_{crit.2}}$ to be about 300 for a wire trip, whilst for their protruding cylindrical excrescences and their sandpaper trip the corresponding values were about 600 and 400, respectively. From equation 2(43) for $k/\delta \ll 1$ we can expect that for constant $R_{k_{crit.2}}$ and zero pressure gradient

$$\frac{u_e k_{crit.2}}{\nu} = \text{const.} R_{xk}^{0.25} \quad 2(46)$$

which differs somewhat from the Gibbings-Hall relation, equation 2(45). Van Driest & Blumer (Reference 2.48) inferred from tests at supersonic speeds of spherical roughness arranged in a band round a cone, as well as from tests of similar excrescences on a flat plate at zero incidence at low speeds, that

$$\frac{u_e k_{crit.2}}{\nu} = 42.6 R_{xk}^{0.25} \left[1 + \frac{(\gamma - 1)}{2} M_e^2 \right] \quad 2(47)$$

where M_e is the Mach number at the outer edge of the boundary layer and γ is the ratio of the specific heats (1.4 for air). It should be noted that some distance was increasingly evident between the trip and the transition position with increase of Mach number (see Figure 2.13).

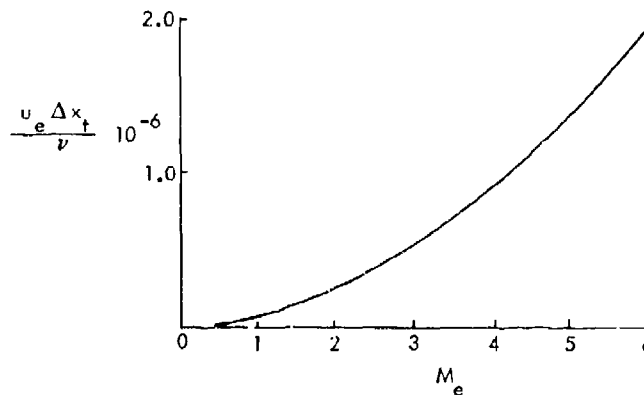


Figure 2.13. Interval (Δx_t) Between Transition T_1 (Band of Spherical Elements) and Transition as Function of Mach Number (Van Driest & Blumer)

It seems that in the absence of more data and convincing analysis of the effects of pressure gradient and external turbulence we can predict $k_{crit.2}$ in incompressible flow on the basis of an assumed value of R_k $_{crit.2}$ in the range 300 to 400 for wire trips and about 600 for roughness bands. For speeds at which compressibility effects are significant, equation 2(47) indicates that the factor $[1 + (\gamma - 1)/2 M_e^2]$ should be applied to the low speed value of R_k $_{crit.2}$. From the value of R_k $_{crit.2}$ and a given value of x_k the corresponding value of $k_{crit.2}$ (just as for $k_{crit.1}$) can be determined from equation 2(43) or equation 2(44) (or Figure 2.9) depending on the order of magnitude of $k_{crit.2}/\delta$. Alternatively, the Gibbings-Hall relation, equation 2(45), could be used for wire trips, whilst equation 2(47) could be used for spherical roughness bands.

It should be noted that all forms of trip will cause an increase in the momentum defect in the boundary layer because of their drag. For example for a wire trip, if C_{D_h} is the drag coefficient in terms of its height h times its span and the velocity u_h , i.e.

$$D = C_{D_h} \frac{\rho}{2} u_h^2 h, \text{ per unit span,}$$

then the momentum thickness will be increased by the wire by an amount

$$\Delta \theta = \frac{D}{\rho u_e^2} = C_{D_h} \left(\frac{u_k}{u_e}\right)^2 h \quad 2(48)$$

Preston (Reference 2.49) has shown that turbulent flow cannot be sustained for values of $R_\theta < 320$. It follows that to stimulate transition the total θ after the trip must be such that R_θ there must exceed this value. A trip that is made up of spanwise pieces may prove more effective in provoking transition than a continuous trip because of the drag associated with the eddies generated by the flow round the ends of the pieces.

2.2.4 The Effects of Sweep

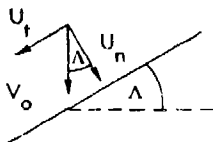
So far we have ignored the effects of sweep and this is probably justified as long as the secondary flows in the boundary layer are small, i.e. the flow direction in the boundary layer is not markedly variable across it. However, in the region of the leading edge of a swept wing, where there are strong pressure gradients normal to the leading edge as well as a flow component in the spanwise direction, the secondary flows are important and the effects of roughness and transition present special features.

In two dimensional unswept flow the boundary layer at the front stagnation point of a round nosed wing is of finite thickness which for small s , the distance from the stagnation point, is independent of s . The scale of the velocity in the boundary layer is determined by u_e where u_e is the velocity just outside the boundary layer. For small s , we find that

$$u_e = \beta s, \text{ where } \beta \propto V_0/r'$$

r denotes the radius of curvature of the wing leading edge and V_0 is the undisturbed stream velocity (the constant of proportionality depends on the section).

Now consider an infinite swept wing. For the laminar boundary layer near the leading edge the so-called principle of independence applies, i.e. the flow in planes normal to the leading edge is independent of that parallel to it (Reference 2.50). The boundary layer flow there is therefore a combination of that derived for two dimensional flow normal to the leading edge in a main stream flow of velocity $U_n = V_0 \cos \Lambda$ and a flow parallel to it with main stream component $U_t = V_0 \sin \Lambda$, where V_0 is the resultant main stream velocity and Λ is the angle of sweep.



We here use suffixes n and t to denote components normal and parallel to the leading edge. We have seen that the former will change rapidly with s being determined in scale by $U_{en} = \beta s$ with β now proportional to $V_0 \cos \Lambda / r$. The boundary layer velocity components parallel to the leading edge are constant in scale and change relatively little in form with s. The resulting boundary layer velocity distributions therefore have component profiles in some directions which have points of inflection and can therefore be expected to have a tendency to be unstable to small disturbances along such directions above a relatively low Reynolds number. This kind of instability can be controlled by a relatively modest degree of boundary layer suction (Reference 2.51). However, in addition a more potent source of transition can arise since the boundary layer is of finite thickness along the leading edge and can be tripped to become turbulent by excrescences there for which the Reynolds number is above some critical value determined by U_t and θ_t , the momentum thickness in the spanwise direction. Gaster (Reference 2.52) has analysed some wind tunnel and flight data to determine the critical value of $R_{\theta t} = U_t \theta_t / \nu$ above which turbulence once introduced will propagate along the leading edge however long it is and so contaminate the boundary layer over the surface downstream. He found the critical value to be about 100. The turbulence can arise from the wing-body junction or be induced by roughness in the region of the leading edge. Using trip wires of diameter d fixed round the leading edge he found that the critical size of wire to provoke turbulence close to the wire was given by

$$\left(\frac{dU}{\nu}\right)_{crit.} = 47 R_{\theta t}^{1/2} \quad 2(49)$$

It is interesting to note that this is quite close to the relation one would deduce from equation 2(43) for the critical wire size if one uses the value given by Fage & Preston for $R_{k crit.2}$ for a wire trip on a flat plate with zero pressure gradient, namely 400, which leads to

$$\left(\frac{u_e k}{\nu}\right)_{crit.} = 43 R_{\theta}^{1/2},$$

where $R_{\theta} = u_e \theta / \nu$. This agreement presumably reflects the fact that the velocity profile in the direction of the leading edge of a swept wing is not greatly different from that of a laminar boundary layer in two dimensional flow and with zero pressure gradient.

$$\begin{aligned} \text{Theory yields} \quad \theta_t &= 0.40 \sqrt{\nu/\beta} \\ \text{and} \quad \theta_n &= 0.27 \sqrt{\nu/\beta} \end{aligned} \quad 2(50)$$

Since $\beta \approx 2V_0 \cos \Lambda / r$, it follows that a decrease of wing sweep or of leading edge radius r help to increase the critical roughness height.

29

REFERENCES

- 2.1 Schlichting, H. 1979 Boundary Layer Theory. McGraw-Hill, 7th (English) Edition, also 1965 Grenzschichttheorie, Braun Verlag Karlsruhe, 5th (German) Edition.
- 2.2 Duncan, W. J. 1970 Mechanics of Fluids. Ed. Arnold. 2nd Thom, A. & Edition. Young, A. D.
- 2.3 Cebeci, T. & 1977 Momentum Transfer in Boundary Layers. Bradshaw, P. McGraw-Hill.
- 2.4 White, F. M. 1974 Viscous Fluid Flow. McGraw-Hill.
- 2.5 Klebanoff, P. S. 1955 Characteristics of Turbulence in a Boundary Layer with Zero Pressure Gradient, NACA Report 1247.
- 2.6 Squire, H. B. 1948 Reconsideration of the Theory of Free Turbulence Phil. Mag. 39, 1-20.
- 2.7 Van Driest, E. R. 1956 On Turbulent Flow near a Wall. J. Aero. Sc. 23, No. 11, 1007-
- 2.8 Coles, D. 1953 The Problem of the Turbulent Boundary Layer. J. P. L. Cal. Inst. Tech. Rep. No. 20-69.
- 2.9 Clauser, F. H. 1956 The Turbulent Boundary Layer. Advan. App. Mech. 4, 1-
- 2.10 Clauser, F. H. 1954 Turbulent Boundary Layers in Adverse Pressure Gradient. J. Aero. Sc., 21, No. 91.
- 2.11 Coles, D. 1956 The Law of the Wake in the Turbulent Boundary Layer. J.F.M., 1, 191-
- 2.12 Ludwig, H. & 1949 Untersuchungen über die Tillmann, W. Wandschubspannung in Turbulenten Reibungsschichten. Ing.Arch. 17, 288-299. Also NACA TM 1285
- 2.13 Head, M. R. 1960 Entrainment in the Turbulent Boundary Layer. ARC R & M 3152.
- 2.14 Head, M. R. & 1969 Improved Entrainment Method for Cal- Patel, V. C. culating Turbulent Boundary Layer Development. ARC R & M 3643.

- 2.15 Truckenbrodt, E. 1952 Ein Quadrat verfahren zur Berechnung der Laminaien und Turbulenten Reibungsschicht bei ebener und rotationssymmetrischer Stromung. Ing.Arch. 20, 211-228
- 2.16 Truckenbrodt, E. 1973 Neuen Erkenntnisse über die Berechnung
1974 von Strömungsgrenzschichten mittels einfacher Quadraturformula. Pt. I. Ing. Arch. 43, 9-25, Pt. II, Ing. Arch 43, 136-144
- 2.17 Bradshaw, P., Ferris, D. W. & Atwell, N. P. 1967 Calculation of Boundary Layer Development using the Turbulent Energy Equation. J.F.M. 28, 593-
- 2.18 Michel, R., Quemard, C. & Durand, R. 1969 Application d'un Schema de Longueur de Mélange à l'Étude des Couches Limites Turbulentes d'Equilibre. ONERA, Note Technique No. 154.
- 2.19 Cebeci, T. & Smith, A. M. O. 1974 Analysis of Turbulent Boundary Layers. Academic Press, New York.
- 2.20 Jones, W. P. & Launder, B. E. 1972 The prediction of laminarization with a two-equation model of turbulence. Int. J. of Heat & Mass Transfer, 15, 301-
- 2.21 Launder, B. E. Reece, C. J. & Rodi, W. 1975 Progress in the Development of a Reynolds Stress Turbulence Closure. J. F. M. 68, 537-
- 2.22 1979 Turbulent Boundary Layers - Experiments, Theory & Modelling. AGARD Conference Proceedings No. 271.
- 2.23 Coles, D. 1964 The Turbulent Boundary Layer in a Compressible Fluid. J. F. M. 7, 1403-1423.
- 2.24 Sommer, S. C & Short, B. J. 1956 Free-Flight Measurements of Skin Friction of Turbulent Boundary Layers with High Rates of Heat Transfer at High Supersonic Speeds. J. Ae. Sc. 23, No. 6, 536-
- 2.25 Young, A. D. 1949 Skin Friction in the Laminar Boundary Layer in Compressible Flow. Aero.Qu. I, 137-164
- 2.26 Luxton, R. E. & Young, A. D. 1965 Boundary Layer Drag of Bi-Convex Wing Sections with Heat Transfer at Supersonic Speeds. ARC R & M No. 3393.

- 2.27 Green, J. E. 1972 Application of Head's Entrainment Method to the Prediction of Turbulent Boundary Layers and Wakes in Compressible flow. RAE Tech. Rep. 72079.
- 2.28 Bradshaw, P. & Ferris, D. H. 1971 Calculation of Boundary Layer Development using the Turbulent Energy Equation: Compressible Flow on Adiabatic Walls. J. F. M. 46, 83-110.
- 2.29 Quemard, C. & Archimbaud, J. P. 1974 Différences Finies en Couche Limites Bidimensionnelles avec Flux de Chaleur. ONEKA, Note Technique No. 10/5005.
- 2.30 Prieur, J. 1976 Étude Aerodynamique Fondamentale de l'Injection Localisée en Couche Limite Turbulente. These No. 8', l'Univ. de Poitiers (ENSMA), France.
- 2.31 Fernholz, H. M. E. & Finlay, P. J. 1980 A Critical Commentary on Mean Flow Data for Two Dimensional Compressible Turbulent Boundary Layers. AGARDograph No. 253.
- 2.32 Cooke, J. C. & Hall, M. G. 1962 Boundary Layers in Three Dimensions. Progress in Aeronautical Sciences, Vol. 2.
- 2.33 Smith, P. D. 1966 Calculation Methods for Three Dimensional Turbulent Boundary Layers. ARC R & M 3523.
- 2.34 Cebeci, T. 1974 Calculation of Three Dimensional Boundary Layers. Pt. 1. Swept Infinite Cylinders & Small Cross Flow. AIAA J. 12, 779-
- 1975 Calculation of Three Dimensional Boundary Layers. Pt. 2. Three Dimensional Flows in Cartesian Coordinates. AIAA J. 13, 1056.
- 2.35 Cousteix, J. 1974 Analyse Theorique et Moyens de Prevision de la Couche Limite Turbulente Tridimensionnelle. ONERA, Publication 157, FR ISSN 0078-379X.
- 2.36 Rotta, J. C. 1977 A Family of Turbulence Models for Three Dimensional Thin Shear Layers. Symposium on Turbulent Shear Flows. Pennsylvania State University.

- | | | | |
|------|--|---------------------|--|
| 2.37 | Smith, P. D. | 1974 | An Integral Prediction Method for Three Dimensional Compressible Turbulent Boundary Layers. ARC R & M No. 3739. |
| 2.38 | AUPOIX, B. | 1979 | Étude Fondamentale d'Écoulements Cisailles Tridimensionnels (Couche Limite et Sillage). These No. 15, L'École Nationale Supérieure de L'Aéronautique et de L'Espace, France. |
| 2.39 | Bradshaw, P. | 1971 | Calculation of Three Dimensional Turbulent Boundary Layers. J. F. M. <u>46</u> , 417- |
| 2.40 | | 1977 | Laminar-Turbulent Transition. AGARD Conference Proceedings, No. 224. |
| 2.41 | Schiller, L. | 1932 | Handbuch der Experimental - Physik. <u>IV</u> . Pt. 4, 189- |
| 2.42 | Smith, A. M. O. & Clutter, D. W. | 1959 | The Smallest Height of Roughness Capable of Affecting Boundary Layer Transition. J. Aero. Sc. (April) 229-245. |
| 2.43 | Braslow, A. L. | 1960 | Review of the Effect of Distributed Surface Roughness in Boundary Layer Transition. AGARD Rep. No. 254. |
| 2.44 | Fage, A. & Preston, J. H. | 1941 | On transition from Laminar to Turbulent Flow in the Boundary Layer. proc. Roy. Soc. A <u>178</u> , 201-227. |
| 2.45 | Flebanoff, P. S., Schubauer, G. B. & Tidstrom, K. D. | 1955 | Measurements of the Effects of Two Dimensional and Three Dimensional Roughness Elements on Boundary Layer Transition. J. Aero. Sc. <u>22</u> , 803-4 |
| 2.46 | Gibbings, J. C. & Hall, D. J. | 1969
(Mar./Apr.) | Criterion for the Tolerable Roughness in a Laminar Boundary Layer. J. Aircraft 171- |
| 2.47 | Tani, I. | 1967 | Review of Some Experimental Results on Boundary Layer Transition. |
| 2.48 | Van Driest, E. R. & Blumer, C. B. | 1960 | Effect of Roughness on Transition in Supersonic Flow. AGARD Rep. No. 255. |
| 2.49 | Preston, J. H. | 1957 | The Minimum Reynolds Number for a Turbulent Boundary Layer and the Selection of a Transition Device. J. F. M. <u>3</u> , Pt. 4, 373- |

- 2.50 Rosenhead, L. (Ed.) 1963 Laminar Boundary Layers, Ch VIII. O.U.P.
- 2.51 Edwards, B. 1977 Laminar Flow Control. Concepts, Experiences, Speculations. Special Course on Concepts in Drag Reduction. AGARD Rep. No. 654.
- 2.52 Gaster, M. 1967 On the Flow along Swept Leading Edges. Aero. Qu. XVIII, Pt. 2, 165-184.
- 2.53 Spalding, D. B. & Chi, S. W. 1964 The Drag of a Compressible Turbulent Boundary Layer on a Smooth Plate with and without Heat Transfer. J. F. M. 18, Pt. 1, 117-143.
- 2.54 ESDU Data Sheets
- Smooth Surfaces:- W020402, W020403, 68020, 78019.
- Rough Surfaces:- W020400, 73016, 75028, 75031, 76008.

3. DISTRIBUTED ROUGHNESS IN TURBULENT BOUNDARY LAYERS (ZERO OR SMALL PRESSURE GRADIENTS)

3.1 Basic Effects. Sand Roughness and Critical Roughness Heights

In what follows a typical height of a roughness element will be denoted as k and it will be assumed that in general k is small compared with the boundary layer thickness. Larger excrescences will be included under the heading 'discrete' and discussed in Section 4.

Our basic understanding of the effects of distributed roughness in turbulent boundary layers owes much to the classical experiments of Nikuradse (Reference 3.1) using sand roughness on the inner surfaces of circular sectioned pipes. The sand grains were kept closely uniform for any one test and were fixed in a closely packed arrangement. The tests covered a range of grain sizes and of pipe radii. An illustrative plot of some of his results for skin friction is given in Figure 3.1. In that figure $c_{fm} = \tau_w / \frac{1}{2} \rho u_m^2$, where u_m is the mean velocity over the pipe cross section, a is the pipe radius and k_s is the sand grain height.

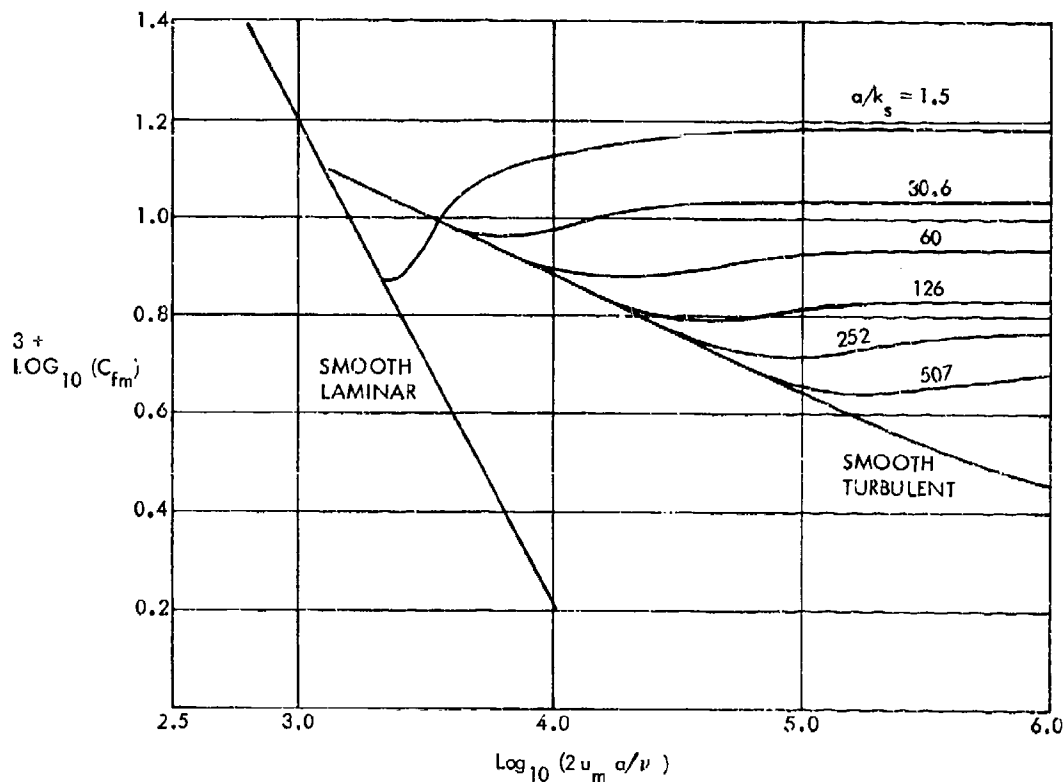


Figure 3-1. Friction Coefficients of Sand-Roughened Pipes as Functions of Pipe Reynolds Number (Nikuradse)

It will be seen that for each roughness size there is a critical pipe Reynolds number ($u_m 2a/\nu$) below which there is no effect of the roughness on c_{fm} . The surface is then referred to as hydraulically smooth. With increase of Reynolds number above the critical value the skin friction coefficient increases above that of the smooth pipe

showing that the roughnesses are then shedding eddies into the flow which contribute to the momentum loss. This drag increment is a combination of the sum of the pressure (or form) drags of the excrescences and the accompanying changes of the local surface friction, but the former rapidly becomes dominant as the Reynolds number is increased. Finally, we note that above a second critical Reynolds number c_{fm} is constant and independent of any further increase of Reynolds number. We infer that at that stage the drag is almost wholly due to the pressure drag increments of the roughnesses and hence becomes insensitive to Reynolds number. We call the flow regime in the pipe at that stage fully developed roughness flow. The intermediate flow regime between the two critical Reynolds numbers is sometimes referred to as the 'transition regime', but to avoid confusion with the more common use of 'transition' to describe the change from laminar to turbulent flow in the boundary layer, we will refer to this regime as the intermediate rough regime.

It is generally accepted that the hydraulically smooth regime is one where the roughnesses do not protrude through the viscous sub-layer. The argument is that this layer is one of high damping of eddies and so eddies generated by the roughness within it do not convect downstream and add to the momentum loss, instead they remain between the roughnesses effectively smoothing the surface. This reasoning implies that roughnesses for which the flow is hydraulically smooth must satisfy:

$$0 \leq u_{\tau} k/\nu \leq 5, \quad 3(1)$$

if we take 5 as a safe lower limit for determining $y_l^+ = u_{\tau} y_l/\nu$, where y_l is the thickness of the viscous sub-layer. This relation is consistent with Nikuradse's measurements.

The beginning of the fully developed roughness regime is likewise characterised by a value of $u_{\tau} k/\nu$ which in Nikuradse's experiments on sand roughness in incompressible flow is shown to be about 70, i.e.

$$u_{\tau} k_s/\nu \geq 70 \quad 3(2)$$

for this regime. Here we use suffix s to denote the sand roughness as tested by Nikuradse since for other types of roughness we can expect the limiting value of $u_{\tau} k/\nu$ for fully developed roughness to differ.

These pipe flow results can be readily adapted to determine the effects of sand roughness on the flow over a flat plate at zero incidence. We replace the pipe radius a by the boundary layer thickness δ which is then a growing function of x the distance from the leading edge. Hence, with a given roughness uniformly distributed over the plate we can expect an initial region of fully developed roughness flow followed by a region of intermediate rough flow, and if the plate chord is of sufficient length there will finally be a region of hydraulically smooth flow. Plots of the limiting roughness heights for fully developed rough and hydraulically smooth flows, deduced from equations 3(1) and 3(2) above are presented in Figure 3.2 in the form of $\log_{10}(x/k)$ as a function of $\log(R_x)$. It is of interest to note that the minimum roughness height to provoke transition in the laminar boundary layer for a given R_x is several times larger than the limiting value for hydraulically smooth flow with the boundary layer turbulent. This can be readily inferred from Figure 2.9, 2.10 and 3.2 by considering typical values of $R_{k \text{ crit.1}}$ and R_{xk} .*

* For example, if $(R_{k \text{ crit.1}}) = 20$ and $R_{xk} = 10^6$ we find from Figure 2.9 that $k_{\text{crit.1}}/x_k = 10^{-3}$, whilst from Figure 3.2 we find that for hydraulically smooth flow with $R_x = R_{xk} = 10^6$ we must have $k/x_k < 10^{-3.9}$.

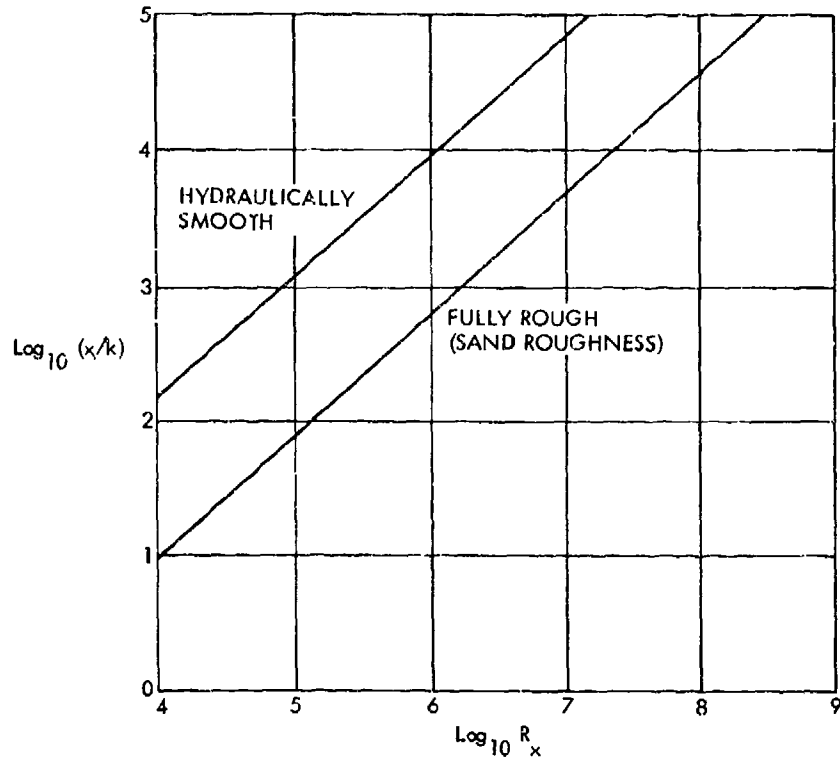


Figure 3-2. Limiting Roughness Sizes (k) for Hydraulically Smooth Flow and for Fully Rough Flow With Sand Roughness. Turbulent Boundary Layer

Prandtl and Schlichting (Reference 3.2) have adapted Nikuradse's results to determine the local and overall skin friction coefficients on sand roughened plates at zero incidence for a wide range of the ratio roughness height/plate chord (k_s/c) and of the plate Reynolds number. Their results are presented in Figure 3.3 and 3.4, with Figure 3.3 showing the local skin friction coefficient c_f as a function of $R_x = V_o x / \nu$ for different values of x/k_s , whilst Figure 3.4 shows the overall skin friction coefficient C_F as a function of $R_C = V_o c / \nu$ for different values of c/k_s . The latter can be conveniently presented in a somewhat different way (Figure 3.5) as $\Delta D/D$ as a function of R_C for different c/k_s , where D is the drag of the smooth plate and ΔD is the drag increase due to the roughness.

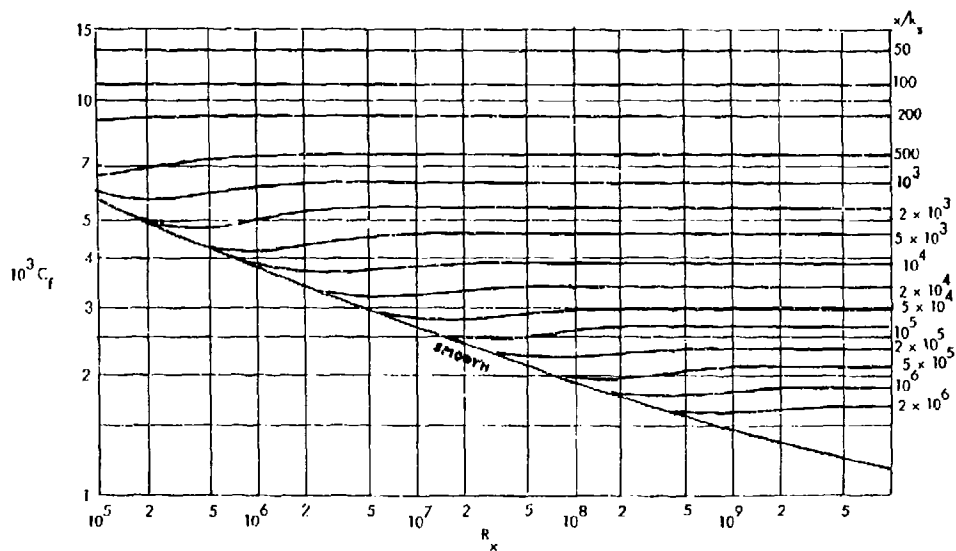


Figure 3-3. Local Skin Friction Coefficient of Sand-Roughened Plate (Prandtl-Schlichting Deductions from Nikuradse's Pipe Flow Experiments)

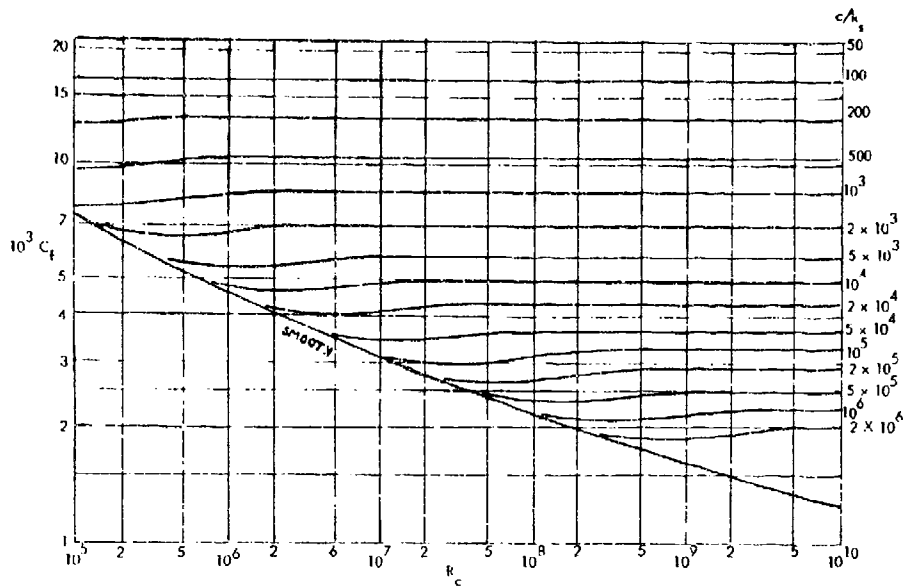


Figure 3-4. Overall Skin Friction Coefficient of Sand-Roughened Plate (Prandtl-Schlichting Deductions from Nikuradse's Pipe Flow Experiments)

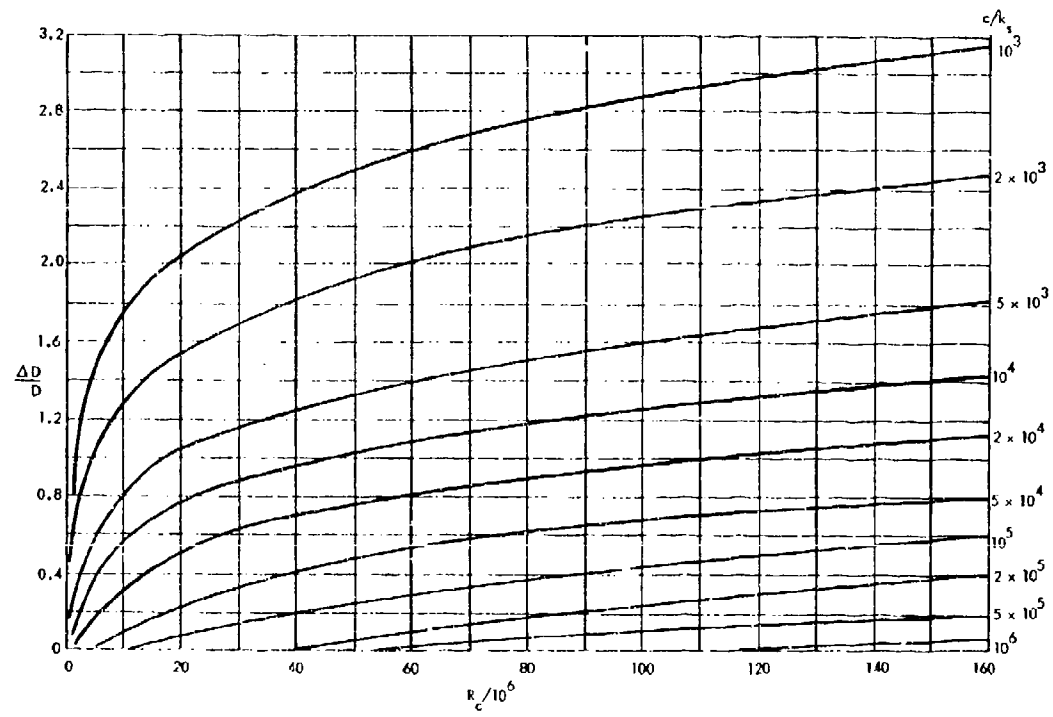


Figure 3-5. Fractional Drag Increase Due to Sand Roughness

The above formulae etc., refer to incompressible flow. The effects of compressibility and heat transfer on roughness effects have not been thoroughly investigated and reliable generalised relations are not yet available. However, it can be plausibly argued that the above relations will still apply provided the relevant density and viscosity values are taken at their wall values since these are the values in the flow region in which the roughnesses operate. Thus, for u_{τ} we should understand $u_{\tau w} = (\tau_w / \rho_w)^{1/2}$ and for ν we should understand ν_w . Now τ_w will itself vary with

Mach number and wall temperature and if we accept the Sommer and Short mean enthalpy formula we find that:

$$\tau_w \propto (T_e/T_m)^{0.65}, \text{ approx.}$$

where

$$\frac{T_m}{T_e} = 0.55 + 0.45 \frac{T_w}{T_e} + 0.036 M_e^2,$$

and T_e is the local free stream temperature.

It follows that if a critical roughness height k_s is such that $u_{\tau w} k_s / \nu_w = \text{const.}$ independent of Mach number, then

$$\frac{k_s}{k_{si}} = \left(\frac{T_w}{T_e} \right)^{1.39} (0.55 + 0.45 \frac{T_w}{T_e} + 0.036 M_e^2)^{0.325} \quad 3 (3)$$

where k_{si} is the value for incompressible flow. Here we have taken the coefficient of viscosity $\mu \propto T^{0.89}$.

For zero heat transfer $T_w/T_e = 1 + [(\gamma - 1)/2] M_e^2 r$, where r is the recovery factor $\doteq 0.89$ for air, and $\gamma = c_p/c_v$ (the ratio of specific heats) = 1.40 for air. Then we get

$$\frac{k_s}{k_{si}} = (1 + 0.178 M_e^2)^{1.39} (1 + 0.214 M_e^2)^{0.325} \quad 3 (4)$$

Thus, for $M_e = 1$, $k_s/k_{si} = 1.34$; and for $M_e = 2$, $k_s/k_{si} = 2.58$. These results reflect the known increase of the viscous sub-layer thickness with Mach number.

Pursuing this argument further Berg (Reference 3.3) has collected data for roughnesses on a flat plate indicating that over a wide range of Mach numbers up to 6 and a variety of roughness forms the drag increment due to the roughnesses as a ratio of the smooth surface drag was a unique function of $u_{\tau w} k_s / \nu_w$, where k_s is the equivalent sand roughness height in incompressible flow (see Section 3.3). This implies that Figure 3.5 can be taken as applying to compressible flow provided one replaces k_s by

$$k_{sw} = k_s \frac{\nu_e}{\nu_w} \left(\frac{\rho_e}{\rho_w} \right)^{1/2} = k_s (T_e/T_w)^{1.39} \quad 3 (5)$$

For zero heat transfer $k_{sw} = k_s / [1 + (\gamma - 1)/2 M_e^2 r]^{1.39} \quad 3 (6)$

which for $M_e = 1$ gives $k_{sw} = 0.8 k_s$; and for $M_e = 2$ we get $k_{sw} = 0.47 k_s$.

This indicates that the proportional effect of a given roughness on drag for zero heat transfer decreases with Mach number as might be expected from the fact that the drag increment would be largely determined by the air density at the wall ρ_w . However, the results analysed by Berg appear to be all for roughnesses small enough to be immersed in the subsonic part of the boundary layer and so would not contribute to the drag by generating shock waves. It cannot therefore be assumed that results based on Figure 3.5

and equations 3(5) or 3(6) will apply to roughnesses large enough to penetrate into the supersonic part of the boundary layer.

3.2 Velocity Distributions in the Boundary Layer

The eddies generated by distributed roughnesses of height small compared to the boundary layer thickness rapidly get absorbed in the local turbulence of the boundary layer without significantly changing its structure. The main effect is therefore to increase the value of the shear stress in the region of the boundary layer close to the surface but there is no loss of validity of the general dimensional reasoning underlying the law of the wall and the defect velocity law derived for smooth walls (see Section 2.12).

Thus, we can again infer that in the law of the wall region for incompressible flow

$$u = Au_{\tau} \ln y + B \quad 3(7)$$

where $A = 1/K$, K being the von Karman constant (0.4-0.41), as for a smooth wall, but B is a constant that will in general depend on the roughness size and geometry.

To examine the nature of B more closely we can argue that there must be some lower limit of y , say y_0 , below which 3(7) cannot be expected to apply, and y_0 will be a function of k , the roughness height, u_{τ} and ν as well as of the roughness shape. For similar shaped roughnesses we therefore write:

$$y_0/k = f(u_{\tau} k/\nu), \text{ say,}$$

where f is some function of the roughness geometry.

Hence
$$u - u(y_0) = A \ln(y/y_0) = A \ln(y/fk).$$

But since $u(y_0)$ will depend on u_{τ} , k and ν we may expect $u(y_0)/u_{\tau}$ to be a function of $(u_{\tau} k/\nu)$ and so we can write

$$u/u_{\tau} = A \ln(y/k) + h(u_{\tau} k/\nu), \quad 3(8)$$

where $h(u_{\tau} k/\nu)$ is some function of $u_{\tau} k/\nu$ as well as of the form and distribution of the roughnesses concerned.

Nikuradse's results for sand roughened pipes provided good support for this relation and the resulting function h for closely packed sand grains is illustrated in Figure 3.6. We find that for $u_{\tau} k_s/\nu < 5$ his function h is approximately given by

$$h(u_{\tau} k_s/\nu) = 5.5 + 2.5 \ln(u_{\tau} k_s/\nu)$$

so that with Nikuradse's value of $A = 2.5$

$$u/u_{\tau} = 2.5 \ln(u_{\tau} y/\nu) + 5.5 \quad 3(9)$$

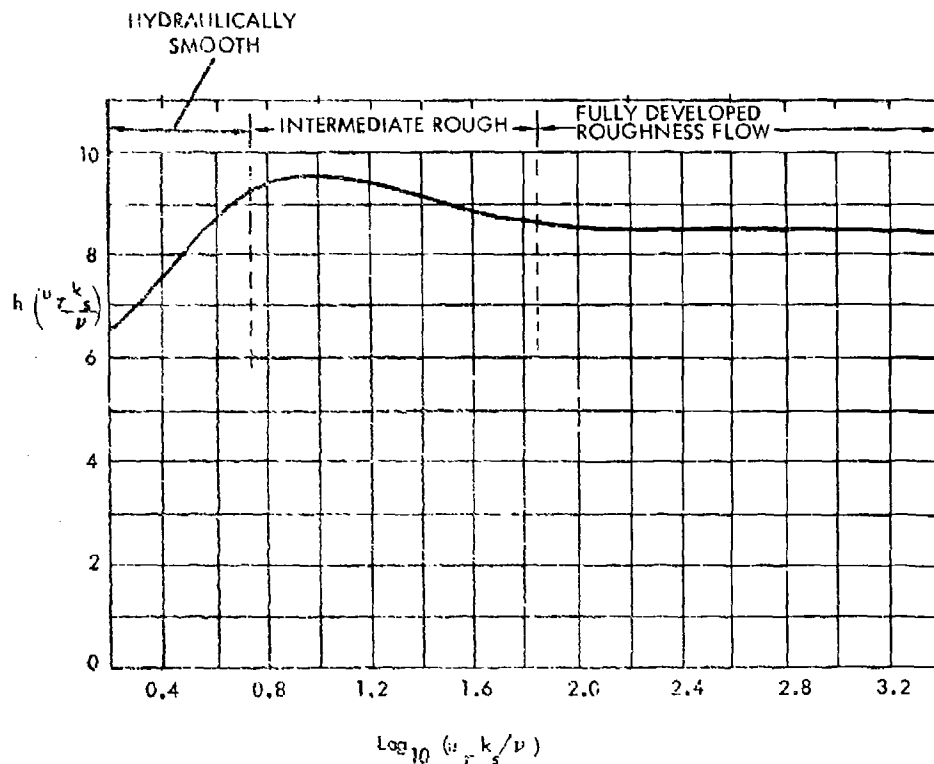


Figure 3-6. The Function $h(u_{\tau} k_s / \nu)$ for Sand Roughness (Nikuradse)

in agreement with the law of the wall for a smooth surface [cf. equation 2(11)]. This therefore defines the range of $u_{\tau} k_s / \nu$ for which the flow is hydraulically smooth.

On the other hand for $u_{\tau} k_s / \nu \gg 70$, approx., we see that Nikuradse's function h is a constant = 8.5, so that then

$$u/u_{\tau} = 2.5 \ln(y/k_s) + 8.5. \quad 3(10)$$

This therefore corresponds to the range of roughness for which the velocity profile and surface friction are independent of Reynolds number - i.e. the regime that we have labelled fully developed roughness flow. For the intermediate rough regime $5 < (u_{\tau} k_s / \nu) < 70$ both the viscous and the roughness form drag contributions to the total roughness drag can be important.

Equation 3(8) can be regarded as the generalised form of the logarithmic law of the wall for walls with distributed roughness. There are other ways of expressing it which have their uses. Perry and Joubert (Reference 3.4) argued that since the direct effects of the roughness were apparent only in the thin inner region of the boundary layer where the direct effects of viscosity are also confined, the roughness could be regarded as equivalent in its effect on the velocity distribution to a change of kinematic viscosity from ν to ν_{eq} , say. Hence the logarithmic law of the wall should take the form:

$$u/u_{\tau} = A \ln(y u_{\tau} / \nu_{eq}) + B$$

where B is now the same constant as for a smooth wall (5.5 if A is taken as 2.5). But on dimensional grounds one can expect v_{eq}/v to be a function of ku_T/v and it follows that 3(11) can also be written

$$u/u_T = A \ln(y/k) + h(u_T k/v)$$

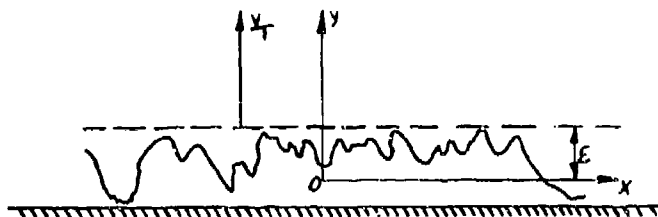
in agreement with 3(8). Further, from equation 3(11), we see that we can write

$$\begin{aligned} u/u_T &= A \ln(y u_T/v) + B - A \ln(v_{eq}/v) \\ &= A \ln(y u_T/v) + B - \Delta u/u_T \end{aligned} \quad 3(12)$$

where $\Delta u/u_T$ is a function of $u_T k/v$.

Hence, for the logarithmic law of the wall region, the plot of u/u_T as a function of $\ln(y u_T/v)$ for any given roughness is linear with slope A, independent of the roughness, and displaced parallel to the basic plot for a smooth surface; the displacement $\Delta u/u_T$ is a function of $u_T k/v$ for roughnesses of similar shape. A wide range of experimental results of different workers amply confirms this conclusion (see References 2.9, 2.10, 3.4, 3.5, 3.6, 3.7 and 3.8).

However, a difficulty arises in the analysis of experimental data since the above relations cannot be expected to apply for values of y less than the tops of the roughnesses nor indeed can velocity measurements there readily fit any generalised formulae. Even on a smooth wall a displaced origin for y must be assumed to achieve a realistic blending with the viscous sub-layer (see equation 2(12)). A displaced origin is therefore also required for the analysis of data on a rough wall particularly for the flow region close to the roughness tips. This origin is taken to be a distance ϵ below the maximum roughness height:-



Thus, instead of 3(12) we write

$$u/u_T = A \ln[(y_T + \epsilon) u_T/v] + B - \Delta u/u_T \quad 3(13)$$

where y_T is the value of y measured from the highest roughness tip. Following Clauser we can multiply this equation by u_T/u_e to get

$$u/u_e = A(c_{fe}/2)^{1/2} \ln[(y_T + \epsilon) u_e/v] + (c_{fe}/2)^{1/2} [A \ln(c_{fe}/2)^{1/2} + B - \Delta u/u_T] \quad 3(14)$$

where $c_{fe} = 2\tau_w / \rho u_e^2$.

Hence, given A and B from smooth surface data the correct choice of ϵ should lead to a linear relation between u/u_e and $\ln [(y_T + \epsilon) u_e / \nu]$ with slope given by $A(c_{fe}/2)^{1/2}$, so that c_{fe} can be determined from this slope. Further, the ordinate intercept should be $(c_{fe}/2)^{1/2} [A \ln(c_{fe})^{1/2} + B - u/u_T]$ when $\ln[(y_T + \epsilon) u_e / \nu] = 0$, and hence $A u/u_T$ can be determined from it. However, it is not always easy to establish the value of ϵ to the accuracy required. The methods that have been adopted cannot be gone into in detail here, the interested reader is referred to References 3.4 and 3.8 for such details; but it may be noted that the use of other methods for estimating c_{fe} (eg. the momentum integral equation or hot wire measurements to determine the eddy stress near the wall) can provide independent checks on the above 'Clauser plot' approach. It appears that $\epsilon/k \doteq 0.5$ for zero pressure gradient and $\epsilon/k \doteq 0.2$ for moderate adverse pressure gradients. The experimental data of a number of different workers all provide strong support for the above analysis.

From equation 3(8) we have seen that for fully developed roughness flow

$$u/u_T = A \ln(y/k) + C,$$

where C is a constant dependent only on the roughness form. If we compare this with equation 3(12) we see that we can write

$$\Delta u/u_T = A \ln(ku_T/\nu) + D, \quad 3 (i5)$$

where D is a constant dependent only on the roughness form.

Figure 3.7 taken from Reference 3.8 shows $\Delta u/u_T$ plotted against $\log_{10}(ku_T/\nu)$ for a variety of regular shaped roughnesses and Figure 3.8 also from Reference 3.8 shows similarly some results for surfaces covered with commercial abrasive papers in zero and a moderate adverse pressure gradient. Perry and Joubert (Reference 3.4) tested roughness elements identical to those of Moore illustrated in Figure 3.7 but in the presence of adverse pressure gradients and their results fit with relatively small scatter the mean line shown in Figure 3.7 passing through Moore's results. These results show that the above law of the wall relations for rough surfaces, like the law of the wall for a smooth surface, are insensitive to pressure gradients and for the same basic reason, namely, that the flow in the region concerned is determined solely by u_T , y and ν .

The above discussion refers to what is described in the literature as k type roughnesses, i.e. roughnesses which generate eddies which are convected into the boundary layer above the roughnesses as a continuous process and they merge with the turbulence there to augment the overall momentum loss. However, exceptionally, if the excrescences are of a simple and uniform geometry so spaced that regular vortices form in the gaps between the excrescences and remain trapped there then the excrescences and vortices may form what is in effect a smooth contour for the boundary layer flow above to follow with no additional eddies being generated to disturb it. The main effect on the boundary layer is that it has a mixed boundary condition at the level of the excrescences of partly free and partly solid surface and the streamlines are relatively smooth and undisturbed. Such roughnesses are referred to as d type. The distinction between the two types is illustrated in Figure 3.9. It is evident that for the d type

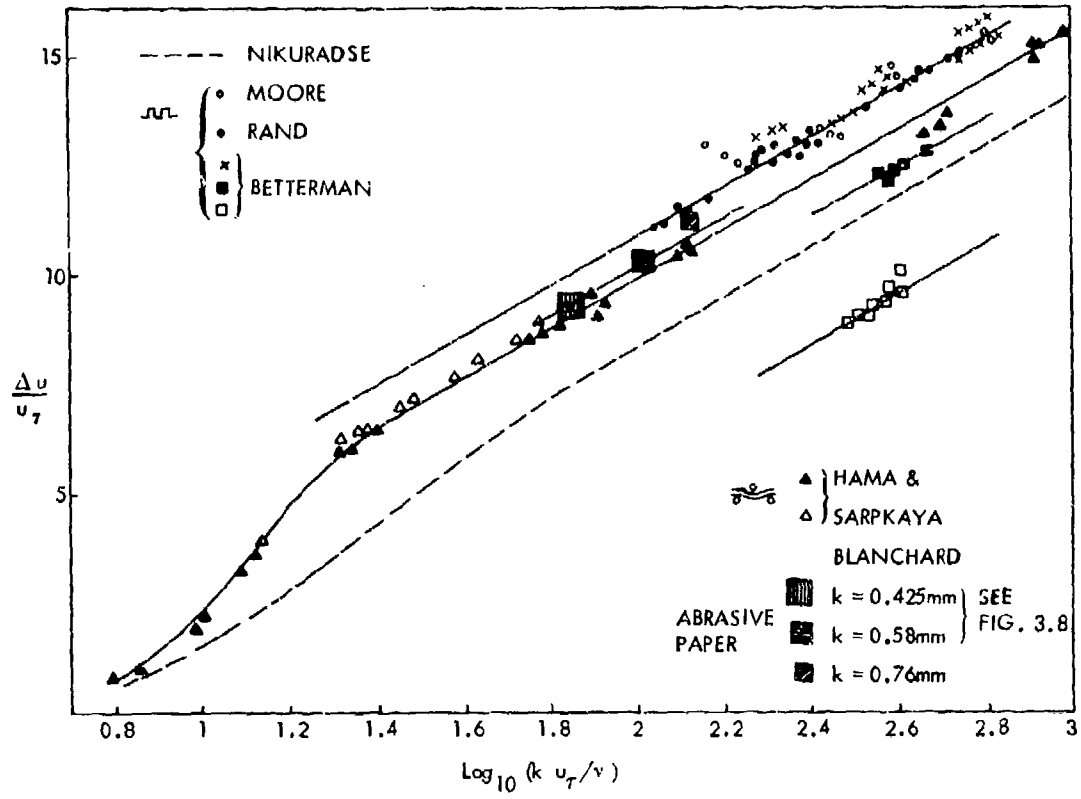


Figure 3-7. $\Delta u/u_\tau$ for Different Roughnesses

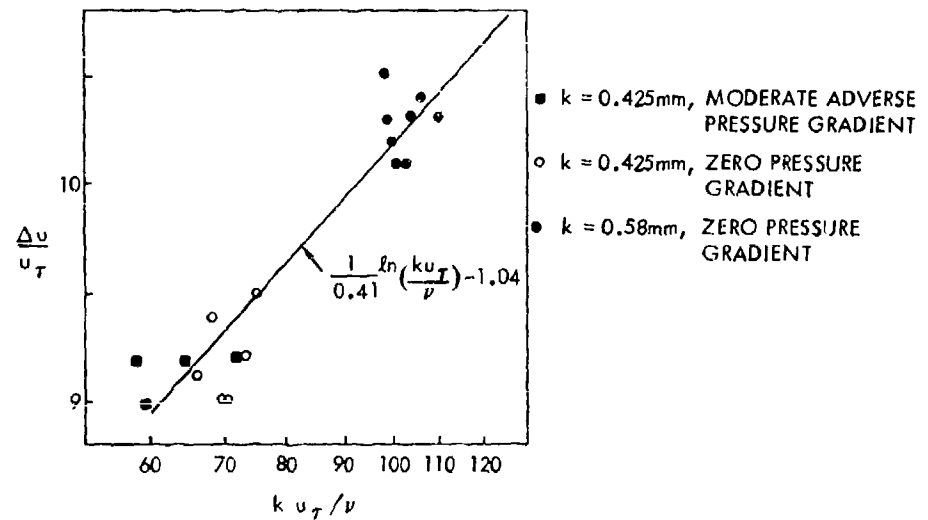


Figure 3-8. $\Delta u/u_\tau$ for Abrasive Papers in Zero and Moderate Adverse Pressure Gradients (Due to Blanchard)

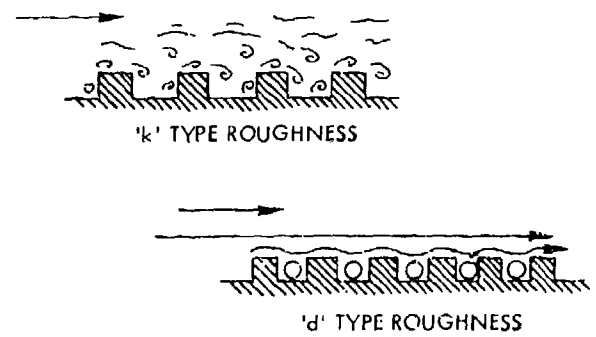


Figure 3-9. Sketches Illustrating 'k' and 'd' Type Roughnesses

the excrescences must be very uniform in height, since small variations can readily introduce some of the characteristics of k type roughnesses into the flow. Their drag and flow effects are of course much smaller than for k type roughnesses and do not reveal any direct dependence on the excrescence height, the important length dimension seems to be that of the overall flow, e.g. pipe diameter for flow in a pipe or boundary layer thickness for flow over a plate.

The existence of the d type roughness has been revealed almost accidentally in a few investigations of regular excrescence patterns and of the effects of grooves regularly scribed in an otherwise smooth surface. Perry, Schofield and Joubert (Reference 3.9) have made careful investigation of a d type flow formed by transverse rectangular section bars about one height apart in both zero and two different adverse pressure gradients. In addition, Wood and Antonia (Reference 3.10) have examined the turbulence components in the boundary layer above the excrescences and have noted little difference from the corresponding results for a smooth surface. A fuller discussion of the drag effects of discrete excrescences isolated or in arrays will be given in Section 4.

We come now to the description of the boundary layer velocity distribution outside the region where the law of the wall applies, i.e. the region of the velocity defect law. Applying the arguments already applied to a smooth wall (see Section 2.1.2) we again infer that there

$$\begin{aligned} \frac{u_e - u}{u_\tau} &= f(y/\delta), \text{ for a plate with zero pressure gradient,} \\ &= g(y/a), \text{ for flow in a pipe,} \end{aligned} \quad 3(16)$$

where f and g are functions to be determined by experiment. For flows with appreciable pressure gradients additional parameters involving these gradients are required on the right hand side.

From the argument that roughness effects are essentially confined to the law of the wall region we may infer that the forms of the functions f and g are the same for rough as for smooth walls. This is well borne out by experimental results. Thus, if we make use of Coles law of the wake hypothesis (see Section 2.1.2, equation 2(18)) we can write for the velocity distribution in the boundary layer

$$u/u_\tau = A \ln[(y_\tau + \epsilon)u_\tau/\nu] + B - \Delta u/u_\tau + \Pi A w(y/\delta) \quad 3(17)$$

where $w(y/\delta)$ is Coles' wake function, given with good approximation in equation 2(19) and Π is the form parameter determined by the pressure distribution. From 3(17) it follows that for the flow over a plate

$$u_e/u_\tau = A \ln(\delta u_\tau/\nu) + B - \Delta u/u_\tau + 2\Pi A \quad 3(18)$$

and hence

$$\left. \begin{aligned} \frac{u_e - u}{u_\tau} &= -A \ln(y/\delta) + \Pi A [2 - w(y/\delta)] \\ \text{where we have written } y &= y_\tau + \epsilon. \\ \text{For the flow in a pipe} \end{aligned} \right\} \quad 3(19)$$

$$\frac{u_e - u}{u_\tau} = -A \ln(y/a) + \Pi A [2 - w(y/a)].$$

These are the same expressions as for a smooth wall, the only effect of the roughness being on the scaling velocity u_r .

From equations 3(15) and 3(18) it follows that for fully developed roughness flow

$$u_g/u_r = A \ln(\delta/k) + B - D + 2\pi A$$

$$\text{or } (2/c_{fe})^{1/2} = A \ln(\delta/k) + B - D + 2\pi A. \tag{20}$$

3.3 Equivalent Sand Roughness Concept

The wide scope of Nikuradse's results for the closely packed sand roughness that he tested on the inner surfaces of pipes of circular section and the ready applicability of the Prandtl-Schlichting relations based on these results for similarly roughened plates, wings and bodies leads to the hope that they can be used for other forms of roughness. Thus, we seek to determine whether for any given form of roughness there is an equivalent sand roughness so that its effect on surface drag etc., can be quickly derived from Nikuradse's results or the Prandtl-Schlichting curves (Figures 3.3, 3.4 and 3.5).

From equation 3(8) we can write for fully developed roughness flow

$$u/u_r = A \ln(y/k) + h_{fr}$$

where h_{fr} is a constant dependent only on the type and distribution of the roughness. For Nikuradse's sand roughness $h_{fr} = 8.5$, equation 3(10). If the velocity profile and the corresponding value of u_r for a given type of roughness are to be the same as for an equivalent sand roughness then it follows that

$$A \ln(k/k_s) = 8.5 - h_{fr} \tag{21}$$

where k and k_s are the representative heights of the roughness and its sand equivalent. Thus, if we determine h_{fr} from the measured velocity profile for the roughness k under test we can use equation 3(21) to determine the equivalent sand roughness k_s .

Schlichting (Reference 3.11) performed a series of tests on various forms of distributed but regular excrescences in the form of spheres, spherical segments, cones, right-angled corner pieces of various sizes and spacings on one wall of a pipe of rectangular section. He was able to establish in all cases an equivalent sand roughness as described above. Young (Reference 3.12) measured by means of the pitot traverse method the profile drag of a wing of NACA 0012 section at zero incidence with various paint finishes of different roughness over a range of subsonic speeds and he likewise concluded that for each surface an equivalent sand roughness could be determined. A similar result followed from tests of thread roughnesses in pipes by Streeter (Reference 3.13) and by Moebius (Reference 3.14), commercially rough pipes by Moody (Reference 3.15) and of transverse rods on a plate by Betterman (Reference 3.7). It should be emphasised, however, that equation 3(21) applies only to the fully developed roughness regime as the equivalence does not necessarily hold in the intermediate rough regime.

Various attempts have been made to relate the ratio $\alpha = k/k_s$ to the spacing and shape of the roughnesses in order to derive a method for predicting α . The most effective appears to be that of Grabow and White (Reference 3.16) who have predicted α as an empirical function of a parameter Λ given by

$$\Lambda = (u_r/k) (A_s/A_p)^{4/3}, \tag{22}$$

where l_r is the mean distance between roughness elements, k is the mean roughness height, A_P is the maximum cross-section area of a roughness normal to the flow, A_s is the surface area of a roughness forward of the section of maximum cross-section area. We can interpret l_r as $N^{-1/2}$, where N is the number of roughness elements per unit surface area. A presentation of Grabow and White's correlation updated by Blanchard (Reference 3.8) to include his own results is shown in Figure 3.10. It will be seen that on the whole the mean lines shown provide a reasonable fit to the data analysed which include a wide range of different forms of roughness, although the scatter is somewhat masked by the logarithmic scaling. A striking result is that there is a minimum value of α (≈ 0.15) which occurs for $\Lambda \approx 5$; this reflects the fact that for a given form of roughness there is a density of surface packing that yields a maximum drag increment. If the roughnesses are more closely packed than this then they become increasingly immersed in the wakes of upstream roughnesses and the total drag increment is reduced. If they are less tightly packed then their numbers are reduced per unit area and again the total drag increment is reduced. Nikuradse's sand grains were packed as close as possible and their drag increment was well below the maximum.

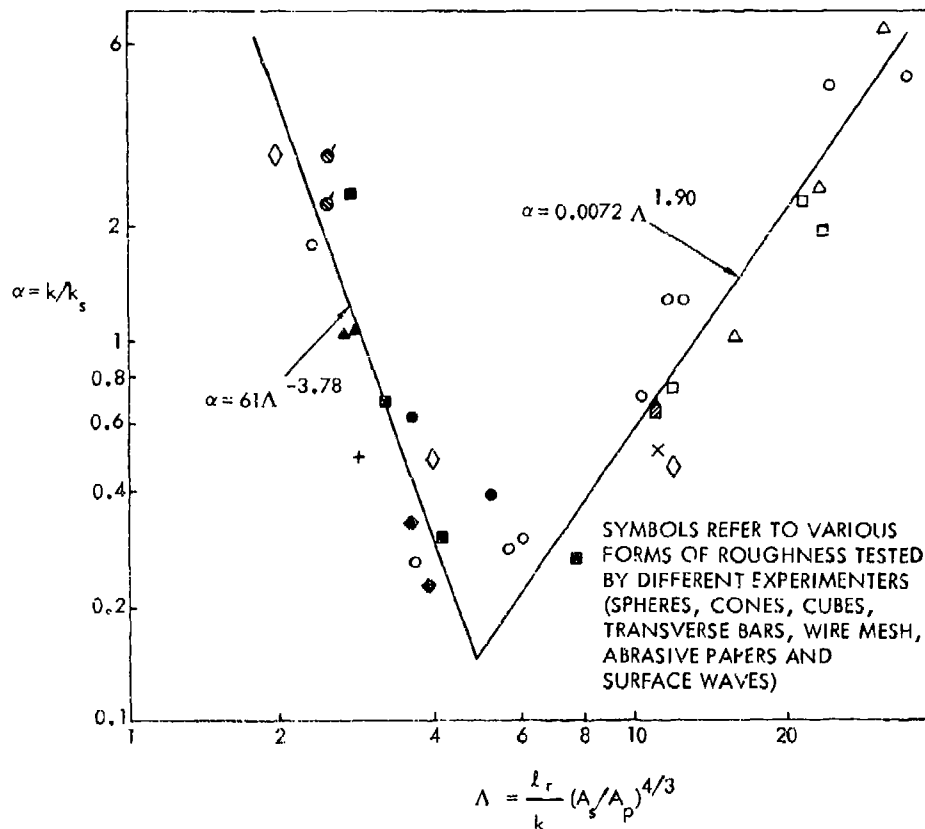


Figure 3-10. The Equivalent Sand Roughness, According to Grabow & White. (Data used Cover Wide Range of Different Types of Roughness)

With the aid of this correlation and Nikuradse's basic sand roughness results (as in Figures 3.3, 3.4 and 3.5) it is therefore possible to make an estimate of the drag effects of a specified form of distributed roughness in turbulent boundary layers in pipes and on flat plates with zero pressure gradient. These can with little further loss of accuracy be extended to wings and bodies, particularly if a plot such as that of Figure 3.5 is used. This last point will become clearer when we discuss in Section 5 in more detail the effects of a non-uniform pressure distribution.

3.4 Discontinuous Changes of Roughness

A number of investigations have been made of the changes in velocity distribution, turbulence characteristics and surface shear stress following a change of surface condition from smooth to distributed roughness and vice versa with and without a streamwise pressure gradient. The results show that the change is associated with the development of an internal boundary layer starting at the point where the change is introduced and growing within the existing one. At a sufficient distance downstream the flow becomes that associated with the downstream surface condition. Schofield (Reference 3.17) has made an analysis of the available data and relevant theoretical work and his main conclusions may be summarised as follows.

Within the boundary layer close to the wall a length scale z can be determined by writing

$$u/u_\tau = A \ln(y/z). \quad 3 (23)$$

For the boundary layer on a smooth wall equations 2(11) and 3(23) lead to

$$z = (2c_{f0})^{1/2} (v/u_\tau) \exp(-B/A) \quad 3 (24)$$

and for a rough wall equations 3(12), 3(15) and 3(23) lead to

$$z = k \exp\left[\frac{D-B}{A}\right]. \quad 3 (25)$$

If we write δ_i for the new internal boundary layer thickness then Schofield found that the available data were reasonably fitted by the empirical relation

$$\delta_i/z_2 = 0.18(X_s/z_2)^{0.92} \quad 3 (26)$$

where z_2 is the value of z downstream of the change and X_s is the streamwise distance from the point at which the change occurs. This proved to be a somewhat better fit to the data and easier to use than a formula previously derived by Townsend (Reference 3.18) for zero pressure gradient.

Almost immediately after the change the internal boundary layer shows a logarithmic region of velocity distribution but close to the point of change the slope and intercept of a Clauser type plot can only be made consistent with other methods of inferring the skin friction if the quantity A , normally constant being the inverse of the Von Karman constant, is assumed to vary there. This is not unexpected since immediately after the change begins the turbulence characteristics and structure still reflect in large measure the upstream conditions. Consequently, the ratio of the eddy stress to the mean velocity gradient, and hence the mixing length l , will differ from that to be expected in a developed equilibrium turbulent boundary layer. Since $A = y/l$ near the wall, the quantity A (and hence the von Karman constant $= 1/A$) can also be expected to differ near the roughness change from its value further downstream. However, such differences become insignificant within a few boundary layer thicknesses downstream of the change, although the surface shear stress may take several boundary layer thicknesses (about 15) to achieve the downstream equilibrium value. The surface shear stress sometimes shows a non-monotonic behaviour close to the point of roughness change.

REFERENCES

- 3.1 Nikuradse, J. 1933 Strömungsgesetze in Rauhren Röhren. Forsch. Arb. Ing. Wes. No. 361
- 3.2 Prandtl, L. & Schlichting, H. 1934 Das Widerstand Gesetz Rauher Platten. Werft-Reederei-Hafen. 1-4.
- 3.3 Berg, D. E. 1979 Surface Roughness Effects on Mach 6 Turbulent Boundary Layers. AIAA J 17, No. 9, 929-930.
- 3.4 Perry, A. E. & Joubert, P. N. 1963 Rough Wall Boundary Layers In Adverse Pressure Gradients. J. F. M., 17, Pt. 2, 193-211
- 3.5 Hami, F. R. 1954 Boundary Layer Characteristics for Smooth and Rough Surfaces. Trans. Soc. Naval Arch. Mar. Eng. 62, 333-
- 3.6 Moore, W. F. 1951 An Experimental Investigation of the Boundary Layer Development along a Rough Surface. Ph.D Dissertation, State Univ. of Iowa.
- 3.7 Betterman, D. 1965 Contribution a l'Étude de la Couche Limite Turbulente le long des Plaques Rugueuses. Centre National de la Recherche Scientifique, Paris, Rep. 65-6.
- 3.8 Blanchard, A. 1977 Analyse Experimentale et Theorique de la Structure de la Turbulence d'Une Couche Limite sur Paroi Rugueuse. Thesis presented at Univ. of Poitiers, No. 97.
- 3.9 Perry, A. E., Schofield, W. H. & Joubert, P. N. 1969 Rough Wall Turbulent Boundary Layers. J. F. M., 37, Pt. 2, 383-413.
- 3.10 Wood, D. H. & Antonia, R. A. 1975 Measurements in a Turbulent Boundary Layer over a 'd' Type Surface Roughness. Trans. ASME, J. App. Mech., 591-
- 3.11 Schlichting, H. 1936 Experimentelle Untersuchungen zum Rauhgkeitsproblem. Ing. -Arch. 7, 1-34.
- 3.12 Young, A. D. 1950 The Drag Effect of Roughness at High Sub-Critical Speeds. J.R.Ae.S, 18, 534-

- 3.13 Streeter, V. L. 1935 Frictional Resistance in Artificially Roughened Pipes. Proc. Amer. Soc. Civil Eng. 61, 163-186.
- 3.14 Moebius, H. 1940 Experimentelle Untersuchungen des Widerstandes und der Geschwindigkeitsverteilung in Rohren mit Regelmässig Angeordneten Rauigkeiten bei Turbulenter Strömung. Phys. Z., 41, 202-225.
- 3.15 Moody, L. F. 1944 Friction Factors for Pipe Flow. Trans ASME, 66, 671-684.
- 3.16 Grabow, R. M. & White, C. O. 1975 Surface Roughness Effects on Nose-Tip Ablation Characteristics. AIAA J., 605-609.
- 3.17 Schofield, W. H. 1977 The Response of Turbulent Shear Flows to Discontinuous Changes in Surface Roughness. Aeronautical Research Labs. (Australia) Mech. Eng. Rep. No. 150.
- 3.18 Townsend, A. A. 1976 The Structure of Turbulent Shear Flow. C.U.P. (2nd. Ed.)

4. DISCRETE ROUGHNESS

In spite of much contrary effort by aerodynamicists, the external surfaces of aircraft are marred by numerous discontinuities and excrescences. Many of these, such as pitot tubes and certain types of antennae are essential to the aircraft mission and must protrude from the surface in order to function. Others are a result of compromises for economy of manufacture, and are in a sense deliberately chosen rather than their smoother, but more expensive alternatives. The process of arriving at these compromises is very inexact because of the dearth of information on the many types of surface imperfections which may be encountered.

Wind tunnel experiments in the years preceding World War II provided systematic data on the drag of the types of roughnesses which were at that time most offensive. This work was inspired to a great extent by a 1929 paper (Reference 4.1) by B. M. Jones titled "The Streamline Aeroplane" which focused attention on the drag components of airplanes which could be eliminated as opposed to those which are unavoidable. "Fluid Dynamic Drag" by Hoerner (Reference 4.2), the first edition of which appeared in 1951, presents a comprehensive review of drag due to surface roughness as well as from other sources.

More recently a number of experiments have been completed, largely by the RAE, updating the basic data on discrete roughness to the flight conditions (Reynolds number and Mach number) which are pertinent to modern aircraft, and utilizing recent developments in boundary layer theory to provide a sound basis for correlation and application. Sections 2 and 3 have reviewed the boundary layer theory and its implications regarding drag due to roughness. This section will review a number of the available data sources to show, where possible, the correlation of the older data with that more recently becoming available, and to show the areas in which information on this subject is still sparse, or weakly substantiated.

4.1 General Considerations

The net drag increase due to surface roughness results from a fairly complex combination of interacting phenomena which might be listed as:

- o Pressure forces on the protuberance itself.
- o Changes in the local surface shear forces forward and aft of the protuberance.
- o A modification in the development of the boundary layer downstream of the protuberance.
- o Potential separation due to the added disturbance.

Since all of these phenomena can be influenced by pressure gradients in the flow about the basic body, it is apparent that the real drag increase can be highly configuration dependent. Practical utilization of general data on this subject demands therefore that experiments be performed with the roughness elements in the total flow field in which they are being considered, or that the unique conditions of the flow field can be adequately accounted for. Fortunately, a number of these effects are small enough to be ignored and others can be handled analytically. Most tests to obtain basic data on roughness drag are therefore conducted on flat plates in a wind tunnel and are

applicable to a wide variety of airplane applications. Methods for extending these results to arbitrary pressure distributions will be discussed in Section 5.

In some instances, References 4.3 to 4.5 for instance, the drag of roughness elements is determined by measurements of the drag of flat plates of limited extent with and without the element attached. The difference between these measurements represents therefore the forces acting on the element plus the difference in skin friction on the plate ahead of and behind the element. In other cases such as Reference 4.6, pressure distributions on the element are integrated to obtain the drag. These two types of data are generally used interchangeably. The change in skin friction on the measuring plate is probably small in comparison with the direct force on the element, but such data could be applied with greater confidence if more were understood regarding this phenomenon and if more were known about changes in skin friction downstream of the plate.

In some few instances, the effect of local pressure gradients has been determined for roughness elements. In Reference 4.6 for instance, it was determined that the pressures on the upstream face of a disturbance consisting of a spanwise plate erected on a wind tunnel wall were unaffected by changes in local pressure gradient. The net drag was changed by as much as 25% however as a result of changes in base pressure when tested in adverse pressure gradients. Only isolated instances of data showing pressure gradient effects exist in the literature.

The adverse pressure gradients which must exist on the after portion of closed bodies can also produce significant effects on the total drag contribution of roughness elements. Nash and Bradshaw (Reference 4.7) present an analysis showing that the drag contribution of such roughness can be magnified by up to 3 or 4 times for downstream pressure gradients which might exist on reasonable airfoil shapes. In Section 5 their analysis is discussed in more detail and some results are presented showing that exceptionally large magnification factors can arise for roughness on sensitive parts of a high lift multi-component airfoil.

There exist in the literature several collections of data on roughness effects, and in some cases data have been generalized to provide prediction techniques. The data sheets provided by the Engineering Sciences Data Unit in the United Kingdom and the Datcom in the United States include examples of the latter. Since these data sources are widely known and generally available, they are not referenced in detail here. The data presented herein in some cases provide an independent evaluation of some of the same information presented in those sources.

4.2 Individual Excrescences or Protuberances

This section will consider those individual, local surface disturbances such as fastener heads, protruding functional devices, and holes as opposed to items such as skin joints which span large percentages of the wing span or chord and which will be taken up in a subsequent section. By far the largest number of surface imperfections on aircraft skins are caused by the fasteners which provide structural attachments. When installed properly, the drag of each such fastener is miniscule, but their large number causes them to become an important consideration.

4.2.1 Fastener Drag

Several different types of data on drag caused by structural fasteners are available in the literature.

- o One type is based on some of the early work done by Schlichting and associates during water channel and wind tunnel tests to establish the "equivalent sand roughness" concept referred to in Section 3.3. Following the Nikuradse pipeflow experiments, Schlichting (1937) tested a number of rough plates with distributed roughness where the geometry of the roughness elements was controlled. He varied the cross-sectional shape and density of various roughness elements and established the equivalent height of sand roughness for which the drag would be equal for each configuration. Some of the shapes tested by Schlichting are crude representations of fasteners: i.e., spherical segments, cones, and indentations representing flush rivets.
- o Wind tunnel and flight test data on airfoils and wings having various fastener patterns represent a second type of data available on fastener drag. These experiments were done during the 1930's and 40's. The results tend to be configuration-dependent. However, they are practical examples of fastener drag.
- o A third type of data for fastener drag is based on the work of Wieghardt (1942) and Tillmann (1944). In these experiments, systematic variations of geometric parameters were carried out. Drag is based on the "single-element" or the discrete roughness approach. These data have more recently been supplanted by the results of tests by Gaudet and Winter, Reference 4.5, for instance.

Three basic methods for calculating the drag of fasteners were determined from the literature and a fourth approach was developed from a correlation similar to those made recently by the RAE for the drag of two-dimensional steps. The latter method is suggested since it follows from the same logic that led the RAE researchers to their approach; the drag of excrescences which are deeply immersed in the boundary layer should be related to the inner boundary layer parameters.

Method A

This method was detailed by Young in 1939 (Reference 4.8) and is an empirical formula approach. The empirical formula is attributed to the previous work of Schlichting in which drag is correlated using velocity at top of the rivet, and a further observation by Young that the drag coefficient for rivets is directly proportional to the height-to-diameter ratio (h/d). This method is a quick (rough order of magnitude) approach.

Method B

This method follows from the distributed roughness data of Schlichting and would be appropriate where the coverage is sufficiently dense to be considered fully rough. However, a modification to this approach is described for cases where there is doubt as to its applicability.

Method C

The third method is based on the experimental work of Wieghardt. This is essentially the method described in Hoerner where an "independent" drag coefficient

is found based on the frontal area and the effective dynamic pressure acting over the rivet.

Method D

This method uses the Wieghardt data of Method C, but the drag coefficient correlation is based on the local skin friction and a Reynolds number based on the roughness height and local friction velocity.

Five of the examples of "practical" fastener experiments were chosen to evaluate the prediction methods. The results are shown in Figure 4.1. Essential details of these five data sources are given below:

$$\Delta C_D = \frac{\text{DRAG INCREASE DUE TO FASTENERS}}{q_o S_W}$$

- WILLIAMS - 1" PLATE (REF 4.9)
- WILLIAMS - NACA 0012 (REF 4.10)
- △ YOUNG - NACA 2417 (REF 4.8)
- ▽ HOOD - NACA 23012 (REF 4.11)
- ◇ FENTER - PLATE, M = 2.23 (REF 4.12)

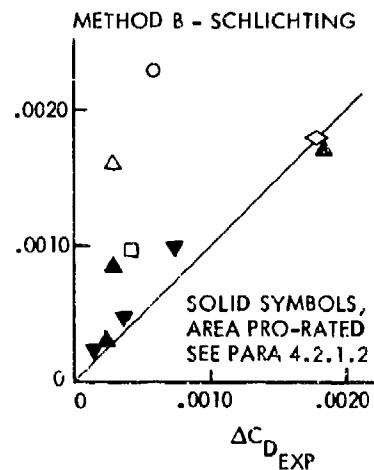
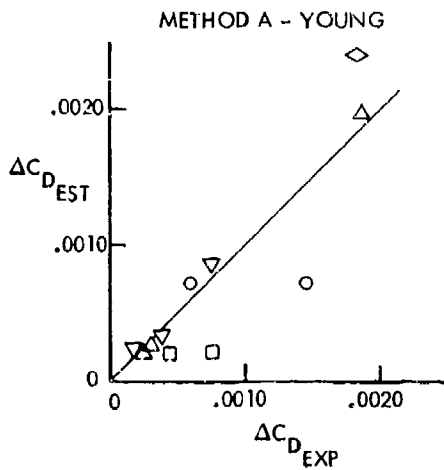
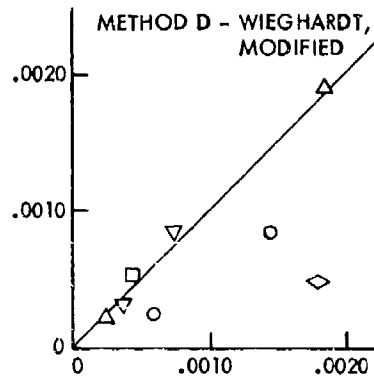
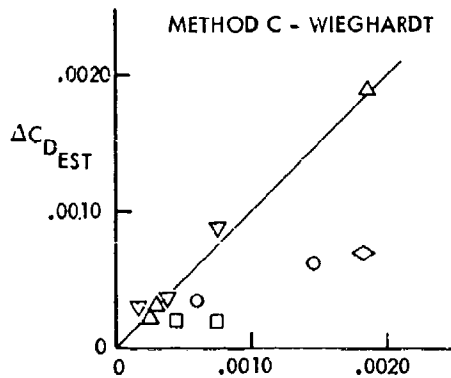


Figure 4.1 Fastener Drag Correlation

Williams 1" Plate, Reference 4.9

Flat plate with rounded nose and tapered trailing edge. Tested with 150 rivets on each surface spaced at 1.5". Reynolds numbers from 1×10^6 to 24×10^6 on 2 foot chord.

Williams NACA 0012, Reference 4.10

5376 simulated rivets on 8-1/4 inch chord two-dimensional airfoil, Reynolds number to 9×10^6 .

Young NACA 2417, Reference 4.8

Glove added to aircraft wing. Tested with various roughness elements. 36, 43, or 49 rows of rivets spaced 1" chordwise and 6" spanwise, Reynolds numbers to 18×10^6 .

Hood NACA 23012, Reference 4.11

2500 Brazier head rivets on 5 foot chord two-dimensional airfoil. Reynolds numbers to 18×10^6 .

Fenter Plate, $M = 2.23$, Reference 4.12

Flat plate in wall of wind tunnel with 117 simulated rivet heads. Reynolds numbers to 20×10^6 .

Estimates of the drag caused by these fastener arrays were made using each of the four methods outlined above. The following paragraphs discuss the basis for each of the estimation methods.

4.2.1.1 Method A. Young (1939), Reference 4.8

He refers to Schlichting's work which suggests that the drag of a rivet is given by

$$D_R = C_f \left(\frac{1}{2} \rho u_h^2 \right) f \quad (1)$$

where D_R = drag of the rivet

C_{fR} = coefficient, function of rivet shape

u_h = velocity in boundary layer at height h of the rivet

f = frontal area of rivet

Young shows several points which substantiate that $C_{fR} = 1.5 (h/d)$.

He goes on to derive equations for the drag increment due to rivets for a wing:

$$\Delta C_{D_R} = 4.05 \frac{h^2}{S} N \left(\frac{h}{c}\right)^{2/7} (1 + 1.5 (t/c)) \quad 4(2)$$

and fuselage:

$$\Delta C_{D_R} = 4.05 \left(\frac{h^2}{S}\right) N \left(\frac{h}{L}\right)^{2/7} \quad 4(3)$$

These equations are developed using approximations for boundary layer thickness and for the superelectricity on the airfoil surface due to thickness ratio, t/c .

Young's method is an application of the "independent" drag coefficient concept where an overall coefficient, in this case C_{f_R} , was chosen. His function

$$C_{f_R} = 1.5 (h/d) \quad 4(4)$$

was derived from some of the early low Reynolds number data and consequently the correlation shown in Figure 4.1 is quite good. Since the method is independent of Reynolds number, the method does not always correlate well for data where the Reynolds number was varied during the experiment. This method might be considered useful for quick estimates and is applicable only to brazier-head fasteners.

4.2.1.2 Method B. Schlichting (1936), Reference 4.13

The primary data base for establishing the effects of density for roughness elements was developed by Schlichting in an effort to relate practical examples of manufacturing roughness on ships to the sand paper roughness experiments of Nikuradse. He systematically varied the spacing of a number of roughness elements, some of which are similar to fasteners, and determined the equivalent height of sand grain particle which matched each roughness configuration. These results can be used, in conjunction with the sand grain roughness data of Nikuradse, to find the drag coefficient for fastener problems where the coverage is dense enough to be considered distributed roughness. Figure 4.2 shows the Schlichting data for each configuration tested. These results have been collapsed into a more general curve relating density and the roughness ratio, k_s/k , in Figure 3.10.

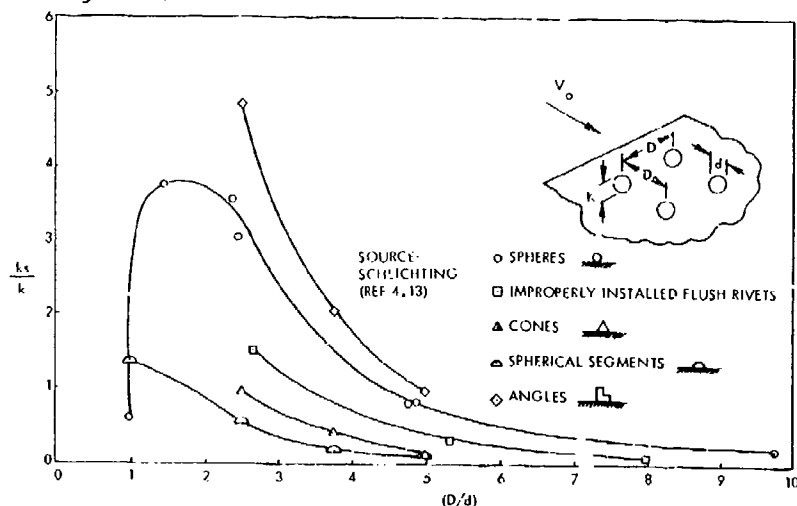
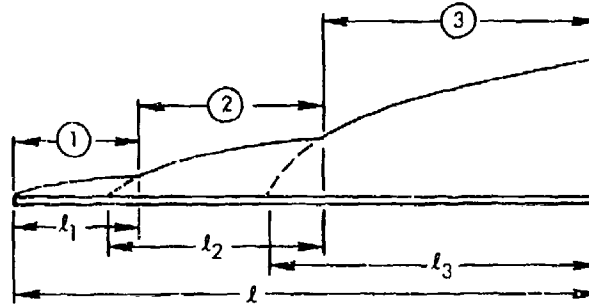


Figure 4.2. Proximity Effect on Equivalent Sand Roughness

Procedure for Implementing Method B:

Since, in general, the entire area may be covered by roughness, some assumptions regarding the flow conditions and apportionment of areas for each segment must be made. The following example illustrates the recommended procedures:



Zone 1 = Laminar Flow

Zone 2 = Smooth Turbulent Flow

Zone 3 = Rough Turbulent Flow

S = TOTAL
P PLATE
AREA

RNF = Freestream Reynolds Number/Foot

The incremental drag due to roughness is calculated by first calculating the total drag for the mixed flow case and then subtracting the drag for an assumed "smooth-flow" case. For the mixed flow case, the total drag is found by determining the total momentum loss at the trailing edge. This requires knowledge of the effective origin of the flow for each segment, illustrated by the dashed extrapolations of Segments (2) and (3) in the sketch.

An approximation to this case can be made by calculating the drag of each segment separately (as an isolated case) with the origin assumed to occur instantaneously at the beginning of the segment. Thus,

For Zone 1, 4(5)

$$R_1 = l_1 \times (\text{RNF})$$

$$C_{D1} = (C_{F_{\text{laminar}}})_{R_1} \times \frac{l_1}{l}$$

where $(C_{F_{\text{laminar}}})_{R_1}$ is the laminar skin friction coefficient

at Reynolds Number = R_1

For Zone 2, 4(6)

$$R_2 = (l_2) \times (\text{RNF})$$

$$C_{D2} = (C_{F_{\text{smooth}}})_{R_2} \times \frac{\textcircled{2}}{l}$$

where $(C_{F_{\text{smooth}}})_{R_2}$ is the smooth turbulent flow skin friction coefficient

at Reynolds number = R_2

For Zone 3,

4(7)

$$R_3 = (l_3) \times (\text{RNF})$$

$$C_{D_3} = (C_{F_{\text{rough}}})_{R_3} \times \left(\frac{3}{l}\right)$$

where

$(C_{F_{\text{rough}}})_{R_3}$ is the rough turbulent flow skin friction coefficient

at Reynolds Number = R_3 and at the equivalent sand roughness.

The total drag is

4(8)

$$C_{D_{\text{mixed flow}}} = C_{D_1} + C_{D_2} + C_{D_3}$$

For the "all-smooth" case, Zone 2 extends to the trailing edge and the drag is similarly calculated for two segments.

Finally, the incremental drag due to roughness is

4(9)

$$(\Delta C_D)_{\text{rough}} = C_{D_{\text{mixed flow}}} - C_{D_{\text{smooth}}}$$

Since this method is based on the assumption that the fasteners are uniformly distributed over the area covered, the use of Figure 3.10 may not provide an accurate prediction where rows of rivets are spaced further apart spanwise than in the flow direction as illustrated below:

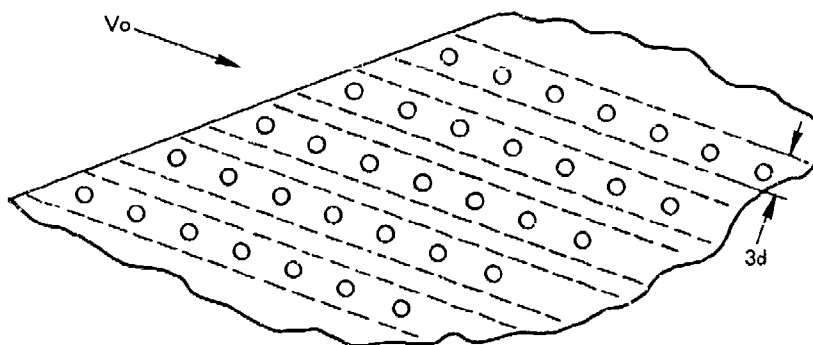


Figure 4.3 Pro-Rated Area Concept

In this case, a better correlation may be possible by using a pro-rated area based on a strip of width equal to three times the diameter of the fastener. It is assumed that no drag increase occurs in the area between strips. This was done for several of the correlations in Figure 4-1 and as can be seen, an improved correlation was possible.

4.2.1.3 Method C. Wieghardt (1942), later Hoerner

This method refers to the general approach of using certain experimental results, as published, for finding the C_{Dm} for a specific type of fastener. Here, $C_{Dm} = D/\bar{q}f$ where \bar{q} is the mean dynamic pressure in the boundary layer up to the height of the fastener and f is fastener frontal area. Since the Wieghardt tests (which were supplemented by Tillmann) (References 4.3 and 4.4), contain the largest available systematic data base, his name was chosen to identify this method. These results also represent the basis for that portion of Hoerner's work covering fastener drag.

Several different investigations were made and these will be discussed separately.

(1) Round-head and flat-round fasteners

Wieghardt tested three different height-to-diameter ratios (h/d) and varied the height and Reynolds number to obtain the data shown on Figure 4.4 (Wieghardt Figure 45 data). These data show a decreasing C_{Dm} with increasing R_h and this trend is counter to the trend observed with other roughness elements. Hoerner explains that this is similar to the "critical Reynolds number" behavior of spheres. The height relative to boundary

R_x	h/d	Source
○ $2.7 \cdot 10^6$	0.2	Wieghardt Fig. 45 (Ref. 4.3)
□	0.3	
△	0.5	
● $7.1 \cdot 10^6$	0.2	Tillmann (Ref. 4.4)
■	0.3	
▲	0.5	
∇ $7.2 \cdot 10^6$	0.01-0.07	Fig. 39 (Hex Head)
× $5 \cdot 10^6$	0.25	
+ $5 \cdot 10^6$	0.42	

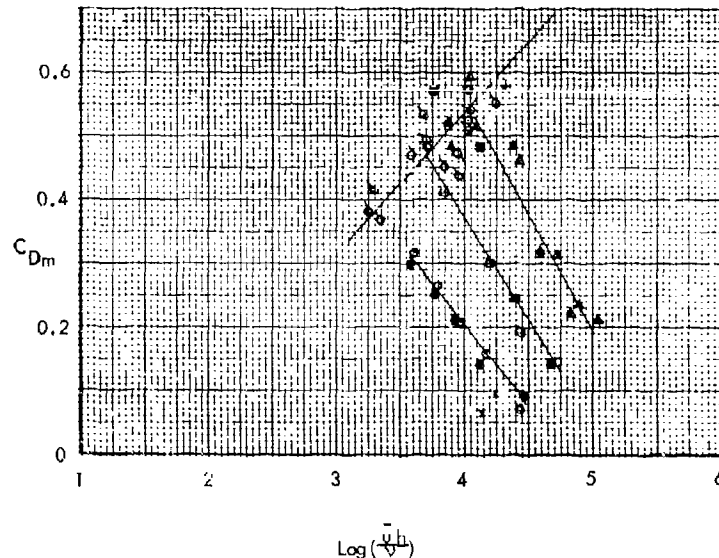


Figure 4.4 Drag of Round and Flat Head Fasteners vs Reynolds Number

layer thickness, h/δ , for the bulk of these configurations was large (.1 → 1.5) so that the behavior would be expected to approach that of freestream isolated bodies - thus a decreasing drag vs. Reynolds number could be experienced at some Reynolds number. It is also observed that results for the lowest h/δ tend to agree with the data taken by Wieghardt for small cylindrical head shapes (Wieghardt's Figure 39 data). Thus, for practical applications, where the h/δ would be quite small, the C_{Dm} might be expected to be larger than indicated by the parametric results, perhaps bounded by the dashed line in Figure 4.4. However, for the correlations shown in Figure 1 for Method C, the parametric results were used.

(2) Cylindrical-head bodies

Wieghardt tested a large range of sizes of cylinders normal to the flow. Those of large diameter to height ratio ($d/h > 10$) and small h/δ are considered representations of rivet heads. These are shown in Figure 4.4 as Wieghardt's Figure 39 data. A linear variation of C_{Dm} vs. R_h is indicated for these data. It is interesting to note that these data, when plotted in the RAE format (C_D/C_F vs. $u_T h/\nu$), agree very well with the drag of forward facing steps, (see Section 4.2.3.1).

(3) Countersunk cylindrical-head

Wieghardt's results for a simulated countersunk rivet are shown in Figure 4.5. Since the h/δ values indicated by these data are very small, $h/\delta = .003 - .015$, the overall accuracy is suspect and these results are only shown as an indication of the trends and relative magnitude. Here $C_{DP} = \Delta D / q_e \frac{\pi}{4} d^2$

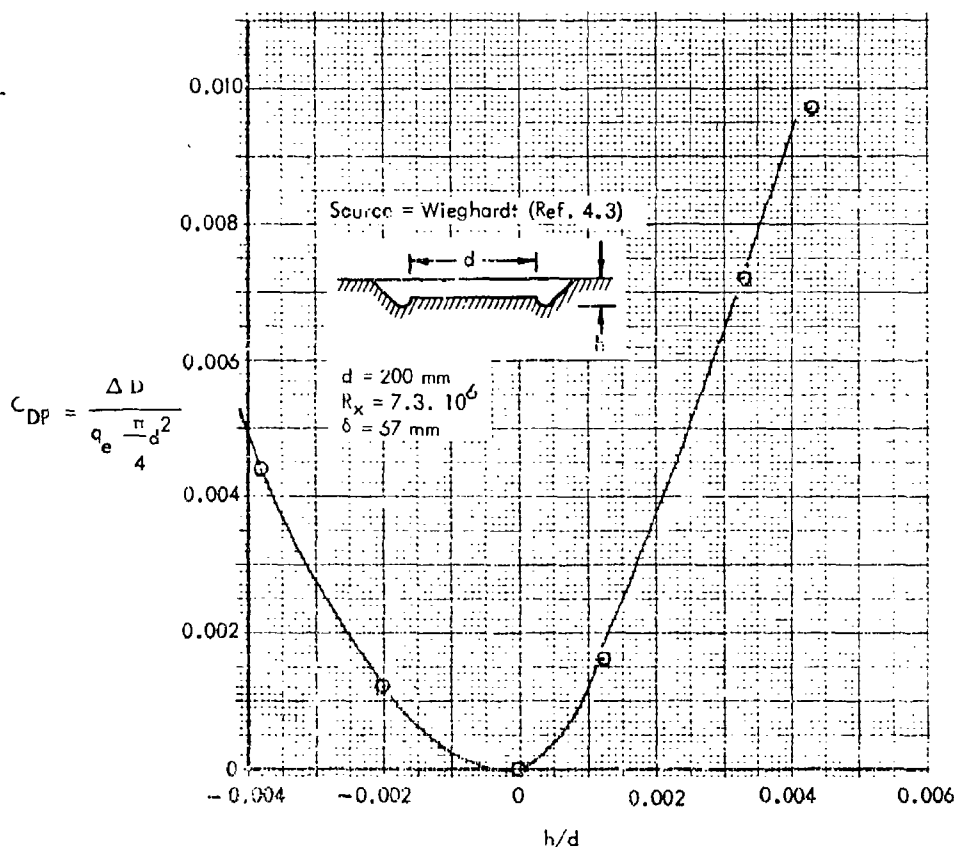


Figure 4.5 Drag of Countersunk Rivets

(4) Special shapes (Three-Dimensional)

Hoerner (Figures 13 and 14) shows single "independent" drag coefficients for a number of 3-D protuberances. He attributes these to Wieghardt and Tillmann. Some of these shapes (cylindrical, round-head, flat-head, flush rivet and bolts) are the same as reported above and he has selected some kind of average or nominal C_{Dm} . One shape, the hex-head nut was tested by Tillmann separately and again Hoerner selected a typical C_{Dm} . Some of the other shapes could not be found (screw, bracket, pins, etc.). In general, the drag coefficients for these different shapes can be approximated by the line previously discussed for cylindrical head shapes (Figure 4.4). The data for Method C shown in Figure 4.1 were estimated using Figure 4.4 and the multiplication factor of Nash and Bradshaw, reference 4.7, (see also Section 5.1). The correlation is generally quite good although the Williams flat plate data and Fenter supersonic data are much lower than the estimate. No multiplication factor was applied to either of these estimates.

4.2.1.4 Method D. Modified Wieghardt Correlation

In order to examine the behavior of Wieghardt's rivet drag results with respect to the newer correlation methods of the RAE research, the round-head fastener data of Wieghardt (his Figure 45) were expressed in the form

$$C_{De}/C_{fe} = f(h^+) \quad (10)$$

where $h^+ = u_\tau h/\nu$ = roughness Reynolds number, and Wieghardt's drag coefficients were converted to $C_{De} = D/q_e f_e$.

The concept of relating the drag of disturbances immersed in a turbulent boundary layer to the law of the wall similarity parameters was discussed in 1967 by Good and Joubert, Reference 4.6. Their measurements of pressures on two-dimensional plates perpendicular to a wall showed that the plate drag was correlated very well by relating C_{Dt} to $u_\tau h/\nu$ for plate heights up to 0.5δ . The forward-face pressure forces, in fact, correlated well for heights greater than δ . A velocity defect concept was evolved which properly correlated the plate drag for all heights tested. These concepts have been found to be very powerful in correlating drag measurements for a variety of excrescences which are smaller than the boundary layer thickness, as is generally the case for surface imperfections.

The results are shown in Figure 4.6. The tendency for the drag coefficient to decrease with increasing Reynolds number still predominates and a linear variation of C_{De}/C_{fe} vs $\log(h^+)$ is indicated. The effect of shape, through the height-to-diameter ratio, is obvious at the higher roughness Reynolds number. For the lower values of h^+ , there is a tendency for the data to follow the characteristic shape of the RAE data for steps and ridges. In fact, the round ridge curve appears to act as a cut-off for the low Reynolds number data for $h/d = 0.5$.

The existence of a cut-off is reasonable when consideration is given to the RAE results. The step and ridge drag coefficients are based on frontal area, normal to the airflow, as are the Wieghardt rivet drag coefficients. Both are also based on freestream dynamic pressure. Thus, it is unlikely that the rivet drag coefficient could significantly exceed that of a 2-D step or ridge of the same height. Consequently, the RAE round-ridge curve is assumed to be the correct variation for values of h^+ below the point of intersection with the constant (h/d) lines of Figure 4.6.

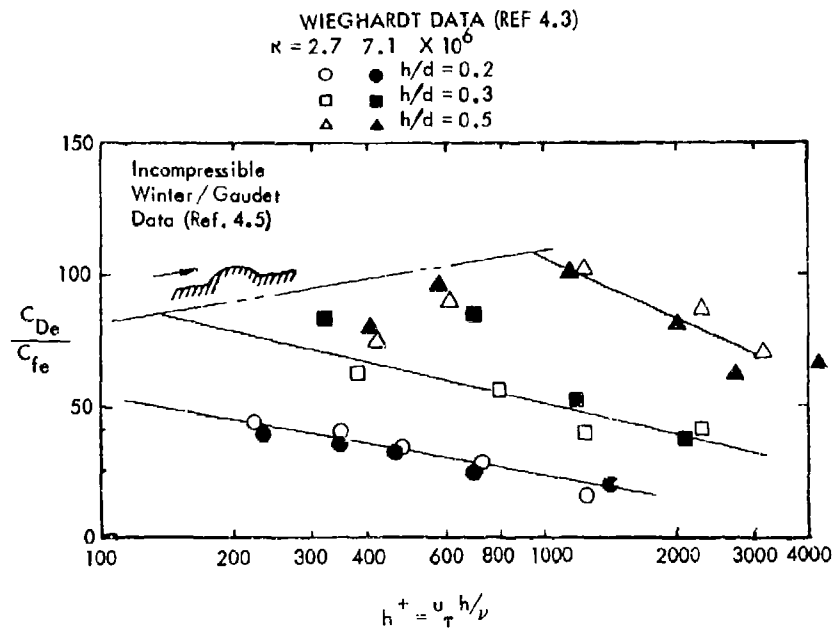


Figure 4.6 Comparison of Weighardt Data for Round-head Fasteners with Winter/Gaudet Data for two Dimensional Round Ridges.

Some additional data for rivets having a h/d equal to 0.2 are shown in Figure 4.6a. As shown, increase of h^+ to values above about 2000 causes a reversal in the variation of C_{De}/C_{fe} and a subsequent rather steep rise. The phenomena underlying these complex variations are not understood.

For the comparison shown in Figure 4.1, data from the correlation of Figure 4.6 were used and increased by a multiplication factor based on the concept of Reference 4.7. In summarizing the comparisons of Figure 4.1, none of the methods stands out clearly from the data presented. From a consideration of the fundamental correlation shown in Figure 4.6 and its compatibility with excellent correlations for other types of protuberances, shown later, Method D is preferred. The failure of the supersonic data to correlate is perhaps not an outstanding drawback and the flat plate data of Williams might be improved slightly if a magnification factor calculated from Reference 4.7 were applied.

4.2.2 Two-Dimensional Cylinders

Since the drag of many aircraft excrescences can be approximated by data on cylindrical models, these models have been studied extensively. While the items for which these results are most useful are generally of high aspect ratio, cylinder data for the complete range from sub-boundary layer lengths to infinite aspect ratio are included in this section for continuity. The small-height data are included also in the section on fastener drag.

4.2.2.1 Circular Cylinder Drag

The circular cylinder has been generally used as the basic model for cylinder drag research, starting with the two dimensional, or infinite length cylinder. For incompressible flow, the drag of a two dimensional cylinder is predominately a function of Reynolds number, normally expressed in terms of the cylinder diameter, R_d .

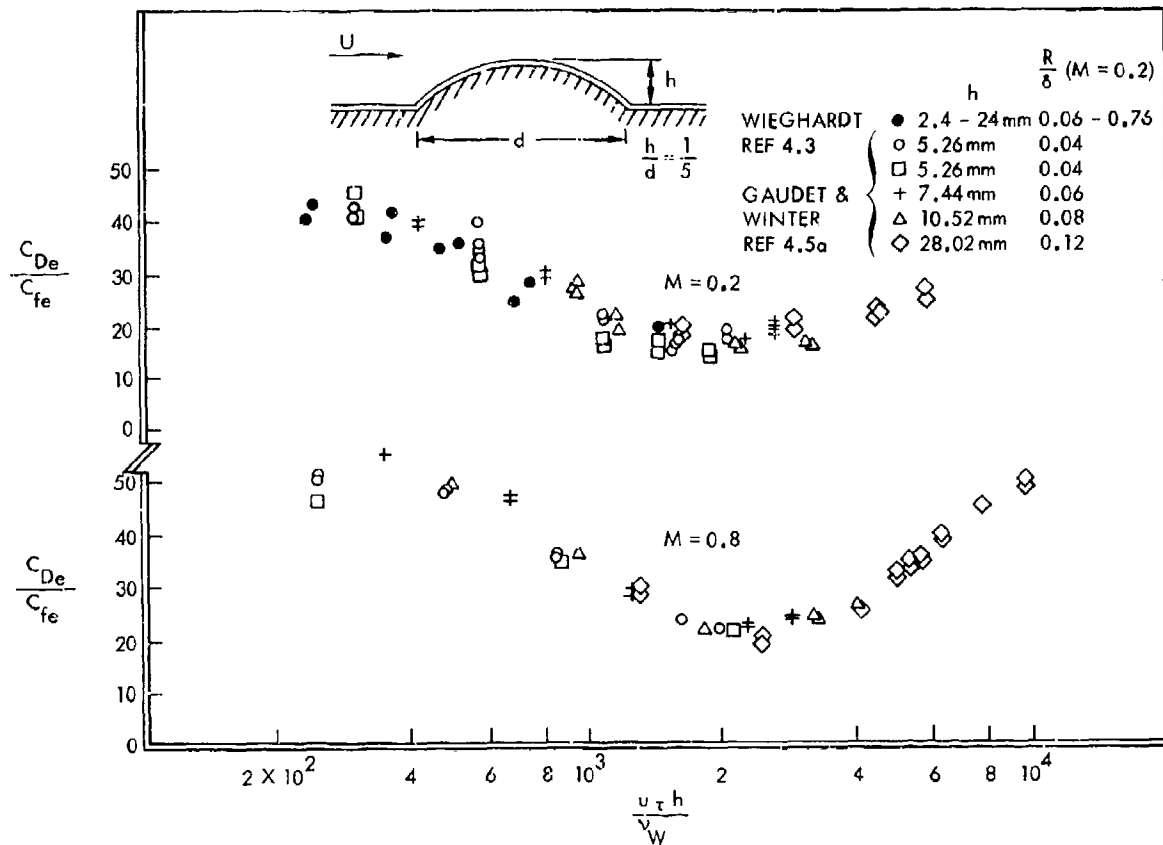


Figure 4.6a Drag of Rivets - Subsonic Speeds

The relationship between cylinder drag based on frontal area, $C_{D\pi}$ and Reynolds number, R_d , has been extensively verified such that the results are considered classical. Hoerner's compilation for this case, Reference 4.2, is repeated in Figure 4.7 for R_d ranging from 0.01 to 10^8 . The critical Reynolds number, where laminar separation transitions to turbulent flow, is seen to occur at $R_d \approx 4 \times 10^5$. An expanded version over the range from $R_d = 10^4$ to 10^6 , from Reference 4.14 is shown in the upper part of Figure 4.7.

4.2.2.2 Roughness Effects

The existence of uniform roughness on the cylinder or turbulence in the freestream tends to cause the transition to turbulent flow to occur at a lower Reynolds number and the cylinder to have a higher supercritical drag coefficient. Typical results from Reference 4.2 are shown in Figure 4.8, where the degree of roughness is expressed as the ratio of sand-grain size, k , to cylinder diameter.

4.2.2.3 Cross-Sectional Shape Variations

The effect of cross-sectional shape on 2-D cylinder drag was investigated for a number of conventional shapes by Delany, Reference 4-14. The results for the "sub-critical" Reynolds number ranges are summarized in Figure 4.9. Rounding the corners was determined to have a profound effect on the sub-critical drag coefficient as well as the supercritical Reynolds number effects. Since, for most practical aircraft applications, the Reynolds number for cylindrical components would be subcritical, the effects of rounding on the supercritical drag variation is not included here.

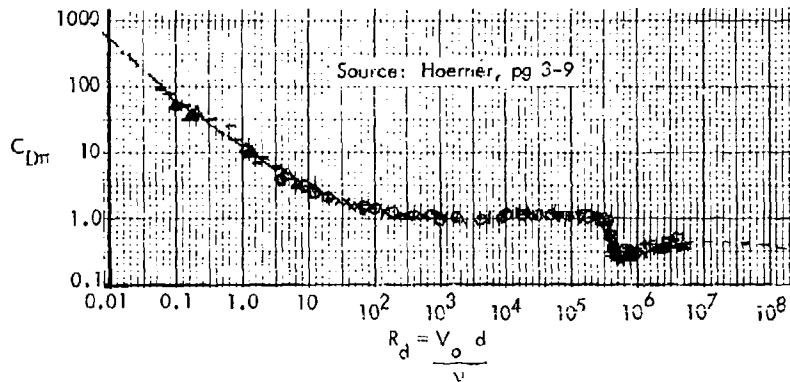
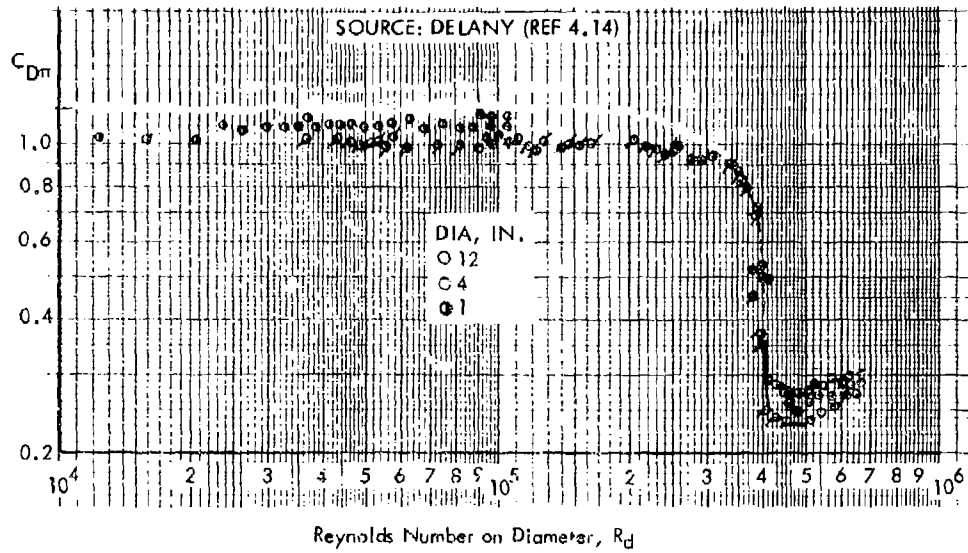


Figure 4.7 Drag of a Circular Cylinder Normal to the Flow

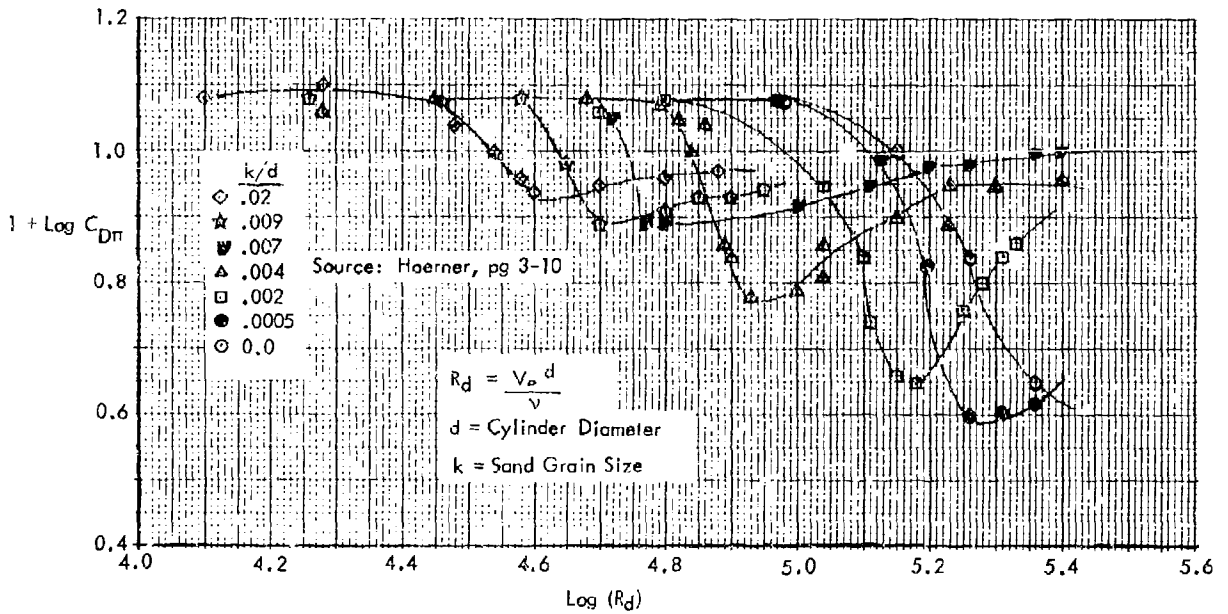


Figure 4.8 Effect of Surface Roughness on the Drag of a Circular Cylinder

SOURCE: NACA TN 3038, 1953
 DELANY, N. K. & SORENSEN, N. E.
 LOW-SPEED DRAG OF CYLINDERS OF VARIOUS SHAPES

MODEL: CIRCULAR, ELLIPTICAL, RECTANGULAR, DIAMOND AND
 TRIANGULAR SHAPED CYLINDERS SPANNING A WIND TUNNEL

TEST CONDITIONS: LOW SPEED, RN UP TO 2.3×10^6 PER FOOT AND
 PER DIAMETER (1 FT DIAMETER)

FLOW →	FINENESS RATIO l/w	CORNER RADIUS RATIO r/w		$(C_{D_{\pi}})$ SUB-CRIT.	FINENESS RATIO l/w	CORNER RADIUS RATIO r/w		$(C_{D_{\pi}})$ SUB-CRIT.
	1.0	.5		1.0		.5	.021 .083 .167	1.8 1.7 1.7
	.5	-		1.6		1.0	.015 .118 .235	1.5 1.5 1.5
	2.0	-		.6		2.0	.042 .167 .333	1.1 1.1 1.1
	.5		.021 .083 .25	2.2 1.9 1.6		1.0	.021 .083 .25	1.2 1.3 1.1
	1.0		.021 .167 .333	2.0 1.2 1.0		1.0	.021 .083 .25	2.0 1.9 1.3
	2.0		.042 .167 .5	1.4 .7 .4				

Figure 4.9. Effect of Cross-Sectional Shape on 2-D Cylinder Drag

4.2.2.4 Cylinder Inclined to Flow (Wires)

For a cylinder inclined to the flow direction, such as a tow cable or antenna wire, Reference 4.2 has shown that the drag may be related to the basic cylinder by the cross-flow principle. Under cross-flow conditions, the net force normal to the cylinder is only related to the velocity component normal to the basic cylinder axis. At some flow angle, α , the effective velocity component is $V_0 \times \sin \alpha$ and the dynamic pressure is $q \times \sin^2 \alpha$. Thus, the normal force coefficient, based on area along the cylinder axis and freestream q , is

$$C_N = C_{D_{\pi}} \times \sin^2 \alpha \quad 4(11)$$

and the drag coefficient in the freestream direction is

$$(C_D)_{\text{inclined}} = C_{D_{\pi}} \times \sin^3 \alpha \quad 4(12)$$

For a circular cylinder, at sub-critical Reynolds numbers, the drag coefficient would be

$$(C_D)_{\text{inclined}} = 1.0 \sin^3 \alpha \quad 4(13)$$

where the 1.0 value for $C_{D\pi}$ is shown on Figure 4.7. Reference 4.2 points out that the cross-flow principle cannot be applied for supercritical Reynolds number conditions. A constant $C_{D\pi}$ value of 0.2 is recommended for sweep angles up to 50 degrees.

It must be kept in mind that the above argument is based on a drag coefficient defined using a constant area as viewed along the cylinder axis. Some later data (Sections 4.3.1.2.3 and 4.3.2.3) consider a drag coefficient defined using projected frontal area, in which case the drag coefficient varies as $\sin^2 \alpha$.

4.2.3 Finite Length Cylinders

One of the first comprehensive studies of finite length or protruding cylinders was accomplished during the systematic investigation of surface irregularities by Wieghardt, Reference 4.3. Through use of a moveable floating-element balance technique, and by varying geometric parameters, he produced a very useful data base for the drag of numerous aircraft surface irregularities. In particular, he determined the effects of height, diameter and Reynolds number on circular cylinders which are small relative to the local boundary layer. These results were obtained at incompressible flow conditions and sub-critical Reynolds numbers.

More recently, Gaudet and Winter at RAE, Reference 4.5, and Pallister at ARA, Reference 4.15 have investigated Mach number as well as Reynolds number and geometry effects on protruding cylinders.

This work bridges the gap between the infinite cylinder (free of the boundary layer) and the finite cylinder, deeply immersed in the boundary layer, as studied by Wieghardt.

For drag estimation purposes, three categories of finite cylinders are distinguished:

- o The first category pertains to cylinders which are deeply submerged in the boundary layer. For small diameter protrusions (similar to fasteners), the drag estimation is based on a correlation of Wieghardt's data.
- o The second category also pertains to cylinders which are submerged in the boundary layer but which extend up to the edge of the boundary layer. Drag is estimated with the drag defect method outlined in Reference 4.5.
- o The third category contains those cylinders which protrude into the freestream. The correlations of Reference 4.5 and 4.15 are also used for drag estimation for these cases.

4.2.3.1 Cylinders Deeply Submerged in the Boundary Layer

The Wieghardt results for cylindrical bodies are summarized in Figure 4.10. Two types of geometric series were tested: one where the height-to-diameter ratio, h/d , was less than 0.07; and the other where h/d varied from 0.05 to 4.0. The C_{Dm} values are based on the cylinder frontal area and the average dynamic pressure acting on each cylinder. These data were converted to the form C_{De}/C_{De}^+ vs h^+ and are compared to the

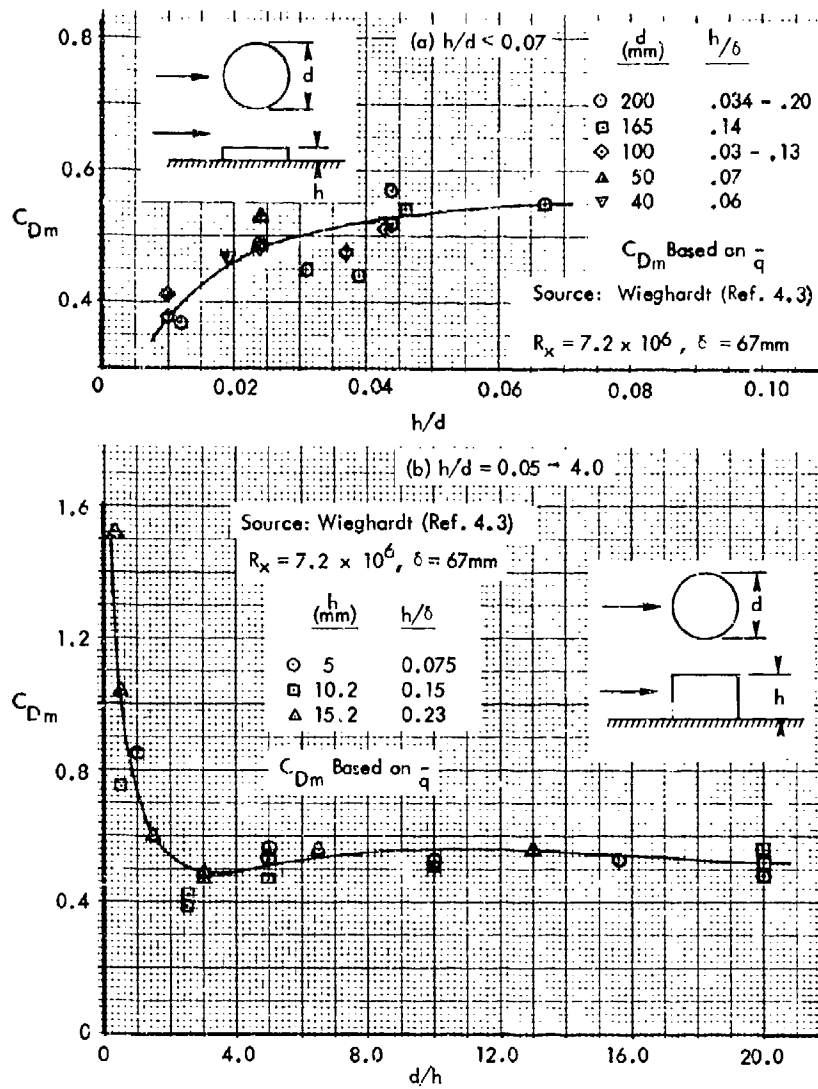


Figure 4.10 Drag of Cylinders Immersed in the Boundary Layer - Correlated Wiegardt Method

incompressible results of Reference 4.3 for various 2-D excrescences in Figure 4.11. This comparison shows that, for $h/d < 0.5$, the drag of these small cylinders is essentially modeled by the 2-D forward-facing step drag. Above $h/d = 0.5$, the C_{De} increases substantially and is not modeled by this method.

4.2.3.2 General Method for Cylinders in a Turbulent Boundary Layer

The method described in this section stems from the attempt in Reference 4.5 to determine a drag defect function for cylinders, similar to the incompressible 2-D bluff plate function of Good and Joubert, Reference 4.6. Mach number dependency was found in Reference 4.5 and a single drag defect function could not be established. Consequently, a series of correlation functions are required. The subsequent investigations of Pallister, Reference 4.15, were directed at supplementing the RAE data by providing a better coverage of the transonic speed range. These later results do complement the RAE data in some respects, but also highlight the large difference possible in the transonic range.

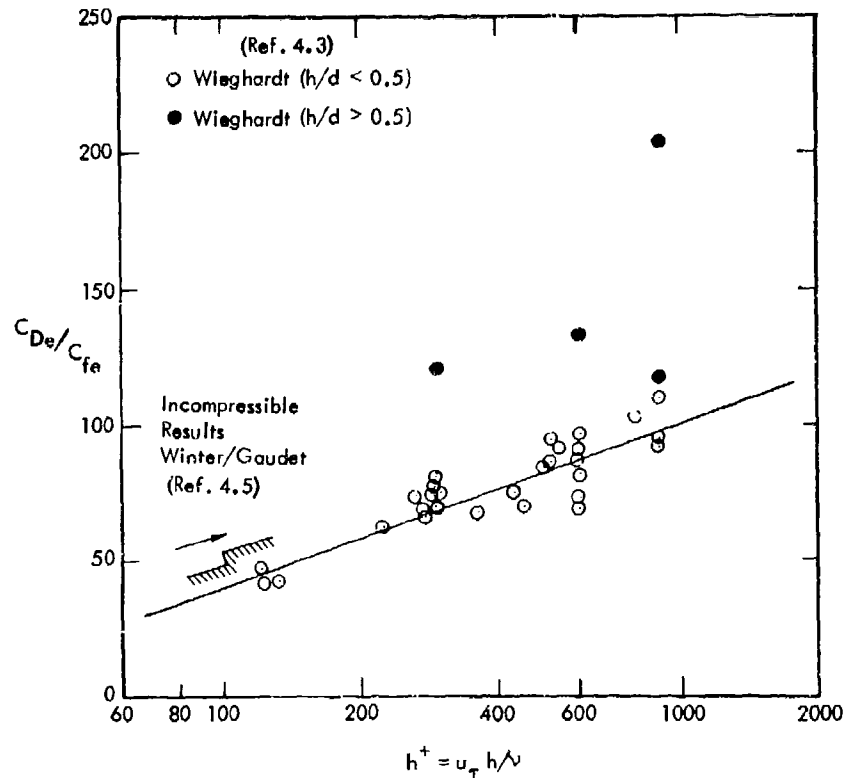


Figure 4.11 Comparison of Incompressible Cylinder Drag with RAE Results for Various Excrescences

From the basic test data for each Mach number, plots were made of C_{De} vs δ/h and extrapolated to determine the drag coefficient of an equivalent infinitely long cylinder, $C_{D\infty}$. The results are shown in Figure 4.12. The constant slopes obtained for $C_{D\infty}$ vs R_d enables a correction for Reynolds number to be made and the data plotted against Mach number, Figure 4.13. Data from Pallister and others are included on Figure 4.13. Prior to Pallister's results, the Mach number effect through the transonic range was not well established. His results confirm the general shape determined earlier by Welsh and the levels at $M = 0.8$ and $M \geq 1.4$ obtained by Winter and Gaudet.

The next step taken in Reference 4.5 to establish the drag function was to examine the ratio of the drag of a cylinder of height, $h = \delta$, where δ is the boundary layer thickness, to the drag of an infinitely long cylinder. Figure 4.14 compares results from References 4.5 and 4.15. Without the later results, the RAE observed that within a small range, $C_{D\delta}$ was proportional to $C_{D\infty}$ at a given Mach number. A drag defect function was then defined in the form

$$\frac{C_{D\delta} - C_{Dh}}{C_f} = F\left(\frac{h}{\delta}\right) \quad 4(14)$$

where $C_{D\delta}$ = drag coefficient of a cylinder with a height equal to the boundary layer, δ .

C_{Dh} = drag coefficient of a cylinder with arbitrary height.

Gaudet and Winter's results are shown in Figure 4.15. Winter and Gaudet could not find a function independent of Mach number and consequently concluded that drag could be estimated by use of Figures 4.13, 4.14, and 4.15. Pallister's data provide previously unavailable information for transonic mach numbers.

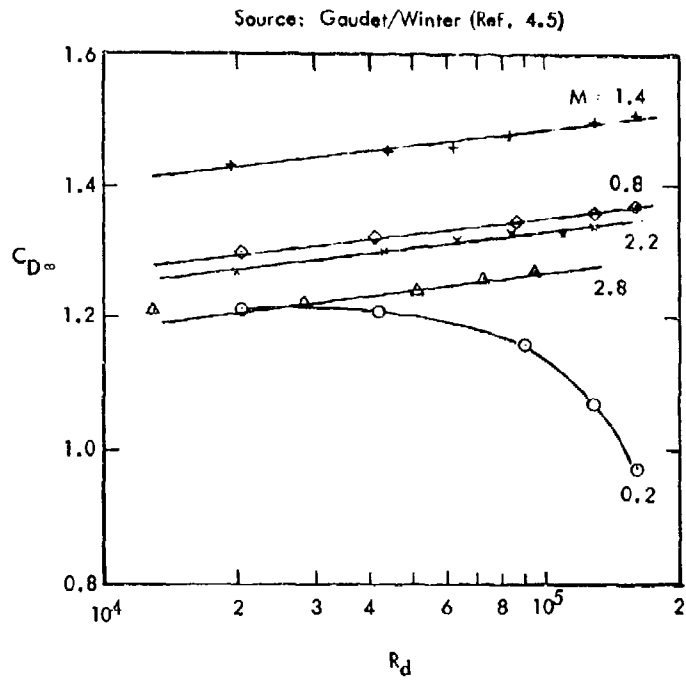


Figure 4.12 Drag Coefficient of Circular Cylinder of Infinite Length

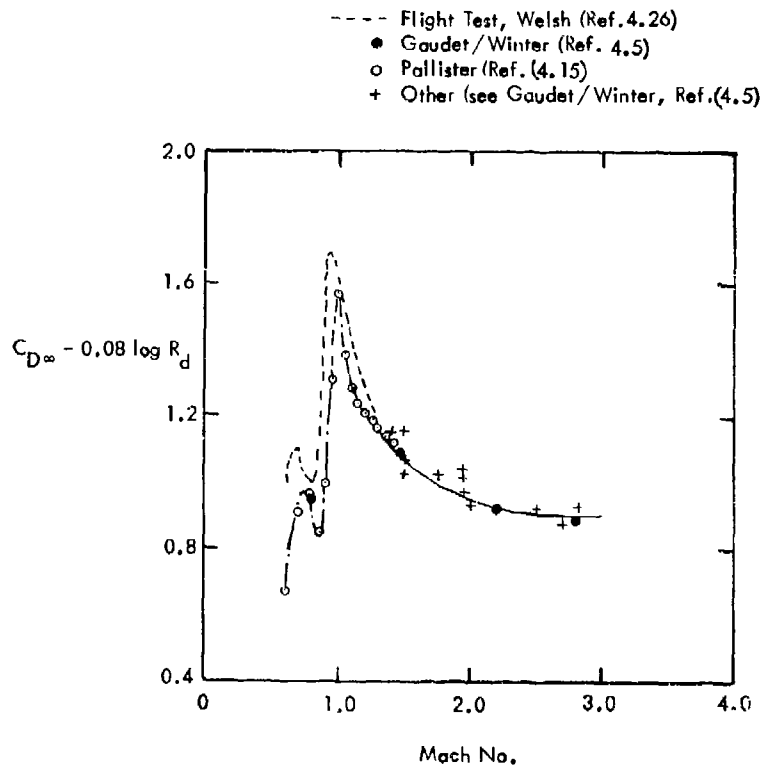


Figure 4.13 Comparison of Circular Cylinder Drag Measurements

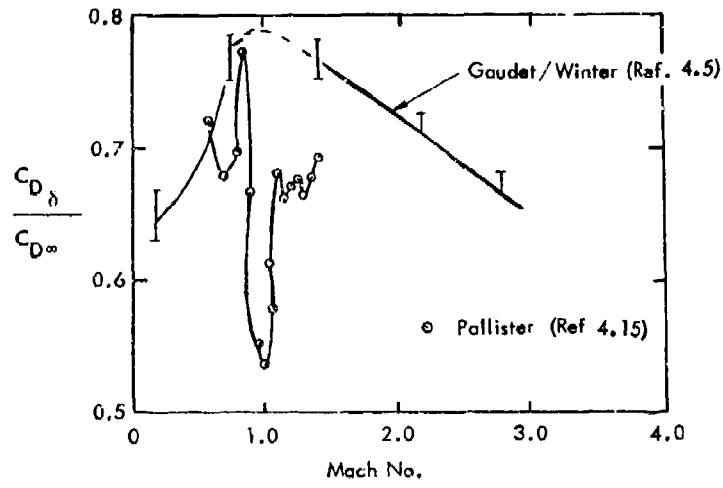


Figure 4.14 Effect of Mach Number on the Ratio of the Drag of a Finite Cylinder Immersed in the Boundary Layer to the Drag of an Infinitely Long Cylinder

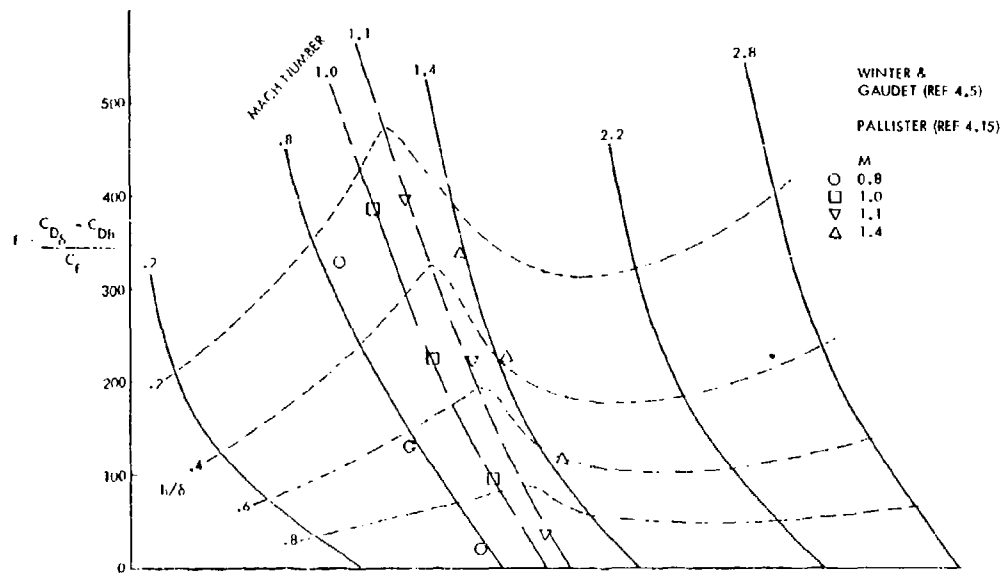


Figure 4.15 Drag Defect Function for Circular Cylinders

4.2.3.3 Cylinders Completely Immersed in Boundary Layer

Following the suggestion of Gaudet and Winter, the drag of cylinders completely immersed in the boundary layer can be found from

$$C_D = C_{D\delta} - F \times C_f \quad 4(15)$$

where

$$C_{D\delta} = \left[\frac{C_{D\delta}}{C_{D\infty}} \right] \times [C_{D\infty}]$$

Figure 4.14 Figure 4.13

and $F = F(M, h/\delta)$ Figure 4.15

4.2.3.4 Cylinders Extending Outside the Boundary Layer

For cylinders with a height greater than the local boundary layer thickness, the drag is found by pro-rating the submerged and exposed areas with the proper drag:

The drag of the submerged portion is

$$\frac{\delta}{h} (C_{D\delta})$$

and for the exposed portion the drag is

$$\left(1 - \frac{\delta}{h}\right) C_{D\infty}$$

The total drag for cylinders extending into the freestream is thus

$$C_D = \frac{\delta}{h} [C_{D\delta}] + \left(1 - \frac{\delta}{h}\right) C_{D\infty} \quad 4(16)$$

where $C_{D\delta}$ and $C_{D\infty}$ are determined from Figures 4.13, 4.14, and 4.15.

4.2.4 Stub Wings/Antenna

Although the drag of protrusions such as stub wing-like antennae tend to be highly configuration oriented, recent work by Gaudet/Winter, Reference 4.5, and Marshall/Williams, Reference 4.25, has led to a few generalizations which are useful for some applications. In Reference 4.5, an attempt was made to analyze test results on a series of stub wings of varying span along the lines of their cylinder drag defect function approach (see Section 4.2.2.1). This was only partially successful. Additional data were made available through Reference 4.25 which can be supplementary to the RAE results.

For bodies protruding into the freestream, the Reference 4.5 approach assumed that the drag can be determined by:

$$C_D = \frac{\delta}{h} C_{D\delta} + \left(1 - \frac{\delta}{h}\right) C_{D\infty} \quad 4(17)$$

where

$C_{D\delta}$ = the drag of the body with a height equal to the boundary layer thickness

$C_{D\infty}$ = the drag of the body with infinite length

For most airfoil or streamlined shapes used for stub-wing antennas, the value of $C_{D\infty}$ would be known by converting the zero-lift section drag coefficient for the actual airfoil used, to a coefficient based on frontal area.

The value of $C_{D\delta}$ would not normally be known or obtainable from sources convenient in design work. Data in References 4.5 and 4.25 would indicate that typical values of $C_{D\delta}/C_{D\infty}$ are approximately 0.85 at subsonic speeds and 0.7 at supersonic speeds.

For excrescences, such as stub wings, totally submerged in the boundary layer, generalized results are not available. Reference 4.5 utilized the drag defect function such that

$$C_D = C_{D\delta} - F \times C_f \quad 4(18)$$

and found that the defect function, F , varied with Mach number and h/δ in a manner somewhat similar to that shown for a cylinder, Figure 4.15 of Section 4.2.3.2, but with the values scaled by a factor of 0.75. Again, this was applied to the supersonic results only. Reference 4.25 offered that a better method would be to account for the reduced dynamic pressure through the boundary layer by integrating:

$$C_D = C_{D\infty} \times \frac{\delta}{h} \int_0^{h/\delta} \left(\frac{\bar{u}}{u}\right)^2 d(y/\delta) \quad 4(19)$$

This method relies on knowledge of the existing boundary layer profile and actually is a version of the Hoerner effective dynamic pressure method. Thus, no improved general method beyond the two described above is available.

4.2.5 Drag of Holes and Surface Cut-outs

The data base for the drag of holes is taken from two series of experiments - one carried out in Germany during the period 1936-1942, References 4.3, 4.4, and 4.16, and the other being the recent British work, References 4.17, 4.5, and 4.15. Although these experiments cover a wide range of geometric and flow parameters, it has not been possible to generalize the results into accurate drag prediction methods. In fact, Reference 4.5 concludes that because of the complexity of the three-dimensional flow pattern within a hole, it is not likely that a simple analysis will produce methods for describing all the possible combinations. In the special case of circular holes, Reference 4.17 shows a reasonably good correlation based on the kind of analysis successfully used by the British for many types of excrescences.

Careful scrutiny of all the various experimental results shows that the drag of holes is only a weak function of scaling parameters (Reynolds number, skin friction, boundary layer characteristics). Geometric factors, such as depth and hole aspect ratio (width-to-length ratio) tend to predominate. Consequently, the use of the actual test results as reported becomes a valid candidate as a method of estimating hole drag. For several types of holes correlations have been derived which can be used for estimation purposes.

Two basic categories of holes are identified by planform shape: those with a curved planform (round or elliptical holes), and those with rectangular planforms. The latter does not include slots or cut-outs which are small relative to the boundary layer thickness. These are covered in Section 4.3.3.

4.2.5.1 Circular Holes

The early experiments of circular holes covered a large range of d/h ratios (see References 4.3, 4.4, and 4.16 for incompressible flow and were conducted at low Reynolds numbers (R_x less than 7.5×10^6). At these conditions, the drag was found to be essentially independent of Reynolds number and a function of the diameter-to-height ratio. A cyclical variation of the drag coefficient vs. h/d was observed which dampened as h/d increased, see Figure 4.16. This cyclic variation is probably associated with changing flow patterns in the region of the hole. Thus, with some geometries the vortices that form within the hole remain there and the flow is relatively steady and stable. The external flow then passes over an effectively smooth free surface defining the upper surface of the hole and the drag is low. For other geometries vortices are continuously generated by the hole and convect downstream as a wake; the drag contribution is then high.

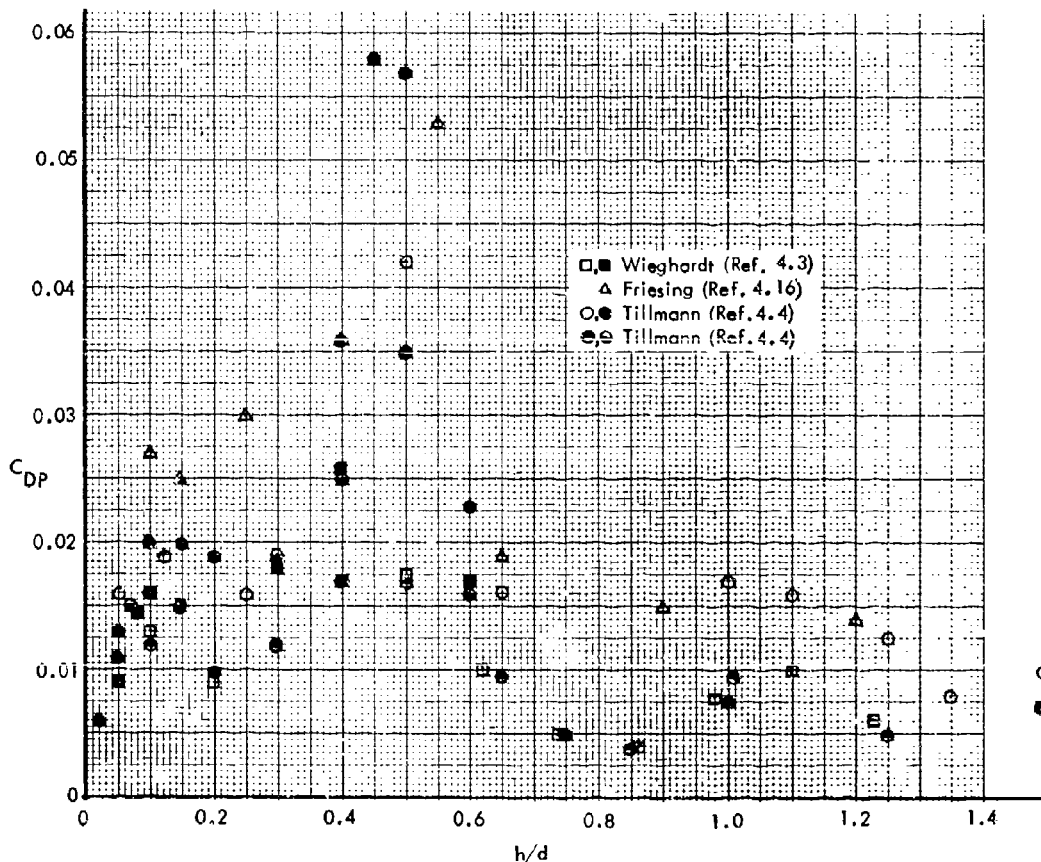


Figure 4.16 Comparison of Some Early Experimental Results on the Drag of Circular Holes

Subsequently, the experiments of References 4.15 and 4.17 have indicated a moderate influence of Reynolds number as well as Mach number effect. These data confirm the cyclical nature of the variation with h/d and a correlation was made based on the observation that a power law relationship exists between the drag ratio, C_{DP}/C_f , and the roughness Reynolds number ($u_\tau d/\nu$). Note that the drag coefficient for holes is $C_{DP} = \Delta D/q_c S_p$ where S_p is the planform area of the hole. This relationship takes the form

$$C_{DP}/C_f = A \left\{ \frac{u_\tau d}{\nu} \right\}^B \quad 4(20)$$

The value of B was found to be a function of Mach number, but the parameter A was dependent upon both h/d and M , and is the cyclical effect noticed in Figure 4.16. In order to see the degree of correlation between the early low speed data and the latest results, the correlation shown in Figure 4.17 was made. Assuming the low speed value for B, given in Reference 4.17, values were calculated for A,

$$A = (C_{D_{II}} / C_f) \times (u_{\tau} d / v)^{-B} \quad (4.21)$$

where values for C_f and $u_{\tau} d / v$ were calculated for the known test conditions for each data source.

Considering the large difference of test parameters between the early experiments and the more recent tests, the general agreement shown in Figure 4.17 is very good. In view of this correlation, a single method for calculating the drag of circular holes is acknowledged. That method is as developed by the RAE (Reference 4.17) and confirmed by ARA (Reference 4.15). Since the ARA experiments contain a more detailed evaluation of Mach number effects and extend to higher values of h/d , the recommended approach is based on the Reference 4.15 results.

The basic equation is, from Reference 4.17,

$$C_D / C_f = A \left\{ \frac{u_{\tau} d}{v} \right\}^B \quad (4.22)$$

where $A = f(h/d, M)$ as shown in Figure 4.17 (Figure 26 of Reference 4.15) and $B = f(M)$ shown in Figure 4.18 (Figure 6 of Reference 4.15). For Mach numbers higher than $M = 1.4$, the data of Reference 4.17 can be used, but only for $h/d < 0.33$. These latter results are included on Figure 4.19.

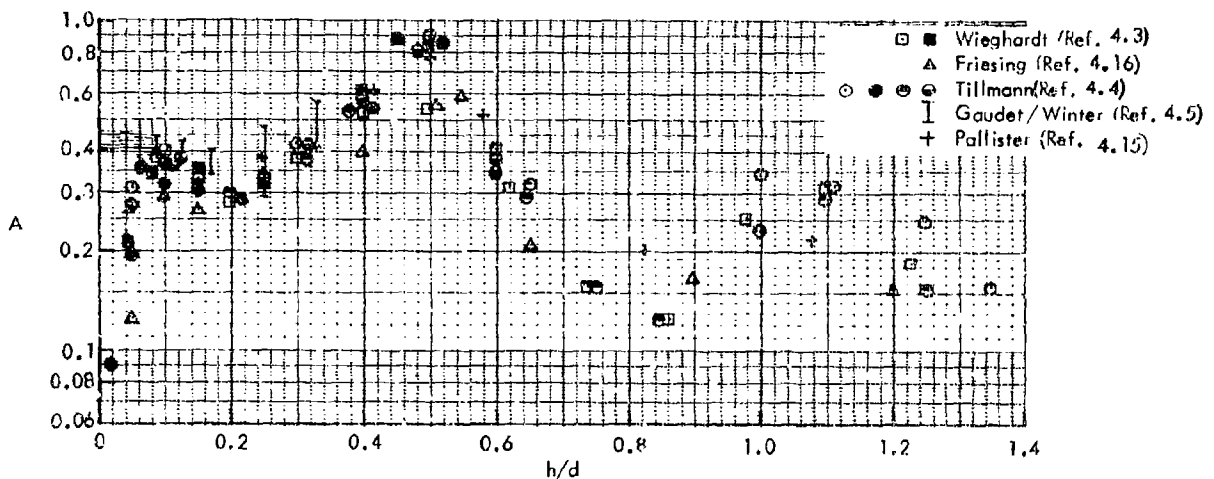


Figure 4.17 Comparison of Correlation Parameter (A) for Circular Hole Drag Obtained from Various Data Sources

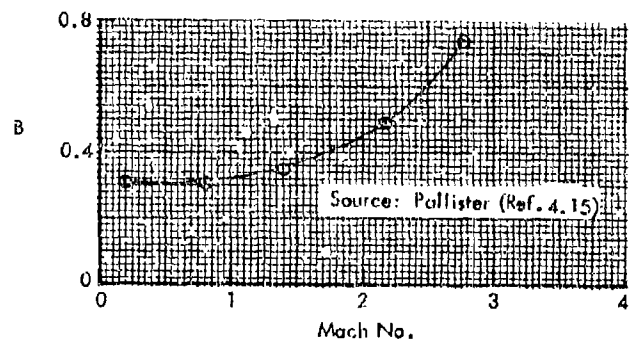


Figure 4.18 Effect of Mach Number on Correlation Parameter (B)

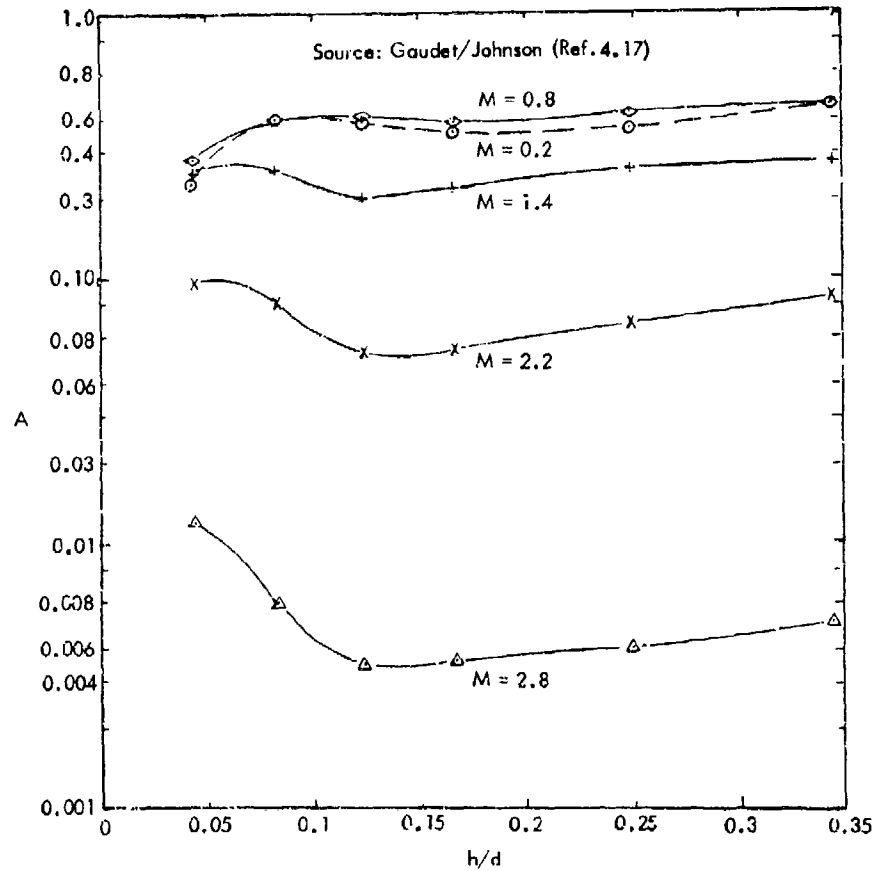


Figure 4.19 Effect of Mach Number on Circular Hole Drag Correlation Parameter (A)

4.2.5.2 Holes with Elliptical Planform

The only source found for determining the effects of elliptical planform on the drag of holes is the early work of Friesing, Reference 4.16. In the case of elliptical holes, Friesing only evaluated configurations with the major axis of the ellipse normal to the direction of air flow. His results are shown in Figure 4.20.

Although these results are somewhat scattered, there are several noticeable characteristics which can be used to make some useful generalizations. First, the cyclical nature of the curve C_{DP} vs h/d for circular holes, observed in Figure 4.16, is also evident for the elliptical planform holes. This implies that the drag for the elliptical case may be obtained by correcting circular hole drag in some way. Since it is also apparent that the extreme peak in C_{DP} for circular holes, over the range $h/l = 0.4$ to 0.6 , does not occur for the elliptical holes, a modified shape is necessary for this portion of the data.

Another useful characteristic observed is the somewhat consistent trend of decreasing C_{DP} due to increasing the ratio of hole width to hole length, w/l . This occurs for h/l values less than 0.8 . Above $h/l = 0.8$ the results are generally scattered about a mean line. Thus, for $h/l < 0.8$, the ratio of the drag coefficients for elliptical holes to that for a circular hole can be used to determine the relationship between the two.

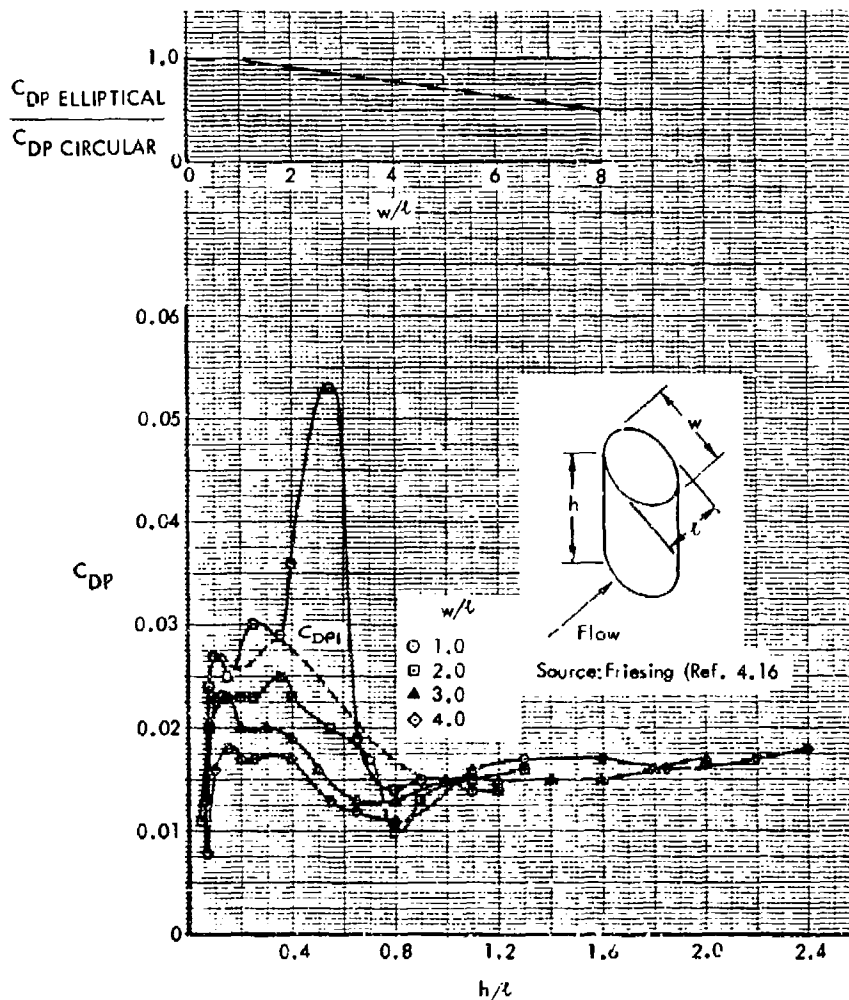


Figure 4.20 Drag of Elliptical Holes

If the very high values of drag coefficient at h/l near .5 are discarded and small adjustments are made elsewhere, the curve for $w/l = 1.0$ can be redrawn, as shown by the dashed line in Figure 4.20, to be one of a family with w/l as parameter. Using this dashed curve as a datum the drag ratio $C_{DP \text{ Elliptical}}/C_{DP \text{ Circular}}$ is very nearly a constant for each value of w/l . The drag of elliptical holes can then be reduced to the dashed curve multiplied by the ratio $C_{DP \text{ Elliptical}}/C_{DP \text{ Circular}}$ on the top of Figure 4.20.

In summary, the drag coefficient for an elliptical hole is found from:

$$(a) \quad h/l < 0.8$$

$$C_{DP \text{ Elliptical}} = \frac{(C_{DP})_{\text{Elliptical}}}{(C_{DP})_{\text{Circular}}} \times (C_{DP})_1 \quad 4(23)$$

where

$$\frac{(C_{DP})_{\text{Elliptical}}}{(C_{DP})_{\text{Circular}}} = f(w/l) - \text{Figure 4.20}$$

and

$$(C_{DP})_1 = f(h/l) - \text{Figure 4.20}$$

(b) $h/l > 0.8$

4(24)

$$C_{DP \text{ Elliptical}} = (C_{DP})_{\text{Circular}}$$

Care must be exercised however to recognize that the dashed curve C_{DP1} is only a fictitious datum rather than showing real values for circular holes. Some singular flow condition within the hole apparently occurs for circular holes having a depth near 0.5 x diameter which results in the very high drag values shown in Figures 4.16, 4.17, and 4.20.

4.2.5.3 Holes With Rectangular Planform

The data base for holes with rectangular planform is scanty, consisting of early data such as Friesing, Reference 4.16, and a few recent measurements contained in Reference 4.5. As noted in Reference 4.5 very few generalizations can be made with these results because of insufficient combinations of planform aspect ratio and depth-to-length ratio. In any event, the data have been plotted in the form of the drag ratio, C_{DP}/C_{fe} , vs. the depth ratio h/l in Figure 4.21. A mean curve has been provided for general use.

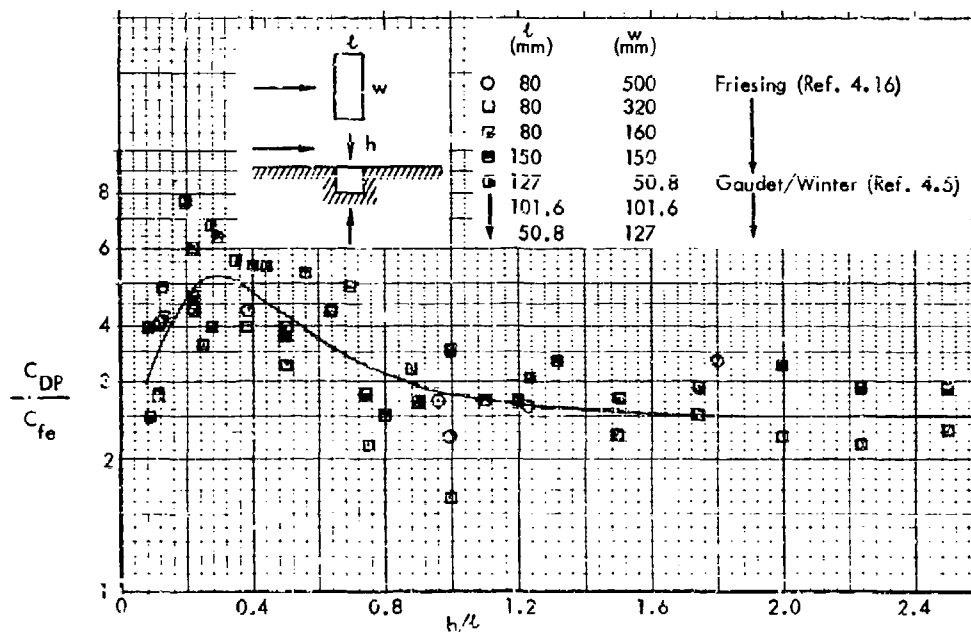


Figure 4.21 Rectangular Hole - Drag as a Function of Depth Ratio, h/l

Mach number effects for a square and a rectangular hole configuration, obtained from Reference 4.5 are shown in Figure 4.22. These results are obviously inadequate and only indicate general trends. Until such time as a better data base is available, the use of these data as shown is recommended for estimating the drag of rectangular holes.

4.3 Spanwise/Longitudinal Discontinuities

Skin joints in the external surfaces of aircraft, and similar surface imperfections, form a second type of roughness which is a significant drag producer. Spanwise skin splices for instance cover the entire wing from tip to tip and no portion of the wing is free of their effect.

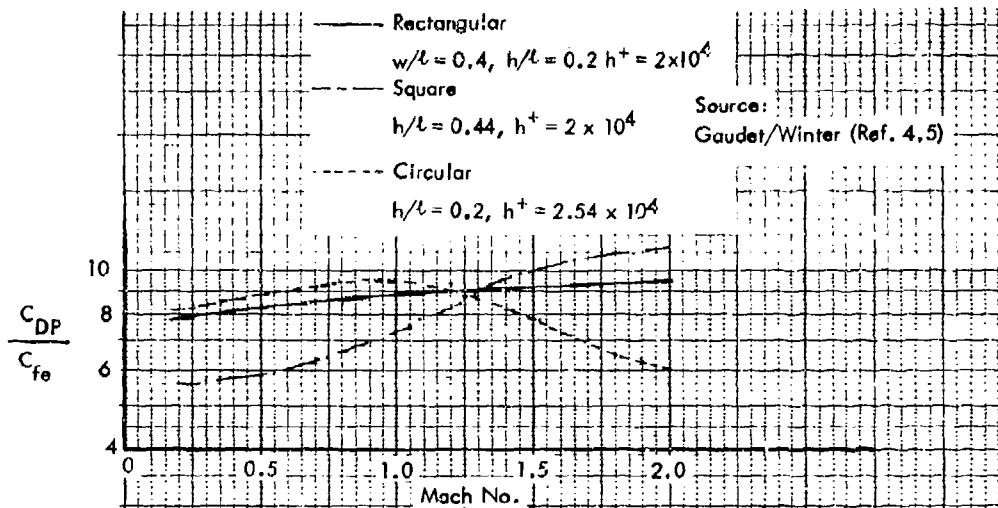


Figure 4.22 Mach Number Effect on Hole Drag

4.3.1 Spanwise Steps and Ridges

Excrescences which extend across the flow with the long axis normal to the flow direction are generally categorized as steps or ridges. Steps have only one side exposed to the flow, which can be facing forward or aft, whereas ridges have some combination of both forward and aft-facing steps.

The usual starting point in a study of these kinds of excrescences is the two-dimensional step with a 90° forward-facing surface. Investigations using this basic configuration have been more numerous than for most surface irregularities. Even so, some uncertainties still exist with respect to defining the drag of such steps. The most comprehensive and useful studies were made during the RAE and ARA research (References 4.5 and 4.15). Results from these studies provide the basis for the methods described in the following sections.

4.3.1.1 Forward-Facing Step

4.3.1.1.1 Two-Dimensional Step Normal to the Flow

Figure 4.23 summarizes some of the forward-facing step drag results using the approach originally presented in Reference 4.5. The experiments by the RAE were conducted on steps deeply immersed in the boundary layer ($h < 0.03 \delta$). It was reasoned that since the step height was so small compared to the boundary layer, that the flow would depend on the same parameters as the inner region of the boundary layer. A roughness Reynolds number was defined as

$$h^+ = u_\tau \frac{h}{\nu} \quad (25)$$

where

h = height of step

u_τ = friction velocity based on the wall conditions $(\tau/\rho)^{1/2}$

ν = Kinematic viscosity at the wall

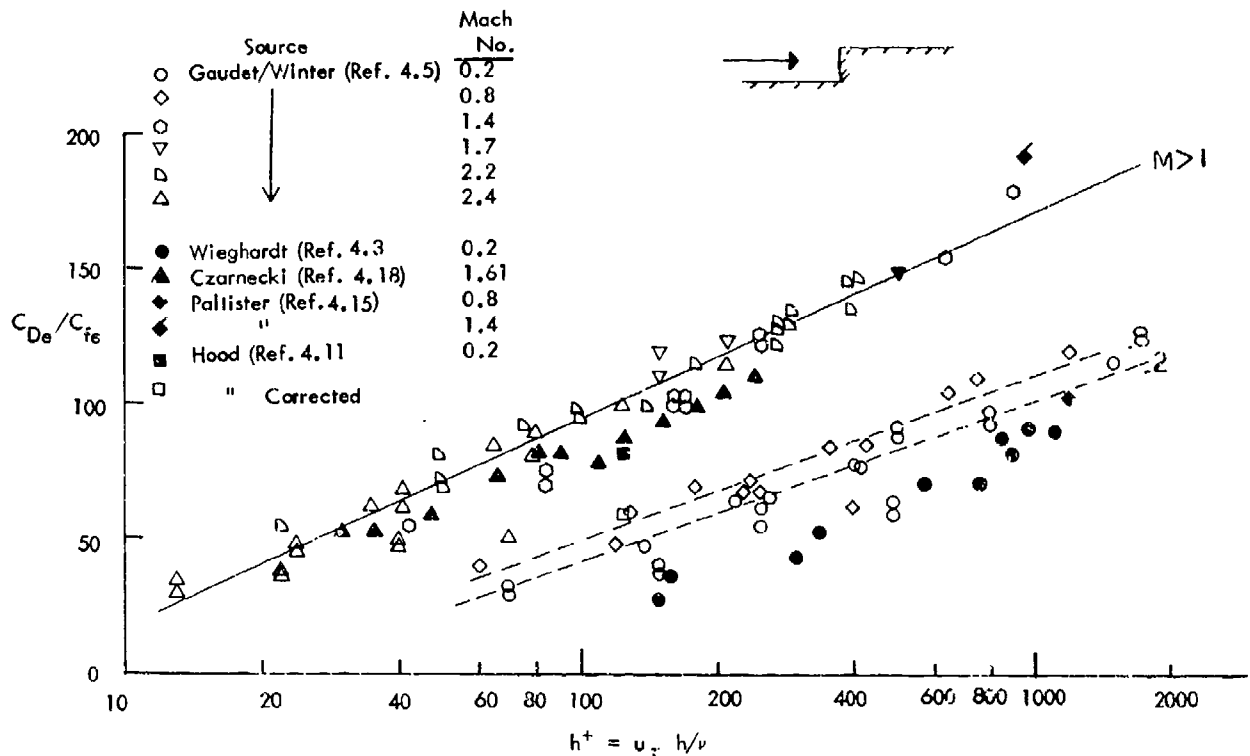


Figure 4.23 Drag of 2-D Forward-Facing Steps Normal to the Flow

Likewise, a drag parameter was defined as the ratio the drag per frontal area to the local skin friction coefficient, C_{De}/C_{fe} . Plotted in the form $C_{De}/C_{fe} = f(h^+)$, some unique relationships were determined as shown in Figure 4.23. Despite a large amount of scatter, a linear variation can be defined which has some Mach number dependence up to about $M = 1.4$. Data from other sources tend to support the linear variation, although absolute levels and slopes are different. These differences could be related to test technique but also there is the possibility that the degree of submersion of the step within the boundary layer is a factor. The Wieghardt results, for example, covered a range of heights from 3.6% to almost 50% of the boundary layer thickness. These steps would tend to have less dependence on the inner boundary layer parameters. As can be seen, the Wieghardt data have the same slope as the incompressible RAE data, but an overall lower drag ratio.

In the case of the supersonic results ($M > 1.4$), Reference 4.5 notes that all the data seem to be along a single line as shown on Figure 4.23. Because of the large difference between the subsonic and supersonic data, Reference 4.5 suggested the need to investigate the transonic speed range ($M = .8$ to 1.4). This was accomplished in a limited fashion by Pallister, Reference 4.15. Pallister repeated the procedures of Reference 4.5 for $M = 0.6$ to 1.4, but for a narrow range of roughness Reynolds number, h^+ . His results for $M = 0.8$ and 1.4 are shown to agree with the RAE data on Figure 4.23. The variation with Mach number through the transonic range is shown in Figure 4.24.

Other forward-facing step drag results for multiple step configurations are also included on Figure 4.23. Hood, Reference 4.11, tested lapped joints on a NACA23012 airfoil. An equivalent value for C_{De}/C_{fe} was determined and is considerably higher than the corresponding incompressible RAE data. This is not surprising for several reasons. First, some additional drag may be present on the airfoil due to transition movement between the smooth and rough airfoil configurations. More significantly, the influence

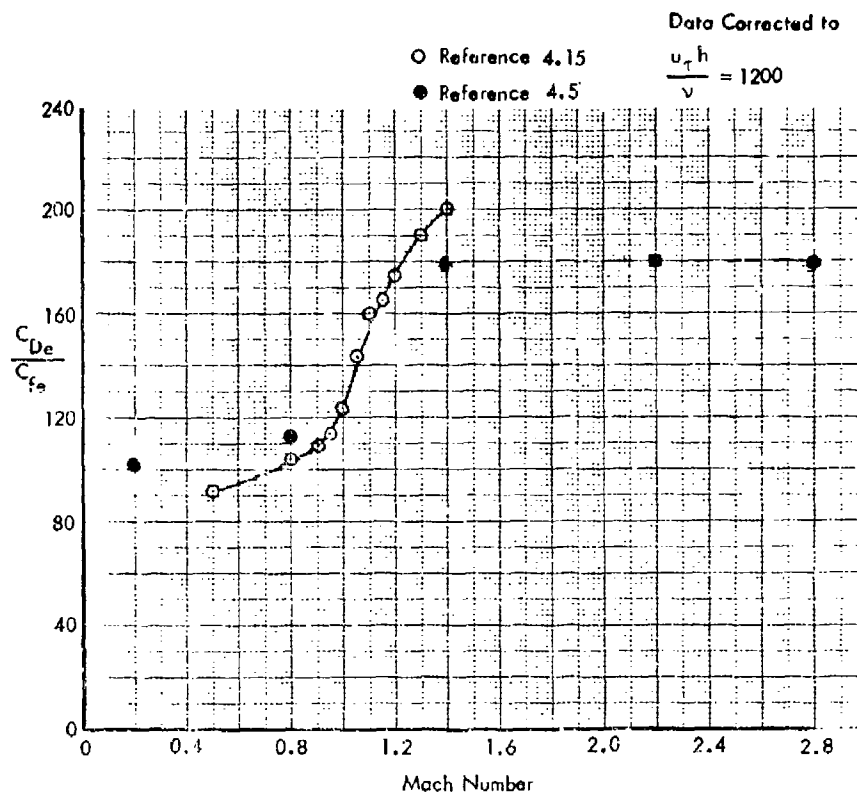


Figure 4.24 Variation of 2D Forward-Facing Step Drag in the Transonic Speed Range

of excrescences on the boundary layer in the presence of an adverse pressure gradient is known to be greater than for a zero-pressure gradient flow, Reference 4.7. These data have been "corrected" to an equivalent flat plate condition by extracting the Nash and Bradshaw multiplying factor. As shown in Figure 4.23, this accounts for the majority of the difference between this and other low speed data.

The multiple-step supersonic data of Czarnocki, et al, Reference 4.18, is also represented on Figure 4.23 as an equivalent single 2-D step. In this case, the effects of pressure gradient and transition are not present and the drag ratio is in fact lower than the RAE supersonic data. Reference 4.5 attributes this to the mutual interference between the steps.

Because of the observed differences there may still be some question as to the universality of the RAE results. However, present judgment dictates the use of the RAE and ARA correlations for step drag. Therefore, the recommended procedure for estimating the drag of 2-D steps is as described below.

For $M < 0.8$ and $M > 1.4$, the Reynolds number variations of Figure 4.23 are used. For transonic Mach numbers between $M \approx 0.8$ and 1.4, an interpolation is suggested based on the data of Figure 4.24 and is shown in Figure 4.25.

Thus, for $M < 0.8$, > 1.4 ,

$$C_{De} = F(C_f, M, h^+) \quad (\text{Figure 4.23}) \quad 4(26)$$

and for $M > 0.8$ and < 1.4 ,

$$(C_{De}/C_{fe})_M = (C_{De}/C_{fe})_{M=0.8} + PC_1 \left[(C_{De}/C_{fe})_{M=1.4} - (C_{De}/C_{fe})_{M=0.8} \right] \quad (4.27)$$

where $PC_1 = F(M)$, Figure 4.25, and the C_{De}/C_{fe} values are taken from Figure 4.23 at the appropriate roughness Reynolds number.

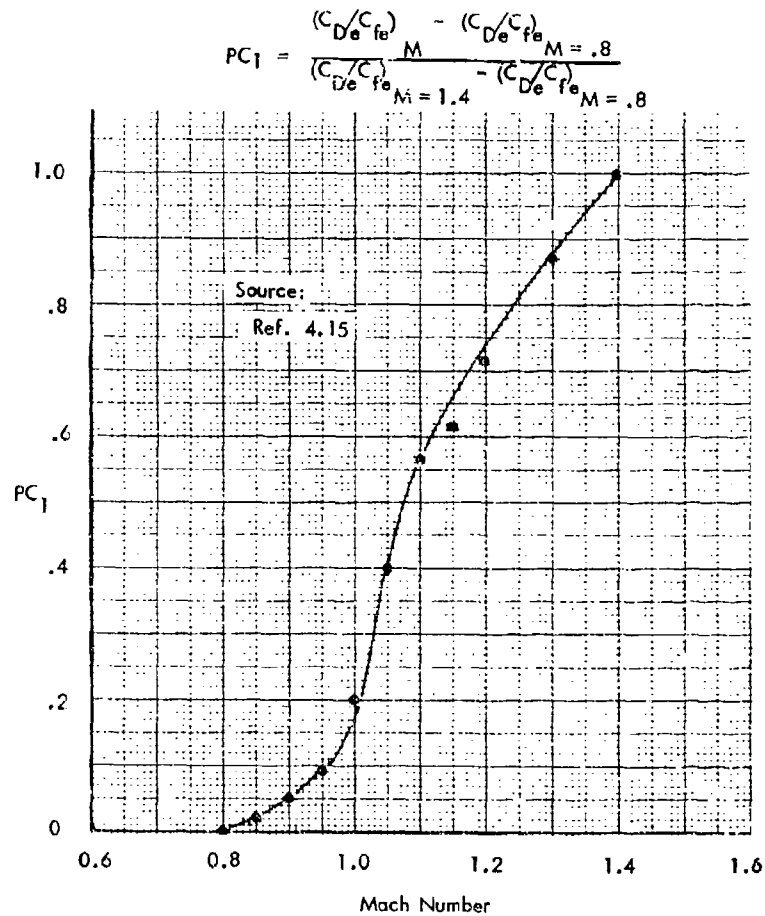
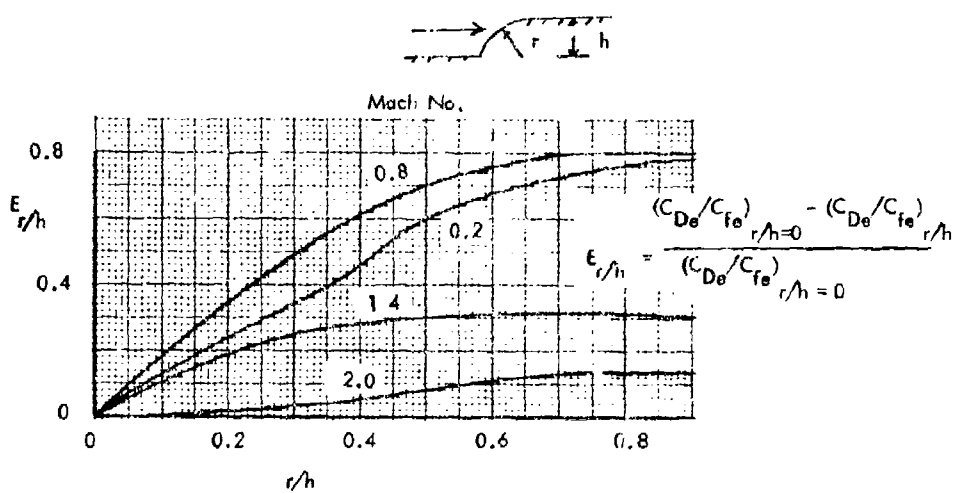


Figure 4.25. Effect of Mach Number in the Transonic Range On the Drag of Forward-Facing Steps

4.3.1.1.2 Effect of Chamfering or Rounding

The effects of rounding and chamfering the face of a forward-facing step were determined for $h^+ = 200$ and 1000 at four Mach numbers during the RAE experiments. The data were re-plotted for use herein in the form shown on Figure 4.26. The effect of roughness Reynolds number, h^+ , is small and an average curve was drawn through the $h^+ = 200$ and 1000 values for each Mach number.

(a) Rounding



(b) Chamfer

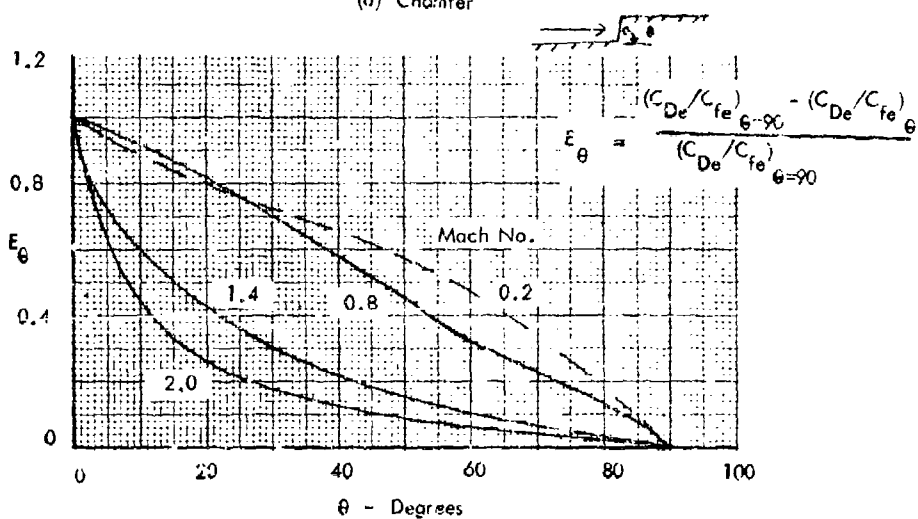


Figure 4.25 Effect of Rounding and Chamfering on Forward-Facing Step Drag

The method for estimating the drag of a rounded or chamfered 2-D step is as follows:

For a rounded step,

$$C_{De}/C_{fe} = (C_{De}/C_{fe})_{r=0} \times [1 - E_{r/h}] \tag{4.28}$$

where $(C_{De}/C_{fe})_{r=0}$ = drag ratio for a normal 2-D step from Section 4.3.1.1.1

$E_{r/h} = F(r/h, M)$ from Figure 4.26(a)

For a chamfered step,

$$(C_{De}/C_{fe})_{\theta} = (C_{De}/C_{fe})_{\theta=90} \times (1 - E_{\theta}) \tag{4.29}$$

where $(C_{D_e} / C_f) =$ drag ratio for a normal 2-D step from Section 4.3.1.1.1

$$\theta = 90^\circ$$

$E = f(\theta, M)$ from Figure 4.26(b)

4.3.1.1.3 Effect of Flow Angle

The effect of cross-flow on the drag of 2-D excrescences is discussed in Section 4.3.2.3. It is assumed that the results of Figure 4.45 are applicable for forward steps. Thus, the drag coefficient in cross-flow is given by:

$$(C_{De})_\alpha = (C_{De})_{\alpha=90} \times \sin^2 \alpha \quad 4(30)$$

where

$\alpha =$ cross-flow angle (see Figure 4.45)

$(C_{De})_{\alpha=90} =$ drag coefficient of a plain 2-D step from above.

4.3.1.2 Rearward-Facing Step

4.3.1.2.1 Two-Dimensional Step Normal to the Flow

Some recent results for rearward-facing steps are shown in Figure 4.27 for $M = 0.8$ and 1.4. The data of Reference 4.5 are shown for these two Mach numbers for comparison with Reference 4.15. The amount of scatter and/or uncertainty is significantly greater than for forward-facing steps. Both References 4.5 and 4.15 note this fact and Reference 4.15 suggests several reasons. First, the approaching boundary layer in the Reference 4.15 experiments was the product of "rough-turbulent" flow rather than the smooth-turbulent flow of Reference 4.5. This would tend to amplify differences down in the region of the laminar sub-layer (1% of boundary layer height). Second, the buoyancy correction for the balance set-up used in Reference 4.15 was a larger percentage of the total incremental force being measured than in Reference 4.5. Accordingly, Pallister tends to discredit the data in Reference 4.15 for the lowest step height (1.27 mm).

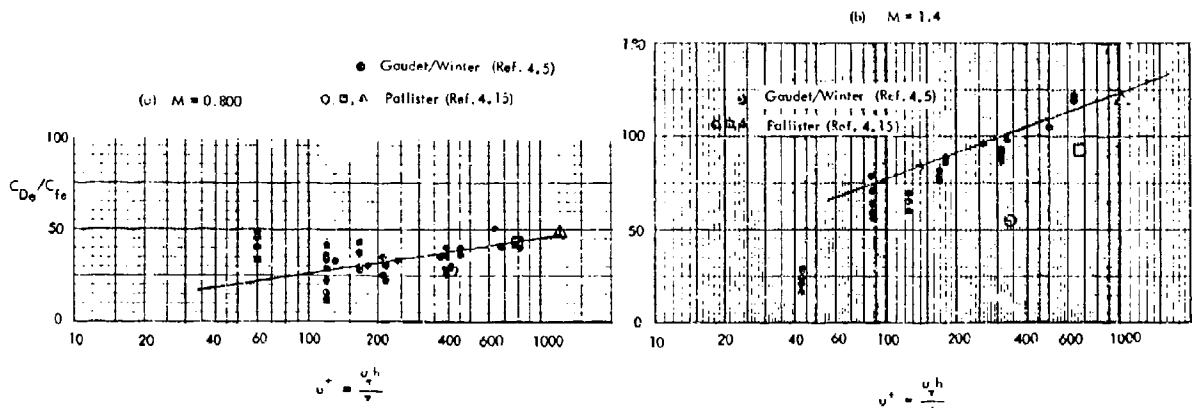


Figure 4.27 Drag of Rearward Facing Steps at $M = 0.8$ and 1.4

The lines faired through the results in Figure 4.27 are taken from Reference 4.5. These lines, plus those for the other Mach numbers tested and reported in Reference 4.5 are repeated in Figure 4.28. Data from several other sources are included for comparison.

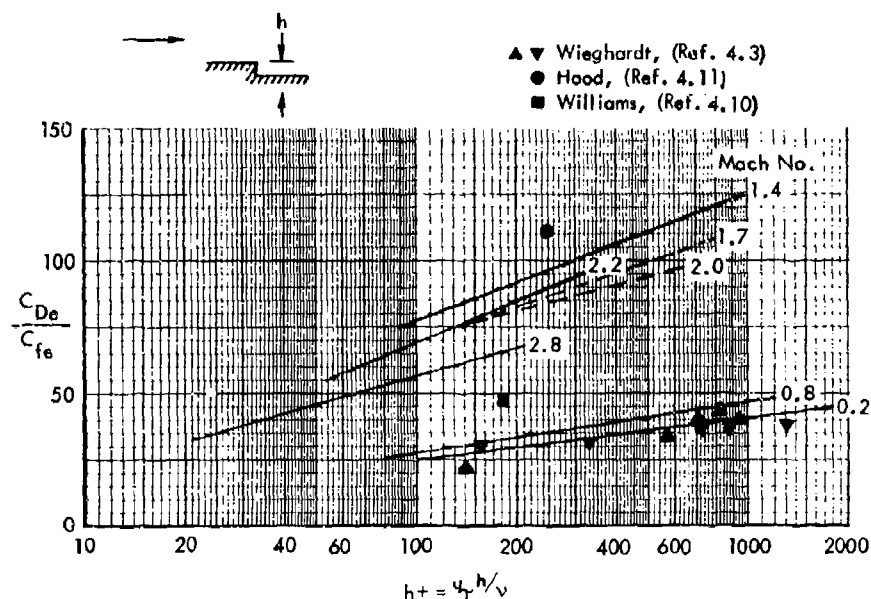


Figure 4.28 Drag of Plain Rearward Steps

The linearity of the forward-facing step data, C_{De}/C_{fe} vs h^+ , is also apparent in the rearward step results. However, the variations with Mach number are more pronounced. Whereas, the drag of the forward step increases with Mach number up to about $M = 1.4$ and then remains essentially constant, the drag of rearward steps starts to decrease at $M = 1.4$.

The transonic range was investigated in Reference 4.15, and these results are compared with the Reference 4.5 data in Figure 4.29. This is done at a constant $h^+ = 1000$ since the Reference 4.15 tests were at a nearly constant Reynolds number. Three heights of step were tested and a different Mach number variation was obtained for each. Noting that the variation for the largest height (3.81mm) tends to agree with the Reference 4.5 results, and recalling that the agreement for the forward step was also based on this step height (where no other heights were tested), it is reasoned that the $h = 3.81$ mm results are most nearly correct. This conclusion is also supported by the fact that Reference 4.15 tends to discount the results for the smaller steps. Therefore, the recommended method for estimating the drag of rearward steps includes use of the Reynolds number effect of Reference 4.5 and the Mach number effect as shown in Figure 4.29 for the 3.81 mm step.

Figures 4.28 and 4.30 summarize the data required for estimating the drag of rearward-facing steps normal to the flow. For $M < 0.8$ and > 1.4 ,

$$C_{De} = F(C_f, M, h^+) \quad (4.31)$$

as found in Figure 4.28. For Mach numbers between 0.8 and 1.4, an interpolation can be made using Figure 4.30,

$$\left(\frac{C_{De}}{C_{fe}}\right)_M = \left(\frac{C_{De}}{C_{fe}}\right)_{M=0.8} + PC_2 \left[\left(\frac{C_{De}}{C_{fe}}\right)_{M=1.4} - \left(\frac{C_{De}}{C_{fe}}\right)_{M=0.8} \right] \quad (4.32)$$

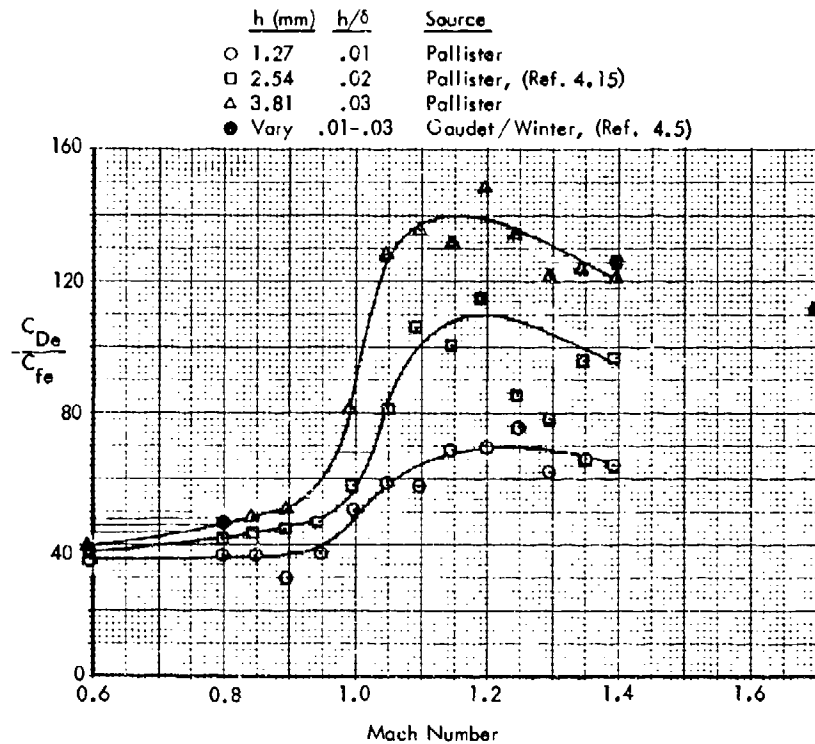


Figure 4.29 Effect of Mach Number on the Drag of Rearward Steps

$$PC_2 = \frac{(C_{De}/C_{fe})_{M=1.4} - (C_{De}/C_{fe})_{M=.2}}{(C_{De}/C_{fe})_{M=1.4} - (C_{De}/C_{fe})_{M=.8}}$$

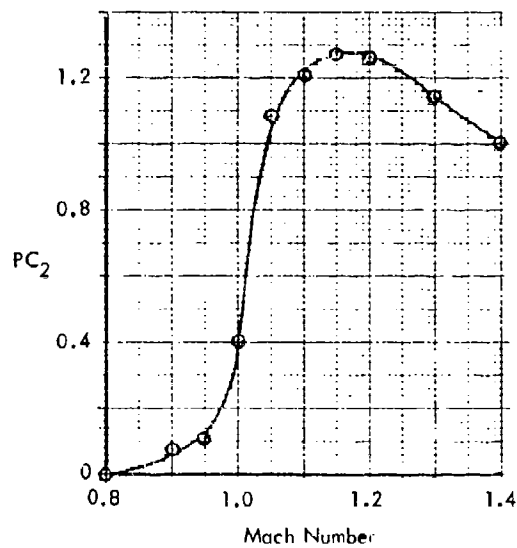


Figure 4.30 Mach Number Factor for off Facing Steps over the Transonic Range

4.3.1.2.2 Effects of Chamfering or Rounding

The effects of chamfering on the drag of a rearward-facing step were investigated over the Mach number range from 0.2 to 2.0 in the experiments of References 4.5, and 4.15. The results, re-plotted in Figure 4.31, show that for chamfer angles down to 45° , almost no change occurs in the drag. At some Mach numbers, there is a slight increase in drag until the angle is less than 12° . Below 12° , there is a sharp drop for all Mach numbers. Wieghardt also found a similar effect, with an even greater increase for angles greater than about 20° .

The effect of rounding the edge of a rearward step has only been summarily checked for two values of radius and for Mach numbers between 0.6 and 1.4, Reference 4.15. The results, re-plotted in Figure 4.32, show a slight increase in drag due to rounding. Reference 4.15 offers no explanation for this increase, however, it is apparently similar to the increases noted for the smaller chamfer angles.

For drag estimation purposes, data of Figures 4.31 and 4.32 have been generalized in a manner similar to the forward step results. For chamfers, the results are shown in Figure 4.33. The ratio, G_θ , represents the degree of change in drag from the un-chamfered base.

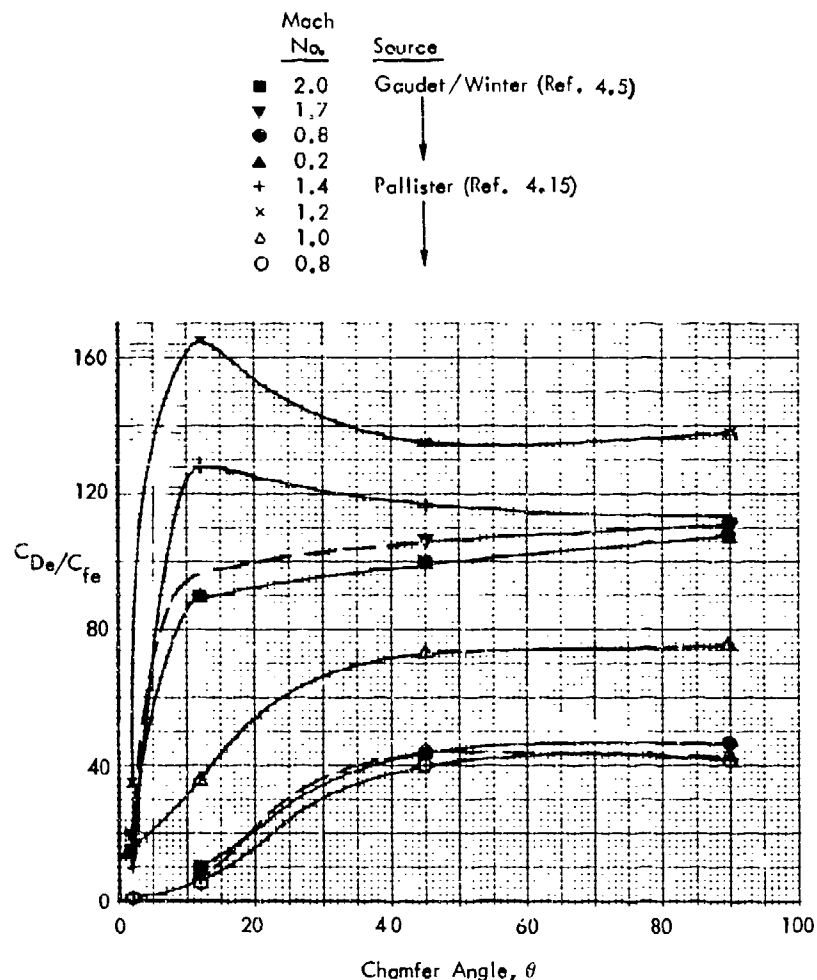


Figure 4.31 Comparison of Results on the Effect of Chamfer on Rearward Step Drag

Source: Pallister, (Ref. 4.15)

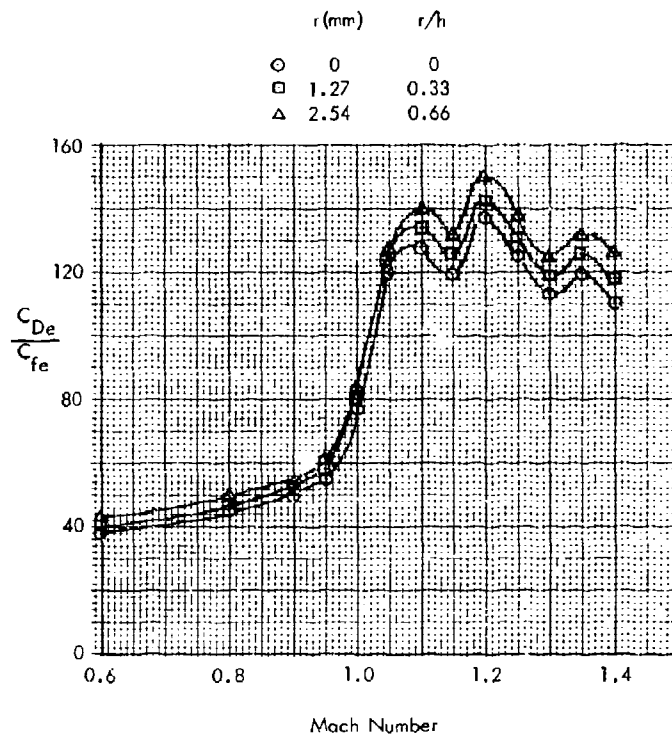


Figure 4.32 Effect of Rounding on the Drag of Rearward Steps

Data/Symbols, Same as Figure 4.31

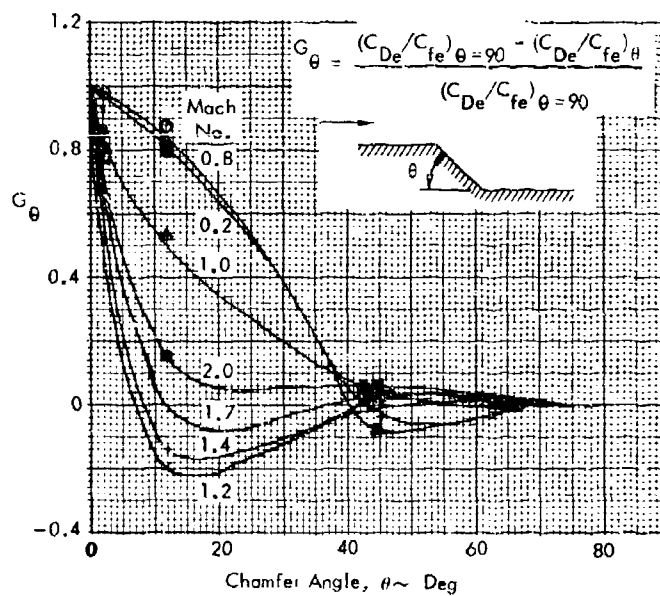


Figure 4.33 Effect of Chamfer Angle on the Drag of Rearward Steps

Thus, for a given chamfer angle, θ , the drag may be estimated by:

$$(C_{De}/C_{fe})_{\theta} = (C_{De}/C_{fe})_{\theta=90} (1 - G_{\theta}) \quad 4(33)$$

where

$$(C_{De}/C_{fe})_{\theta=90} = \text{drag ratio for a normal 2-D step from Section 4.3.1.2.1}$$

$$G_{\theta} = F(\theta, M) \text{ from Figure 4.33.}$$

Because the effect of rounding was so small, a single relationship was chosen, independent of Mach number, representing an average of the Figure 4.32 results. Thus,

$$(C_{De}/C_{fe})_{r/h} = [1 + 1.43(r/h)] (C_{De}/C_{fe})_{r=0} \quad 4(34)$$

where

$$(C_{De}/C_{fe})_{r=0} = \text{drag ratio for a normal 2-D step from Section 4.3.1.2.1}$$

4.3.1.2.3 Effect of Flow Angle

The effect of cross-flow on the drag of 2-D excrescences is discussed in Section 4.3.2.3. It is assumed that the results of Figure 4.45 are applicable for rearward steps. Thus, the drag coefficient in cross-flow is given by:

$$(C_{De})_{\alpha} = (C_{De})_{\alpha=90} \times \sin^2 \alpha \quad 4(35)$$

where

$$\alpha = \text{cross-flow angle (see Figure 4.45)}$$

$$(C_{De})_{\alpha=90} = \text{drag coefficient of a plain 2-D step from above.}$$

4.3.2 Combined Forward and Aft Facing Steps - Ridges and Plates

Excrescences which displace the flow upwards, as by a forward facing step, and subsequently return the flow to the original plane, and which do so in a short distance, are termed ridges. A plate normal to the flow is an example of a ridge with zero thickness. The basic experimental model for ridges has been the simple two-dimensional square ridge where the height is equal to the thickness. The drag of this elementary shape has been extensively explored by Gaudet/Winter Reference 4.5 and Pallister Reference 4.15 and their results provide the basis for the methods described herein. Early studies at low speeds and Reynolds numbers provide some additional insight into the effect of geometric shape on the drag of ridges.

4.3.2.1 Two-Dimensional Ridge Normal to the Flow With Vertical Faces

For plain 2-D ridges deeply immersed in the boundary layer, Reference 4.5 reported linear variations of the parameter C_{De}/C_{fe} vs h^+ , similar to those for 2-D steps. Figure 4.34 summarizes their results for the Mach numbers tested. The addition by superposition of the forward and rearward step drag produces a total which is about 50% below the drag of square ridges at the lower Mach numbers. This implies a substantial interference drag for the combined configuration. This difference subsides at the higher Mach numbers and is not present in the $M = 2.8$ data.

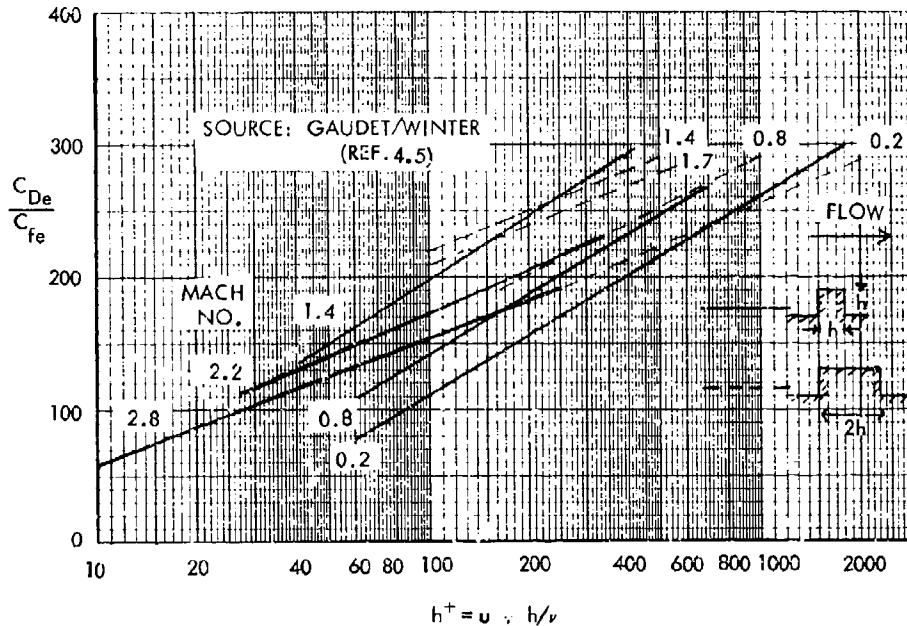


Figure 4.34 - Drag of Plain Ridges

The incompressible results for square ridges are compared in Figure 4.35 with some of the early experiments of Wieghardt, Reference 4.3 and Tillmann, Reference 4.4. The relatively good agreement with the Tillmann data is considered fortuitous, since these experiments were on three-dimensional models (plates and bars). The ledges tested by Wieghardt are similar to the 2-D ridges of Reference 4.5. In general, these results show the validity of the C_{De}/C_{fe} vs h^+ approach for these kinds of excrescences.

The transonic experiments of Reference 4.15 further corroborated the Reference 4.5 data and provided a more detailed coverage of the transonic speed range. Figure 4.36 compares the $M = .8$ and 1.4 data for square ridges from the two sources and Figure 4.37 shows how the compressibility effect compares at a constant roughness Reynolds number ($h^+ = 1200$). As the flow becomes supersonic the drag increases substantially to a level 50% higher than the subsonic drag. Above $M = 1.0$ the drag decreases back to the low-speed level. This sharp variation over the transonic range makes clear the need to obtain careful experimental measurements over this speed range and to properly account for Mach number effects during drag estimation.

To assist with the latter, the transonic data of Reference 4.15 for square and rectangular ridges was used to derive a Mach number factor to approximate the variation between $M = 0.8$ and 1.4. Since the drag variation with roughness Reynolds number at $M = 0.8$ and 1.4 is known (Figure 4.34) it is convenient to relate the transonic effect to these data. Thus, the drag increase above $M = 0.8$ was ratioed to the known difference between $M = 0.8$ and 1.4. This was done for the square and rectangular ridge data of Reference 4.15 and an average curve obtained. The result is shown in Figure 4.38.

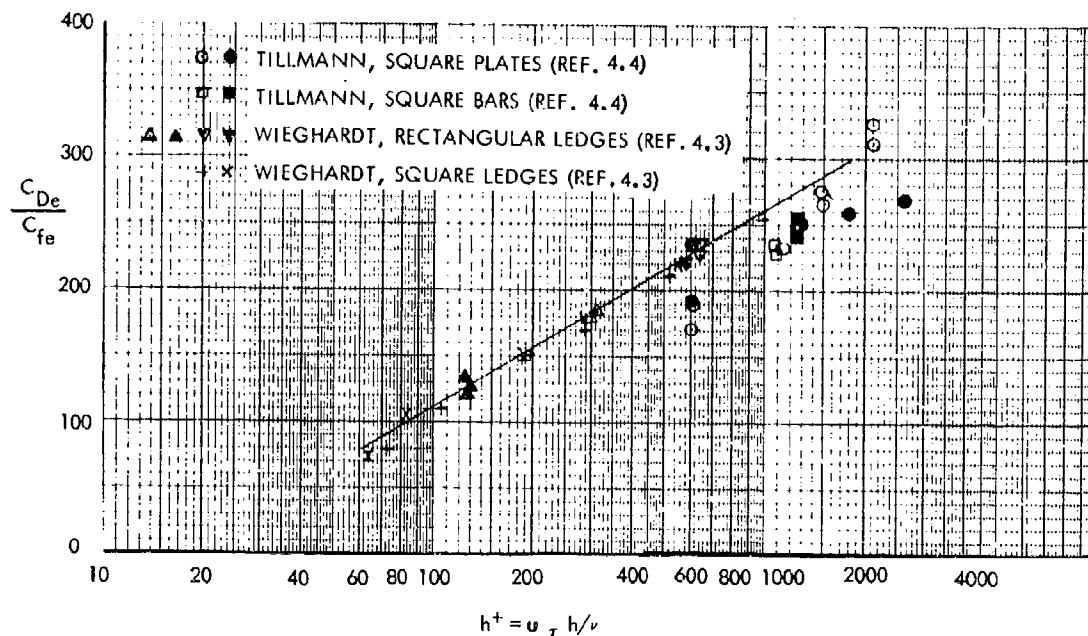


Figure 4.35 - Comparison of Low Speed Data on Ridge Drag

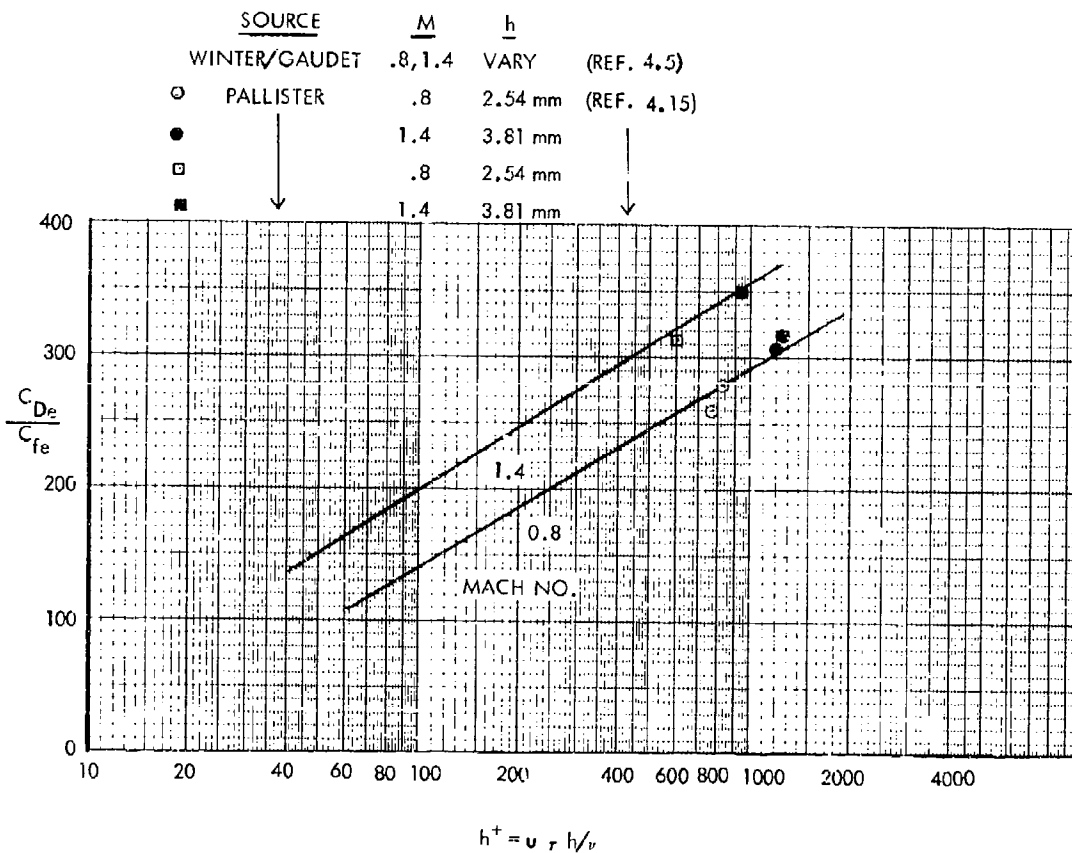


Figure 4.36 - Comparison of Plain Ridge Drag at M = 0.8 and 1.4

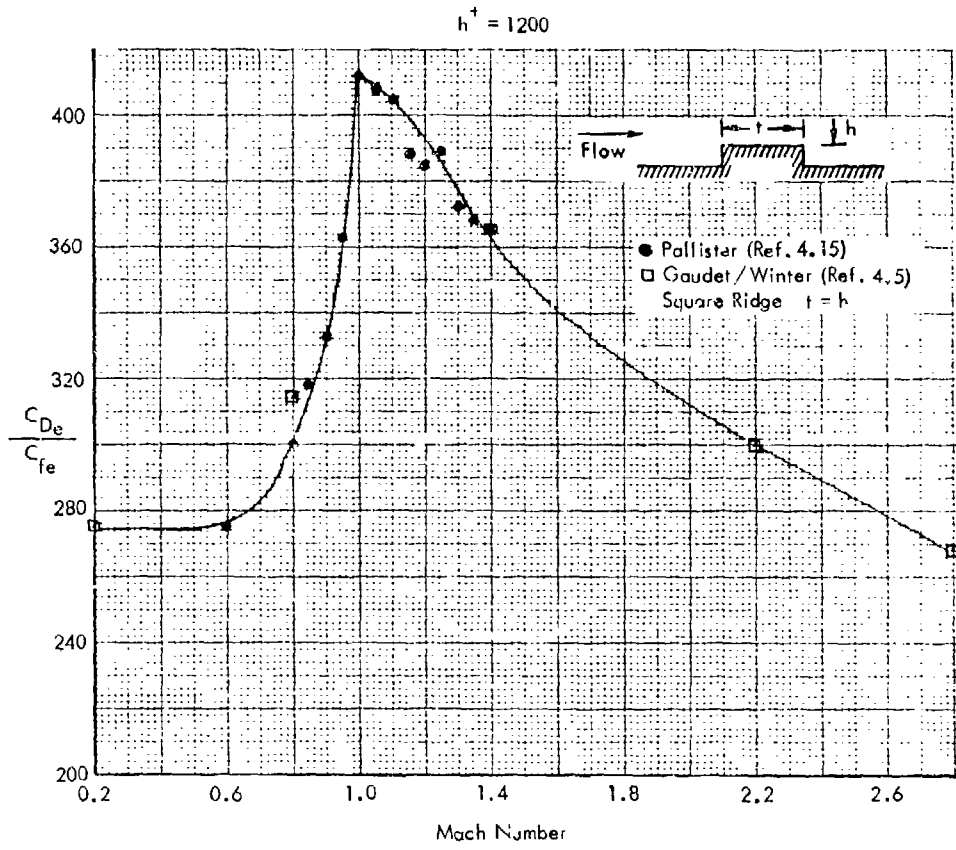


Figure 4.37 Comparison of Experimental Data on the Mach Number Effect on Ridge Drag

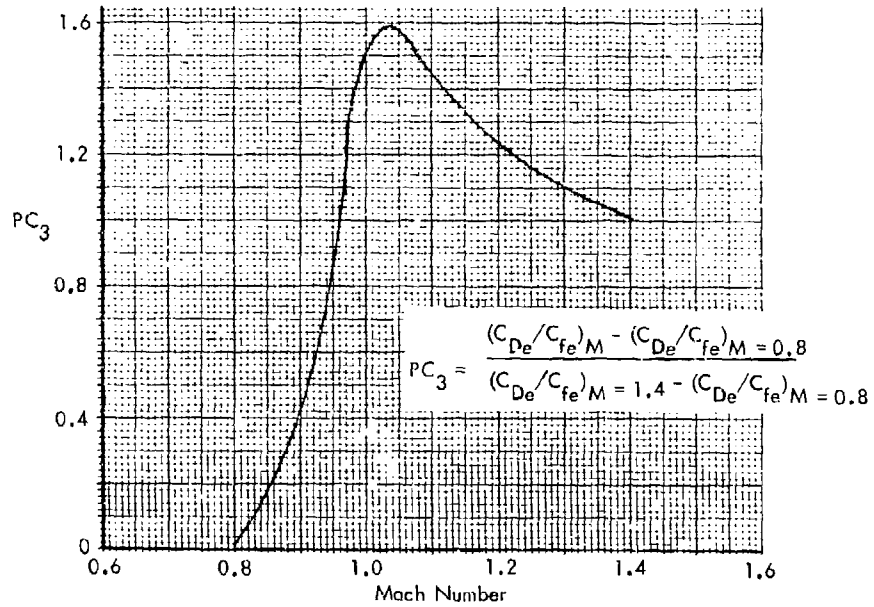


Figure 4.38 Mach Number Factor Over the Transonic Range for Ridge Drag

The drag of rectangular plain ridges with a thickness twice the height was also investigated in some detail in References 4.5 and 4.15. Figure 4.34 contains the Reference 4.5 summary of the Reynolds number variation for comparison with the square ridge data. For low values of h^+ , where h/δ was about 0.01 to 0.02, the drag of the rectangular ridge is higher than for square ridges. Reference 4.15 experiments were at h^+ values near the cross-over point and do not clarify this effect. At higher values of h^+ , where h/δ was near 0.03 in the Reference 4.5 tests, the drag of the rectangular ridge becomes less than for an equivalent square ridge, see Figure 4.34. Wieghardt's experiments also show a decreasing drag with increasing thickness of the ridge for a constant roughness Reynolds number. In this case, the heights of the ridges were all greater than 3 percent of the boundary layer thickness. This effect is shown on Figure 4.39. These latter results can be used to approximate the effect of increasing the ratio of thickness to height for rectangular ridges.

The drag of plain ridges is calculated as follows:

Square Ridges:

$$C_{De}/C_{fe} = A \log(h^+) + B \quad 4(37)$$

where

<u>M</u>	<u>A</u>	<u>B</u>
.2	150	-190
.8	150	-160
1.4	160	-125
2.2	110	-42
2.8	100	-44

for $0.8 < M < 1.4$:

$$(C_{De}/C_{fe}) = (C_{Le}/C_{fe})_{M=.8} + PC_3 \left[(C_{De}/C_{fe})_{M=1.4} - (C_{De}/C_{fe})_{M=.8} \right] \quad 4(38)$$

where $PC_3 = f(M)$, Figure 4.38, and the drag ratios at $M = 0.8$ and 1.4 are calculated as above.

Similarly, for rectangular ridges

(a) $t = 2h$

<u>M</u>	<u>A</u>	<u>B</u>
.2	105	-55
.8	115	-60
1.4	100	8
1.7	100	20

The variation between $M = 0.8$ and 1.4 is the same as for square ridges.

(b) $t = \text{variable}$

The data of Figure 4.39 have been converted into a more general form in Figure 4.40. Thus, for any value of t/h ,

$$\left(\frac{C_{De}}{C_{fe}}\right)_{t/h} = T \left(\frac{C_{De}}{C_{fe}}\right)_{t/h=1} \quad 4(39)$$

where $\left(\frac{C_{De}}{C_{fe}}\right)_{t/h=1}$ is the drag ratio for a square ridge of the same height, and

$T = f(t/h)$, Figure 4.40.

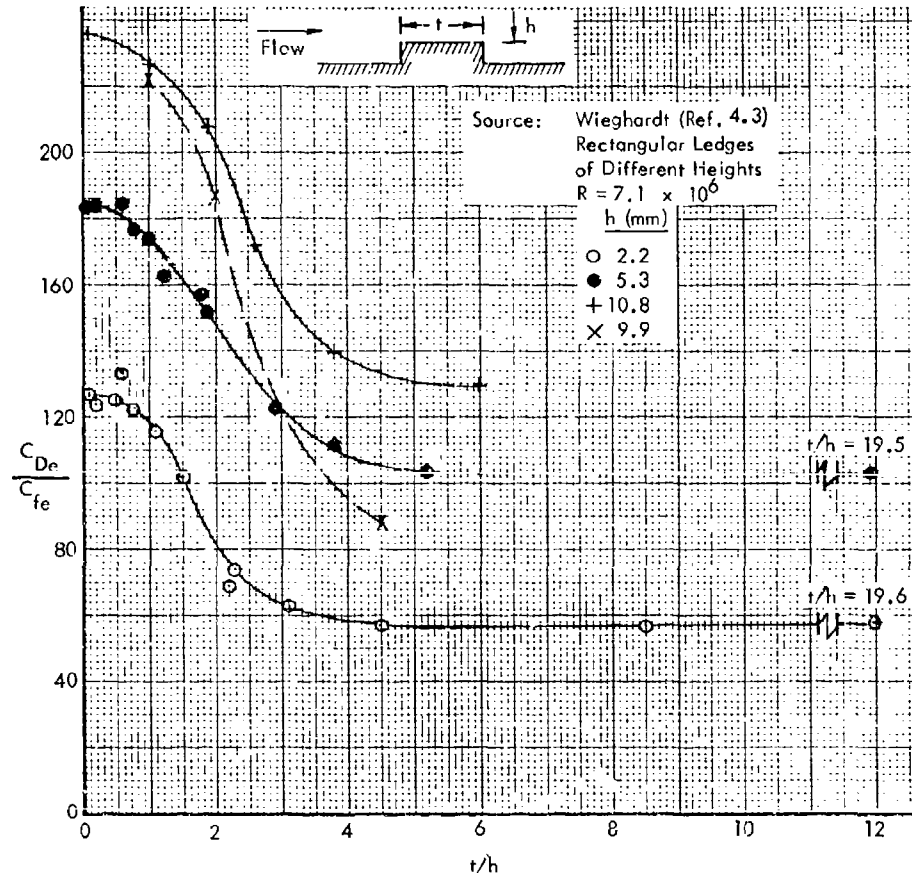


Figure 4.39 Drag of Rectangular Ridges of Varying Height and Thickness

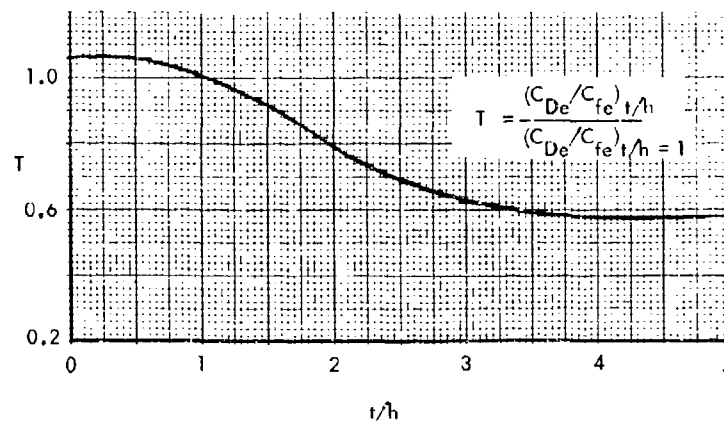


Figure 4.40 Effect of Thickness on the Drag of Rectangular Ridges

4.3.2.2 Ridges With Different Cross-Section

(a) Rounded Edges

References 4.5 and 4.15 determined the effects of rounding the edges of a rectangular ridge. The results are compared in Figure 4.41. By re-plotting the data of Figure 4.41 into the form shown in Figure 4.42 several factors can be seen. First, the low speed data ($M < 0.8$) all tend to be concentrated about a common mean curve, as do the results for $M > 1.4$. The shapes of the curves are similar for each Mach number indicating that the Mach number effect between 0.8 and 1.4 is uniform. This implies that a single curve can be used to represent the basic effect of rounding with a separate Mach number effect. The curves of Figure 4.43 resulted.

A second observation to be made from the Figure 4.42 data is that the greatest change seems to occur with the initial amount of rounding and essentially no change is manifested by further rounding. When the radius approaches the value of the height of the ridge, a slight increase in drag is seen. Singular values, corresponding to $r/h \geq 1$, were obtained from several other sources and are included on Figure 4.42. These seem to substantiate the overall results.

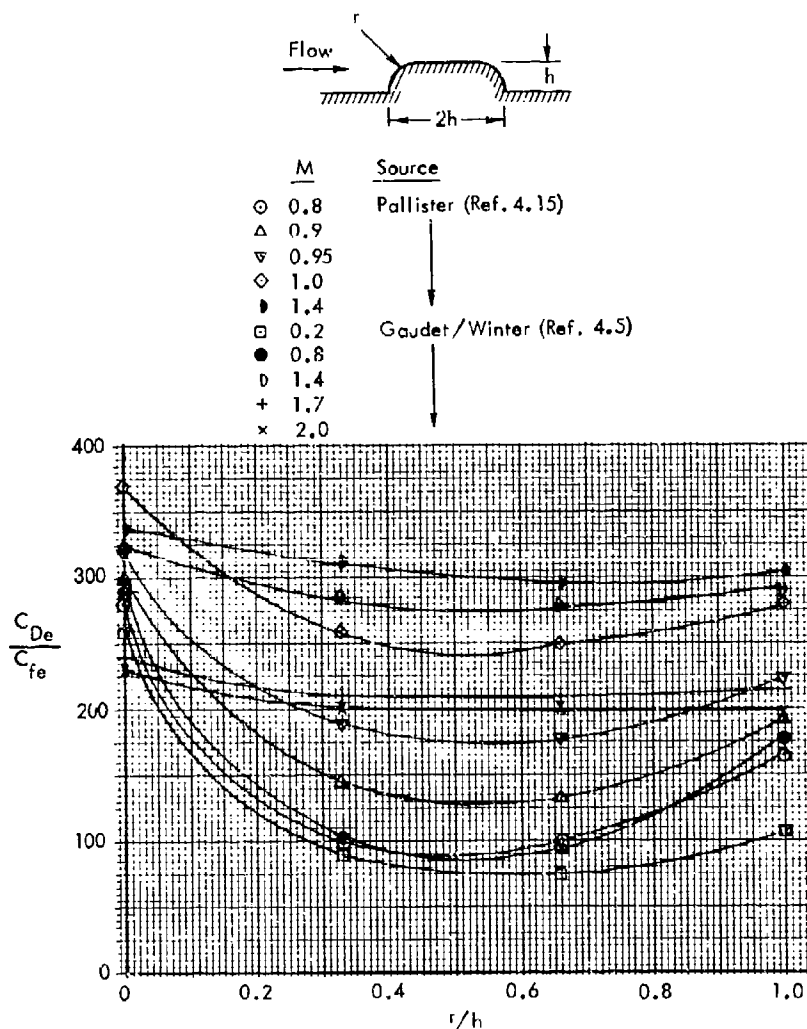


Figure 4.41 Comparison of Experimental Results for Rounded Rectangular Ridges

$$Z_{r/h} = \frac{(C_{De}/C_{fe})_{r/h}}{(C_{De}/C_{fe})_{r/h} = 0}$$

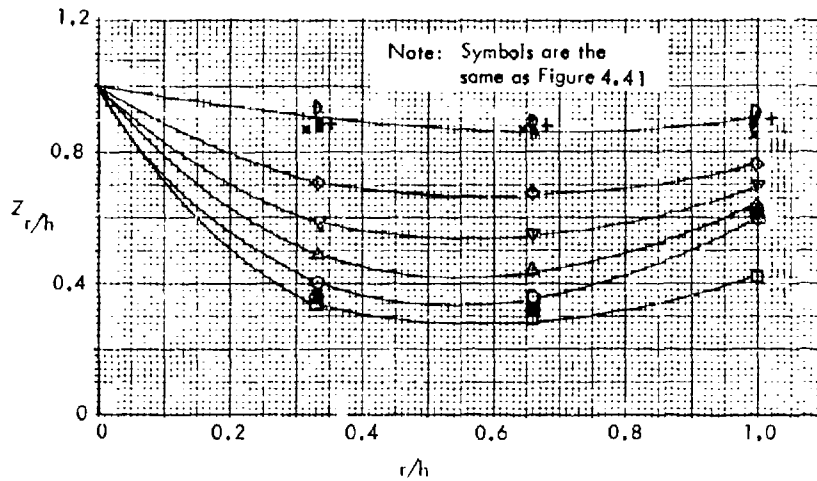


Figure 4.42 Ratio of the Drag of Rounded Ridges to that of Plain Ridges

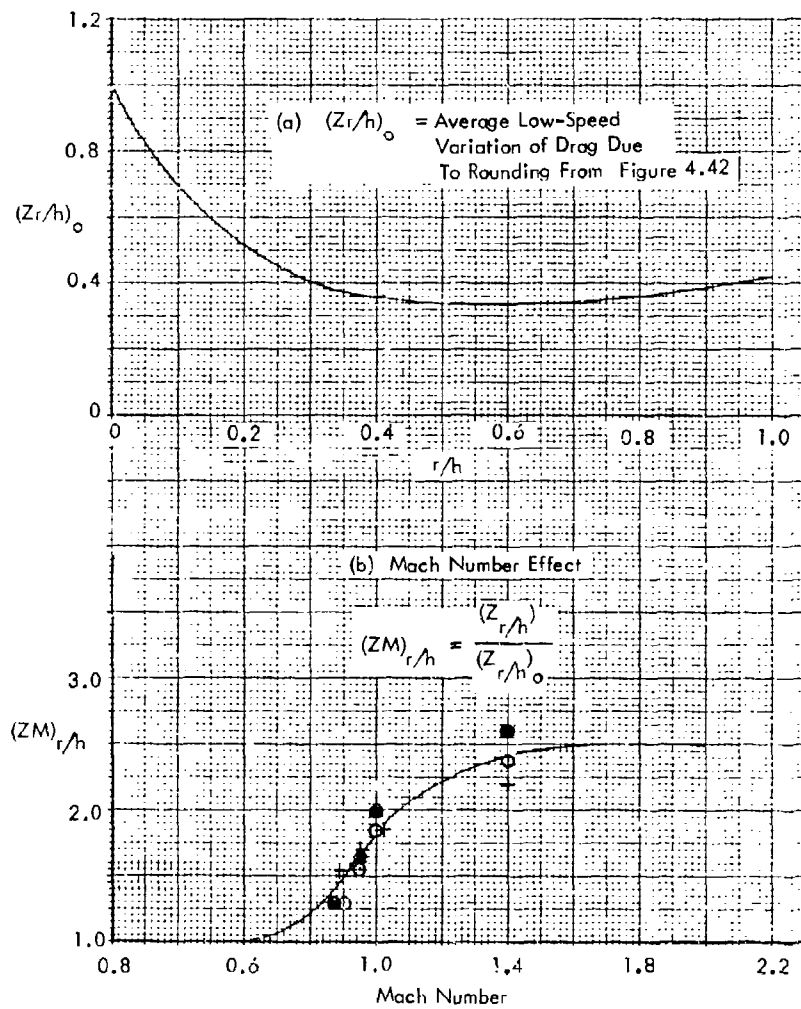


Figure 4.43 Factor for the Effect of Rounding on the Drag of Rectangular Ridge

The effect of rounding the edges of a ridge, or the drag of a rounded profile ridge, is estimated by correcting the rectangular ridge of the same height by:

$$\left(\frac{C_{De}}{C_{fe}}\right)_{\text{Rounded Ridge}} = \left(\frac{C_{De}}{C_{fe}}\right)_{r/h=0} \times (ZM)_{r/h} \times (Z_{r/h})_0 \tag{4.40}$$

where $\left(\frac{C_{De}}{C_{fe}}\right)_{r/h=0}$ = drag of plain ridge as determined in Section 4.3.2.1,

$(ZM)_{r/h}$ = Mach number effect on rounding from Figure 4.43(b).

$(Z_{r/h})_0$ = effect of rounding at low speed from Figure 4.43(a).

(b) Other Profile Shapes

Data for ridges with profile shapes other than square, rectangular or rounded are very scarce. In the original work of Wieghardt, Reference 4.3, ledges with different profile shapes were tested over a range of thickness-to-height ratio. The results are repeated here, Figure 4.44, so that some guidance may be given relative to the degree of difference in drag for the various shapes.

Since the Mach number effects are similar for the square, rectangular and rounded shapes, it may be reasoned that the same is true for the other shapes as well. Based on this reasoning, the drag for any other-shaped profile may be found by first evaluating the drag for one of the basic shapes at the appropriate Mach number and roughness Reynolds number and then correcting for shape using the data of Figure 4.44.

Source: Wieghardt (Ref. 4.3)

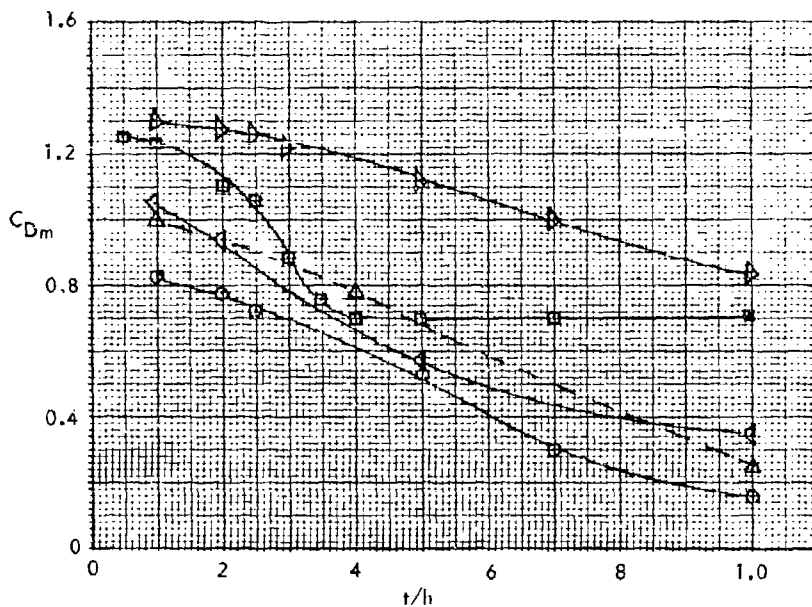
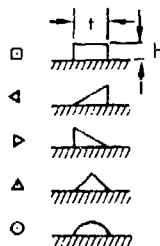


Figure 4.44 Drag of Spanwise Ledges of Different Profiles

4.3.2.3 Effect of Flow Angle

In cross-flow the drag of an excrescence, such as a ridge or ledge, based on the projected frontal area should be reduced by the effect of the reduced velocity vector normal to the ridge face. Since the drag coefficient is normalized on velocity-squared, the drag coefficient would then be reduced by approximately the square of the velocity reduction. The validity of this principle can be demonstrated in the case of 2-D or plain ridges.

Two sources present data showing the effect of cross-flow on the drag of rectangular ridges. These sources, Wieghardt, Reference 4.3 and Kovalenko, Reference 4.19 have been used to correlate the effect of flow angle. The results are summarized in Figure 4.45. The reduction in drag coefficient, represented by the ratio $\frac{C_{De}(\alpha)}{C_{De}(\alpha=90)}$ has been plotted vs flow angle, α , and compared with the value of $\sin^2 \alpha$. The agreement is excellent and, considering the diverse conditions of the two sources, it is concluded that the $\sin^2 \alpha$ function can be used to approximate the effect of cross-flow on ridge drag coefficients.

Although it has not been substantiated, the cross-flow described above is believed applicable to other 2-D type excrescences, such as forward and rearward facing steps. This assumption has been made and in Section 4.3.1.1 and 4.3.1.2 the cross-flow effect on 2-D step drag is based on this assumption.

In summary, the drag coefficient of a ridge in cross-flow is calculated from

$$(C_{De})_{\alpha} = (C_{De})_{\alpha=90} \times \sin^2 \alpha \quad 4(41)$$

where

α = cross-flow angle (see Figure 4.45)

$(C_{De})_{\alpha=90}$ = drag coefficient of the plain ridge as determined in 4.3.2.1 or 4.3.2.2.

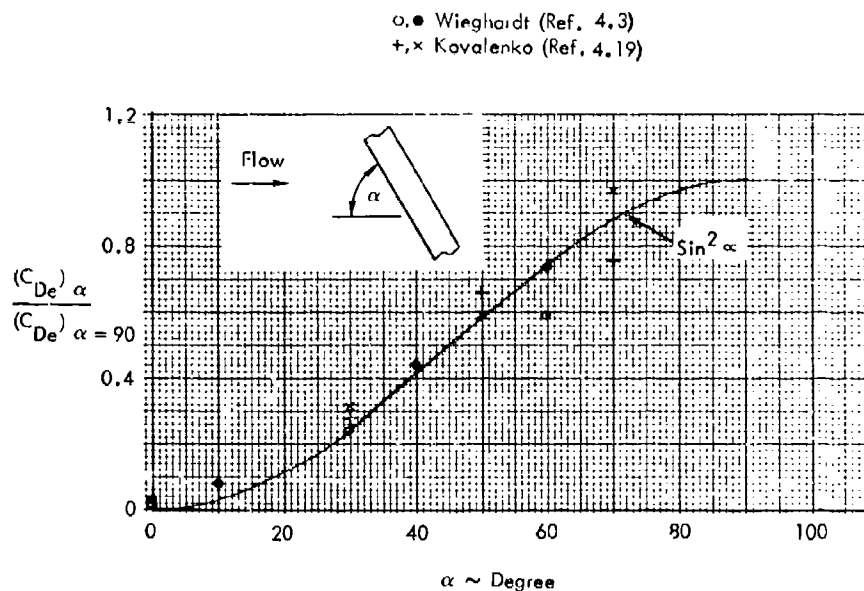


Figure 4.45 Effect of Flow Angularity on the Drag of Ridges

4.3.2.4 Multiple Ridges in Series

Lacey, Reference 4.27 has made low speed measurements on arrangements of a number of spanwise ridges of square section on a plate in zero pressure gradient and some of his salient results are summarized in Figure 4.46. There is plotted the ratio of the drag of a system of ridges to that of a single ridge in the leading ridge position as a function of ridge spacing to height ratio (s/h) or of the ratio of the area covered by the ridges to the total plate area (A_R/A) (called ridge density).

The individual curves correspond to values of the ratio of the plate length to ridge height (L/h).

The number (N) of ridges is given by

$$N = L/s = \frac{L}{h} / \frac{s}{h} \tag{4.42}$$

It will be seen that for any given plate length and ridge height, there is a critical spacing (and hence N) leading to a maximum drag increase. This spacing is about $10h$. For a more sparse spacing the interference effect of the wake of a ridge on downstream ridges is small and the drag decreases as s increases because N decreases; whilst for a closer spacing the interference effects increase so that the drag decreases

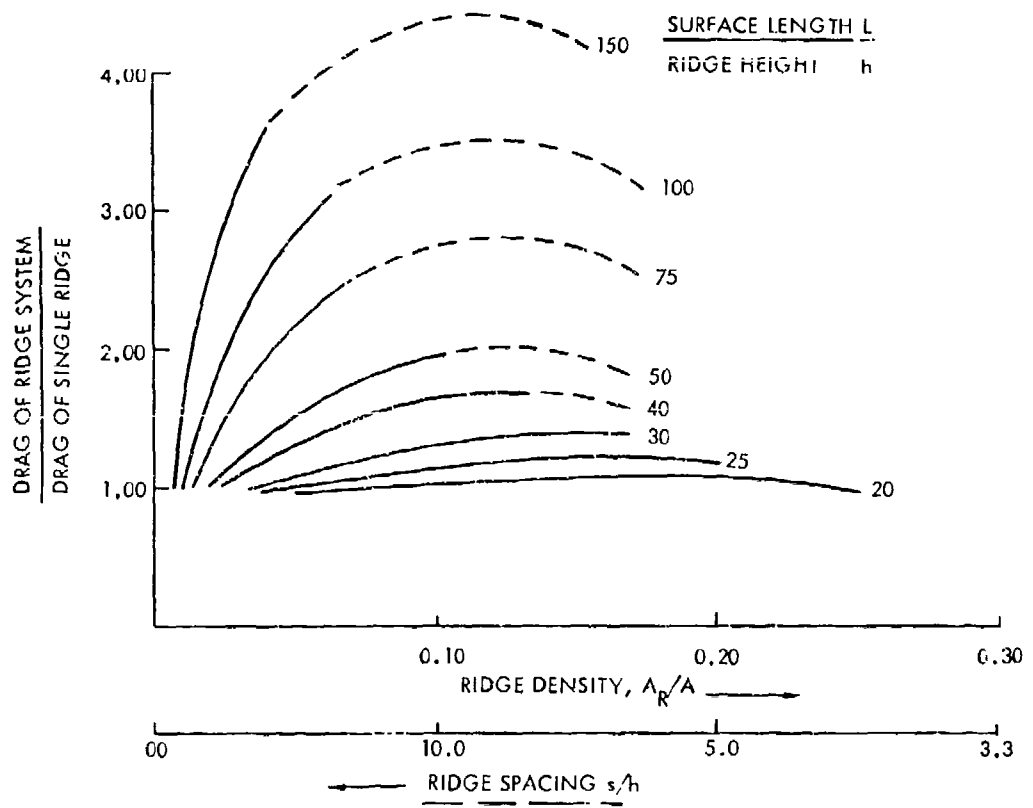


Figure 4.46 Variation of Drag with Selected Surface Length and Ridge Density in Zero Pressure Gradient

in spite of the increase in N . The experiments show that 2 ridges less than about $8h$ apart have a drag less than that of a single ridge. However, there is some evidence that h_w^+ plays a small but not insignificant part in these interference effects and this has not been explored adequately. These same data are shown in Figure 4.47 plotted as the total drag divided by the drag of a single ridge multiplied by the number of ridges being tested. It is seen that forward ridges provide a significant shielding of the ridges behind for all of the cases shown here. (The ridge spacing must exceed 75 ridge heights before the system drag is equal to the sum of individual ridge drags.) As shown by Figure 4.47 this shielding effect is substantial and increases as the number of ridges increases.

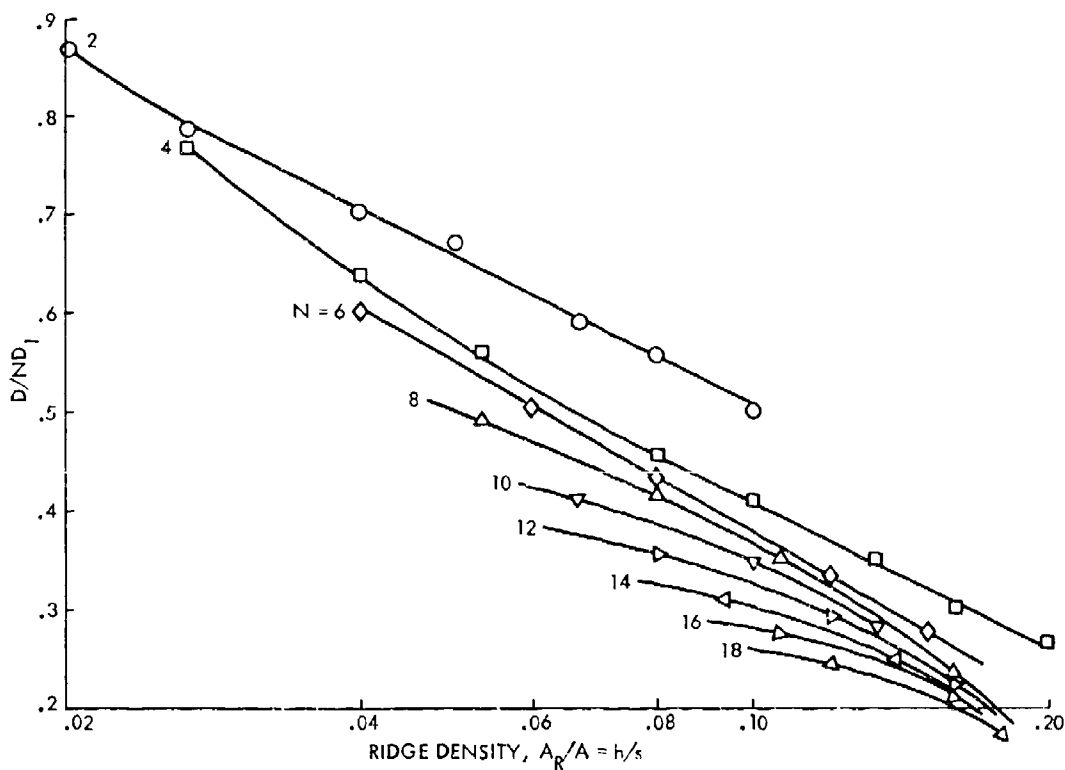


Figure 4.47 Effect of Ridge Density on the Drag of a System of Spanwise Ridges

4.3.3 Gaps and Grooves

The category of gaps and grooves includes those excrescences such as gaps between joints, gaps caused by control surfaces, and spanwise grooves, slots, or contours, all of which are normally small compared to the configuration geometry (airfoil, wing, etc.) and the local boundary layer. The data discussed here do not consider open cases where fluid might flow through the gap. For a discussion of the drag of control gaps with flow through them see Section 5.4. In general, the magnitude of the drag of spanwise gaps is also small and consequently difficult to measure experimentally. In fact, in one of the most recent and careful experiments on excrescence drag, Reference 4.5, it is stated that the measurements of the drag of grooves are considered poor because of the problem of obtaining small increments from much larger overall measurements. Thus, the available experimental data base for spanwise gaps contains a lot of scatter and is difficult to correlate. Reference (4.5) determined that the drag ratio, C_{DF}/C_{fe} ,

evidences a weak dependence on roughness Reynolds number. An earlier publication, Reference 4.20 showed a family of curves where the depth ratio, h/l , was also a significant parameter. As in the case of circular holes, the drag coefficient C_{DP} is based on the planform area of gaps or grooves.

An independent evaluation has been made for the present work and the stronger dependence has been found to be with respect to the depth ratio. Both of these methods will be described.

4.3.3.1 Gaps Normal or Parallel to the Flow

Data are presented in this section for spanwise gap configurations which have the long axis normal or parallel to the flow direction. The effect of flow inclination on the drag of spanwise gaps is given in the next section.

Reference 4.5 gives a small linear dependence of C_{DP}/C_{fe} on h^+ for slots or grooves normal to the flow:

$$C_{DP}/C_{fe} = 2 \log (h^+) - 2 \tag{4.13}$$

In Figure 4.48, the available slot data has been plotted as a function of the depth ratio, h/l . A distinction has been made between slots with the long dimension normal to the flow direction and those where the long dimension is parallel to the flow. Since there is an order-of-magnitude difference in the values of h/l for the two categories, the depth ratio was based on the shortest side for each case. This type of presentation produced the most consistent trends with the least amount of scatter.

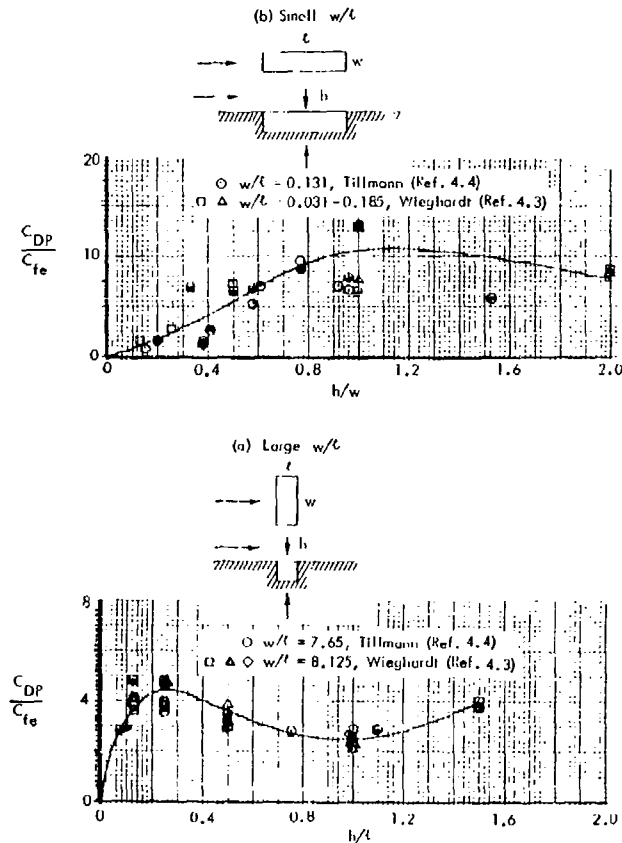


Figure 4.48 Drag of Slots

Since the geometry effects seem to be more predominant, the mean curves of Figure 4.48 are recommended for the drag of spanwise gaps. It must be pointed out that the range of h^+ for these data is limited to approximately 1×10^3 to 3×10^4 and that at higher values of h^+ , the Reynolds number effect of Reference (4.5) may predominate for spanwise grooves. In the case of longitudinal or chordwise grooves, Reference 4.5 found that the drag change was roughly equal to the drag of the increased skin friction on both sides of the groove. This would be a reasonable alternative to the use of Figure 4.48 for longitudinal grooves.

4.3.3.2 Gaps Inclined to the Flow

The only data on the effect of flow inclination on gap drag is found in Reference 4.3. The results are summarized in Figure 4.49. As can be seen, the variation with flow angle, α , for the configurations tested is not the same. No convenient correlation can be derived and consequently, the data of Figure 4.49 can only be used as a general guide for the effect of flow inclination.

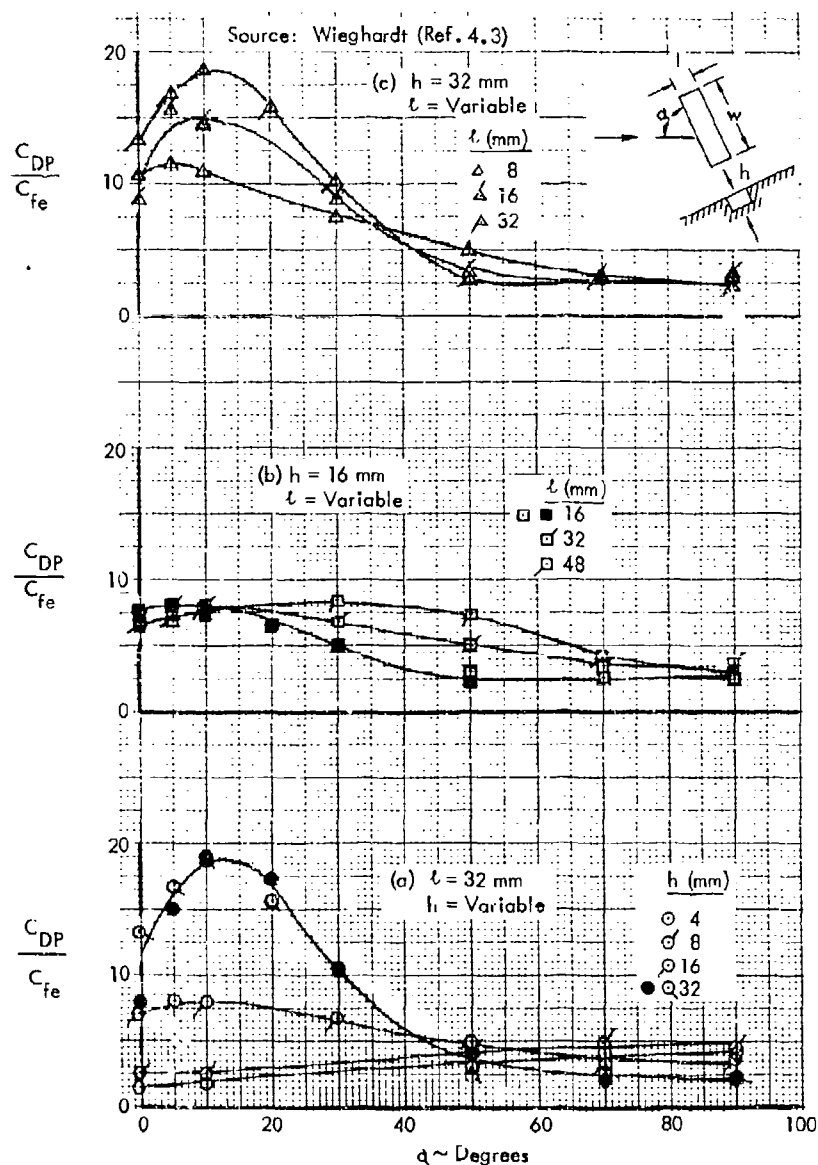


Figure 4.49 Effect of Flow Inclination on the Drag of Gaps

4.3.4 Surface Waviness

Surface waviness may be described as a repeated deviation in surface contour which has the effect of imposing a sinusoidal-type displacement of the local flow in the streamwise direction. On aircraft, it is generally present where multi-panel manufacturing techniques are employed such that the seamed areas along the panel edges more rigidly follow the intended contour than the panel centers. Bulges or indentations occur which more-or-less have a repetitive wave-like appearance on the surface. This situation may be worsened under flight load conditions where local stresses may increase the amplitude of such deviations. Pressurized fuselages, in particular, may undergo significant amounts of bulging at the high cruise altitudes typical of today's transport aircraft.

A review of the literature on the subject of drag due to waviness as applied to aircraft surfaces reveals an outstanding example of the problem caused by a lack of adequate methods to assess roughness drag. Hoerner's approach to this particular source of drag was to correlate C_{Dm} , based on projected frontal area, against a relative waviness parameter, h/l , where h is the wave amplitude and l is the wave length. His results are shown in Figure 4.50. This correlation was based on two sources: the airfoil test of Hood, Reference 4.23, where two heights of sinusoidal-type waves were tested, and the Wieghardt data 4.3 for a rounded spanwise ledge. Some more recent results from Reference 4.21 have also been included on Figure 4.50 for comparison. The drag coefficient C_{Dm} is equal to $\Delta D/q_m f_e$ where q_m is the mean dynamic pressure over the height of a wave and f_e is the projected frontal area of all waves present.

The basic problem with the correlation of Figure 4.50 is the applicability of data with large values of h/l to surface waviness on aircraft where a reasonable h/l value is at least an order of magnitude smaller. Hood recognized in Reference 4.23, that the relative waviness of his experiments was much larger than would be representative of aircraft of his time (1939). Although there is no doubt that Figure 4.50 correctly models the drag for surface waviness at large h/l , the validity of the vanishingly small C_{Dm} for small h/l values is questionable.

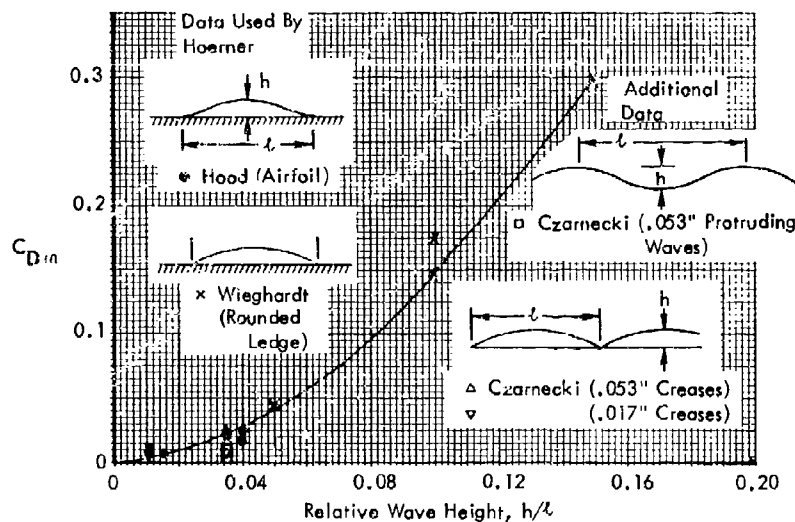


Figure 4.50 Low Speed Drag of Surface Waves vs Relative Wave Height

Some insight into this problem was made as a result of Reference 4.22. A Boeing 720 was instrumented to measure fuselage boundary layer with the objective of determining the effect of cabin pressurization on the fuselage drag. Several observations can be made from this work.

- o First, the degree of waviness, h/l , caused by overpressure deformation of the fuselage surface was measured to be 0.00175. This corresponds to a bulge height of 0.035 inches and a spacing between fuselage frames of 20 inches.
- o The measured drag increase was determined to be $C_D = 0.0001$, which is approximately 5% of the fuselage drag.
- o The measured drag includes the effects of any leakage or air exhaustion which would occur under pressurization. No quantitative breakdown was made of the relative magnitude of drag due to leakage as opposed to skin bulging. Speculation was made that the latter would be less of a factor.

The degree of waviness determined in this example, $h/l = 0.00175$, is an order of magnitude smaller than the smallest value shown on Figure 4.50. Use of Figure 4.50 for a C_{Dm} value corresponding to this level of waviness would be meaningless. Although the actual size of the additional drag due to the surface bulges in Reference 4.22 is not known, a rational assumption of one-third of the total would imply a C_{Dm} value of about 0.015. This value is not compatible with the curve of Figure 4.50, although it is in general agreement with the results for the smallest h/l tested.

In order to investigate the possibility of a more useful correlation, the available test data have been converted into the form C_{Dm}/C_{fe} vs h^+ , Figure 4.51. Additional data from Reference 4.21 on creases has also been included, Figure 4.52, since this particular roughness configuration is very similar to the wave configuration.

At the higher Mach numbers, where there is significant wave drag, the familiar linear variations observed for other excrescence forms are also present in these data. A fairly orderly progression with Mach number is observed. However, the subsonic ($M < 0.7$) data do not exhibit the characteristic drag increase with increasing roughness Reynolds number. In fact, the data are more or less scattered about a residual level of C_{Dm}/C_{fe} of approximately 5.0. A constant value of C_{Dm}/C_{fe} of 5.0 would correspond to a 10 to 20 percent increase in skin friction drag for the conditions covered by the data.

In Reference 4.24 where correlations of the wave drag from the Reference 4.21 experiments were made with theory, it was also concluded that an added drag coefficient was present in the order of 10-15% of surface friction. This level of skin friction was attributed to the formation of Gortler vortices which are generated in the concave regions of the waves. At some wave height the vortex strength becomes sufficient to affect the friction drag and the amount of additional drag increases roughly with the increase in h/l . Apparently, from the experience of Reference 4.22, a relative wave height of $h/l = .00175$ was sufficient to cause increased skin friction. However, this has not been sufficiently substantiated and the problem of an inadequate data base is further underscored. In the subsonic range and for low h/l , use of a constant value of $C_{Dm}/C_{fe} = 5.0$ seems to represent a conservative approach until this problem is resolved.

At higher speeds the linear variations with roughness Reynolds number, Figure 4.51, 4.52, can be used to account for Mach number and Reynolds number effects due to surface waviness. Unfortunately, there are large differences in the slopes of C_{Dm}/C_f vs h^+ for the configurations tested and generalization of the results is not possible. The recommended approach is to use the guidance of either Figure 4.51 or 4.52 based on the degree of similarity of the actual surface waviness to those represented by the data.

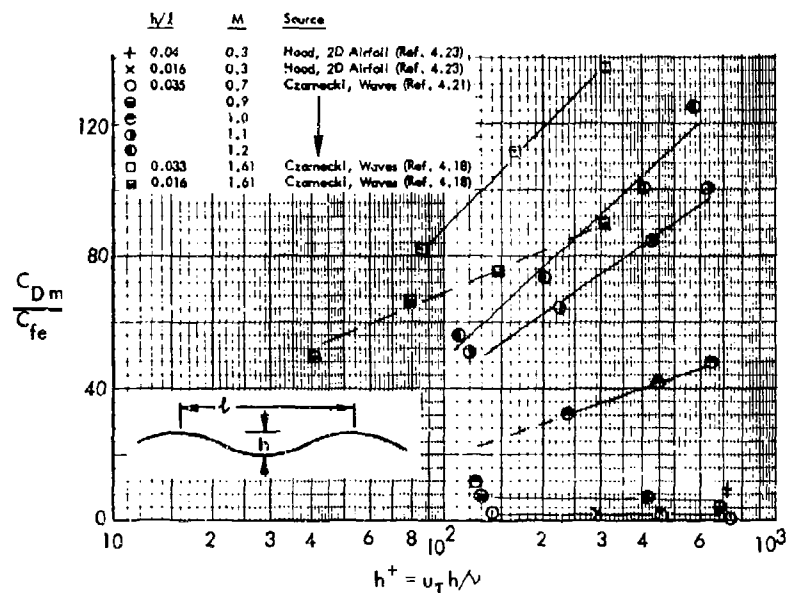


Figure 4.51. Drag of Surface Waves vs Roughness Reynolds Number

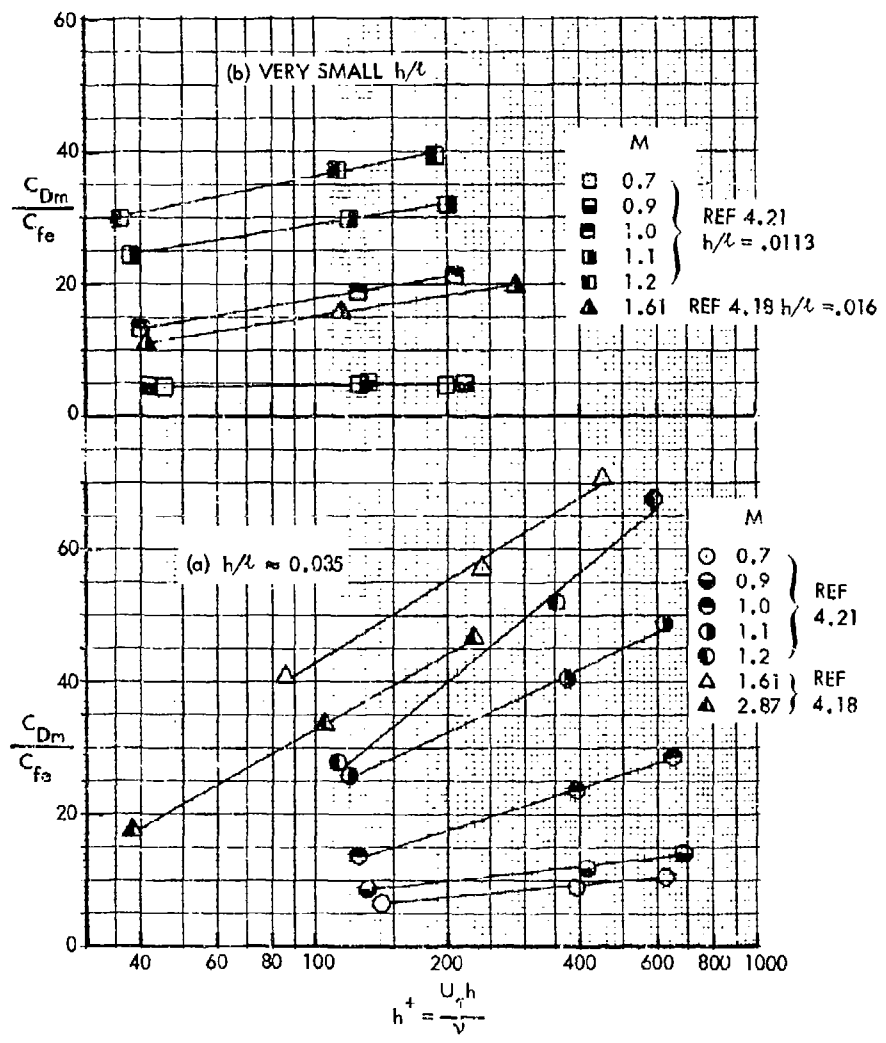


Figure 4.52 Drag of Surface Creases vs Roughness Reynolds Number

REFERENCES

- | | | | |
|------|--|------|---|
| 4.1 | Jones, B. M. | 1929 | "The Streamline Aeroplane," Journal K. Ae. S. |
| 4.2 | Hoerner, S. F. | 1958 | "Fluid Dynamic Drag," Published by the Author |
| 4.3 | Wiegardt, K. | 1946 | "Increase in Turbulent Skin Friction Caused by Surface Irregularities," MAP R&T No. 103, Translation of FB1563, ZWB 1942. |
| 4.4 | Tillmann, W. | 1951 | "Additional Measurements of the Drag of Surface Irregularities in Turbulent Boundary Layers," NACA TM 1299. |
| 4.5 | Gaudet, L. and Winter, K.G. | 1973 | "Measurements of the Drag of Some Characteristic Aircraft Excrescences Immersed in Turbulent Boundary Layers," RAE Tech. Memo Aero. 1538. |
| 4.5a | Winter, K. G. | | Unpublished Data Received. |
| 4.6 | Good, M. C., and Joubert, P. N. | 1968 | "The Form Drag of Two-Dimensional Bluff-Plates Immersed in Turbulent Boundary Layers," Journal of Fluid Mechanics, Vol. 31, Part 3, pp. 547-582. |
| 4.7 | Nash, J. F. and Bradshaw, P. | 1967 | "The Magnification of Roughness Drag by Pressure Gradients," Journal R. Ae.S. Vol. 71, pp. 44-49. |
| 4.8 | Young, A. D., Serby, J. E. and Morris, D. E. | 1939 | "Flight Tests on the Effect of Surface Finish on Wing Drag," ARC R&M No. 2258. |
| 4.9 | Williams, D. H. and Brown, A. F. | 1938 | "Experiments on a Riveted Wing in the Compressed Air Tunnel," ARC R&M 1855. |
| 4.10 | Williams, D. H. and Brown, A. F. | 1937 | "Tests on Rivets and Backward-Lapped Joints in the Compressed Air Tunnel," ARC R&M 1789. |
| 4.11 | Hood, M. J. | 1939 | "The Effects of Some Common Surface Irregularities on Wing Drag," NACA TN 695. |
| 4.12 | Fenter, F. W. and Lyon, W. C. | 1958 | "An Experimental Investigation of the Effects of Several Types of Surface Roughness on Turbulent Boundary Layer Characteristics at Supersonic Speeds," DRL No. 411. |
| 4.13 | Schlichting, H. | 1937 | "Experimental Investigation of the Problem of Surface Roughness," NACA TM 823. |
| 4.14 | Delany, N. K. and Sorensen, N. E. | 1953 | "Low Speed Drag of Cylinders of Various Shapes," NACA TN 3038. |
| 4.15 | Pallister, K. C. | 1974 | "Wind Tunnel Measurements of the Transonic Drag of Excrescences Immersed in a Turbulent Boundary Layer," ARA Report 37. |
| 4.16 | Friesing, H. | 1936 | "Measurement of the Drag Associated with Recessed Surfaces: Cutouts of Rectangular and Elliptical Planform," ZWB (Germany) FB 628. |
| 4.17 | Gaudet, L. and Johnson, P. | 1971 | "Measurements of the Drag of Excrescences Immersed in Turbulent Boundary Layers at Mach Numbers Between 0.2 and 2.8: Circular Holes," RAE TR 71181. |

4.18	Czarnecki, K. R., Sevier, John R. and Carmel, M. M.	1958	"Effects of Fabrication-Type Roughness on Turbulent Skin Friction Drag at Supersonic Speeds," NACA TN 4299.
4.19	Kozalenko, V. M. and Nesterovich, N. I.	1975	"The Drag of Ridges of Finite Length in a Turbulent Boundary Layer," RAE Library Translation 1852.
4.20	Winter, K. G. and Gaudet, L.	1967	"A Programme of Tests on the Drag of Excrescences Proposed for the 8 Ft. x 8 Ft. Wind Tunnel and a Brief Analysis or Some Previous Measurements," RAE TM Aero. 1005.
4.21	Czarnecki, K. R. and Monta, W. J.	1969	"Roughness Drag Due to Two-Dimensional Fabrication-Type Surface Roughness on an Ogive Cylinder from Force Tests at Transonic Speeds," NACA TN D-5004.
4.22	Gyorgyfalvy, D.	1965	"Effect of Pressurization on Airplane Fuselage Drag," Journal of Aircraft.
4.23	Hood, M. J.	1939	"The Effects of Surface Waviness and Rib Stitching on Wing Drag," TN 729.
4.24	Rogers, K. H.	1974	"Boundary-Layer Theory for Pressure and Drag of a Wavy Surface," Journal of Aircraft, Vol. II, No. 7.
4.25	Marshal, V. L. and Williams, R. G.	1978	"An Evaluation of Large Scale Excrescences," British Aerospace, Aero/FM/Report 062.
4.26	Welsh, C. J.	1953	"The Drag of Finite-Length Cylinders Determined from Flight Tests at High Reynolds Numbers for a Mach Number Range From 0.5 to 1.3," NACA TN 2941.
4.27	Lacey, J.	1974	"The Aerodynamic Drag of Square Ridges, University of Leicester, M.Sc. Thesis.

5. FLOW OVER ROUGH SURFACES WITH NON-UNIFORM PRESSURE DISTRIBUTION

5.1 Drag and Momentum Loss Magnification Factors of Isolated Excrescences

An early approach (Reference 5.1) to the problem of the drag increment due to an isolated excrescence in a non-uniform pressure distribution was to assume that the increment expressed as a coefficient in terms of local free stream conditions was the same as in a uniform flow, so the drag was simply proportional to the local free stream dynamic pressure. However, in 1967 Nash and Bradshaw (Reference 5.2) demonstrated that the subsequent history of a boundary layer after encountering an excrescence was important in determining the associated drag increment, and this could be very different and was often larger than that calculated on the assumption of simple proportionality to the local free stream dynamic pressure at the excrescence position. Their argument was developed for incompressible flow and was briefly as follows for the flow over an aerofoil section.

The Momentum Integral Equation for a turbulent boundary layer can with certain acceptable assumptions be shown to lead to (see Reference 2.2, p336)

$$\theta^{6/5} u_e^{4.2} - \theta_o^{6/5} u_{eo}^{4.2} = 0.0106 \nu^{1/5} \int_{x_o}^x u_e^4 dx.$$

Here, suffix o refers to quantities at the position of the excrescence, u_e is the local free stream velocity at the edge of the boundary layer, and the Reynolds number is assumed to be high enough for the 1/9th. power law for the velocity distribution to be applicable (see Section 2.1.2). Hence at the trailing edge (suffix T)

$$\theta_T^{6/5} u_{eT}^{4.2} = \theta_o^{6/5} u_{eo}^{4.2} + 0.0106 \nu^{1/5} \int_{x_o}^{x_T} u_e^4 dx. \quad 5(1)$$

Now suppose that the excrescence produces an effective change in the local value of θ from θ_o to $\theta_o + \Delta \theta_o$, θ_o being the value at the excrescence position in the absence of the excrescence. It is assumed that $\Delta \theta_o \ll \theta_o$ and that the excrescence produces no change in the free stream flow and that any local modification in the form of the boundary layer velocity profile due to it can be neglected. Then from equation 5(1) the corresponding change in θ_T is given by

$$1.2 \Delta \theta_T \theta_T^{1/5} u_{eT}^{4.2} = 1.2 \Delta \theta_o \theta_o^{1/5} u_{eo}^{4.2}.$$

Hence
$$\Delta \theta_T / \Delta \theta_o = (\theta_o / \theta_T)^{1/5} (u_{eo} / u_{eT})^{4.2}. \quad 5(2)$$

We refer to $\Delta \theta_T / \Delta \theta_o$ as the momentum magnification factor (although strictly it is the momentum thickness increment magnification factor) and we shall write it as m_m .

If we now use the method due to Squire and Young (Reference 5.3) for solving the momentum integral equation for the wake to relate θ_T to the value of θ far downstream and hence to the drag coefficient C_D , then the change in C_D due to the excrescence is

found to be given by

$$\Delta C_D = 2 (u_{eT}/V_o)^{3.2} \Delta \theta_T/c.$$

Here c_D is based on the aerofoil chord c and the undisturbed stream velocity V_o . Hence, making use of 5(2) we have

$$\Delta C_D = 2 (u_{eo}/V_o)^{4.2} (V_o/u_{eT}) (\theta_o/\theta_T)^{1/5} (\Delta \theta_o/c) \quad 5(3)$$

For the same excrescence on a short element of a flat plate and zero pressure gradient with undisturbed free stream velocity u_{eo} we have

$$(\Delta C_D)_{fp} = 2 \Delta \theta_o/c,$$

where we have referred $(\Delta C_D)_{fp}$ to the length c .

$$\text{Hence} \quad \Delta C_D / (\Delta C_D)_{fp} = m_d, \quad 5(4)$$

$$\text{where} \quad m_d = (u_{eo}/V_o)^{4.2} (V_o/u_{eT}) (\theta_o/\theta_T)^{1/5}, \quad 5(5)$$

and m_d is called the drag magnification factor.

We see that m_d can be readily underestimated by the earlier assumption that $m_d = (u_{eo}/V_o)^2$, if $u_{eo} > V_o$. Figure 5.1 shows m_d plotted as a function of u_{eo}/V_o for various values of θ_o/θ_T ; it will be seen that m_d is not very sensitive to variations in θ_o/θ_T . Nash and Bradshaw did some experiments which broadly supported their analysis and demonstrated the inadequacy of the earlier assumption for non-uniform pressure distributions.

It is clear that one can adopt any other method of prediction of boundary layer development to determine the magnification factor and in particular the effects of compressibility can be included. Cook (Ref. 5.4) used the Green form of the lag entrainment method (Ref. 2.27) combined with the compressible form of the Squire-Young wake relation and compared the resulting predictions with measurements that he made on square-sectioned ridge excrescences on two aerofoils over a range of subsonic Mach numbers up to 0.77, Reynolds numbers up to 15×10^6 and values of C_L up to 0.6. His basic zero pressure gradient data were derived from the Gaudet, Jonsson, Winter results (Ref. 5.5, 5.6, 5.7). Some comparisons are shown in Figures 5.2 and 5.3 for the predicted and measured drag increments. On the whole the prediction method underestimated the increment by about 10% for conditions where the local flow was sub-critical, but it is evident that at higher Mach numbers when shock waves develop near the excrescences the predictions become less reliable because of the effects of the excrescence on the shock wave, on the shock wave-boundary layer interaction and the development of a shock wave from the excrescence itself. It will be seen that in all

cases the old assumption of a magnification factor simply proportional to the local dynamic pressure is seriously in error. It must also be noted that in order to achieve increments large enough to be measured with adequate accuracy Cook's excrescences sometimes extended to about $\delta/3$ in height and were then partially outside the logarithmic law of the wall region to which the basic Gaudet, Johnson, Winter data apply. This may well explain the 10% or so underestimate of m_d noted above when no shock wave was present.

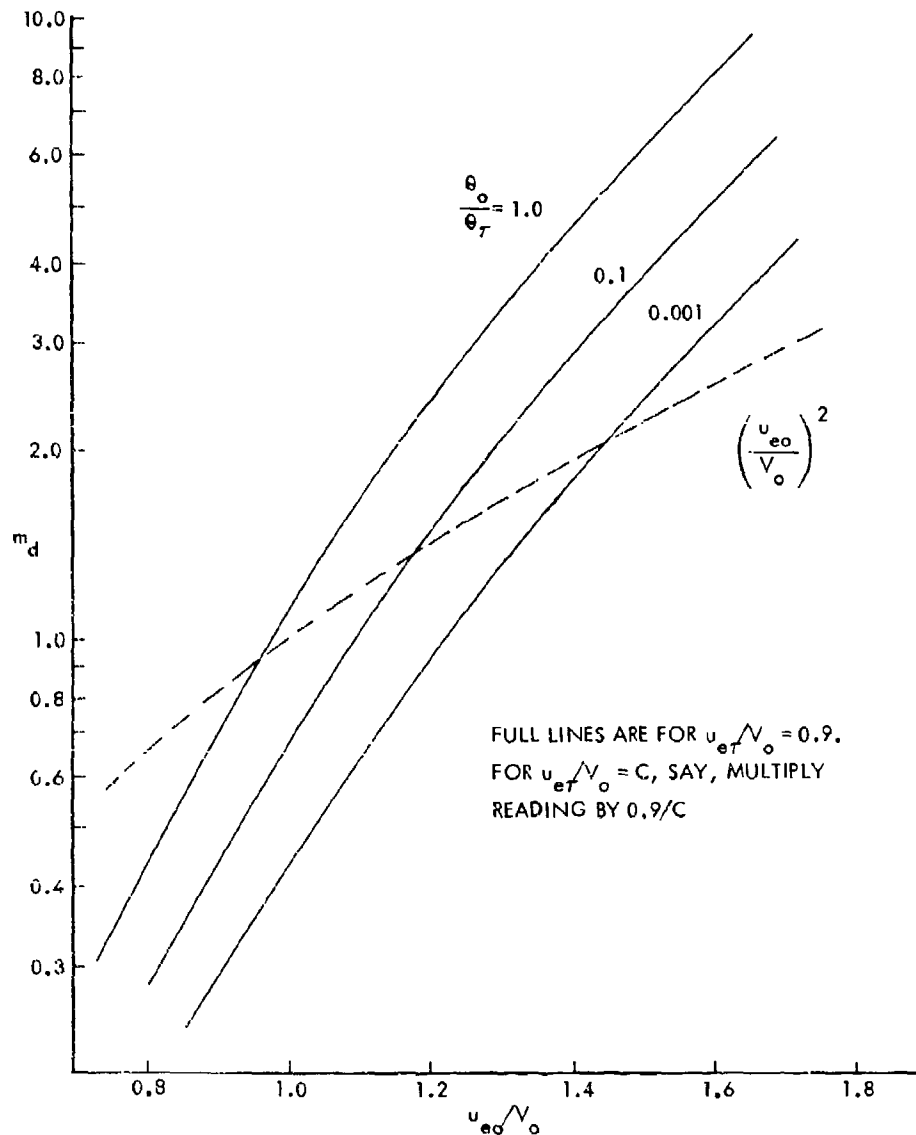


Figure 5.1 Drag Magnification Factor According to Nash-Bradshaw Theory

- EXPERIMENT
 GAUDET AND JOHNSON DATA SCALED BY RATIO OF LOCAL TO FREESTREAM DYNAMIC PRESSURES
 - - - GAUDET AND JOHNSON DATA SCALED BY MAGNIFICATION FACTOR ESTIMATED USING GREEN BOUNDARY LAYER METHOD AND COMPRESSIBLE FORM OF SQUIRE & YOUNG LAW

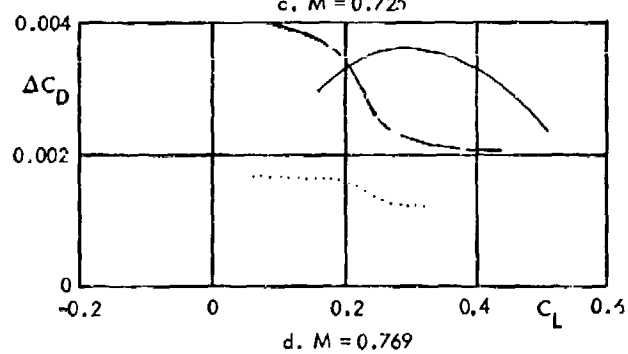
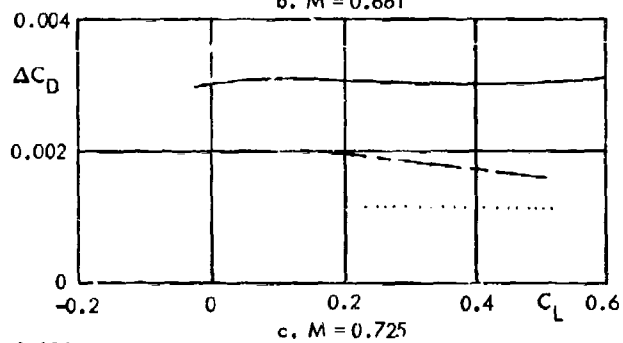
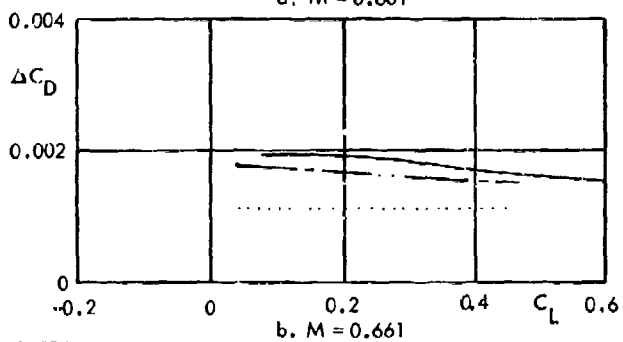
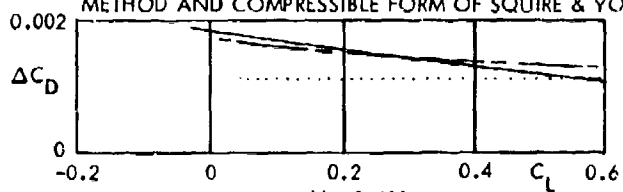


Figure 5.2 Drag Due to Square Ridge Excrescence at $x/c = 0.43$ on Lower Surface of Section 2814: $R = 7.5 \times 10^6$

————— EXPERIMENT
 GAUDET AND JOHNSON DATA SCALED BY RATIO OF LOCAL TO FREESTREAM DYNAMIC PRESSURES
 - - - - - GAUDET AND JOHNSON DATA SCALED BY MAGNIFICATION FACTOR ESTIMATED USING GREEN BOUNDARY LAYER METHOD AND COMPRESSIBLE FORM OF SQUIRE & YOUNG LAW

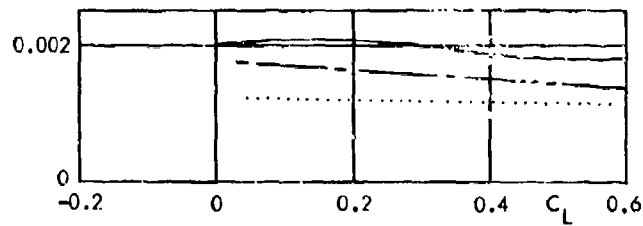
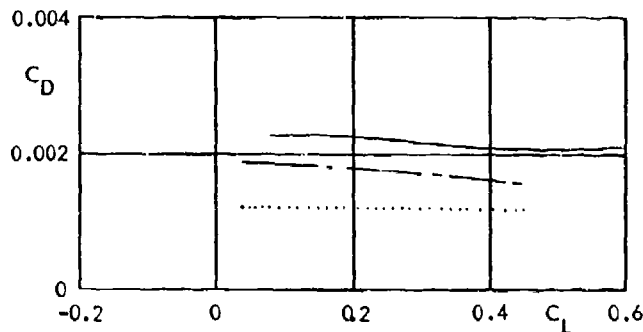
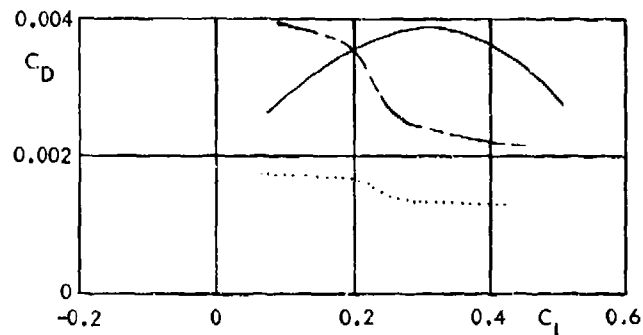
a) $M = 0.601$ b) $M = 0.661$ c) $M = 0.769$

Figure 5.3 Drag Due to Square Ridge Excrescence at $x/c = 0.43$ on Lower Surface of Section 2814; $R = 15 \times 10^6$

Ambitious theoretical studies have been made by Keates (Reference 5.8, 5.9) on the effects of excrescences on the characteristics of a two dimensional high lift configuration. The configuration he examined consisted of a wing (RAE 2815 section) with a 17% chord leading edge slat and a 40% chord Fowler type trailing edge flap. Two arrangements were considered, takeoff with slat angle = 28° , flap angle = 10° , and landing with slat angle = 28° and flap angle = 30° . Keates adapted Irwin's integral method (Reference 5.10) to calculate the momentum magnification factor m_m over the rear of the wing for various positions of a two dimensional excrescence on the wing and he also calculated m_m over the rear of the flap for various excrescence positions over the front of the flap. Irwin's method is designed to predict the development of the boundary layer on one component of a multi-component lifting system in the presence of the wake from an upstream component. Suitable analytic forms for the velocity profiles of the boundary layers and wakes are chosen so as to represent their initial separate

development and eventual merging, with an appropriate number of unknown parameters to be determined by applying the momentum integral equation to the appropriate regions of the boundary layer and wake plus assumptions regarding the entrainment rate into the outer part of the wake and the shear stress values at a number of positions across the boundary layer and wake.

Keates made the usual assumption that the local effect of an excrescence was completely defined by an increment in momentum thickness related to its drag coefficient on a flat plate as determined in the Gaudet et al. experiments. Initial smooth surface values to start the calculations were derived from RAE experimental data for the configuration considered (References 5.10, 5.11). The calculations of the magnification factor on the wing due to an upstream excrescence on the wing were not carried over on to the flap, although further changes in the factor must be expected as the wing plus slat wake pass over the flap. The results of the calculations were compared with the predictions of the Nash-Bradshaw formula, equation 5(2), and in some instances with results obtained using the Green-Head entrainment method (Reference 2.27) for determining the viscous flow development treated as a single boundary layer (i.e. the wake modification of the velocity profile was not allowed for, but its additional momentum defect was included).

In general Keates found that the effect of different excrescence heights on m_m was small, and such changes that there were reflected the effects on the merging position of the boundary layer and the wake of the preceding element. Figure 5.4 illustrates the effects of incidence on m_m at the rear of the wing portion in the take-off arrangement due to excrescences at three different positions. For all the excrescences the ratio $\Delta\theta_o/\theta_o$ was kept constant and equal to 0.1. It should be noted that this implies an increase of $\Delta\theta_o$ with rearward movement of the excrescence since θ_o increases with distance downstream. Also shown are the corresponding values of m_m given by the Nash-Bradshaw formula (m_{mNB}) and it will be seen that the two sets of predictions are in reasonable agreement for incidences up to about 14° but for incidences greater than 14° the Nash-Bradshaw predictions are appreciably lower than those of the Irwin type calculation. The large values of m_m with the excrescences well forward in regions of high local suction are particularly noteworthy. Similar results for the landing configuration are shown in Figure 5.5 and some results obtained for excrescences on the flap for the take-off configuration and $\alpha = 15^\circ$ are shown in Figure 5.6.

5.2 Magnification Factors for Multiple Excrescences and Distributed Roughnesses

Following Lacey's work on square sectioned ridges in zero pressure gradient flow (see Section 4.3.2.4) similar work was done by Rabbo at Leicester University (Reference 5.13) in two adverse gradients. Both cases were planned to achieve equilibrium turbulent boundary layers with a free stream velocity distribution of the form $u_e = u_o(x/x_o)^{-a}$, where x is the distance downstream from an appropriate datum, x_o is the value of x for the first ridge and u_o is the value of u_e at the first ridge. Some resulting deductions are presented in Figure 5.7 and 5.8 in the same form as the results for zero pressure gradient in Figure 4.46. In one case the index $a = 0.13$ and it corresponded to a value of the Coles' pressure gradient parameter $\Pi = 1.2$, in the other case $a = 0.2$, corresponding to $\Pi = 2.0$. In each case the drag per unit span of the ridge system ΔD is as measured immediately downstream of the last ridge.

It will be seen from Figure 5.7 and 5.8 that with increase of the adverse pressure gradient the maximum drag increment for a given array tended to decrease presumably because of the accompanying reduction in pressure drag of the excrescences. Also the spacing s/h for maximum drag increment for a given L/h decreased somewhat from about 12 for zero pressure gradient to about 10 for $\Pi = 2$. This was associated with a small

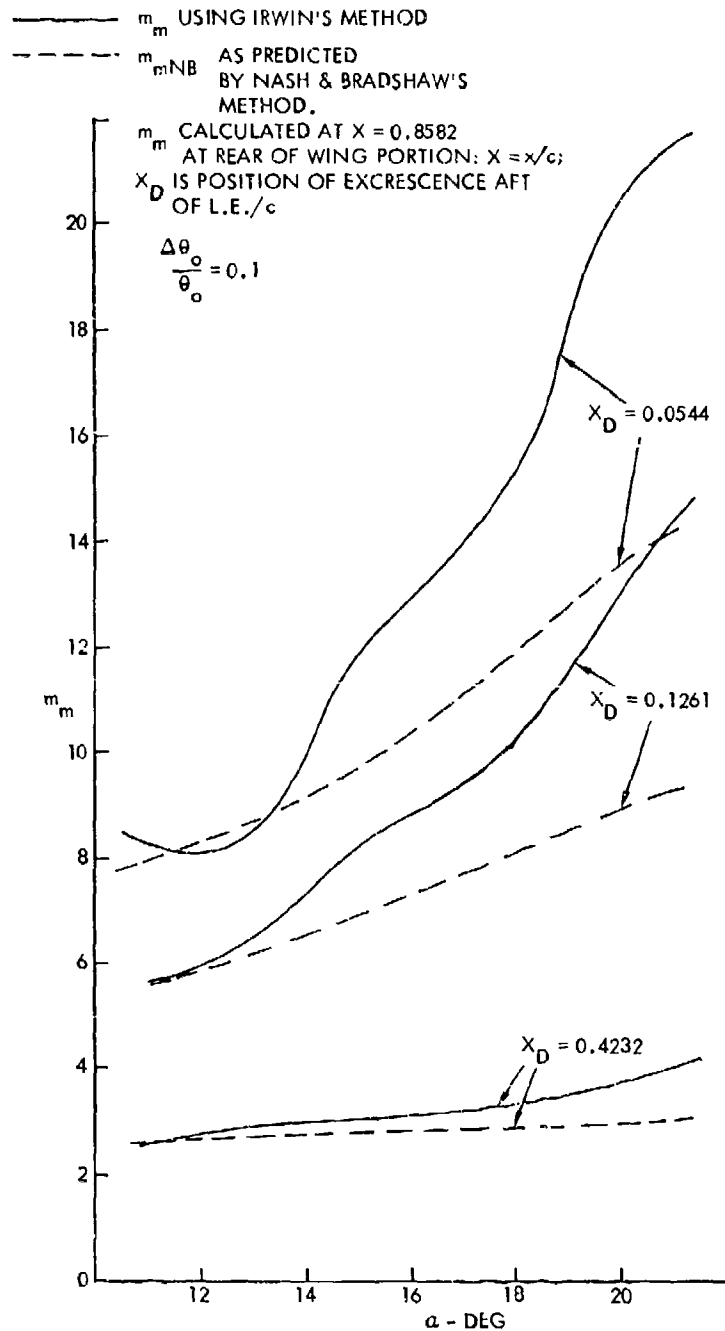


Figure 5.4 Effect of Incidence on Magnification Factor on Wing for Take-Off Configuration (Keates)

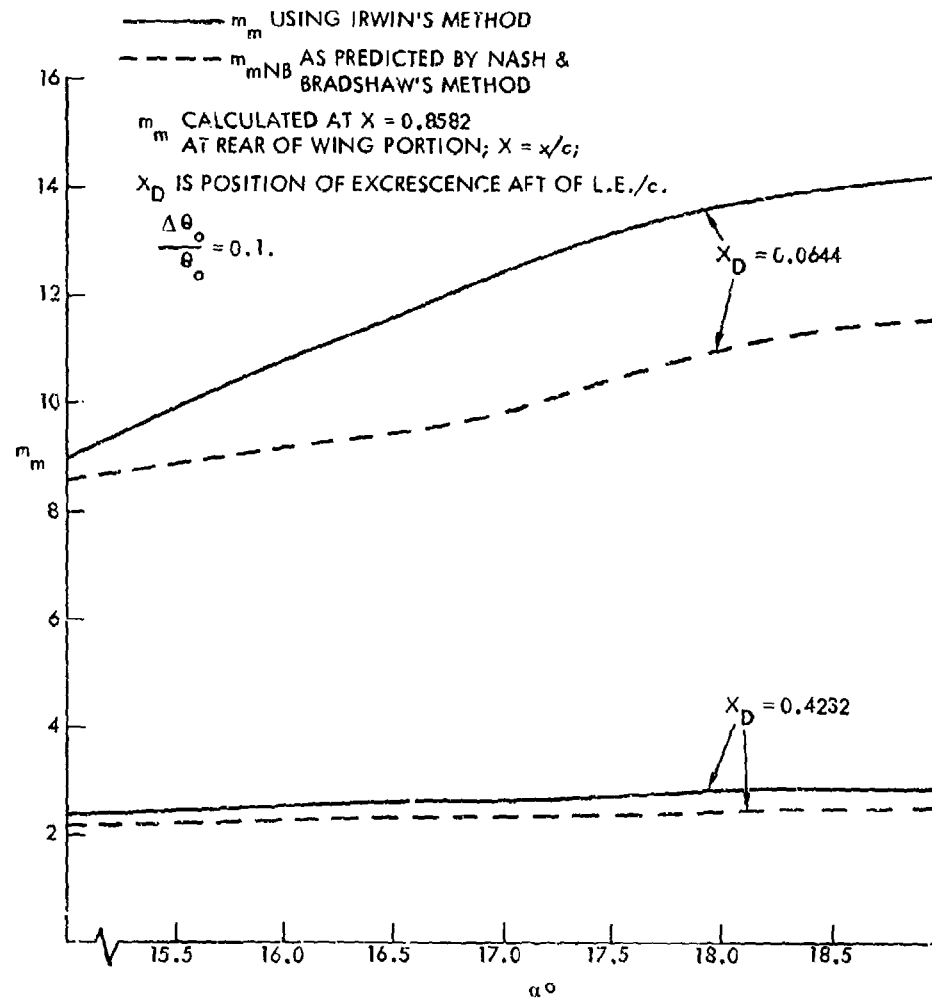


Figure 5.5 Effect of Incidence on Magnification Factor on Wing for Landing Configuration (Keates)

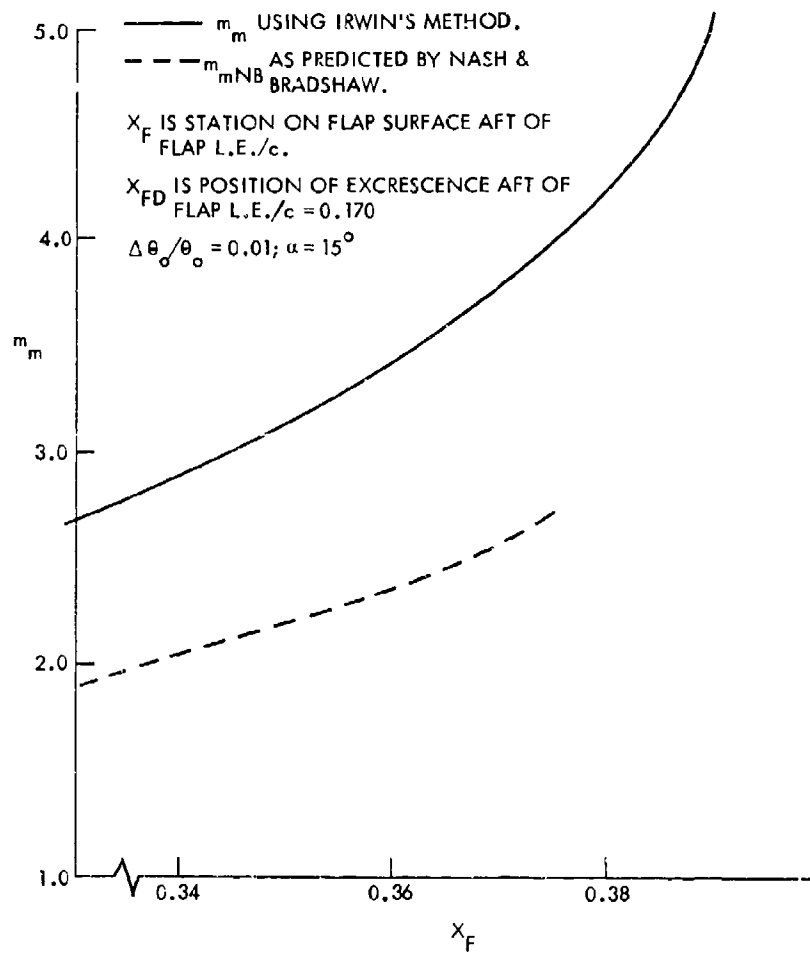


Figure 5.6 Variation of Magnification Factor Along Flap Surface Due to Excrescence at 0.17C Aft of Flap LE for Take-Off Configuration (Keates)

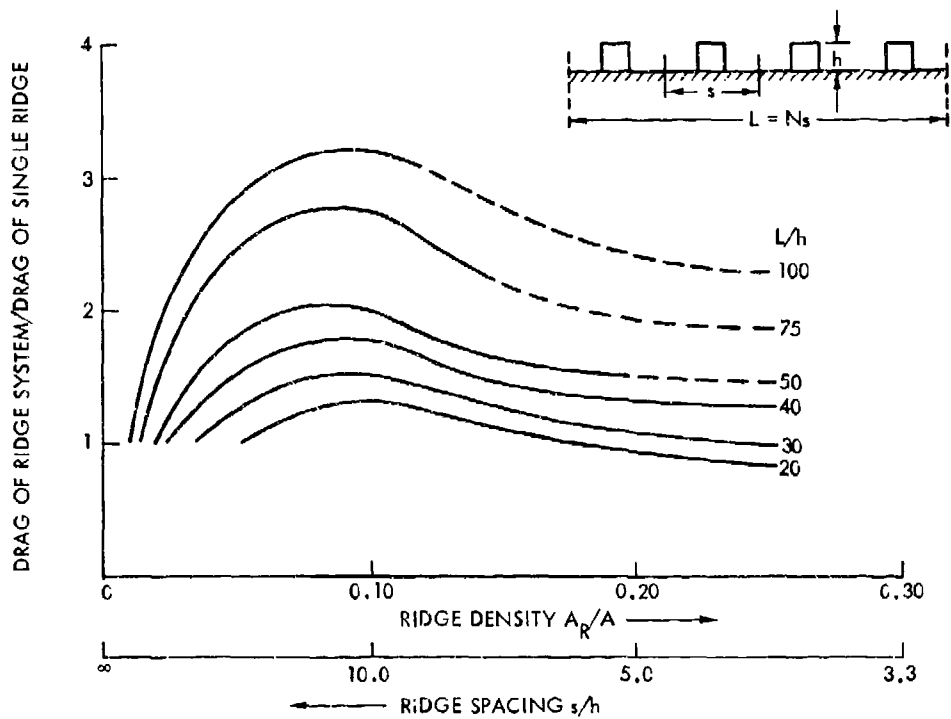


Figure 5.7 Variation of Drag with Selected Surface Length and Ridge Density in an Adverse Pressure Gradient, $II = 1.2$ (Robba)

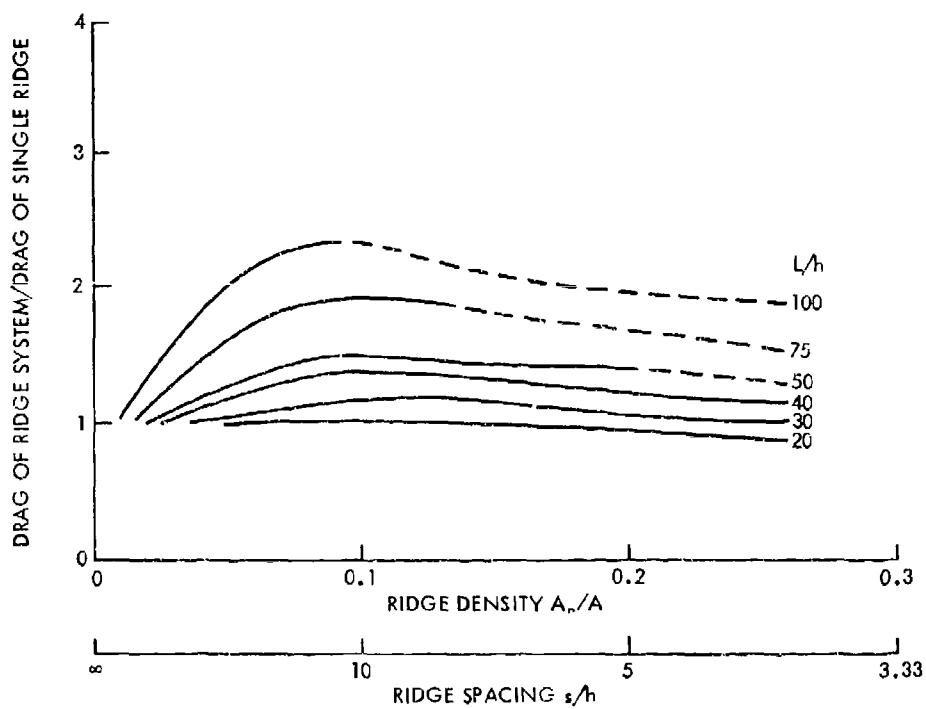


Figure 5.8 Variation of Drag with Selected Surface Length and Ridge Density in an Adverse Pressure Gradient $II = 2.0$ (Robba)

reduction with adverse pressure gradient in the length of the downstream separation bubble for a single ridge from about $8.7h$ with zero pressure gradient to about $7h$ for $II = 2$. It should be noted, however, that these results were for pressure gradients much smaller than that required to bring the boundary layer close to separation. They will not apply when the possibility arises that the excrescences may trigger separation and hence produce large changes in drag much greater than those illustrated in Figure 5.7 and 5.8. Such changes would then be accompanied by large lift changes if the excrescences were on a wing. It should also be noted that for bluff excrescences extending outside the boundary layer somewhat longer separation bubbles may be expected of about $12h$ in length (see for example Reference 5.14).

For uniformly distributed roughness in non-zero pressure gradients it seems reasonable to assume that Figure 3.5 may be expected to be applicable for determining the drag increment ΔD , if D is the drag of the smooth surface, provided that the equivalent sand roughness height is small compared with the boundary layer thickness and the boundary layer is not close to separation. This assumption is based on the argument that the magnification factor is already accounted for in D since the drag contribution of each element of the smooth surface will be subject to the associated magnification factor in making its contribution to D and any local roughness contribution will be subject to the same factor. Analysis of the results obtained by Jones and Williams (Reference 5.15) using carborundum roughness on two aerofoils, by Ljungstrom (Reference 5.16) using aluminum oxide grinding paper on an aerofoil with a flap and slat and by Young (Reference 5.19) using camouflage paint shows the results to be reasonably consistent with this hypothesis.

It may be recalled that Nikuradse's sand roughness grains were fairly uniform in size and were closely packed, and their drag effect was appreciably less than if they had been distributed some ten grain sizes apart. It may be inferred that any similarly closely packed and nearly uniform roughnesses will have an equivalent sand roughness height much the same as the average roughness height. On the other hand, the camouflage paints tested by Young had roughness heights showing considerable variation and for each the equivalent sand roughness height was some 60% larger than the average; it could be equated with the largest roughness height that occurred with fair frequency but at sufficient distance apart for the roughnesses not to seriously interfere with each other.

Further discussion of predictive methods for determining the development of the boundary layer and its characteristics in the presence of distributed roughness is given in Section 5.5.

5.3 Effect of Excrescences on C_{Lmax} of Aerofoils

In regions of strong adverse pressure gradient the increase due to upstream or local roughness of the boundary layer momentum thickness as well as the associated changes of the boundary layer velocity profile may trigger or hasten flow separation. Hence an aerofoil with excrescences on its upper surface will in general demonstrate some reduction of C_{Lmax} depending on the size of the excrescences, their location and the Reynolds number. Not surprisingly, it is excrescence locations close to the leading edge on the upper surface for which the reduction of C_{Lmax} can be very marked since the adverse gradients are high there at incidences near the stall and the magnification factors are very large. The situation is complicated by the fact that depending on the wing geometry as well as the factors referred to above the flow separation may either occur close to the excrescence and spread rapidly downstream or it may start from the rear of the wing and spread forwards. The former is the more likely the larger the excrescence and the smaller the nose radius of curvature of the wing.

For the effects on C_{Lmax} of uniformly distributed roughness over the upper surface of a wing or high lift configuration there are only a few sources of data to which we can refer, namely, Jones and Williams (Reference 5.15), Gregory and O'Reilly (Reference 5.17), Weeks (5.18) and Ljungstrom (5.16). These last three references were directed at the effects of hoar frost and surfaces that would not be exposed under normal conditions (e.g. parts of the wing leading edges under slats when closed) were not covered with roughnesses when tested. In each case an attempt has been made in analyzing the data to relate the ratio $\Delta C_{Lmax}/C_{Lmax}$ (clean) for a given roughness to the corresponding ratio $\Delta D/D$ for the roughness on both surfaces of a flat plate at zero incidence and the Reynolds number of the wing under test in terms of its mean chord length. Given the equivalent sand roughness height the latter can be determined from Figure 3.5; in the absence of adequate details of the roughnesses tested the equivalent sand roughness height was taken as 1.6 times the average roughness height (in view of the results of Reference 5.19). This was done in the cases of the data of Weeks and of Ljungstrom, in the other two cases there were sufficient data to enable direct estimates of $\Delta D/D$ to be made without the intermediate step of determining an equivalent sand roughness height. The results are presented in Figure 5.9 where three mean curves are indicated for the cases of the wing alone (W), wing with flap (WF), and wing with flap and slat extended (WFS). The likely accuracy of these curves can be inferred from the scatter, but it is as well to note that the data are all for wind tunnel Reynolds numbers (i.e. of the order of $2.5-6 \times 10^6$), although it is to be hoped that the use of the ratio $\Delta D/D$ as abscissa will implicitly account in large measure for Reynolds number effects.

It can be seen that the greatest sensitivity to small to moderate roughnesses is shown by the wing with flap extended, presumably due to the very high suction near the leading edge engendered by flap movement and the associated large magnification factors. In contrast, a leading edge slat helps to reduce the suction intensity over the wing and hence the sensitivity to roughness.

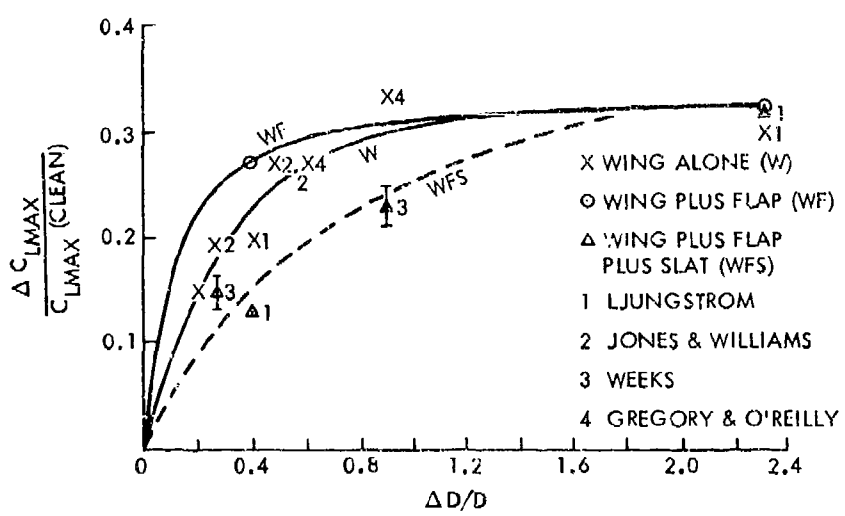


Figure 5.9 $\Delta C_{LMAX} / C_{LMAX} (CLEAN)$ as Function of $\Delta D/D$ Due to Uniformly Distributed Roughness over Upper Surface of Various Wing Arrangements

Keates (Reference 5.9) has estimated the effect of an upper surface isolated excrescence on C_{Lmax} for the high lift configuration that he considered (see Section 5.1) in the take-off arrangement. He assumed that in all cases C_{Lmax} was attained when the value of the boundary layer form parameter H was the same at the rear of the wing portion as for C_{Lmax} as measured without the excrescence on the wing (1.83). The validity of such an assumption is by no means established but the results are of some interest. Figure 5.10a shows the calculated values of $\Delta C_{Lmax}/C_{Lmax}$ as a function of $\Delta\theta_o/\theta_o$ and different roughness locations X_{WD} (it will be recalled that $\Delta\theta_o$ increases as X_{WD} increases for a given value of $\Delta\theta_o/\theta_o$). Also shown in Figure 5.10b are the calculated values of $\Delta C_{Lmax}/C_{Lmax}$ (clean) against excrescence position for a rearward facing step of height $1mm$ ($h/c = 0.0011$); here the rapid increase in sensitivity of C_{Lmax} to forward movement of the excrescence location is clearly evident.

5.4 The Effects of Control Gaps

Control gaps can increase drag for a variety of reasons. The inevitable disruption of the contour of the main lifting surface may induce some changes in the boundary layer development and possible local flow separation. Flow through the gap due to the pressure difference across it will be accompanied by losses which may be augmented by this flow interfering adversely with the boundary layer into which the flow emerges and may induce separation there. The disrupted geometry effects may be expected to be relatively insensitive to changes of incidence and lift coefficient but the effects due to the flow through the gap, being associated with the pressure difference between upper and lower surfaces there, will be closely dependent on the lift coefficient.

Hoerner (Reference 5.1) has analyzed some data for two dimensional controls and has presented the wing drag coefficient increments as a function of gap/chord ratio. With some scatter his results fall reasonably close to a mean curve given by:

$$\Delta C_D = 0.007 (e/c)^{3/5}, \text{ for the control at zero setting.}$$

Here ΔC_D is based on the wing area and e is the sum of the upper and lower surface gap width where both exist. The definition of gap width is somewhat arbitrary, the sketches of Figure 5.11 illustrate the conventions adopted by Hoerner.

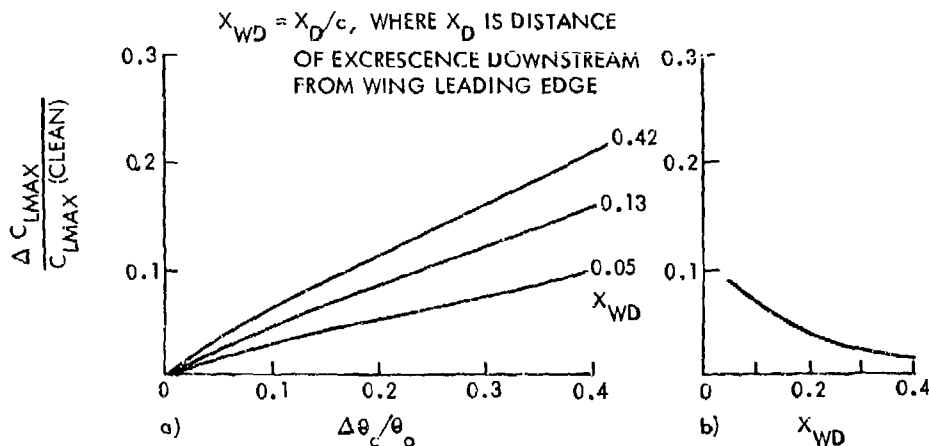


Figure 5.10 $\Delta C_{LMAX}/C_{LMAX}$ (CLEAN) as Function of $\Delta\theta_o/\theta_o$ for Various Excrescence Locations on Wing Portion of High Lift Configuration; b) As Function of X_{WD} for a Rearward Facing Step of Height $1mm$ ($0.0011c$) (Keates)

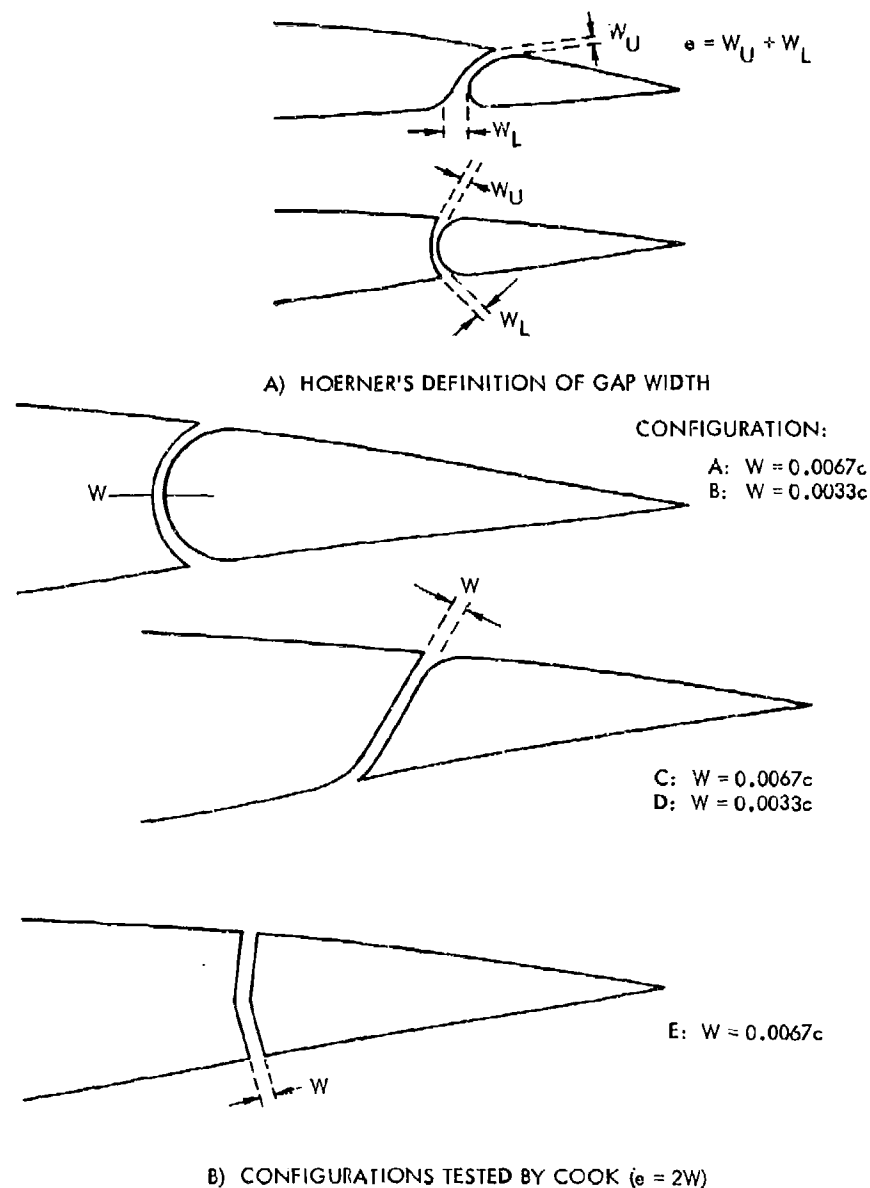


Figure 5.11 Spanwise Control Gaps

However, we have to note that this formula does not reflect any variation with wing C_L and hence cannot properly account for variations in the flow through the gap. Also the data used were predominantly for slotted flaps where the gap entry contours can be carefully designed to minimize drag effects for zero control angle and the flow through can be blocked by an upper surface shroud. We can therefore expect this formula to be somewhat optimistic when compared with results for ordinary controls where the geometry is more limited by the need to operate the control effectively in both directions from the zero setting.

Cook (Reference 5.4) has tested a number of two dimensional control configurations illustrated in Figure 5.11 for a range of Reynolds numbers up to 15×10^6 and a Mach number of 0.665. The wing section was the 2815 section ($t/c = 0.14$). His results showed little effect of Reynolds number on the drag increment and they also illustrated the fact that the control gaps produced significant changes in the pressure distribution over the whole of the wing surface resulting in a small reduction in lift at a given incidence. The drag increments due to the gaps also showed a variation proportional to

(gap width)^{3/5}. Cook then argued that the mass flow through the gap can be expected to be approximately a function of e^3/l_g where l_g is the length of the gap passage from entry to exit. This is based on the theoretical result for the flow through a channel of length l_g with an applied pressure difference. Hence, Cook argued that $\Delta C_D (l_g e^2/w^3)^{1/5}$ should be a function of $(c_{pLS} - c_{pUS})$ where c_{pLS} is the pressure coefficient on the lower surface at the position of the gap and c_{pUS} is that on the upper surface. Also w is a single gap width and corresponds to $e/2$. His resulting plot is shown in figure 5.12 for the three types of configuration that he tested and it will be seen that a reasonable collapse of the data resulted for each type, with types A, B, C and D collapsing close to a common curve. Not surprisingly, E with its sharp edges at entry and exit results in a curve departing from the others at the higher values of the pressure difference. The value indicated for the A, B, C and D configurations with zero pressure difference was deduced from measurements made with the gap blocked internally so that there was no flow through it and the dashed part of the curve is an inferred extrapolation.

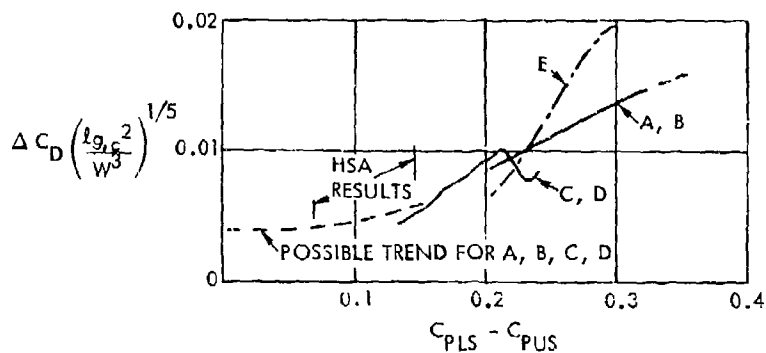


Figure 5.12 Cook's Analysis of Spanwise Control Gap Drag

Some wind tunnel data have been obtained on a model of the outer panel of the HS125 wing tested with a variety of ailerons, both internally balanced and with round noses, and with a range of gap widths. These data have been similarly analyzed in terms of the presentation of Figure 5.12. Such an analysis is inevitably approximate as quantities such as l_g are difficult to define, let alone measure, for internally balanced controls; fortunately the presentation is relatively insensitive to l_g . It is also difficult to determine gap width with adequate precision if it varies considerably throughout the gap passage as with the round nosed ailerons tested. For what they are worth the results are indicated in Figure 5.12 by the vertical lines showing the range of values obtained corresponding to $C_L = 0.1$ and 0.4 . The upper end of each vertical line corresponds to the round nosed ailerons, whilst the lower end corresponds to the internally balanced ailerons. It seems that for preliminary prediction purposes Figure 5.12 could be used to provide a rough guide to the values of ΔC_D (based on control span \times local wing chord) to be expected for the spanwise gaps associated with trailing edge controls at zero setting.

Hoerner also presents some results for longitudinal slots in the form of drag coefficient increments based on slot plan area (width \times length). For a slot alongside a moving trailing edge control he quotes an increment so based of 0.5, as compared with a slot alongside a leading edge control for which the increment is 1.5. Cook tested some trailing edge control longitudinal gaps and on the same basis his drag coefficient increment was about 0.3 and was practically independent of C_L up to $C_L = 0.6$.

Finally, we must note the observation of Hoerner that when the contour of a trailing edge control was slightly proud of the wing surface ahead some reduction of the spanwise gap drag occurred. This reduction was about 40% for each surface for a value of $\Delta h/t \approx 0.15$, where Δh = maximum height of the control contour above the local wing contour and t = thickness of the control. A negative value of Δh results in an even more dramatic increase of the drag increment. These results need further investigation before they can be generally accepted.

5.5 Prediction Methods for Distributed Roughness

We have already briefly described in Section 5.1 methods that have been adopted for dealing with the drag effects of isolated excrescences. For such cases we have seen that the excrescences can be regarded as equivalent to a local jump in the momentum thickness with possibly a change in the form parameter H and the calculation can then proceed as for a smooth surface. For distributed roughness, however, there are important changes in the boundary conditions at the surface and associated changes in the mean velocity distribution and turbulence characteristics near the surface due to the roughness that must be taken into account. How this is done depends on the particular smooth surface method that is being adapted to deal with the rough surface problem. For integral methods it is clear that the changes in the law of the wall region due to changes in the skin friction must carry most weight, whilst for differential methods the changes in local turbulence characteristics must also play a part depending on the form of method chosen.

An early integral method for incompressible flow was that of Van Driest (Reference 2.7). He argued that roughness would modify his suggested viscous damping factor $F = [1 - \exp(-y^+/A_0)]$ so that the factor would become unity for roughnesses large enough to destroy the viscous sub-layer and he inferred from Nikuradse's experiments as well as Laufer's measurements (Reference 5.20) that this condition corresponded to fully developed roughness flow ($k_s^+ \approx 60$). Accepting the value 26 for the constant A_0 he therefore postulated that for a rough surface

$$F = 1 - \exp(-y^+/26) + \exp(-60y^+/26k_s^+) \text{ for } 0 \leq k_s^+ \leq 60 \quad 5(6)$$

where k_s is the equivalent sand roughness height. He deduced from this and the momentum integral equation a law of the wall relation between u^+ , y^+ , and k_s^+ . For $k_s^+ > 60$ he argued on dimensional grounds and the available experimental data, as in Section 3.2, that

$$u^+ = \text{const.} + \frac{1}{K} \ln(y/k_s).$$

We remind the reader that $u^+ = u/u_\tau$, $y^+ = yu_\tau/\nu$, $k^+ = ku_\tau/\nu$, etc.

He deduced for pipe flow with the walls smooth that

$$1/(c_{fm})^{1/2} = -0.39 + 4.08 \log_{10}(R_m c_{fm}^{1/2}),$$

whereas Prandtl's formula (Reference 5.21) based on Nikuradse's experiments is

$$1/(c_{fm})^{1/2} = -0.4 + 4 \log_{10} (R_m c_{fm}^{1/2}).$$

With the walls rough enough for fully developed rough flow he similarly deduced that

$$1/(c_{fm})^{1/2} = 3.64 + 4.08 \log_{10} (a^+ / k_s^+). \quad (57)$$

We can compare this to the best fit to the available data

$$1/(c_{fm})^{1/2} = 3.48 + 4 \log_{10} (a^+ / k_s^+). \quad (58)$$

Here C_{fm} is the skin friction coefficient based on the mean velocity and R_m is the Reynolds number based on the mean velocity and the pipe diameter (2a).

Similarly he was able to determine, using 5(6), the local skin friction coefficient as a function of R_m and k_s for the intermediate regime (i.e. $k_s^+ \leq 60$), but the results do not lend themselves to any simple analytic formulation. It will be noted that he did not consider any form of roughness other than Nikuradse's sand roughness.

Subsequently Dvorak (Reference 5.22) directed his attention to the problem of a surface with any general form of distributed roughness large enough for fully developed roughness flow in a non-uniform pressure distribution. We have from equation 3(18)

$$(2/c_{fe})^{1/2} = A \ln (\delta^* u_e / \nu) + B + 2A \Pi - \Delta u / u_\tau + A \ln (\delta u_\tau / \delta^* u_e).$$

But from equation 3(19) we can deduce that

$$\delta u_\tau / \delta^* u_e = 1/A (1 + \Pi) = \text{function of the Clauser parameter } G, \text{ only,}$$

and so we can write

$$(2/c_{fe})^{1/2} = A \ln (\delta^* u_e / \nu) + C - \Delta u^+, \quad (59)$$

where $C = B + 2A + A \ln (\delta u_\tau / \delta^* u_e)$ and is also a function of G only, and $\Delta u^+ = \Delta u / u_\tau$.

For zero pressure gradient $G = 6.7$ and $C = 4.8$.

Also we have equation 3(15) for fully developed roughness flow

$$\Delta u^+ = A \ln k^+ + D$$

where D is a function of the roughness geometry and spacing (≈ -2.73 for Nikuradse's sand roughness).

Dvorak chose to deal with the effect of pressure gradient by treating C as the sum of its zero pressure gradient value C_0 , say, plus a term $\Delta u_2^+ = \Delta u_2 / u_\tau$ representing the effect of the pressure gradient (and hence a function of G) on the right hand side of equation 5(9). Thus, he wrote

$$(2/c_{fe})^{1/2} = A \ln (\delta^* u_\tau / \nu) + C_0 + \Delta u_2^+ - \Delta u^+ \quad 5(10)$$

and he deduced from experimental data that

$$\begin{aligned} \Delta u_2^+ &= 1.253 (G - 6.7) \text{ for } G > 6.7 \text{ (adverse pressure gradient)} \\ &= 0.404 (G - 6.7) \text{ for } G < 6.7 \text{ (favorable pressure gradient)}. \end{aligned} \quad 5(11)$$

He adopted Head's entrainment relation (Reference 2.13), which he assumed was unchanged by surface roughness since the latter has no effect on the outer region of the boundary layer which controls the entrainment rate. This relation combined with equations 5(10) and 3(15) enabled him to solve the momentum integral equation for any given sand roughness in any prescribed pressure distribution. To determine the equivalent sand roughness for a given roughness of a different kind he used a correlation based on Betterman's data (Reference 3.7) for Δu^+ as a function of λ (= total surface area/roughness area) a correlation that was later improved upon by Grabow and White (Reference 3.16) as reproduced in Figure 3.10. Dvorak compared the predictions of his method with available experimental data and on the whole found satisfactory agreement.

More recently Blanchard (Reference 3.8) has developed a number of different methods, both integral and differential, and compared their predictions with experimental data and assessed their relative merits.

His integral method is an extension of a method developed by Houdeville and Cousteix (Reference 5.23) for smooth surfaces and is similar to that of Dvorak insofar as it involves equation 5(9), the momentum integral equation and the Head entrainment equation. However, he has used a system of similar solutions providing a uni-parametric set of velocity profiles with the Clauser parameter G as the characteristic parameter, and hence he has determined C , δ^* , and θ as functions of G . He has also made use of the Grabow-White correlation (Figure 3.10) to determine the equivalent sand roughness for any given roughness. However, since the concept of an equivalent sand roughness applies strictly to the fully developed roughness regime but not to the intermediate regime, Blanchard developed an empirical set of relations for the latter as follows:-

$$\begin{aligned} \text{For sand roughness } \Delta u_s^+ &= 0, (k^+ \leq 5.32,) \\ &= 22 (k^+)^{0.1} - 26, (5.32 < k^+ \leq 69,) \\ &= \frac{1}{0.41} \ln k^+ - 2.73, (69 < k^+) \end{aligned}$$

For the given roughness for which the equivalent sand roughness height = k/α , calculate Δu_s^+ for $k_s^+ = k^+$,

$$\text{then } \Delta u^+ = \Delta u_s^+ - (a/0.41) \ln \alpha$$

$$\text{where } a = 1 - \exp [-(\Delta u_s^+ / 3.5)^2] .$$

This brief description of Blanchard's integral method applies strictly to incompressible flow. For compressible flow he made use of a series of transformations which formally reduce the basic three equations to forms similar to their incompressible form. In addition the energy equation is introduced and so the heat transfer at the surface is determined along with the other boundary layer quantities given the appropriate initial conditions.

The differential methods considered by Blanchard can be briefly summarized as follows:-

a) The use of the mixing length concept for closure of the momentum and energy equations. Here a method previously developed for smooth surfaces by Quemard and Archambaud (Reference 2.29) was adapted to deal with rough surfaces by assuming a non-zero mixing length at the surface empirically related to the roughness.

b) The use of the transport equations for the kinetic energy of the turbulence (k_t) and the turbulence dissipation (ϵ) with associated closure assumptions (see Section 2.1.4) in addition to the mean momentum and energy equations. This is essentially the method developed by Jones and Launder (Reference 2.20) for smooth surfaces but with assumed non-zero values of k_t and ϵ at the surface related empirically to the roughness. A modification of this method (the so-called 'mixed method') employs the concept of the mixing length in a thin layer adjacent to the surface. The outer boundary of this layer is assumed to be where the Van Driest damping factor $F = 0.99$ and the starting values for k_t and ϵ for the rest of the boundary layer are determined there.

c) There is an assumption involved in a) and b) above of a fictional surface with non-zero turbulence characteristics. Blanchard examined an alternative approach and introduced into the momentum equation a drag term calculated directly from a suitably simplified form of the geometry of the roughnesses coupled with empirical data. This concept was used by Finson (Reference 5.24) who also added associated terms in the k_t and ϵ transport equations but found their effect negligible compared with the direct drag contribution.

All the above methods were extended by Blanchard to deal with transpiration at the surface by the use of the velocity transformation first introduced by Stevenson (Reference 5.25) which leaves the basic relations unchanged in form.

For the mixing length method a) the mixing length l near the surface was taken to be of the form

$$l = (y/A) + l_0 \exp(-\gamma/AC l_0)$$

so that at the surface ($y = 0$) $l = l_0$. The constant C was chosen to yield agreement with Nikuradse's experiments and was determined thus as 1.5. Van Driest's damping function was retained in the form

$$F = 1 - \exp(-l^+ / 10.66),$$

$$\text{with } \tau = \tau_1 + \tau_2 = \mu \partial u / \partial y + \rho F^2 l^2 (\partial u / \partial y)^2, \text{ and } l^+ = l u_\tau / \nu,$$

so that at the surface

$$F_o = 1 - \exp(-t_o^+ / 10.66).$$

Blanchard found that the corresponding ratio at the surface of the turbulent to viscous stress $(\tau_t / \tau_v)_o$ can be related to the equivalent sand roughness height for fully developed roughness flow by

$$(\tau_t / \tau_v)_o = 0.024 k_s^+ + 0.25$$

and it is related to l_o^+ by

$$F_o t_o^+ = (\tau_t / \tau_v)_o^{1/2} \cdot [1 + (\tau_t / \tau_v)_o]^{1/2} \approx (\tau_t / \tau_v)_o + 0.5.$$

For the intermediate regime ($k_s^+ < 90$) he suggested an empirical relation

$$F_o t_o^+ = D(\alpha) [(k/t_o) - 4], \text{ with } D(\alpha) \text{ given by}$$

$$\log_{10} D = 1.89 \alpha^{-1/3} - 2.43.$$

Corresponding to equation 2(23) for the variation of the mixing length over the boundary layer thickness he adopted the relation

$$t/\delta = 0.085 \tanh\left(\frac{K}{0.085} \frac{y}{\delta}\right) + \frac{t_o}{\delta} \exp\left[\frac{-K}{1.5(t_o/\delta)} \frac{y}{\delta}\right].$$

For the transport equations method b) a scale length (L) and scale velocity (U) are introduced such that $L = Ck_t^{3/2}/\epsilon$, $U = k_t^{1/2}/C$, where $C = (2a_1)^{3/2}$ and $a_1 \approx 0.15$ (as for a smooth surface). Then the boundary values k_{to} and ϵ_o at the fictional surface are derived from

$$k_{to}^+ = k_{to}/u_\tau^2 = (CU_o^+)^2, \quad \epsilon_o^+ = \epsilon_v/u_\tau^4 = C^4 (U_o^+)^3/L_o^+,$$

where U_o^+ and L_o^+ are empirically related to $k_s^+ = k_s u_\tau / \nu$ by

$$U_o^+ = U_o/u_\tau = 11 [1 - \exp(-L_o^+/3.3)] \quad \text{and} \quad L_o^+ = L_o u_\tau / \nu = 0.35 (k_s^+)^{1/2}.$$

Blanchard first compared the predictions of the differential methods a) and b) above with the results of his own experiments in incompressible flow involving abrasive paper ($k = 0.6\text{mm}$) in zero pressure gradient. Some of his comparisons are shown in Figure 5.13 and 5.14 and it will be seen that there is little difference between the predictions of the methods but the mixing length method shows closest agreement with the experimental results and is the simplest of the differential methods. The same conclusion emerged from comparisons with the results of tests on a porous surface with transpiration. The predictions of method c) proved somewhat less satisfactory than those of the other methods particularly with regard to the skin friction at the surface.

The integral method can be used for predicting integral quantities only but its predictions proved to be as reliable as those of the mixing length method, as is evident in Figure 5.15. Further comparisons including the case of a moderate adverse pressure gradient confirmed the general reliability of the mixing length method (see Figure 5.16). The predictions of the compressible flow form of the method were compared with the results of F.L. Young's experiments at a Mach number of about 5 and various conditions of heat transfer for smooth and rough surfaces in zero pressure gradient, Reference 5.26. Here the roughnesses took the form of regular transverse ridges of triangular section and a range of roughness height were tested. Some of the comparisons are shown in Figure 5.17 and 5.18 for the displacement and momentum thicknesses, the 'incompressible' form factor H_1 , the skin friction coefficient and Reynolds analogy factor as functions of the ratio of wall temperature to ambient temperature. Although the agreement between predictions and experiment is far from perfect it is fairly satisfactory bearing in mind the experimental difficulties as well as the usual level of agreement found for smooth surfaces for such Mach numbers between existing theories and experiment. However, the integral method gave predictions that were not significantly worse (see Figure 5.19).

It seems reasonable to conclude from these comparisons that of the differential methods considered the relative simplicity and general reliability of the mixing length method makes it the most readily commendable for predicting the effects of distributed roughness on boundary layer characteristics. The even greater simplicity and comparable reliability of the integral method makes it the preferred one for the many engineering applications where only integral quantities are needed.

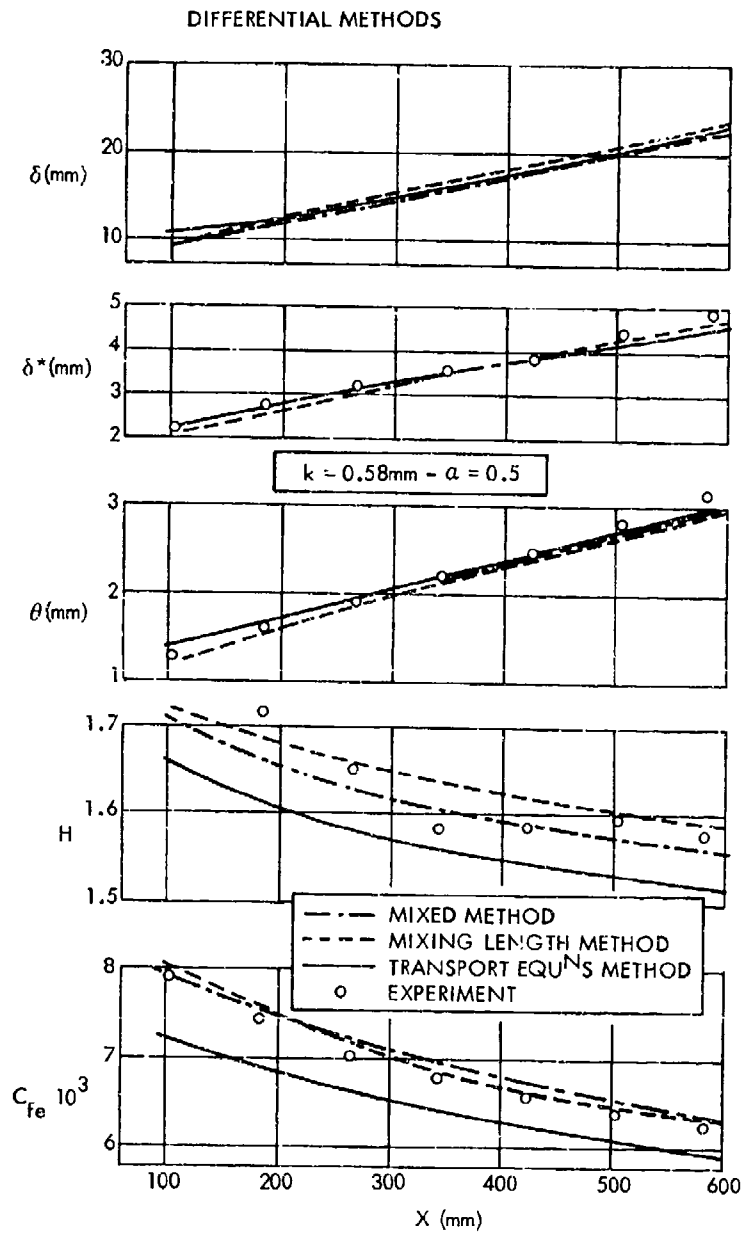


Figure 5.13 Comparisons of Predictions and Experimental Results for a Rough Surface in Zero Pressure Gradient (Blanchard)

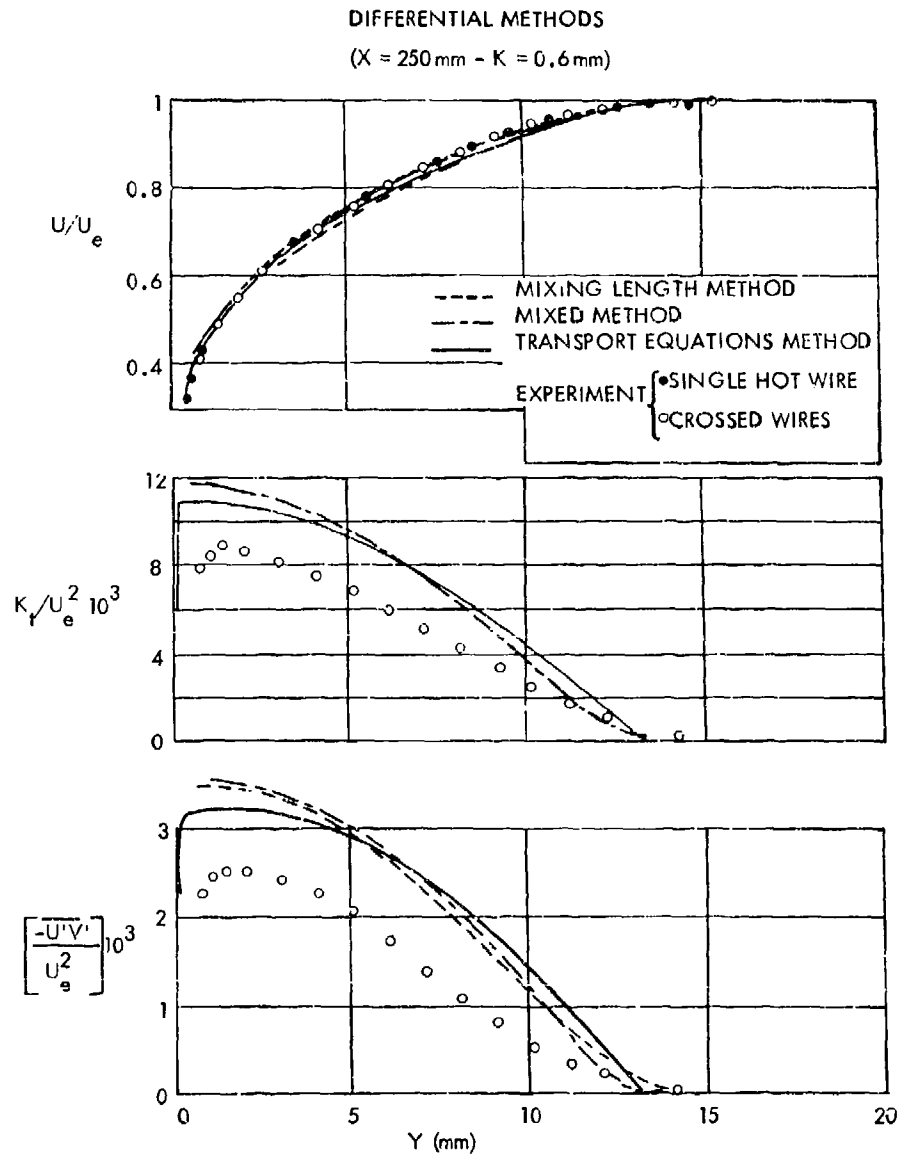


Figure 5.14 Comparisons of Predictions and Experimental Results for a Rough Surface in Zero Pressure Gradient (Blanchard)

$k = 0 \text{ mm} \text{ \& } 0.58 \text{ mm} \quad \alpha = 0.5$

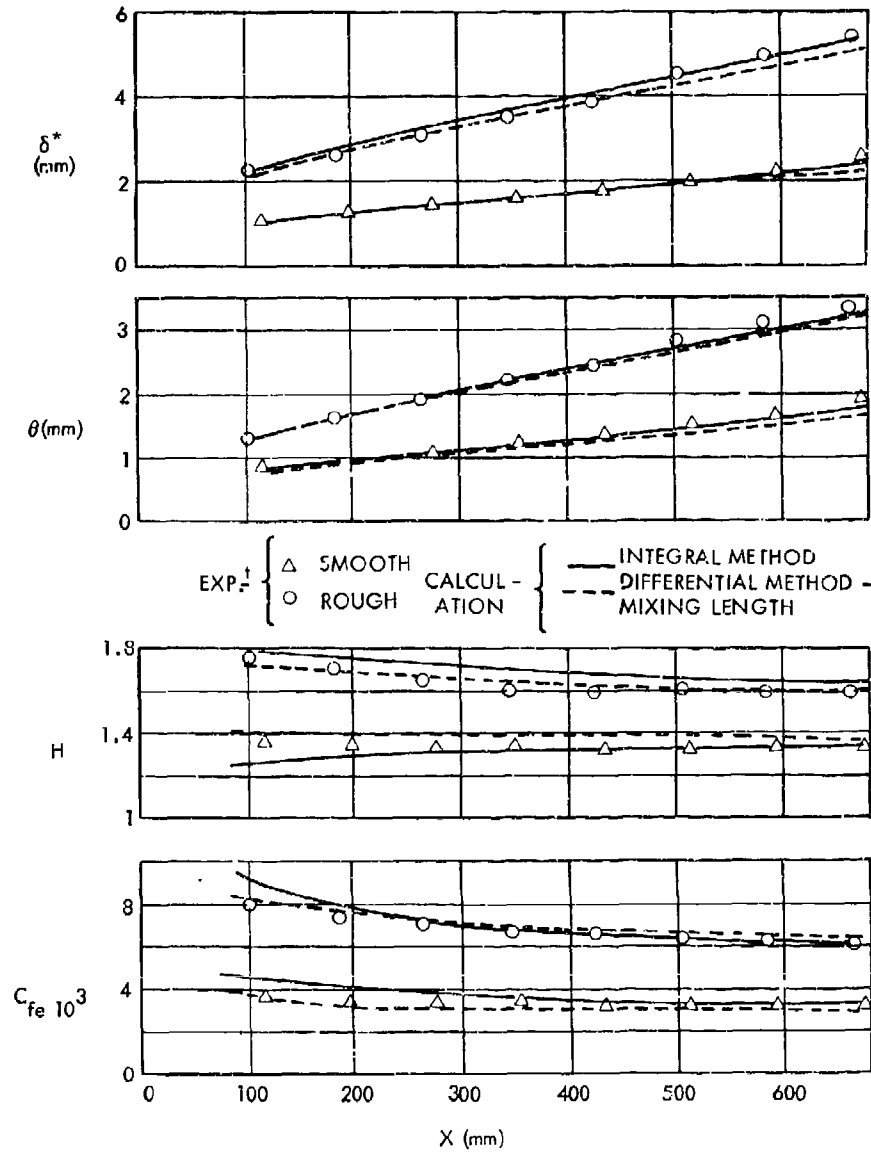


Figure 5.15 Comparison of Predictions of Integral and Mixing Length Methods with Experimental Results for Flat Plate in Zero Pressure Gradient (Blanchard)

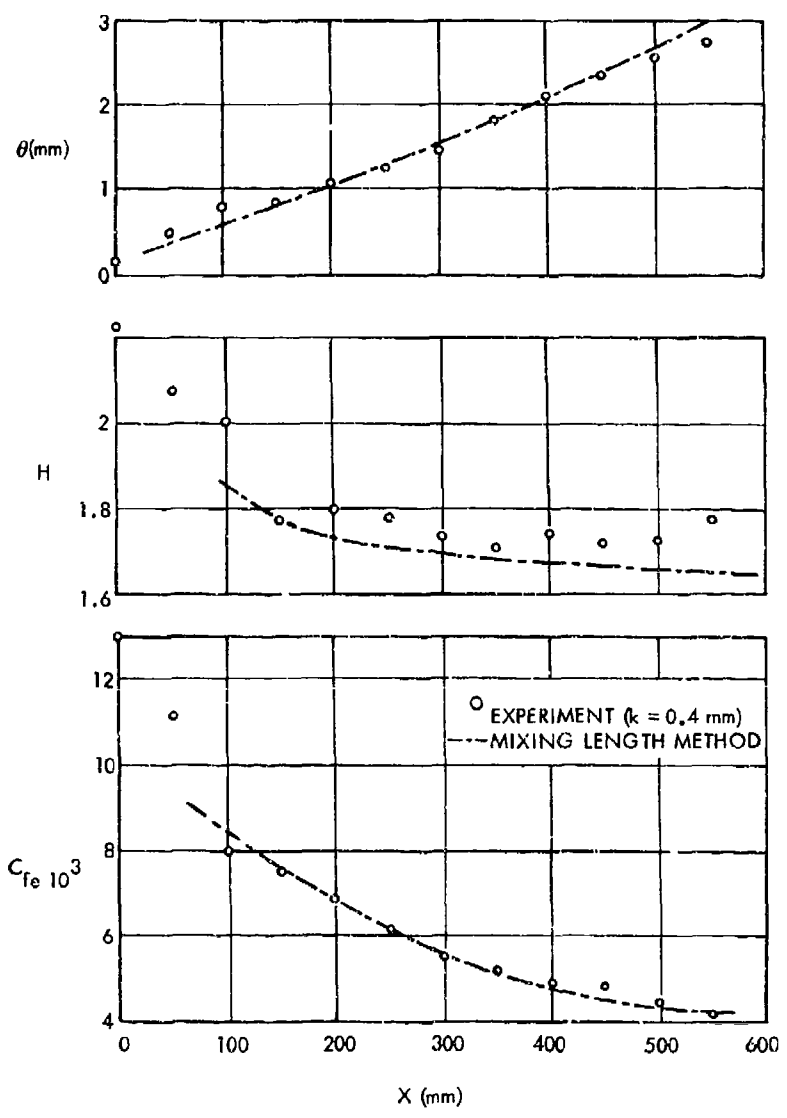


Figure 5.16 Comparison of Predictions of Mixing Length Method and Experimental Results for a Rough Surface ($k = 0.4$ mm) in a Moderate Adverse Pressure Gradient (Blanchard)

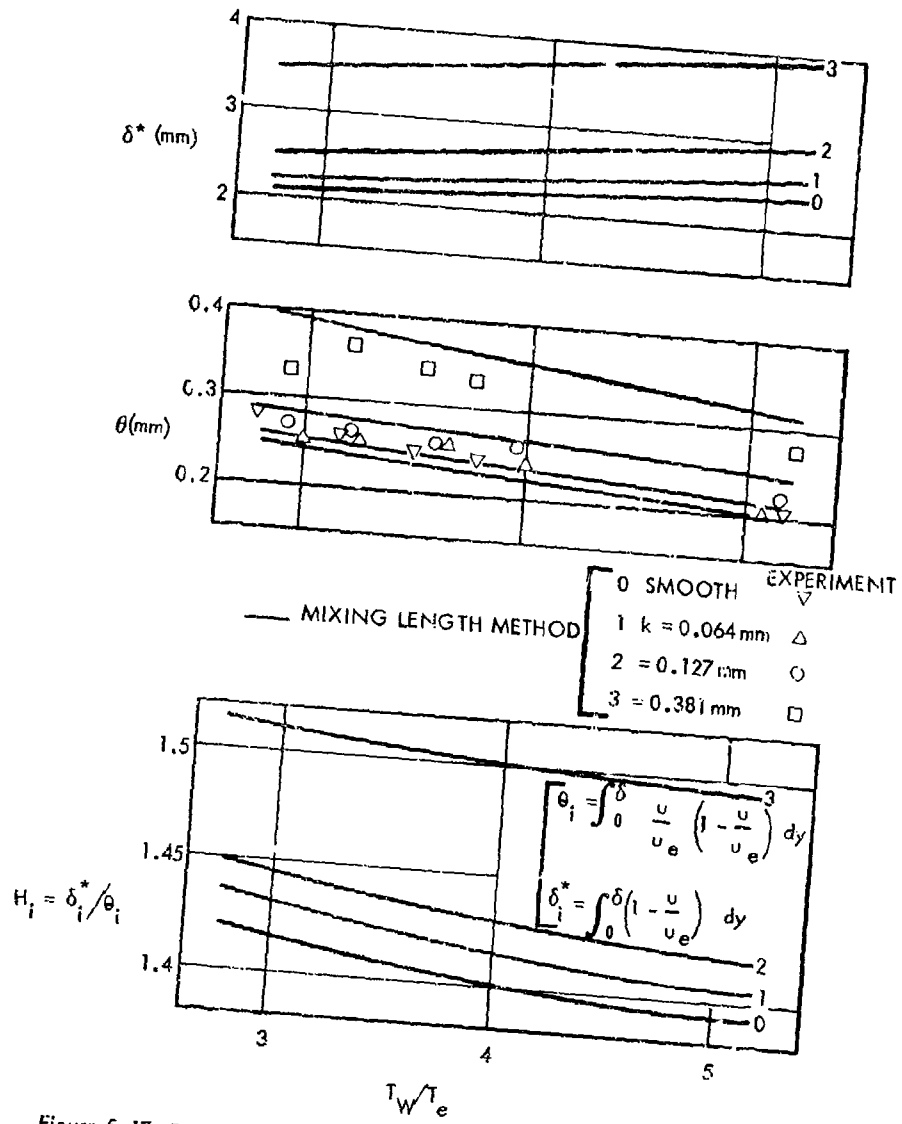


Figure 5.17 Comparisons of Predictions of Mixing Length Method with Experimental Results of F.L. Young for Compressible Flow with Heat Transfer (Zero Pressure Gradient, $M_e \approx 4.93$) (Blanchard)

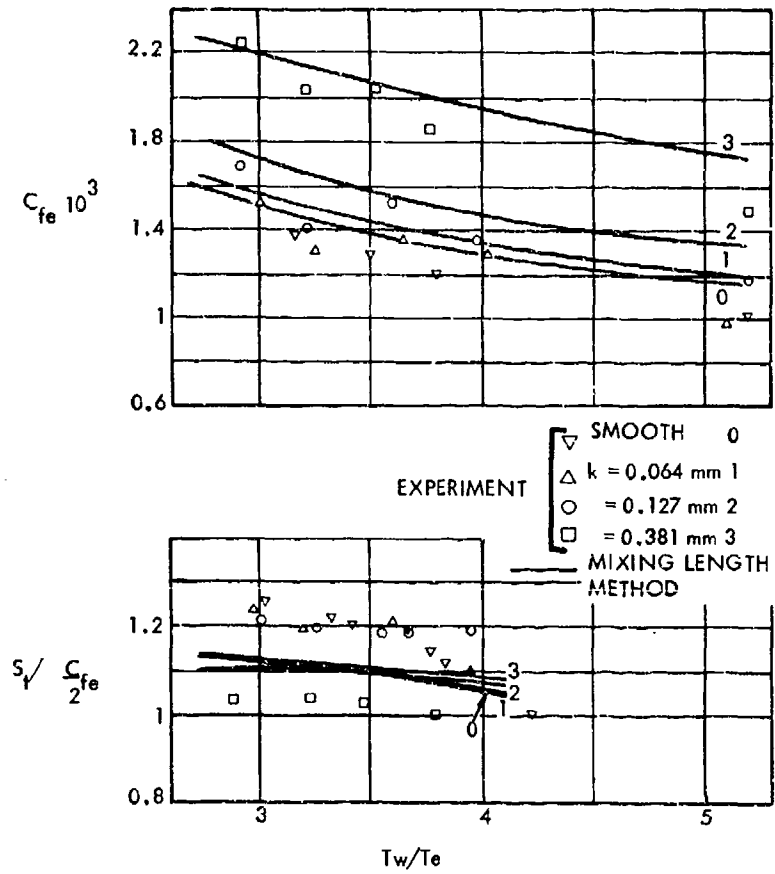


Figure 5.18 Comparisons of Predictions of Mixing Length Method with Experimental Results of F.L. Young for Compressible Flow with Heat Transfer (Zero Pressure Gradient, $M_0 = 4.93$) (Blanchard)

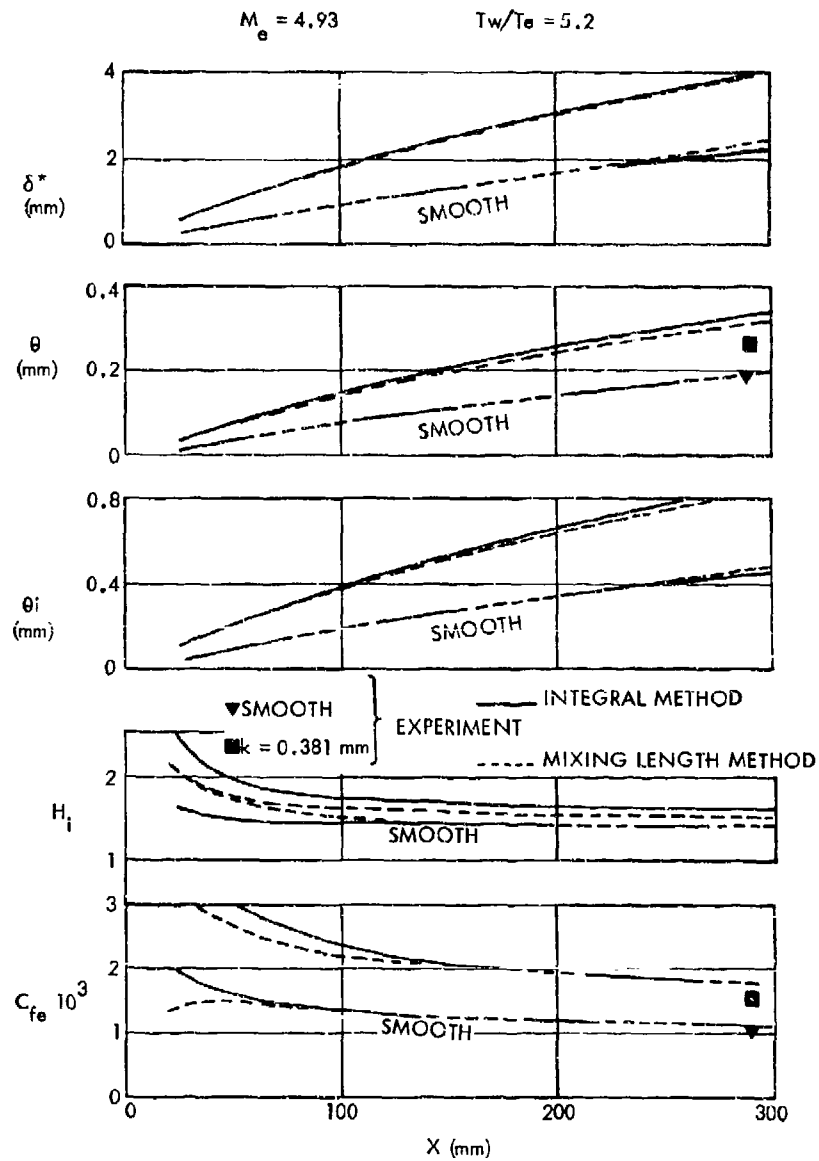


Figure 5.19 Comparisons of Predictions of Integral and Mixing Length Methods with Experimental Results of F.L. Young for Adiabatic Wall (Zero Pressure Gradient) (Blanchard)

References

- 5.1 Hoerner S.F. 1952 Fluid Dynamic Drag (2nd. Ed.) Published by the author.
- 5.2 Nash J. F. & Bradsnaw P 1967 The Magnification of Roughness Drag by Pressure Gradients. J.R.Ae.S, 71, 44-49.
- 5.3 Squire H.B. & Young A.D. 1937 The Calculation of the Profile Drag of Aerofoils ARC R&M No. 1838
- 5.4 Cook T.A. 1971 The Effects of Ridge Excrescences and Trailing Edge Control Gaps on Two-Dimensional Aerofoil Characteristics. ARC R & M No. 3698
- 5.5 Gaudet L. & Johnson P. 1970 Measurements of the Drag of Various Two-Dimensional Excrescences Immersed in Turbulent Boundary Layers at Mach Numbers between 0.2 and 1.8. RAE TR 70190
- 5.6 " 1971 - . Circular Holes. RAE TR 71181.
- 5.7 Gaudet L. & Winter K.G. 1973 Measurements of the Drag of Some Characteristic Aircraft Excrescences Immersed in Turbulent Boundary Layers. AG RD CP No. 124, Aerodynamic Drag, Paper 4.
- 5.8 Keates R.A. 1973 - Effects of Excrescences on Lift and Drag of Aircraft
1974 in High Lift Configurations Pt. 1. Bibliography. Rep. No. HSA-MAD-AERO/MISC/404.

Pt. II. Preliminary Analyses and Suggestions for Future Investigations. Rep. No. HSA-MAE-AERO/MISC/410.
- 5.9 Keates R.A. 1975 - Analytical Study of Excrescence Drag Associated with
1976 Wings in the High Lift Configuration.
Pt. 1 Interim Report. Rep. No. HSA-MAE-R-GEN-0456.
Pt. 2 Final Report. Rep. No. HSA-MAE-R-Gen-0504.
- 5.10 Irwin H.P.A.H. 1972 A Calculation Method for Two-Dimensional Flow over a Slotted Flap. ARC CP No. 1267
- 5.11 Foster D.N. 1970 The Two-Dimensional Flow Around a Slotted Flap.
Irwin H.P.A.H. & Williams B.R. ARC R&M No. 3681
- 5.12 Foster D.N., 1973 The Nature, Development and Effect of the Viscous
Ashill P.R. & Williams B.R. Flow Around an Aerofoil with High Lift Devices.
RAE TR 72227.
- 5.13 Rabbo M.F.A. 1976 Aerodynamic Drag of Ridge Arrays in Adverse Gradients. Univ. of Leicester Ph.D Thesis.

- 5.14 Good M.C. & Joubert P.N. 1968 The Form Drag of Two-Dimensional Bluff Bodies Immersed in Turbulent Boundary Layers. J.F.M., 31, Pt. 3, 547-582.
- 5.15 Jones R.C. & Williams D.H. 1936 The Effects of Surface Roughness on Characteristics of Aerofoils NACA 0012 and RAF 34 ARC R&M No. 1708
- 5.16 Ljungstrom B.L.G. 1972 Wing Tunnel Investigation of Simulated Hoar Frost on a Two-Dimensional Wing Section with and without High Lift Devices. FFA Rep. AU-902
- 5.17 Gregory N. & O'Reilly C.L. 1973 Low Speed Aerodynamic Characteristics of NACA 0012 Aerofoil Section Including the Effects of Upper Surface Roughness Simulating Hoar Frost. ARC R&M No. 3726
- 5.18 Weeks D.J. 1971 Tests on the Effects of Simulated Frost Deposits on Take-Off Performance of a Model of Transport Aircraft (Hawker-Siddeley Trident 3B). RAE TR 71178
- 5.19 Young A.D. 1950 The Drag Effects of Roughness at High Sub-Critical Speeds. J.R.Ae.S., 18, 534-
- 5.20 Laufer J. 1954 The Structure of Turbulence in Fully Developed Pipe Flow. NACA Rep. 1174
- 5.21 Prandtl L. 1935 The Mechanics of Viscous Fluids. Aerodynamic Theory (Ed. W.F. Durand), Vol. III, 144. See also ZVDI, 77, 105-114
- 5.22 Dvorak F.A. 1969 Calculation of Turbulent Boundary Layers on Rough Surfaces in Pressure Gradient. AIAA J, 7, No. 9.
- 5.23 Houdeville R. & Cousteix J. 1974 Couches Limites Turbulentes Bi-Dimensionnelles avec Flux de Chaleur. B. Methode Integrale de Calcul et Comparaisons a l'Experience. ONERA Note Technique No. 4/5005.
- 5.24 Finson M.L. 1975 A Reynolds Stress Model for Boundary Layer Transition with Application to Rough Surfaces. Phys. Sciences Inc., Wakefield, Mass., PSI, TR-34
- 5.25 Stevenson N. 1964 Boundary Layers with Suction or Injection. Ph.D Thesis, Queen Mary College, Univ. of London See also College of aeronautics Rep. 166 & 177 and AIAA J, 2, No. 8, 1500-1502.
- 5.26 Young F.L. 1965 Experimental Investigation of the Effects of Surface Roughness on Compressible Turbulent Boundary Layers, Skin Friction and Heat Transfer Defense Research Lab., Univ. of Texas.

6. DRAG OF AUXILIARY INLETS AND OUTLETS

6.1 Introduction

A significant source of drag for contemporary aircraft is the influx and efflux of air, intentional and unintentional, through orifices other than those used for the propulsion system. Auxiliary air systems are used for cooling people, equipment, and oil; and to provide air for combustion to auxiliary power units. Most of this auxiliary air flow is controlled, but a small percentage flows through leaks. For that portion which is controlled the designer has many options in configuring both external and internal geometry to minimize drag.

A flight line survey of 12 contemporary aircraft revealed that auxiliary inlet and outlet designs provide more opportunity for exercise of individual "design license" than perhaps any other part of the aircraft. A total of 22 inlets and 42 outlets were found on these aircraft - and no two configurations were exactly alike. Nevertheless, there are some general classifications into which these auxiliary inlet and outlets may be placed, and drag data are available to at least guide the designer if his geometry approximates some standard in these various classifications. Figures 6.1 and 6.2 illustrate the many auxiliary inlet and outlet designs observed and show the general classifications into which they will be grouped for discussion.

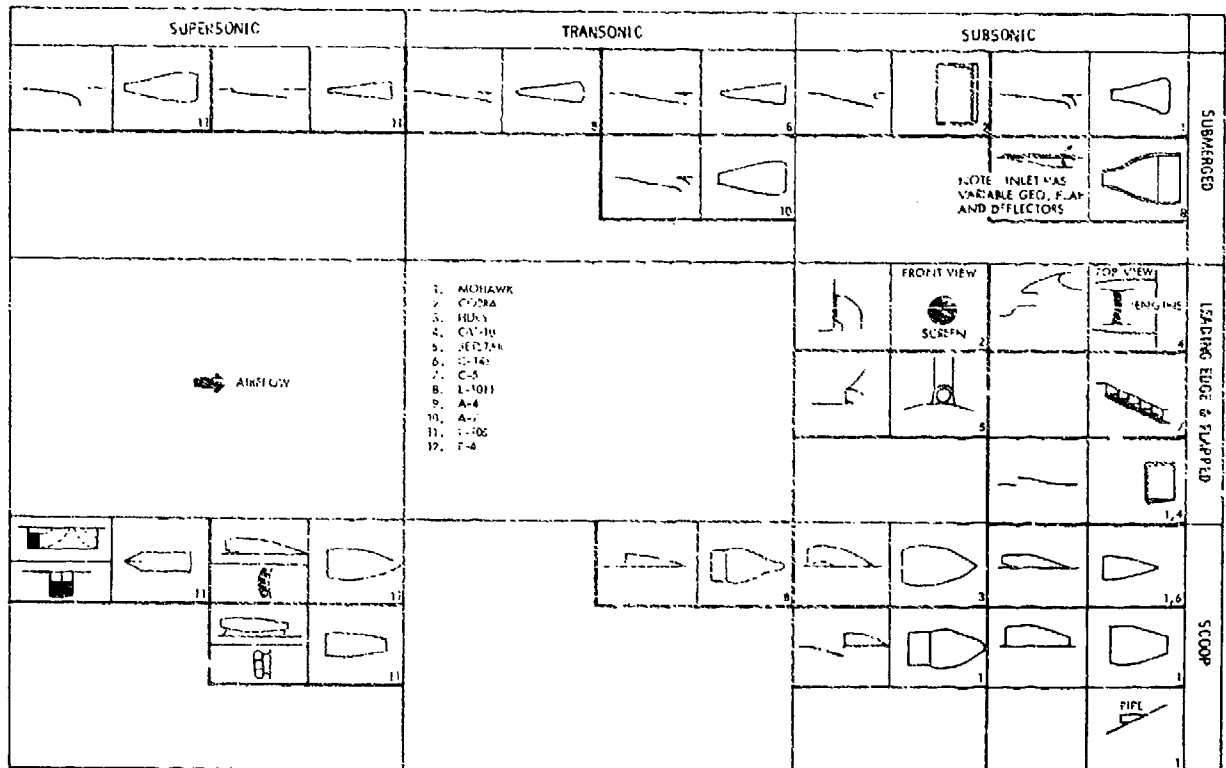


Figure 6.1 Auxiliary Inlets Observed in 12-Airplane Sample

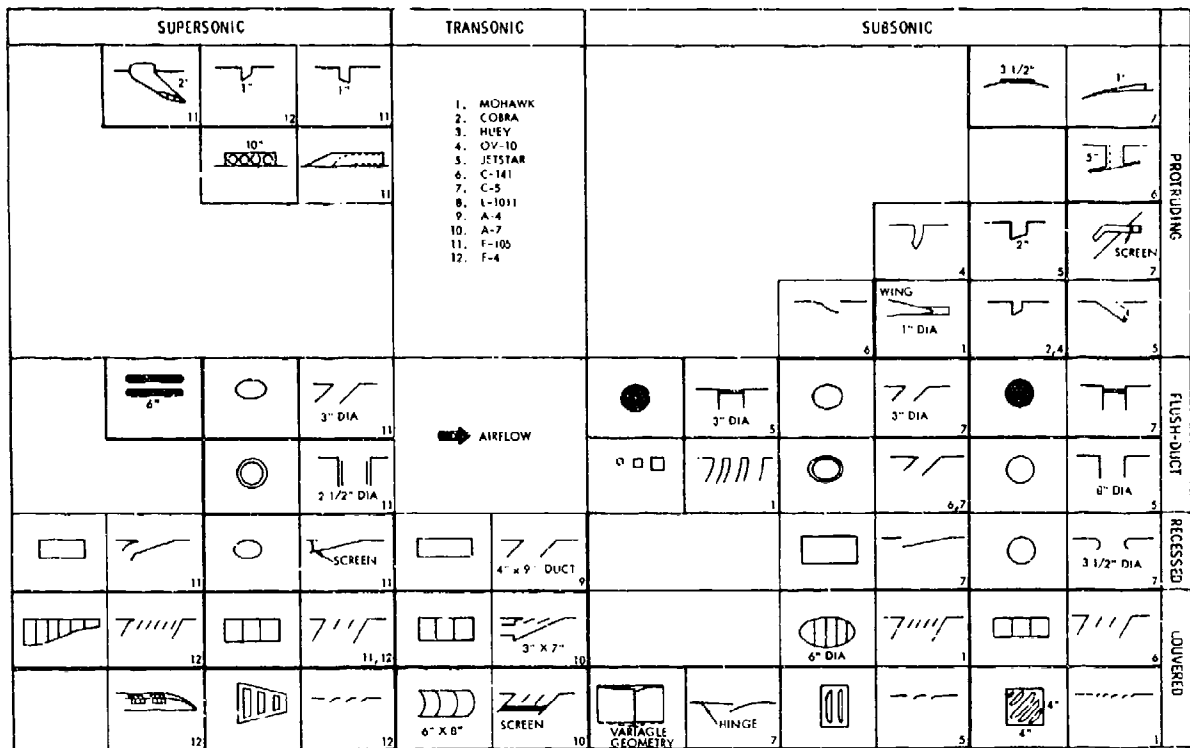


Figure 6.2 Auxiliary Outlets Observed in 12-Airplane Sample

In general, auxiliary air system flow requirements vary considerably over the aircraft's operating environment. One of the simplest examples is that of an air intake and exhaust system for cooling the cabin of a light aircraft. At low altitudes, low speeds, and in warm weather, the system is operated at maximum capacity; but a change in altitude, speed, or weather can completely eliminate the need for such a system and somehow it must be shut off. Therefore, most auxiliary airflow systems operate, in one way or another, with variable geometry. This variable geometry may be part of the inlet or outlet hardware, or it may result from a change in internal resistance. In any case, this variable feature of auxiliary air systems further complicates the generalization of drag data for such systems.

In this section, we shall deal primarily with external drag associated with

auxiliary inlets,

auxiliary outlets, and

uncontrolled leakage.

Internal flow momentum losses have been treated in a number of works and are not considered within the scope of this text. However, in designing auxiliary inlets and outlets for minimum drag, several points should be recognized. First, the total drag of an auxiliary air system is made up of two basic parts - external drag and internal drag. Every bit of momentum extracted from the air flowing past a vehicle results in drag whether that momentum is extracted by the air's flowing around a protuberance or from the air's doing work inside a cooling system. Taking aboard more air than is needed in cruise flight will probably increase vehicle drag even if the inlet drag, for instance, is negligible. The designer therefore needs to give careful consideration to the total auxiliary air system to minimize aircraft drag.

6.2 Auxiliary Inlets

Figure 6.1 shows the many types of auxiliary inlets observed on just a dozen contemporary aircraft. For the purpose of classification these inlets are divided into the following categories.

Submerged inlet - A submerged inlet is defined as one with special contours on the ramps, side walls, or lips but with none of these special contours protruding into the mainstream. An exception is the submerged inlet with boundary layer diverters which do extend above the aircraft surface.

Flush inlet - a flush inlet is generally a hole in the aircraft surface with little attempt made to guide flow into the hole other than corner rounding. These inlets on wing leading edges and other high pressure regions can be quite effective.

Protruding inlet - As the name implies, a protruding inlet extends from the aircraft surface into the mainstream and thus enjoys the advantage and/or disadvantage of exposure to full impact pressure.

Performance characteristics of these inlets are discussed in the following section. The net drag of an inlet depends on a combination of external and internal drag, so that inlet pressure recovery is an important aspect of drag. This is often taken into account through the use of C_{Dcorr} a drag coefficient which is obtained from:

Measured Drag minus available thrust of inducted air
divided by inlet area and local dynamic pressure

There are many reports providing data on auxiliary inlets. Unfortunately the investigations reported covered a wide range of configuration and test condition variables so that it is difficult to arrive at general conclusions concerning the "best" inlet type. Reference 6.1 is one of the better sources of comparison data since both drag and pressure recovery were measured for all three general classes (protruding, flush, and submerged) of inlets. All of the lip contours had sharp edges however, so they do not necessarily represent optimized configurations for subsonic flow. Therefore, some of the conclusions which may be drawn in comparing inlet types might be changed if different lip shapes were used.

Figure 6.3 shows data from Reference 6.1 comparing C_{Dcorr} for a parallel wall flush inlet, a curved diverging wall submerged inlet, and an aspect ratio 4 scoop inlet.

For this comparison the best inlet in each of the three categories was chosen. (This results in comparison of an aspect ratio of 1 for the flush inlets with aspect ratios of 4 for the submerged and scoop inlets.) In the mid-range of mass flow ratios there is not much difference in performance of the three inlets except at $M = 0.55$ where the scoop inlet had a higher drag than the other two. This resulted from the fact that while the scoop had higher external drag than the flush inlets it did not attain higher internal pressure recoveries.

It would be difficult from Figure 6.3 to say that any one of the inlet types shown is universally better than the others. Choice of inlet type must be based on specific application. More detail on the several inlet types is given in the following sections.

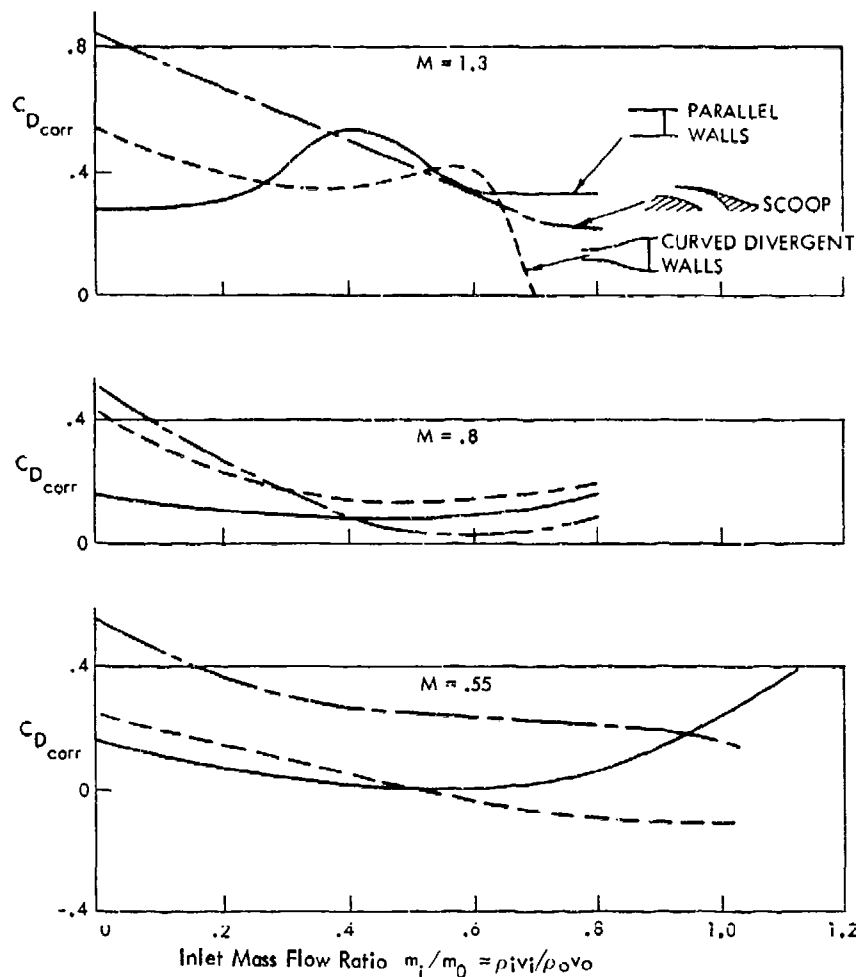


Figure 6.3 Comparison of $C_{D_{corr}}$ for Three Inlet Types at Subsonic and Transonic Speeds (Reference 6.1)

6.2.1 Protruding Inlets

Protruding or scoop inlets are widely used on contemporary aircraft. Figure 6.1 shows that more scoop inlets were found in the 12-aircraft sample than any other type. Scoop inlets are characterized by high pressure recovery and sometimes by high drag. Drag can be minimized however by:

- o contouring the forebody to conform to good nacelle design practice,
- o using rounded inlet lips (for subsonic speeds), and
- o fairing the downstream side of the scoop with a good afterbody shape

Figure 6.4 shows zero-flow drag, C_{D_0} , based on inlet area and free-stream dynamic pressure, for two scoop geometries over a range of Mach numbers. The two-dimensional aspect ratio 4 scoop has less than 1/2 the drag of a circular scoop.

Contouring the forebody was shown in Reference 6.2 to reduce zero flow drag for a semi-circular scoop by 50 percent at subsonic speeds. Details are shown in Figure 6.5.

With inlet lip contouring and afterbody fairing it is estimated that zero flow drag could be further reduced to C_{D_0} values ranging from 0.1 to 0.2.

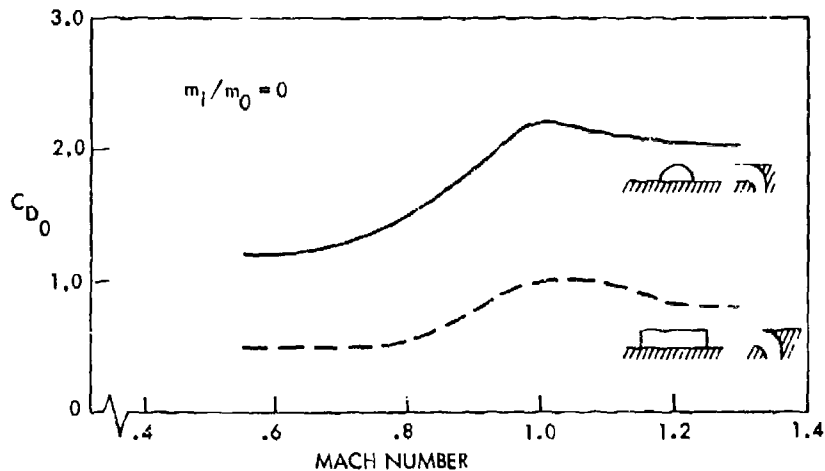


Figure 6.4 Drag of Protruding Inlets (Reference 6.1)

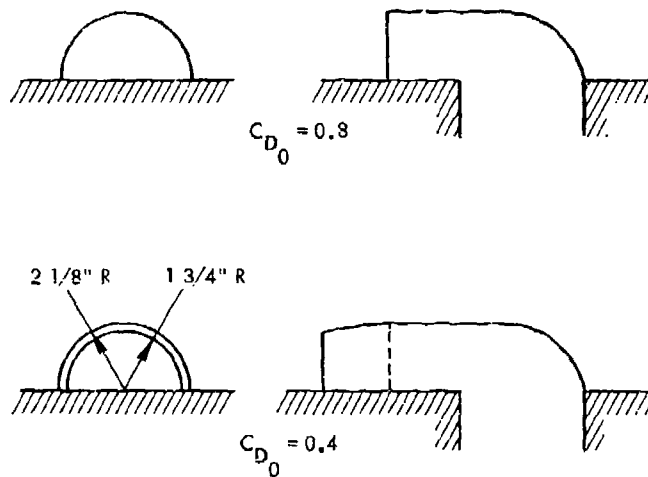


Figure 6.5 Effects on Drag of Contouring a Scoop Forebody (Reference 6.2)

In areas where the aircraft boundary layer is thick, inlet flow and pressure recovery may be significantly impaired unless steps are taken to move the inlet out of the boundary layer. Usually this is done for scoops by mounting the inlet on what amounts to a short pylon. This mounting however results in a significant drag increase, at the least proportional to the frontal area increase of the installation.

To this point all of the data and comments presented have concerned inlet drag for the zero-flow condition. Increasing inlet flow ratio reduces external drag significantly. This can be seen by the curves of Figure 6.6 where $C_{D_{corr}}$ is plotted as a function of mass flow ratio. $C_{D_{corr}}$ is determined from the net drag less the momentum of the internal flow captured by the inlet. The actual drag experienced will of course depend on what happens to the internal flow - how efficiently it is diffused so that dynamic pressure is converted to static pressure. Nevertheless $C_{D_{corr}}$ is a good overall measure of inlet performance since it considers both external drag and pressure losses to the inlet measuring station.

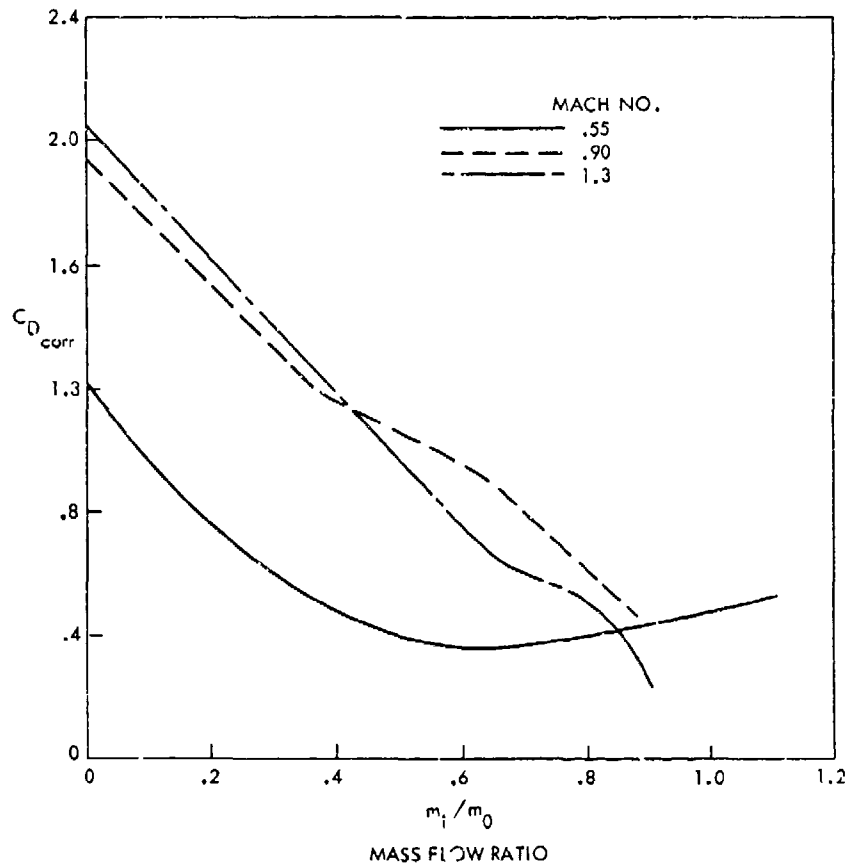


Figure 6.6 Effects of Inlet Flow Ratio on Drag of Circular Scoop, $\theta = 45^\circ$, $x/d = 6.8$ (Reference 6.1)

6.2.2 Submerged Inlets

Submerged inlets can be subdivided, according to wall shape, into the categories - parallel walls, diverging walls, and curved diverging walls. In addition, various boundary layer control devices - bypasses and diverters - are sometimes used. Dynamic pressure recovery, which is a significant internal drag consideration, is shown for these three types of submerged inlets in Figure 6.7. The advantage of diverging the walls can be easily seen in Figure 6.7 and the advantage of adding curvature to the divergence is also obvious. The divergence tends to part the boundary layer and turn more of the higher momentum freestream air into the inlet than can be done with parallel walls.

Net inlet drag will be a combination of internal and external drag but sometimes it is helpful to separate these elements. A measure of external drag is the zero flow drag as shown in Figure 6.8. This figure shows external drag to be lower for parallel walls than for diverging walls - a fact which tends to offset the pressure recovery advantage of the curved diverging wall inlet. Figure 6.8 also shows however that approach ramp angle has a greater impact on zero flow drag than wall contour. The 7° approach ramp causes the freestream flow to turn into the inlet with the result that drag is increased.

A comparison of curved diverging wall and parallel wall submerged inlets in the form of $C_{D,corr}$ is shown in Figure 6.9. At $M = 0.55$ and $M = 1.3$ the curved diverging wall inlet is generally better than the parallel wall inlet, but there may be an advantage for the parallel wall inlet in the transonic ($M = .9$) range.

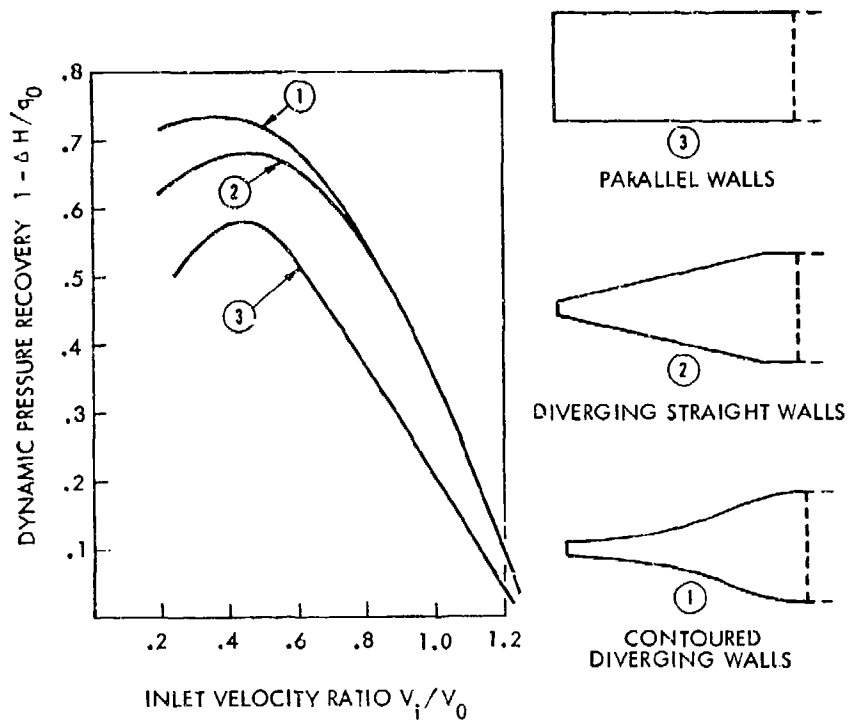


Figure 6.7 Comparison of Pressure Recovery for Three Submerged Inlets (Reference 6.7)

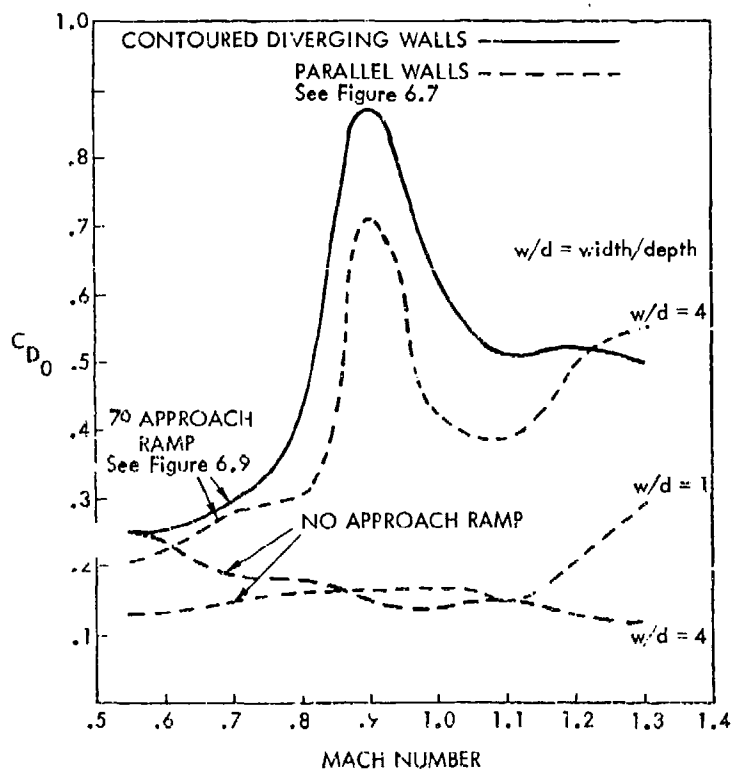


Figure 6.8 Zero-flow Drag for Three Submerged Inlets (Reference 6.1)

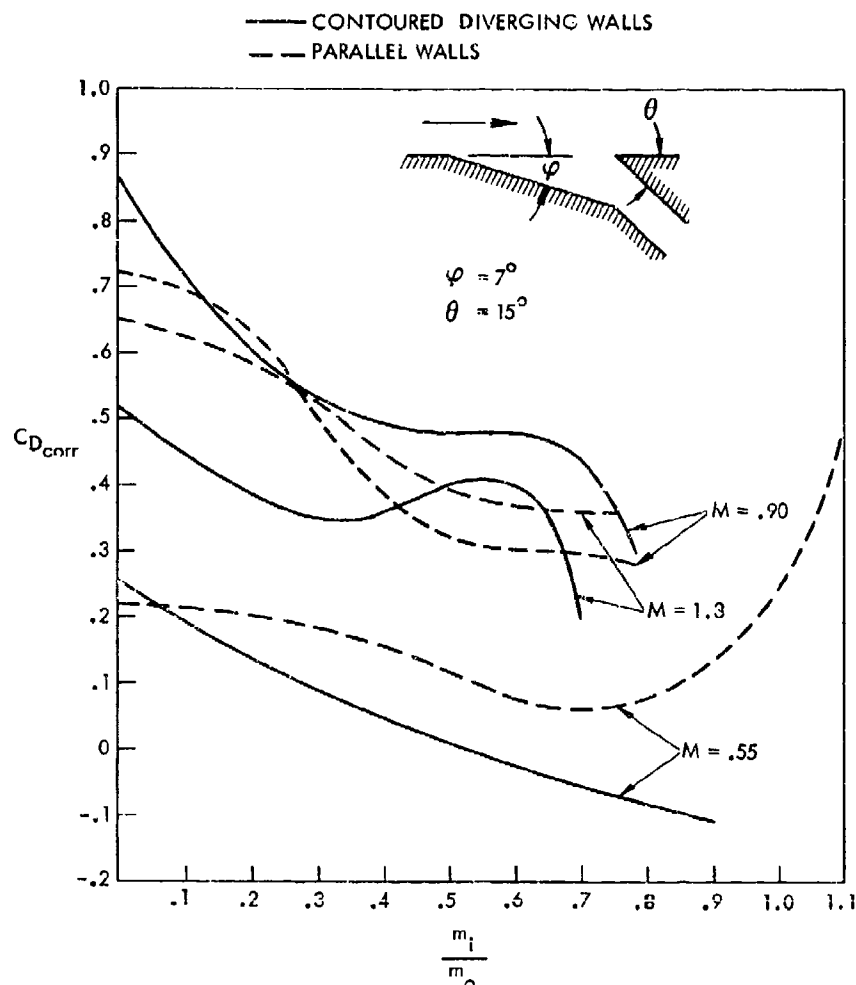


Figure 6.9 Effect of Submerged Inlet Wall Shape on Drag (Reference 6.1)

Inlet inclination angle has a large effect on submerged inlet drag. This is shown for parallel wall inlets of aspect ratio 4 in Figure 6.10. Most of the large effect shown can probably be attributed to the boundary layer's inability to negotiate turns greater than about 15° . Thus the inlet pressure recovery falls off drastically as the inclination angle, θ , is increased. By the same token, boundary layer separation at zero inlet flow causes $C_{D_{corr}}$ to be quite low at values of θ greater than 45° , since the freestream flow feels little inclination to turn into the inlet cavity. An auxiliary air system with large flow demand under static conditions and zero or small demand at cruise might well use a submerged or flush inlet with large inclination angle. Inlet ramp angle is an important parameter and from experimental data should not exceed 10° as indicated by Reference 6.13.

Whenever the boundary layer thickness dimension is significant relative to inlet height or depth, the effect of boundary layer on inlet drag and performance should be considered. For a protruding inlet the impact on external drag will generally be through a reduction in the effective dynamic pressure used to compute drag, and the impact on internal drag will be through a reduction in total pressure recovery because the boundary layer entering the inlet has less momentum than freestream air. For a submerged inlet a thick approaching boundary layer may separate from the inlet ramp at angles which a thinner boundary layer might easily tolerate - thus compounding the boundary layer effect.

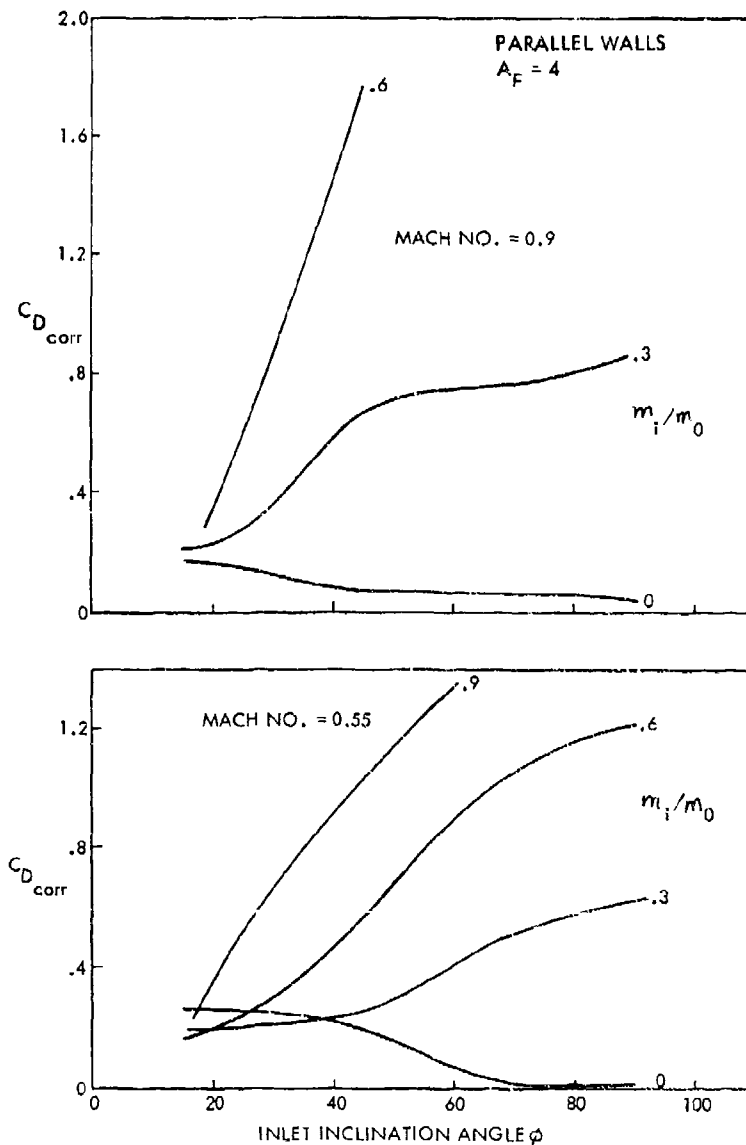


Figure 6.10 Effect of Inlet Inclination Angle on Drag (Reference 6.1)

For situations where boundary layer separation is not a factor, charts of boundary layer mass and momentum are available (Reference 6.3 for instance) to expedite prediction of boundary layer effects.

Experimental data on boundary layer effects on submerged inlet performance are limited. Some are shown however in Figure 6.11 where the effect of boundary layer thickness on pressure recovery has been plotted for a submerged inlet with curved diverging walls. At high inlet velocity ratios, the already low pressure recovery is severely impaired by a doubling of boundary layer thickness while at $V_i/V_0 = 0.4$ doubling the boundary layer thickness reduces pressure recovery about 15 percent.

Boundary layer deflectors which extend above the surface along the edges of the submerged inlet walls can reduce pressure losses due to boundary layer. This is shown by the broken line curve in Figure 6.11 which shows, at $V_i/V_0 = 0.4$, an increase in pressure recovery of 10-15 percent through the use of deflectors. Although drag was not measured in the investigation from which these data were obtained, it should be expected that the increase in pressure recovery will be accompanied by an increase in external drag, so the net gain or loss in $C_{D_{corr}}$ is not known.

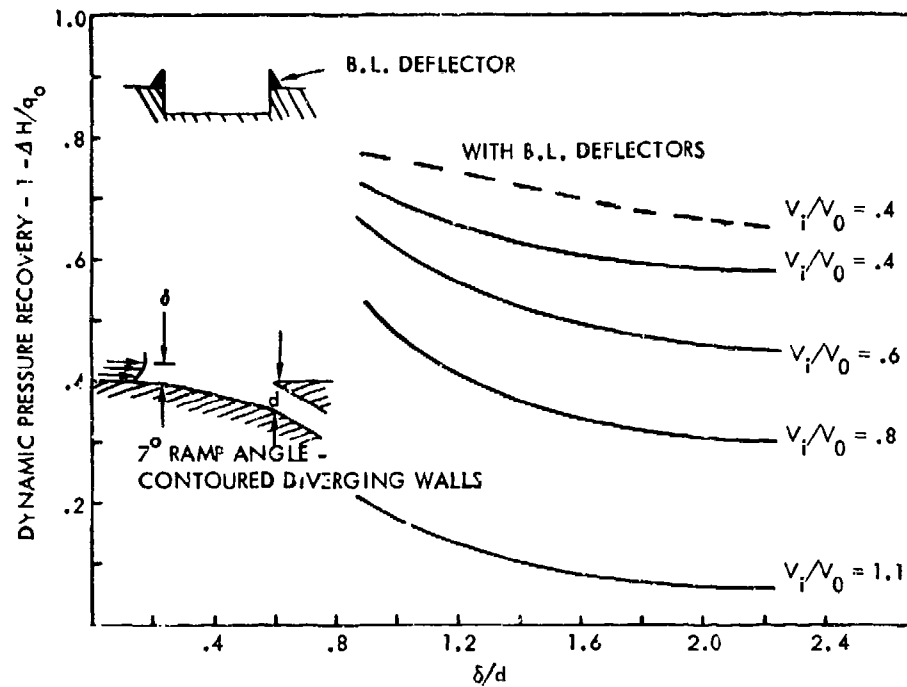


Figure 6.11 Effect of Boundary Layer Thickness on Submerged Inlet Pressure Recovery (Reference 6.7)

6.2.3 Flush Inlets

Flush inlets, if used for in-flight air induction must be located in regions of high static pressure since these inlets employ no ramps or other special air turning devices. They are sometimes used however to supply air to systems which operate only on the ground. In this case the concern from a drag standpoint is that the inlet hole be closed in flight, or that flow be completely stopped and the inlet opening be of such size and shape that drag is negligible.

Reference 6.4 shows that in the subsonic and transonic range the no-flow drag coefficient for sharp-edged 90° flush openings of aspect ratio 4 is about $C_D = 0.03$. Figure 6.12 from Reference 6.5 shows the effect of aspect ratio, w/d , on flush opening drag at $M = 3.25$. The drag coefficients vary from .015 to .03 in the range of moderate aspect ratios. Here C_D is the drag increase due to the inlet divided by free stream dynamic pressure and inlet area.

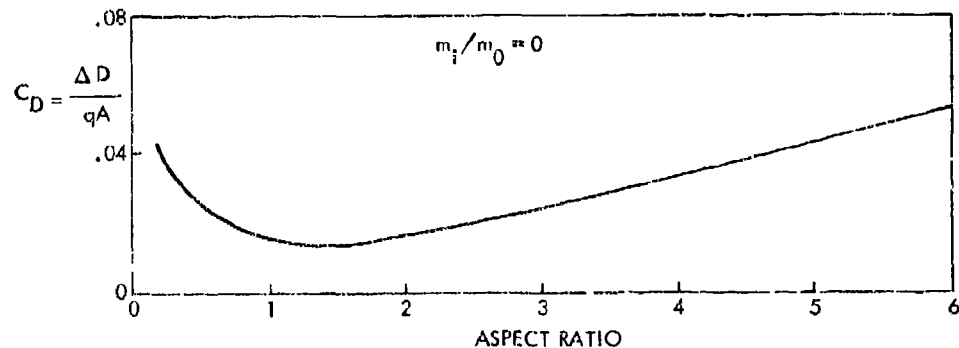


Figure 6.12 Drag of Flush Rectangular Openings at $M = 3.25$. Zero-Flow Conditions (Reference 6.5)

For those applications where flush inlets are located in regions of high static pressure - on the leading edge of wings, for instance - inlet design should follow the guidelines established for nacelles and primary air induction systems. It is possible to optimize such inlets for essentially zero drag in cruise. The reader is referred to such standard guidelines as Reference 6.6.

6.3 Auxiliary Outlets

Auxiliary air exhausted into the mainstream can produce drag or thrust. It can also interact with the boundary layer or other parts of the aircraft so that its effects are magnified. Normally, the outlet air is exhausted aft and the drag is

$$D = -T = -\dot{m}_e V_e \cos \theta \quad (6(1))$$

and for incompressible flow, the outlet drag coefficient based on exit area

$$C_D = -2 \left\{ \frac{V_e}{V_o} \right\}^2 \cos \theta = \frac{D}{q_o A_e} \quad (6(2))$$

where θ is the angle of the exhaust flow relative to the freestream. If the exhaust flow were directed forward, there would be an equal amount of positive drag. If it were exhausted normal to the freestream, there would be ideally no drag or thrust.

Boundary layer and other interactions can be favorable or unfavorable. In some cases outlet flow may cause the boundary layer to separate, while in other cases the boundary layer may be energized by the outlet flow for a significant drag reduction. The designer should take all these factors into consideration when assessing outlet drag.

As was the case for inlets, auxiliary outlets can also be divided into the general categories of protruding, flush, and submerged outlets. When liquids (fuel, etc.) are to be discharged into an airstream, there is generally the requirement that the liquid should not wet the adjacent surfaces. This requirement demands special treatment so that vents and drains will be considered herein as a separate category of protruding outlets.

6.3.1 Protruding Outlets

Protruding outlets can be designed to generate low pressures and thus enhance outlet flow. They also are generally designed to direct the discharge downstream and thus generate thrust. In designing a protruding outlet, the following variables are important.

1. Area of the outlet (which together with the weight flow, w_e , specifies the flow ratio $w_e / (\rho_e V_o A_e)$, where the subscript e denotes exit conditions.
2. Aspect ratio of the outlet, A_F .
3. Flap angle, δ_F , or some other measure of the protrusion.

Reference 6.8 reports an extensive experimental investigation for a range of flapped outlet variables. While it is a good source of specific and detailed design information, it can be used also for some general observation and conclusions. Figure 6.13 shows the configuration tested and defines some of the geometric variables.

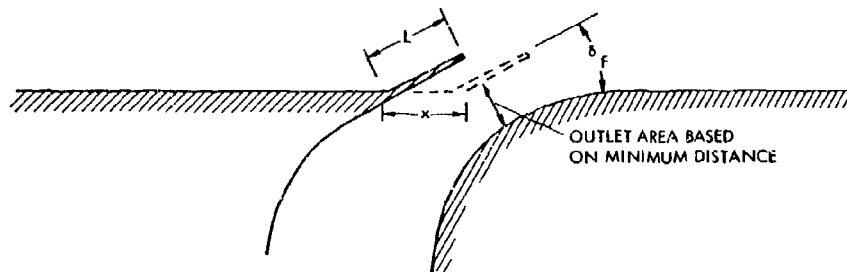


Figure 6.13 Flapped Outlet Test Geometry (Reference 6.8)

Figure 6.14 shows the drag of flapped outlets as a function of flap angle for zero outflow. In this case the drag coefficient is essentially the base pressure coefficient. It can be seen that drag is much lower for $A_F = 2$ than for $A_F = 1$ outlets. Conversely, however, the higher drag of the $A_F = 1$ outlets is accompanied by better discharge coefficients since the flap suction is higher.

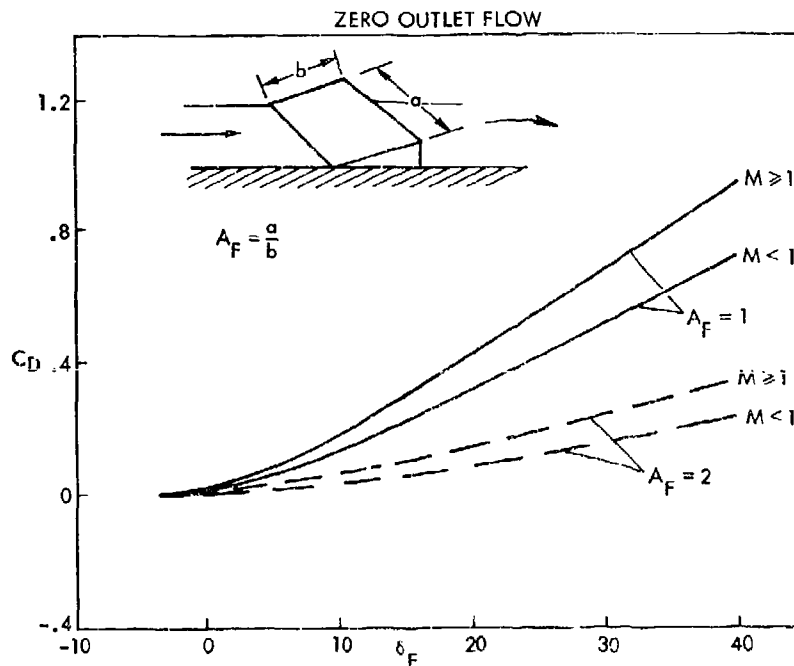


Figure 6.14 Drag of Flapped Outlets - Zero Outlet Flow (Reference 6.8)

The airflow required for zero drag is shown in Figure 6.15 as a function of flap angle. Here again, the $A_F = 2$ flaps show in a better light since mass flow can be reduced to values about half those for $A_F = 1$ before drag is experienced. In a situation favoring fixed flap angles, these data show that an aspect ratio greater than 1 is desirable.

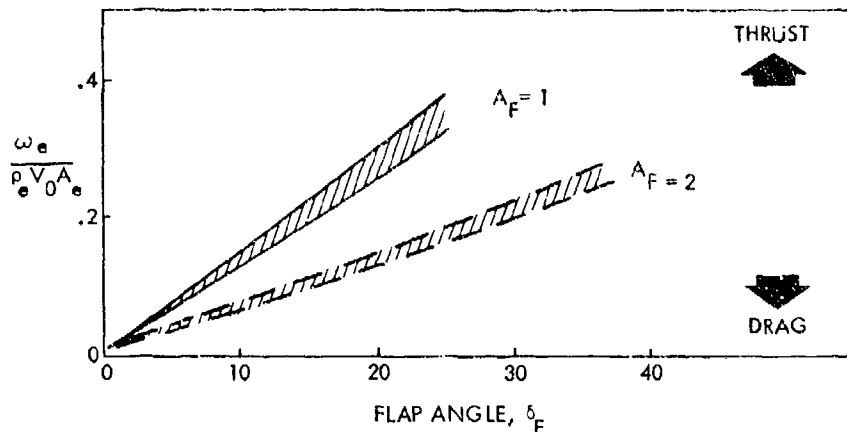


Figure 6.15 Mass Flow for Zero Drag - Flapped Outlets (Reference 6.8)

The data in Figure 6.16 show the apparent thrust (measured thrust minus zero-flow thrust) coefficient for $A_F = 1$ flaps. Also shown is the ideal thrust of the outlet air

$$\Delta C_T = 2 \left(\frac{w_e}{\rho_e V_o A_e} \right) \frac{V_e}{V_o} \quad (6.3)$$

Two things are significant about the curves of Figure 6.16. First it can be seen that δ_F has a second order effect only. As a first approximation it can be assumed that all of the outlet thrust is recovered - not just the horizontal (or $\cos \delta_F$) component. Such an assumption could result in a maximum error in thrust coefficient of about 30 percent at $M = 0.4$ and much smaller errors at high speed. Secondly, the calculated or ideal thrust matches well the measured values at significant levels of ΔC_T . These observations lead to the conclusion that for flap angles up to 30° , the thrust for a flapped outlet is equal to the zero flow thrust (or drag) plus the ideal outlet flow thrust. Thus a reasonable approximation of the thrust or drag of a flapped outlet can be obtained by adding the thrust of the outlet flow to the drag for the zero flow condition which can be obtained from Figure 6.14.

6.3.2 Flush Outlets

Flush outlets with zero outflow usually have zero drag. Exceptions arise for some peculiar shapes and at transonic and supersonic Mach numbers. A long narrow flush outlet with its major axis aligned with the flow will have positive drag at subsonic speeds. In Figure 6.17 data at Mach 3.25 (Reference 6.5) showed all flush outlets to have positive drag at this Mach number. Drag coefficients ranged from about 0.015 at moderate aspect ratios (0.5 to 2.0) up to several times that value at lower and higher aspect ratios.

When flow is added to a flush outlet a thrust is obtained unless the flow is directed upstream. Flush outlets can be divided into two classes - ducted outlets and thin plate outlets - and the drag or thrust characteristics are different for each class. Typical configurations for the two classes are shown in Figure 6.18. For ducted outlets the orientation of the duct sets the outlet inclination angle β while in thin

plate outlets the initial direction of the outlet jet is perpendicular to the mainstream. Nevertheless, there may be some thrust obtained from the thin plate outlets if the aspect ratio is in the range from about 1 to 4.

For ducted outlets with $\beta \leq 30^\circ$ the thrust obtained is, to a first approximation, equivalent to the jet thrust. At higher inclination angles thrust will generally be greater than $T \cos \beta$ but less than T . This can be seen in Figures 6.19(a) and 6.19(b) where thrust coefficients for round ducted outlets at two values of β are shown.

Thrust coefficient decreases with increasing Mach number as shown in Figures 6.20(a) and 6.20(b).

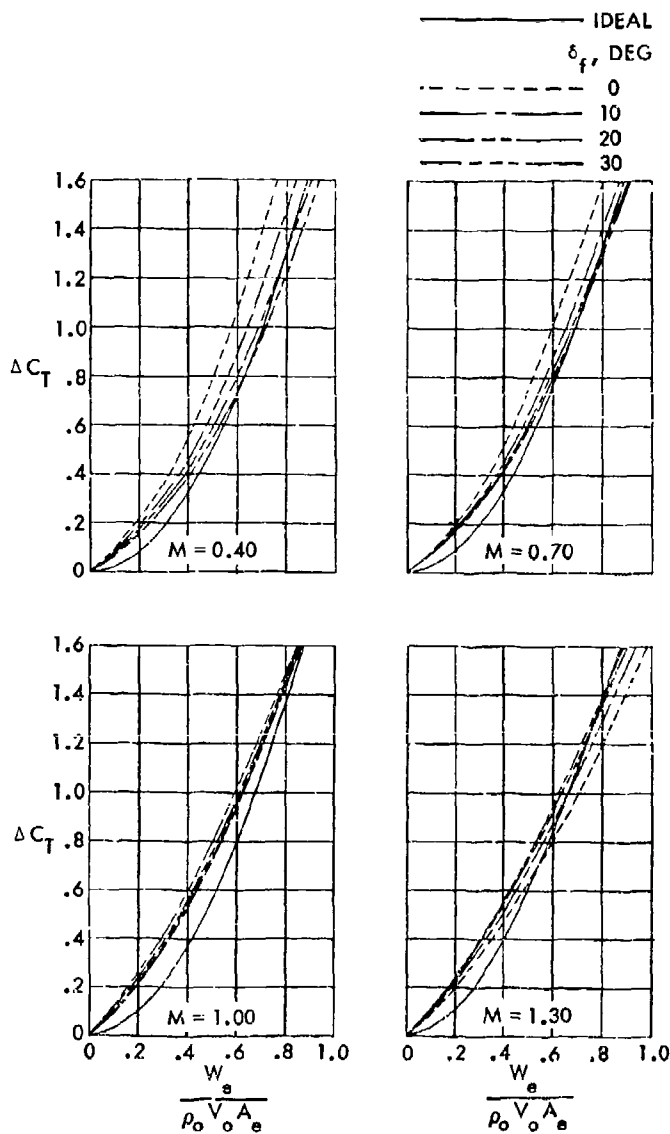


Figure 6.16 Comparisons of Apparent Thrust Produced by Flapped Outlets with Ideal Values. $A_F = 1$; $x/l = 0$ (Reference 6.8)

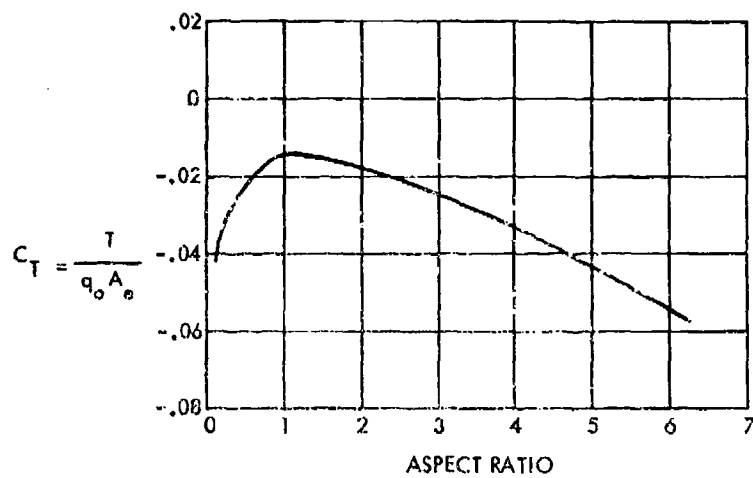


Figure 6.17 Thrust Coefficient at No Flow for Thin-Plate Outlets, $M = 3.25$ (Reference 6.5)

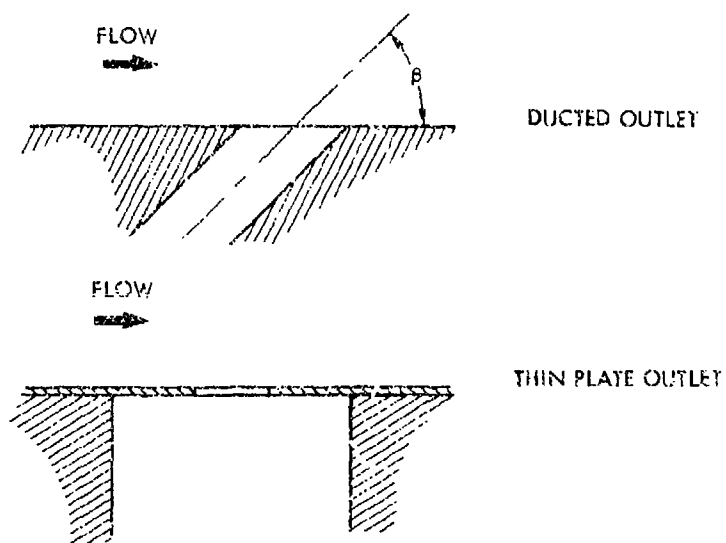
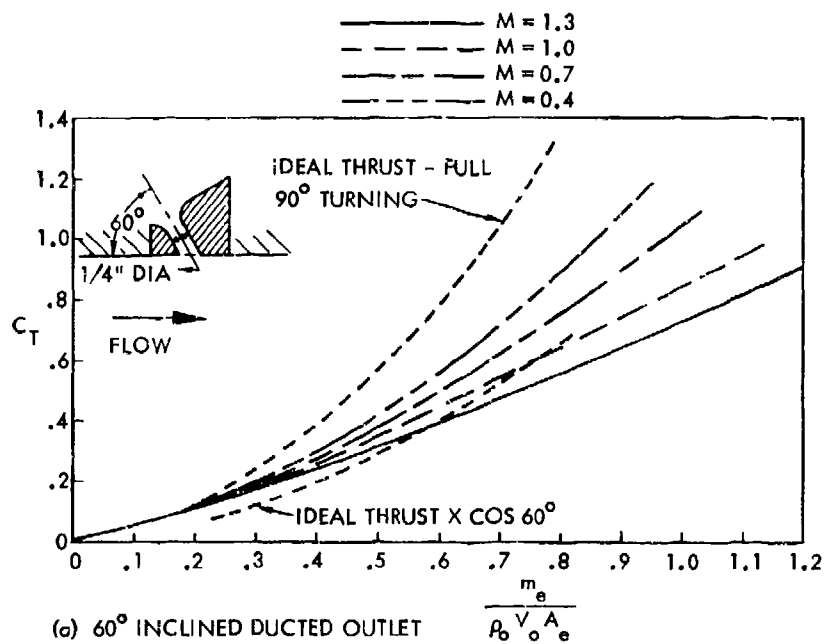
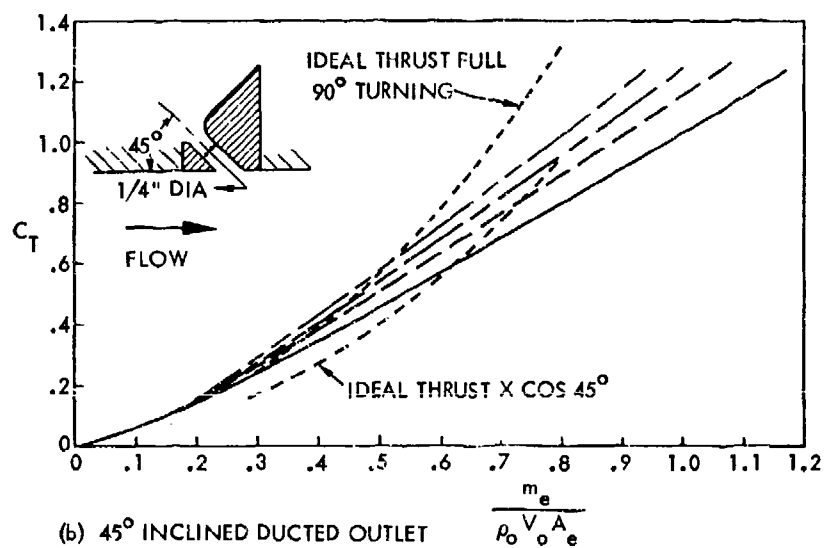


Figure 6.16 Typical Flush Outlet Geometries



(a) 60° INCLINED DUCTED OUTLET



(b) 45° INCLINED DUCTED OUTLET

Figure 6.19 Thrust Coefficients for Circular Ducted Outlets with Various Angles of Inclination (Reference 6.4)

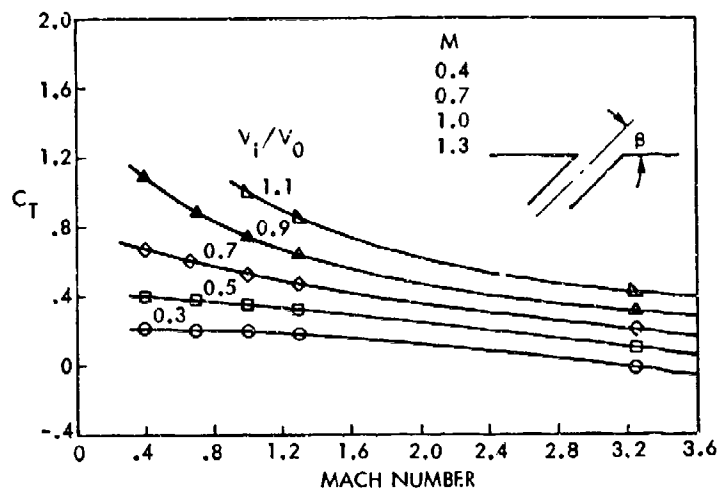
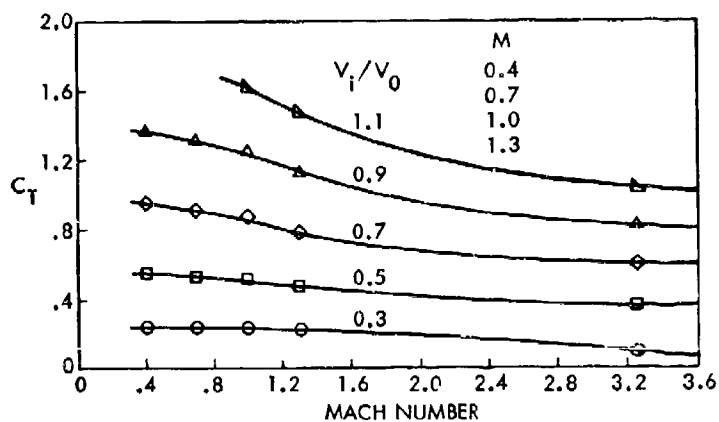
(a) Square Ducted Outlet. $\beta = 60^\circ$ (b) Circular Ducted Outlet. $\beta = 30^\circ$

Figure 6.20 Variation of Thrust Coefficient with Mach Number (Reference 6.5)

6.3.3 Recessed Outlets

Recessed outlets are characterized by a downstream ramp which is recessed below the aircraft surface. At zero outlet flow recessed outlets will generate a negative base pressure and consequently a positive drag. They are, like protruding outlets, useful when needed to aspirate a cavity since the freestream air moving past a recessed outlet will entrain and help to pump the outlet flow. Outlet pressure coefficients for several recessed outlets at zero flow are shown in Figure 6.21. These coefficients are essentially equal to the no-flow drag coefficients.

If a recessed outlet is designed with a good radius on the downstream ramp approach, the outflow should exhaust at a small angle relative to the freestream and all of the exhaust momentum should be recovered as thrust.

6.3.4 Drains

As indicated earlier liquid drains on aircraft fit into a special class of outlets. In normal flight little outflow is expected, and in cases where there is outflow, drag is generally not a critical consideration. An important criterion for drains is generally that the fluid drained should not wet or stain the adjacent surface, and this usually requires that the drain protrude into the freestream flow.

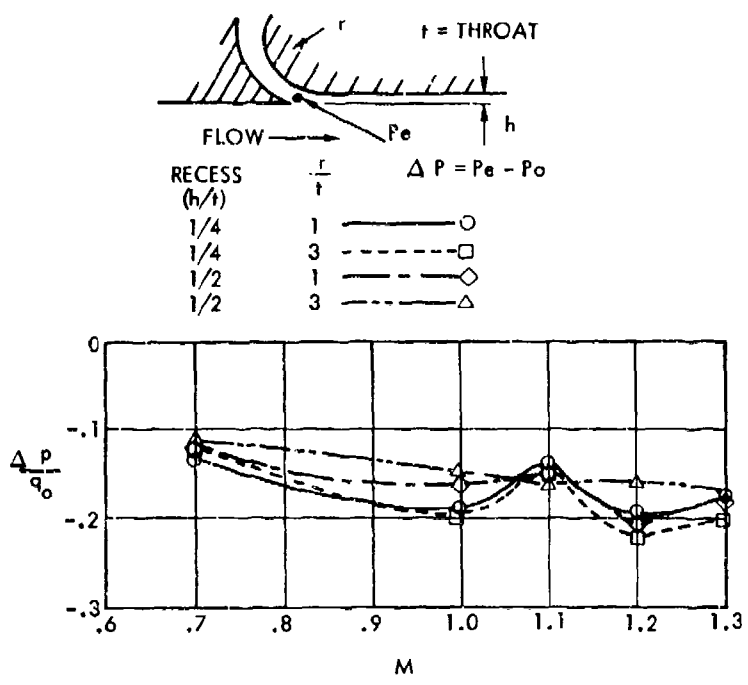


Figure 6.21 Vent Pressures (Reference 6.4) for Recessed Outlets

Reference 6.9 reports an extensive investigation on the ability of various drain configurations to discharge fluid into an airstream without surface staining. Circular and elliptic drains extending normal to the surface always resulted in staining, but the staining was usually eliminated by sweeping the drain 60°. Airfoil-shaped drains - both swept and unswept - were successful in preventing staining.

Drag coefficients for the drains investigated in Reference 6.9 are shown in Figure 6.22. Elliptical cross sections had less drag than circular; swept drains had less drag than unswept; and airfoil shaped drains had the lowest drag. As would be expected, drag with liquid discharge was always lower than with no discharge. External drag for the airfoil-shaped drains was low enough so that flow discharge produced negative drag.

6.4 Leakage Drag

Leakage drag in modern day aircraft is significant primarily because passenger (and often times cargo) compartments are pressurized to maintain tolerable pressure altitudes. As a result, most contemporary high speed aircraft normally operate with internal to external pressure differentials of about 8 psia and small manufacturing defects can result in significant leakage.

Leakage drag also occurs, in a slightly different form, on less sophisticated aircraft which normally operate without cabin pressurization. In this case some pressurization may occur when flow leaks into the aircraft in a high pressure region and leaks out of the aircraft in a low pressure region. If the leaks are flush with the surface, all the drag results from internal flow momentum losses unless the leakage so affects the boundary layer as to cause a significant change in flow pattern.

For conservatism it is generally assumed that leaks exhaust in a direction normal to the freestream so that all the momentum is lost, but in some cases the aircraft structure can be tailored so that leaks exhaust aft and some momentum is recovered.

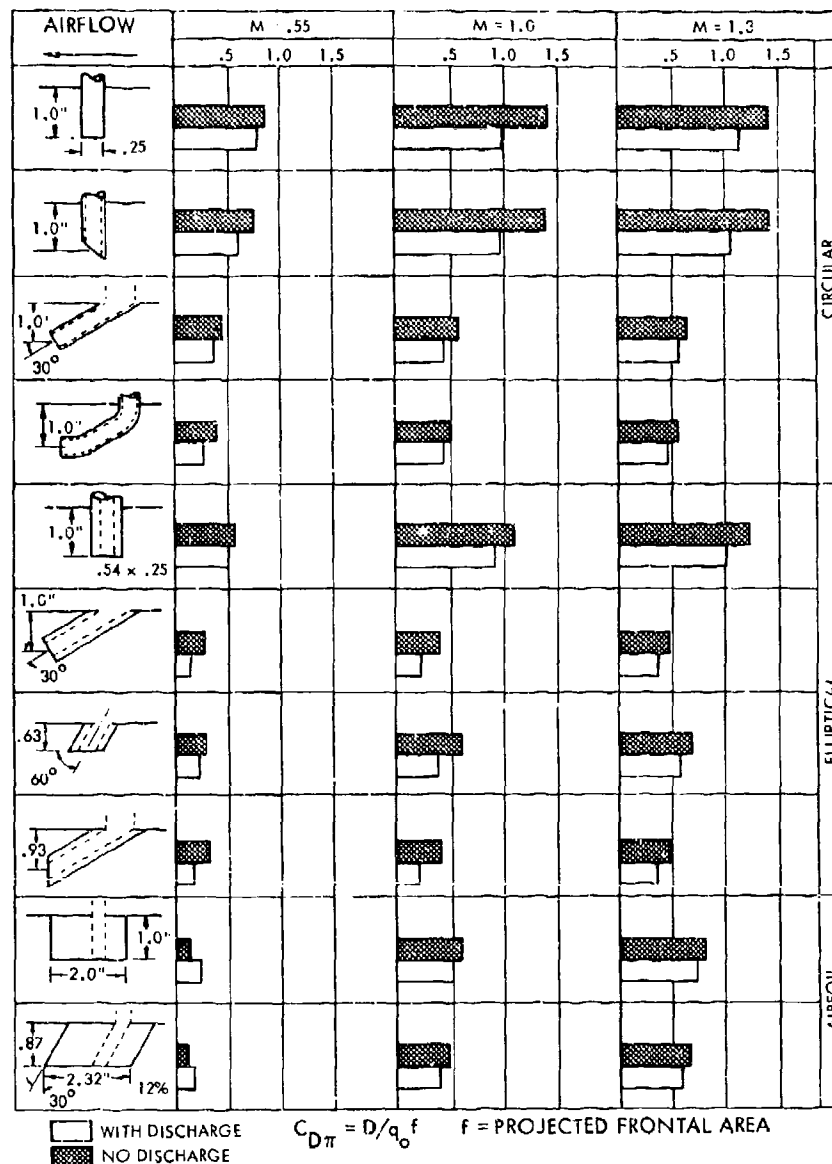


Figure 6.22 Drag of Drains (Reference 6.9)

6.4.1 Leakage Drag - Non-Pressurized Aircraft

As mentioned earlier, external drag due to leaks can generally be neglected since the leakage inlets and outlets are flush with the surface. In this kind of leakage system air flows from the inlet through a duct of some kind thence to the outlet. The duct may be an open bay in the nacelle or fuselage structure for instance. Hoerner (Reference 6.10) defines a drag coefficient for this kind of system in terms of an effective duct cross sectional area A_D in which there is an average velocity w . The drag coefficient based on A_D is then

$$C_{D_{\square \max}} = 2 \frac{w}{V} \quad (\text{where } V \text{ is freestream velocity}). \quad 6(4)$$

$$= D/q_o A_D$$

This is an incompressible flow approximation but is probably valid for those aircraft where this kind of leakage is significant.

Patterson (Reference 6.11) has a more detailed treatment of this kind of leakage drag which takes into account whether the skin joints which leak are forward facing, flush, or rearward facing.

6.4.2 Leakage Drag - Pressurized Aircraft

For those aircraft with pressurized compartments, manufacturing tolerances are usually tight and leakage areas are small. Nevertheless subsonic aircraft leakage drag may approach about 1 percent of total drag. Gyorgyfalvy (Reference 6.12) reports results from flight tests of a Boeing 720 aircraft in which fuselage boundary layer measurements were used to determine drag with the passenger cabin pressurized and unpressurized. He concluded that some additional drag resulted from fuselage bulging and the effects on skin friction, but that most of the 1-1/4 percent drag increase resulted from leakage.

Figure 6.23 shows a plot of leakage area as a function of pressurized volume for a representative group of modern subsonic aircraft. These leakage areas were derived indirectly from measurements of mass flow required to pressurize the aircraft. The data represent three passenger and three cargo aircraft.

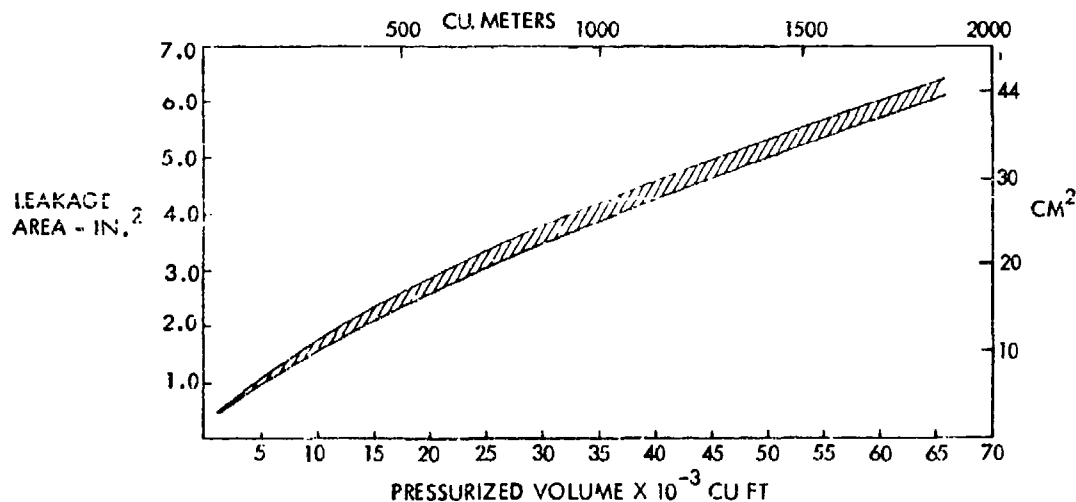


Figure 6.23 Leakage Areas for Modern Pressurized Aircraft

Leakage drag can be estimated from the data of Figure 6.23 when pressure differentials are obtained by specifying cruise altitude and cabin altitude. If it is assumed that all of the momentum of the resulting leakage air is lost, the data of Figure 6.23 will generally not yield drag levels as high as those reported by Gyorgyfalvy. This implies that the impact of leakage on boundary layer flow over the aircraft surface is greater than the leakage air momentum loss effect.

Another word of caution is in order. In determining drag for large complex aircraft, bookkeeping is important. If cabin pressurization air is taken from engine bleed, the airplane's performance may already have been charged with lost momentum of this air which comes through the main propulsion system. In this event the only drag attributable to leakage will be that due to the effects of leakage on the boundary layer flow. If this effect should be favorable or if the leaks are such as to direct the air aft, the leakage momentum could actually result in a drag decrease.

6.5 Supplementary Information

The following list provides additional sources of information concerning the performance of auxiliary and specific designed inlets. However the sources provide no additional drag information.

Dennard, J. S., "A Transonic Investigation of the Mass-Flow and Pressure Recovery Characteristics of Several Types of Auxiliary Air Inlets," NACA RM L57B07, 1957.

Frank, J. L., "Pressure Distribution and Ram-Recovery Characteristics of NACA Submerged Inlets at High Subsonic Speeds," NACA No. RM A50E02, 1950.

Axelson, J. A., Taylor, R.A., "Preliminary Investigation of the Transonic Characteristics of an NACA Submerged Inlet," NACA No. RM A50C13, 1950.

Anderson, W. E., Frazer, A. C., "Investigation of an NACA Submerged Inlet at Mach Numbers from 1.17 to 1.99" NACA RM No. A52F17, 1952.

Simon, P. C., "Internal Performance of a Series of Circular Auxiliary Air Inlets Immersed In A Turbulent Boundary Layer, Mach Number Range 1.5 to 2.0 NACA RM E54L03, 1955.

Sacks, A. H., Spreiter, J. R., "Theoretical Investigation of Submerged Inlets at Slow Speeds," NACA TN 2323, 1951.

Weinstein, M. I., "Performance of Supersonic Scoop Inlets," NACA RM E52A22, 1952.

Boswinkle, R. W., Mitchell, M. H., "Experimental Investigation of Internal-Flow Characteristics of Forward Underslung Fuselage Scoops with Unswept and Sweptback Entrances at Mach Numbers of 1.41 to 1.96," NACA RM L52A24, 1952.

Blackaby, J. R., Watson, E. C., "An Experimental Investigation at Low Speeds of the Effect of Lip Shape on the Drag and Pressure Recovery of a Nose Inlet in a Body of Revolution," NACA TN3170, 1954.

Santman, D. M., "Transonic Performance of a Mach 2.65 Auxiliary Flow Axisymmetric Inlet," NASA CR-2747, 1976.

Dewey, P. E., "A Preliminary Investigation of Aerodynamic Characteristics of Small Inclined Air Outlets at Transonic Mach Numbers," NACA TN 3442, 1935.

Dewey, P. E., Nelson, W. J., "A Transonic Investigation of the Aerodynamic Characteristics of Plate and Bell Type Outlets for Auxiliary Air," NACA RM L52H20, 1952.

Rogallo, F. M., "Wind Tunnel Investigation of Air Inlet and Outlet Openings for Aircraft," NACA MISC 133.

REFERENCES

- 6.1. Dennard, J. S., 1959 "The Total-Pressure Recovery and Drag Characteristics of Several Auxiliary Inlets at Transonic Speeds" NACA Memo No. 12-21-58L.
- 6.2. Rogallo, F. M., 1941 "Internal Flow Systems for Aircraft," NACA Report No. 713.
- 6.3. Simon, P. C. and 1955 "Charts of Boundary-Layer Mass Flow Momentum for Inlet
Kowalski, K. L., Performance Analysis, Mach Number Range, 0.2 to 5.0",
NACA TN 3583.
- 6.4. Dewey, P. E., 1955 "An Investigation of the Discharge and Drag Charac-
Vick, A. R., teristics of Auxiliary Air Outlets Discharging into a
Transonic Stream" NACA TN 3466.
- 6.5. Vick, A. R., 1962 "An Investigation to Determine the Discharge and Thrust
Characteristics of Auxiliary Air Outlets for a Stream
Mach Number of 3.25". NASA TN D-1478.
- 6.6. Baals, D. D.; 1948 "The Development and Application of High Critical-Speed
Smith, N. F.; and Nose Inlets," NACA TR 920.
Wright, J. B.,
- 6.7. Frick, C. W., 1945 "An Experimental Investigation of NACA Submerged-duct
Davis, W. F., Entrances." NACA ACR No. 5120.
Randall, L. M.,
& Mossman, E. A.,
- 6.8. Vick, A. R., 1957 "An Investigation of Discharge and Thrust Charac-
teristics of Flapped Outlets for Stream Mach Numbers
from 0.4 to 1.30", NACA TN4007.
- 6.9. Vick, A. R., 1955 "An Investigation of Drains Discharging Liquid into
Silhan F. V., Subsonic and Transonic Streams", NACA TN3359.
- 6.10. Hörner, S. F., 1958 Fluid Dynamic Drag. Published by the author.
- 6.11. Patterson, G. N. 1938 Estimation and Prediction of Leak Drag. ARC Technical
Report 1939.
- 6.12. Gyorgyfalvy, D. 1965 Effect of Pressurization on Airplane Fuselage Drag.
AIAA J. Aircraft, Vol. 2, No. 6.
- 6.13. Mossman, E. A. & 1947 "An Experimental Investigation of the Design Variables
Randall for NACA Submerged Duct Entrances," NACA RM A7130.

7. CONCLUDING REMARKS AND SUGGESTIONS FOR FUTURE RESEARCH

We have endeavoured in the foregoing to present to the reader the current 'state of the art' of the subject of excrescence and aircraft drag. We have demonstrated the importance of the subject, and as far as possible presented the available information in a way that is readily usable for prediction and design purposes. In particular, we have tried to make it possible for designers to assess realistically the overall net gains that can result from striving for cleanness after allowance for possible extra costs in design effort and weight that may be involved.

We have found it convenient to distinguish between distributed roughness, generally of a scale small in relation to the boundary layer thickness so that the effects are dominated by flow conditions close to the surface, and discrete excrescences where the scale can be much larger and for which main stream flow conditions can be dominant. We have shown how existing methods of predicting the development of turbulent boundary layers on smooth surfaces can be adapted to deal with both distributed and discrete excrescences and the importance of the so-called magnification factors associated with typical pressure distributions over the surface.

It will be evident, however, that a number of important gaps remain in our knowledge where the available information is inadequate for our purpose. The situation is reasonably satisfactory as far as those cases are concerned where two-dimensional data can be adapted with some measure of confidence to provide the answers needed e.g. for aircraft of relatively large aspect ratio and small sweep. With increase of sweep and reduction of aspect ratio the application of such data becomes increasingly uncertain. Our first need, therefore, is for systematic experimental data on the effects of excrescences in three dimensional flows, particularly flows involving large sweep.

Our knowledge of the effects of controls and control gaps as sources of drag is also deficient and more work is needed on the lines of that of Cook described in Section 5.4 but with sweep included as an important parameter.

Another major area of uncertainty due to inadequate basic data is the effects of excrescences on high lift configurations. The importance of these effects goes beyond the question of possible reductions of C_{Lmax} . Any reduction of lift at a given incidence due to excrescences will result in a higher incidence being adopted in order to maintain the lift with a consequent drag increase additional to that due directly to the excrescences. Here again sweep is an important parameter and we should include as excrescences slat and flap brackets and tracks.

We have found relatively little to say about the effects of excrescences at transonic speeds and nothing on their possible effects on shock wave-boundary layer interactions. We know that these interactions can be crucial in determining the overall performance of an aircraft flying at such speeds, and so we must emphasize the need for well planned experiments on possible modifying effects due to excrescences.

Finally we note a paucity of information on the effects of excrescences at supersonic speeds, particularly where the excrescences are large enough to extend into the supersonic region of the boundary layer when they may be expected to generate shock waves additional to those associated with a smooth surface.

It is our hope that those responsible for planning experimental aerodynamic research programs will take careful note of these gaps in our knowledge and will judge them important enough to warrant a considerable effort directed at filling them.

ACKNOWLEDGEMENTS

The authors wish to express their appreciation to our many associates and organizations for suggestions and data included herein. The following colleagues were especially helpful with their advice and assistance - K. Winter (RAE, UK), A. B. Haines (ARA, UK), D. H. Tipper and J. R. Wedderspoon (B. Ae, UK), R. Michel (CERT, France), G. Drougge (FFA, Sweden), and G. Krenz (VFW, Germany). In particular, we wish to thank the Lockheed-Georgia Company for contributions developed with Independent Development funds and for the preparation of the final camera-ready manuscript.

We would like to thank British Aerospace and the Ministry of Defence, UK, for permission to refer to hitherto unpublished material.

We would also like to express our appreciation specifically to W. T. Blackerby for his assistance in the preparation of Chapter IV, to B. H. Little for his assistance in the preparation of Chapter VI and to J. F. Cahill, who reconciled differences in terminology between the authors and edited the final draft.

REPORT DOCUMENTATION PAGE

1. Recipient's Reference	2. Originator's Reference AGARD-AG-264	3. Further Reference ISBN 92-835-1392-4	4. Security Classification of Document UNCLASSIFIED						
5. Originator Advisory Group for Aerospace Research and Development North Atlantic Treaty Organization 7 rue Ancelle, 92200 Neuilly sur Seine, France									
6. Title AIRCRAFT EXCRESCENCE DRAG									
7. Presented at									
8. Author(s)/Editor(s) A.D. Young and J.H. Paterson Edited by J. Lloyd Jones			9. Date July 1981						
10. Author's/Editor's Address (See Flyleaf)			11. Pages 172						
12. Distribution Statement This document is distributed in accordance with AGARD policies and regulations, which are outlined on the Outside Back Covers of all AGARD publications.									
13. Keywords/Descriptors <table border="0" style="width: 100%;"> <tr> <td style="width: 50%;">Aircraft</td> <td style="width: 50%;">Fuselages</td> </tr> <tr> <td>Aircraft protuberances</td> <td>Boundary layer</td> </tr> <tr> <td>Aerodynamic drag</td> <td>Air intakes</td> </tr> </table>				Aircraft	Fuselages	Aircraft protuberances	Boundary layer	Aerodynamic drag	Air intakes
Aircraft	Fuselages								
Aircraft protuberances	Boundary layer								
Aerodynamic drag	Air intakes								
14. Abstract <p>A review has been undertaken of the available data on the subject of the drag of excrescences on aircraft surfaces. Information from this review has been summarized and presented in a way that is readily usable for prediction and design purposes. The basic characteristics of boundary layers are discussed and, where possible, the drag of excrescences is related to those characteristics.</p> <p>In particular, because the size of many types of surface imperfection is small in comparison with boundary layer thicknesses, the drag of such imperfections can be correlated in terms of the properties of inner regions of the boundary layer. Several previously published analyses of this type are highlighted and, where possible, extensions to other data sources or other types of excrescence are presented. The practical problems of applying these data in the varying velocity gradients existing on aircraft surfaces are treated and one section is devoted to the drag of auxiliary air inlet and exit openings. Gaps in existing data which offer opportunities for research effort are pointed out.</p> <p>This AGARDograph was prepared at the request of the Fluid Dynamics Panel of AGARD.</p>									

<p>AGARDograph No. 264 Advisory Group for Aerospace Research and Development, NATO AIRCRAFT EXCRESCENCE DRAG by A.D.Young and J.H.Paterson. Editor: J.Lloyd Jones Published July 1981 172 pages</p> <p>A review has been undertaken of the available data on the subject of the drag of excrescences on aircraft surfaces. Information from this review has been summarized and presented in a way that is readily usable for prediction and design purposes. The basic characteristics of boundary layers are discussed and, where possible, the drag of excrescences is related to those characteristics.</p> <p>P.T.O.</p>	<p>AGARD-AG-264</p> <p>Aircraft Aircraft protuberances Aerodynamic drag Fuselages Boundary layer Air intakes</p>	<p>AGARDograph No. 264 Advisory Group for Aerospace Research and Development, NATO AIRCRAFT EXCRESCENCE DRAG by A.D.Young and J.H.Paterson. Editor: J.Lloyd Jones Published July 1981 172 pages</p> <p>A review has been undertaken of the available data on the subject of the drag of excrescences on aircraft surfaces. Information from this review has been summarized and presented in a way that is readily usable for prediction and design purposes. The basic characteristics of boundary layers are discussed and, where possible, the drag of excrescences is related to those characteristics.</p> <p>P.T.O.</p>	<p>AGARD-AG-264</p> <p>Aircraft Aircraft protuberances Aerodynamic drag Fuselages Boundary layer Air intakes</p>
<p>AGARDograph No. 264 Advisory Group for Aerospace Research and Development, NATO AIRCRAFT EXCRESCENCE DRAG by A.D.Young and J.H.Paterson. Editor: J.Lloyd Jones Published July 1981 172 pages</p> <p>A review has been undertaken of the available data on the subject of the drag of excrescences on aircraft surfaces. Information from this review has been summarized and presented in a way that is readily usable for prediction and design purposes. The basic characteristics of boundary layers are discussed and, where possible, the drag of excrescences is related to those characteristics.</p> <p>P.T.O.</p>	<p>AGARD-AG-264</p> <p>Aircraft Aircraft protuberances Aerodynamic drag Fuselages Boundary layer Air intakes</p>	<p>AGARDograph No. 264 Advisory Group for Aerospace Research and Development, NATO AIRCRAFT EXCRESCENCE DRAG by A.D.Young and J.H.Paterson. Editor: J.Lloyd Jones Published July 1981 172 pages</p> <p>A review has been undertaken of the available data on the subject of the drag of excrescences on aircraft surfaces. Information from this review has been summarized and presented in a way that is readily usable for prediction and design purposes. The basic characteristics of boundary layers are discussed and, where possible, the drag of excrescences is related to those characteristics.</p> <p>P.T.O.</p>	<p>AGARD-AG-264</p> <p>Aircraft Aircraft protuberances Aerodynamic drag Fuselages Boundary layer Air intakes</p>

<p>In particular, because the size of many types of surface imperfection is small in comparison with boundary layer thicknesses, the drag of such imperfections can be correlated in terms of the properties of inner regions of the boundary layer. Several previously published analyses of this type are highlighted and, where possible, extensions to other data sources or other types of excrescences are presented. The practical problems of applying these data in the varying velocity gradients existing on aircraft surfaces are treated and one section is devoted to the drag of auxiliary air inlet and exit openings. Gaps in existing data which offer opportunities for research effort are pointed out.</p> <p>This AGARDograph was prepared at the request of the Fluid Dynamics Panel of AGARD.</p> <p>ISBN 92-835-1392-4</p>	<p>In particular, because the size of many types of surface imperfection is small in comparison with boundary layer thicknesses, the drag of such imperfections can be correlated in terms of the properties of inner regions of the boundary layer. Several previously published analyses of this type are highlighted and, where possible, extensions to other data sources or other types of excrescences are presented. The practical problems of applying these data in the varying velocity gradients existing on aircraft surfaces are treated and one section is devoted to the drag of auxiliary air inlet and exit openings. Gaps in existing data which offer opportunities for research effort are pointed out.</p> <p>This AGARDograph was prepared at the request of the Fluid Dynamics Panel of AGARD.</p> <p>ISBN 92-835-1392-4</p>
<p>In particular, because the size of many types of surface imperfection is small in comparison with boundary layer thicknesses, the drag of such imperfections can be correlated in terms of the properties of inner regions of the boundary layer. Several previously published analyses of this type are highlighted and, where possible, extensions to other data sources or other types of excrescences are presented. The practical problems of applying these data in the varying velocity gradients existing on aircraft surfaces are treated and one section is devoted to the drag of auxiliary air inlet and exit openings. Gaps in existing data which offer opportunities for research effort are pointed out.</p> <p>This AGARDograph was prepared at the request of the Fluid Dynamics Panel of AGARD.</p> <p>ISBN 92-835-1392-4</p>	<p>In particular, because the size of many types of surface imperfection is small in comparison with boundary layer thicknesses, the drag of such imperfections can be correlated in terms of the properties of inner regions of the boundary layer. Several previously published analyses of this type are highlighted and, where possible, extensions to other data sources or other types of excrescences are presented. The practical problems of applying these data in the varying velocity gradients existing on aircraft surfaces are treated and one section is devoted to the drag of auxiliary air inlet and exit openings. Gaps in existing data which offer opportunities for research effort are pointed out.</p> <p>This AGARDograph was prepared at the request of the Fluid Dynamics Panel of AGARD.</p> <p>ISBN 92-835-1392-4</p>